Université catholique de Louvain

École polytechnique de Louvain

Institute of Mechanics, Materials and Civil Engineering

Louvain-la-Neuve, Belgium

STUDY OF VISCOUS DAMPING MODELS FOR NONLINEAR DYNAMIC ANALYSIS OF FRAME STRUCTURES

A dissertation submitted in partial fulfilment of the requirements for the degree of Doctor in engineering sciences

by
Jose Fernando Baena Urrea

2023

Members of the jury:

Chairperson	*Pres. Prof. Hervé Jeanmart*
Supervisor	*Prof. Issam Doghri*
Co-supervisor	*Prof. Jean-François Remacle*
Jury member	*Prof. Vincent Legat*
Jury member	*Prof. Herve Degée*
Jury member	*Prof. Pierre Jehel*

To the victims of earthquakes around the world

ABSTRACT

Nonlinear dynamic analysis of buildings and infrastructure uses viscous damping models to represent energy dissipation sources independent of the materials' constitutive rules. These mechanisms correspond to connections, the interaction between structural and non-structural elements, and the interface between concrete and steel, among others. All these complex sources of energy dissipation have been considered indirectly through viscous damping models since they are expected to have no significant influence on the structure's response. However, it is well known that these models can significantly affect the results when the system enters the inelastic range. This thesis addresses this problem by suggesting modifications for existing models and new approaches. Initially, it is proposed to eliminate the geometric stiffness matrix from the definition of a tangent stiffness proportional viscous damping model. Then, a new condensed damping model proportional to the tangent stiffness matrix is presented to reduce the high energy dissipation caused by the existing condensed models. Finally, new non-linear damping models are formulated that allow limiting the damping forces, ensuring that the assumptions initially used to implement viscous damping models in dynamic analysis are fulfilled.

ACKNOWLEDGEMENTS

I am indebted to the President of the institute (iMMC), Professor Hervé Jeanmart, for all the help and support he gave me during the last year of my PhD.

I am grateful to Professor Issam Doghri and Professor Jean-François Remacle, my supervisor and co-supervisor, during the last stage of my PhD.

I thank Professor Hervé Degée for all the support he gave me during my PhD as part of my supervisory panel.

I also thank Professor Vincent Legat for being part of my supervisory panel at the last stage of my PhD.

I express my gratitude to Professor Pierre Jehel for accepting and dedicating his time to participate as a member of the jury.

I am indebted to all the members of the jury for their time and effort.

I want to thank Professor João Pacheco de Almeida and Professor Ana Acevedo for the opportunity to start my PhD.

I express my deepest gratitude to the Fond Speciaux de Recherche of the Université catholique de Louvain (UCLouvain) for funding this research. Without this support, this dissertation could not have been performed. This financial support is gratefully acknowledged with my deepest present and future feelings.

I am thankful to this magnificent University (UCLouvain), its directors, professors, and staff. These years at this University made me grow personally and professionally. My outlook on life has changed completely.

I am also grateful to my parents for all the support they have given me throughout my life. Especially all those hours dedicated to my education and all the resources they invested in me. Additionally, I would like to thank them and my family for being so patient with me and for the welcome they gave me during my holidays in Colombia.

I want to thank Belgium, this country has given me many friends, good memories, and things. This country will always have a place in my hearth.

I thank my colleagues from GCE, MEMA, and LEMSC for welcoming me to the team. I will never forget all these moments we lived together.

I want to thank my friends, without those good moments and emotional support, this PhD could never have ended.

I am indebted to all those professors and other professionals who trained me.

Finally, I thank the general society in Belgium and Colombia. I could not have gotten that far without the existing conditions and opportunities.

Table of Contents

Notations

Unless otherwise stated, the notation employed in this document is as follows.

a_i	Damping parameters
ALR	Axial load ratio with respect to the full capacity of the section
bsc	An abbreviation that refers to the basic reference system
b	Strain-hardening ratio
$\mathbf{B}$	Cross-section's strain interpolation matrix
$\mathbf{c}^{\mathrm{bsc}}$	Elemental damping matrix at the basic reference system
$\mathbf{c}^{\mathrm{sec}}$	Damping matrix at the sectional level
$\mathbf{c}^{\mathrm{loc}}$	Elemental damping matrix at the local reference system
$\mathbf{c}^{\mathrm{gl}}$	Elemental damping matrix at the global reference system
$\mathbf{C}$	Global damping matrix
CISPD	Condensed initial stiffness proportional damping
CIRD	Condensed initial Rayleigh damping
CTRD	Condensed tangent Rayleigh damping
CTSPD	Condensed tangent stiffness proportional damping
$\mathbf{e}$	Vector of cross section's deformations
E	Young's modulus
E_D	Cumulative energy dissipated by the damping model
E_I	Cumulative energy dissipated introduced by the ground motion record
E_m	Cumulative energy dissipated by the material constitutive rules
EISPD	Elemental initial stiffness proportional damping
EISPD_capped	Elemental initial stiffness proportional damping capped
ETSPD	Elemental tangent stiffness proportional damping
f_c	The compression strength of the concrete
f_t	Tension strength of the concrete
FISPD	Fibre initial stiffness proportional damping
FISPD_bilinear	Fibre initial stiffness proportional damping bilinear
FTSPD	Fibre tangent stiffness proportional damping
$\mathbf{H}$	Matrix containing force or displacement interpolation functions
gl	An abbreviation that refers to the global reference system
GSM	Geometric stiffness matrix
$\mathbf{G}_1^{\mathrm{TanGeoLoc}}$	Component of the geometric stiffness matrix
$\mathbf{G}_{2,3}^{\mathrm{TanGeoLoc}}$	Component of the geometric stiffness matrix
$\mathbf{J_x}$	Influence vector x-axis
$\mathbf{J_z}$	Influence vector z-axis
$\mathbf{k}^{\mathrm{bsc}}$	Elemental stiffness matrix in the basic reference system
$\mathbf{k}^{\mathrm{Tanbsc}}$	Elemental tangent stiffness matrix in the basic reference system
$\mathbf{k}^{\mathrm{sec}}$	Stiffness matrix at the sectional level
$\mathbf{k}^{\mathrm{gl}}$	Elemental Stiffness matrix in the global reference system
$\mathbf{k}^{\mathrm{TanGeoLoc}}$	Geometric component of the elemental tangent stiffness matrix
$\mathbf{k}^{\mathrm{TanLoc}}$	Elemental tangent stiffness matrix at the local reference system
$\mathbf{k}^{\mathrm{TanMatLoc}}$	Material component of the elemental tangent stiffness matrix

$\hat{\mathbf{K}}_{\mathrm{tt}}$	Condensed stiffness matrix defined only in the DoFs with mass
$\mathbf{K}^{\mathrm{Tan}}$	Global tangent stiffness matrix
$\mathbf{K}^{\mathrm{TanGeo}}$	Geometric component of the global stiffness matrix
$\mathbf{K}^{\mathrm{TanMat}}$	Material component of the global stiffness matrix
l	Current length of the beam element
loc	An abbreviation that refers to the local reference system
l_0	Initial length of the beam element
l_{x}	Current distance between the nodes of the beam in the x-local axis
l_{y}	Current distance between the nodes of the beam in the y-local axis
$\mathbf{M}$	Global mass matrix
M_{y}	Yielding moment of the element or cross-section
MD	Modal damping or Wilson and Penzien damping
MSM	Material stiffness matrix
MTSPD	Material tangent stiffness proportional damping
$\mathbf{M}_{\mathrm{tt}}$	Mass stiffness matrix defined in the DoFs with mass
$\mathbf{p}^{\mathrm{bsc}}$	Vector of resisting forces in the basic reference system
$\mathbf{p}^{\mathrm{gl}}$	Vector of elemental resisting forces in the global reference system
$\mathbf{p}^{\mathrm{loc}}$	Vector of elemental resisting forces in the local reference system
P_{y}	Maximum axial capacity
RD	Rayleigh damping
$\mathbf{s}$	Vector of sectional resisting forces
$\mathbf{s}_{\mathrm{m}}$	Vector of sectional material resisting forces
$\mathbf{s}_{\mathrm{d}}$	Vector of sectional damping forces
SPD	Stiffness proportional damping
TIRD	Total initial Rayleigh damping
TISPD	Total initial stiffness proportional damping
TSM	Tangent stiffness matrix
TTSPD	Total tangent stiffness proportional damping
THA	Time history analysis
$\mathbf{u}^{\mathrm{bsc}}$	Vector of basic displacements
$\dot{\mathbf{u}}^{\mathrm{bsc}}$	Vector of basic velocity
$\mathbf{u}^{\mathrm{gl}}$	Vector of elemental displacement at the global reference system
$\dot{\mathbf{u}}^{\mathrm{gl}}$	Vector of elemental velocity at the global reference system
$\mathbf{u}^{\mathrm{loc}}$	Vector of elemental displacement at the local reference system
$\dot{\mathbf{u}}^{\mathrm{loc}}$	Vector of elemental velocity at the local reference system
$\mathbf{U}$	Vector of relative displacement at the global reference system
$\dot{\mathbf{U}}$	Vector of relative velocity at the global reference system
$\ddot{\mathbf{U}}$	Vector of relative acceleration at the global reference system
UCTSPD	Updated condensed tangent stiffness proportional damping
UMD	Updated modal damping
β	Corotating angle
$\mathbf{\Gamma}_{\mathrm{E}}^{\mathrm{bsc-loc}}$	Equilibrium relations between the basic and local reference system
$\mathbf{\Gamma}_{\mathrm{C}}^{\mathrm{gl-loc}}$	Compatibility relations between the global and local reference system
$\mathbf{\Gamma}_{\mathrm{C}}^{\mathrm{loc-bsc}}$	Compatibility relations between the local and basic reference system
$\mathbf{\Gamma}_{\mathrm{E}}^{\mathrm{loc-gl}}$	Equilibrium relations between the local and global reference system

δ	Logarithmic decrement
$\boldsymbol{\varepsilon}_{\mathbf{c}}$	Concrete strain at maximum strength
$\boldsymbol{\varepsilon}_{\mathbf{cu}}$	An ultimate strain of concrete
ε	Strain of the fibre
$\dot{\varepsilon}$	Strain rate of the fibre
ε_0	Strain in the centroid of the cross-section
$\dot{\varepsilon}_0$	Strain rate in the centroid of the cross-section
η	Viscosity modulus
θ	Angle between the local and global reference system
ζ_{eff}	Effective damping ratio
ζ_{i}	Defined damping ratio
σ_y	Yielding stress of the material
χ_{z}	Curvature of the cross-section
$\dot{\chi}_{\mathrm{z}}$	Curvature rate of the cross-section
$\boldsymbol{\Gamma}_{\mathrm{E}}^{\mathrm{bsc-loc}}$	Equilibrium relations between the basic and local reference system
$\boldsymbol{\Gamma}_{\mathrm{C}}^{\mathrm{gl-loc}}$	Compatibility relations between the global and local reference system
$\boldsymbol{\Gamma}_{\mathrm{C}}^{\mathrm{loc-bsc}}$	Compatibility relations between the local and basic reference system
$\boldsymbol{\Gamma}_{\mathrm{E}}^{\mathrm{loc-gl}}$	Equilibrium relations between the local and global reference system

1. Introduction

1.1 Thesis structure

This thesis comprises ten chapters described below to guide the reader through it.

Chapter 1 introduces this document by outlining its structure and context. Then, the problems that motivated its elaboration, objectives, and research methodology are clearly mentioned. Finally, the scientific communication documents derived from this project are indicated.

Chapter 2 contains the state of the art of damping models used in nonlinear dynamic analysis of frame structures. The most relevant existing damping models are described mathematically and conceptually, highlighting their virtues and disadvantages.

Chapters 3, 4, 5, and 6 present the new damping models that address the problems and knowledge gaps indicated in Chapter 1. Following the abstract and introduction to each model, the mathematical formulation and several case studies are shown. Finally, the last section summarises the main conclusions of each chapter.

Chapter 7 provides all the conclusions outlined in the main text. In addition, it highlights the benefits and limitations of the proposed models compared to existing ones. This chapter describes aspects where further research is required.

Chapter 8 lists the references.

Chapter 9 is an annexe introducing fundamental concepts for elaborating nonlinear dynamic analyses of frame structures using distributed plasticity elements.

Chapter 10 is an annexe containing a copy of the finite element software developed by the author during his doctoral thesis for implementing the damping models. Furthermore, this chapter presents a validation of the software by comparing it with OpenSees.

1.2 Context

Earthquakes are sudden movements of the ground caused by the release of energy at the earth's surface. In general, most earthquakes are caused by the interaction of tectonic plates; however, other natural phenomena can cause movements on the earth's surface, such as volcanic activity and ground subsidence due to groundwater scour. In addition, there are sources related to human activities, such as explosions, mine collapse, fracking, and induced seismicity by dam constructions.

Among the different seismogenic sources, the most common and important is the one directly or indirectly related to the movement of tectonic plates. Bolt[1] indicates that 90% of all seismic energy released corresponds to earthquakes occurring on the convergent or transforming tectonic plates, 5% of this energy is released at the divergent plate boundaries, and the remainder is released within the plates.

Earthquake energy is usually released when the crust can no longer deform and the maximum strength of the confined rock is attained, causing the liberation of the elastic energy stored in the crust. This energy is released in two forms: heat and seismic waves propagating through the Earth.

Seismic waves are divided into waves that travel through the body and surface of the Earth. Body waves are classified into P-waves and S-waves. P-waves are longitudinal or compression waves that can travel through solid or liquid-state materials. S-waves are shear waves slower than P-waves and can only travel through solid-state materials. Due to the non-transmissibility of S-waves in liquid-state materials, it is known that part of the earth's core is in this state.

Surface waves are much slower than body waves and cause the greatest damage to human populations, buildings, and infrastructure[2]. The best-known surface waves are called Love and Rayleigh waves. The first kind has a shearing motion perpendicular to the direction of propagation and the second causes particles to move in ellipses in planes normal to the surface and parallel to the direction of propagation.

Earthquakes can affect human populations, buildings, and infrastructure directly or indirectly through other natural phenomena. For example, earthquakes can also cause problems of liquefaction, landslides, and ground failure. In the 20th century, earthquakes triggered damage estimated at 1 trillion dollars adjusted to the year 2000[3]. At today's 2022 values, according to records of inflation and current construction prices, this number could be close to 1.5 trillion dollars. Taking the first value, this represents that the damage caused by earthquakes reached 10 billion dollars each year during the twentieth century. However, this amount is far from the actual damage caused by earthquakes per year since construction prices and existing infrastructure have increased dramatically, and more and more buildings and infrastructure are exposed[4,5]. According to Coburn and Spece[3], the damage caused yearly during the first decade of the 20th century totalled 20 billion dollars.

A better understanding of the behaviour of building materials and structures and advances in structural analysis methods, design methodologies and building codes have resulted in more resilient systems that can achieve the desired performance when exposed to earthquakes. Generally, the vulnerability of buildings and infrastructure after building codes is lower than those analysed, designed, and constructed before. Moreover, this vulnerability is expected to decrease further in newer facilities and infrastructure due to the advances in civil engineering[6,7].

One of these advances is the development of nonlinear dynamic time history analyses (THA). The use of THA is becoming more and more common in the structural engineering community due to the availability of software, computational capacity, and interest in performance-based methodologies. These analyses simulate directly or indirectly the real behaviour of the materials composing the structural elements and the nonlinear geometric effects that appear when the equilibrium equations are formulated in the deformed configuration. This allows a reliable prediction of the structure's response; however, there are still knowledge gaps on nonlinear dynamic THA. One is how to model energy dissipation mechanisms that are not directly considered through the constitutive rules of materials. These energy dissipation mechanisms are the main subject of this doctoral dissertation.

A dynamically loaded structure oscillates until the load disappears, and all the energy introduced is dissipated through several physical mechanisms. In reality, these mechanisms correspond to the constitutive rules of materials, the interface between steel and concrete, connections between structural members, the interaction between structural and non-structural elements, interaction between non-structural components, soil-structure interaction, and air-structure interaction, among other sources. The complexity and number of mechanisms that dissipate energy in a structural system have led engineers to model all these sources of energy dissipation in linear dynamic analysis through simplified viscous damping models.

The use of viscous damping models to simulate complex energy-dissipating mechanisms was first proposed by Lord Rayleigh[8] on the decay of sound waves due to friction. Lord Rayleigh justified his model under the premise that it had “a sufficient degree of approximation for acoustic purposes”[8]. In other words, any inaccuracies would not significantly affect the results.

The Rayleigh damping (RD) model has been used under the same argument in linear dynamic analyses of several linear mechanical SDoF and MDoF systems when the modal analysis is used. Subsequently, Berg[9] and Wilson and Clough[10] suggested defining a damping matrix through RD for the step-by-step analysis of linear MDoF systems where the system of equations is solved directly and not through modal analysis. Wilson and Clough[11] justified this model with the same argument as Lord Rayleigh. However, recognising that the damping mechanisms in a structure are largely unknown.

The RD was used by analogy in nonlinear dynamic analyses when they were developed. Nevertheless, the assumptions made by Lord Rayleigh[8] and Wilson and Clough[10] are not fulfilled. The consequences and problems of traditional and existing damping models have motivated much research over the last decades, where methodologies and new models have been proposed. However, today there is no clear consensus on how to model these energy dissipation sources independent of the materials' constitutive rules. The absence of agreement and the problems of the existing models were the primary motivation for this doctoral dissertation.

The following sub-chapter indicates the gaps in knowledge on this topic identified during this research project. Subsequently, the general and specific objectives of this doctoral dissertation are listed.

1.3 Knowledge gaps, problems and motivation

1.3.1 Presence of the geometric stiffness matrix in a tangent stiffness proportional damping model

Finite element (FE) software packages often use the updated Lagrangian[12–14] or the corotational[15–17] formulations to model nonlinear geometrical effects on beams and other elements. The updated Lagrangian uses the reference configuration of the previous converged step to formulate the FE equations, and it is fixed for a certain period Δt[15], whereas in the corotational formulation, the reference configuration is continuously updated following the displacements and rotation of the element. Even if it is recognized that the corotational formulation is more accurate[18], each formulation has advantages over the others that are not described in this document but can be found elsewhere[18,19].

For extreme loads and systems susceptible to large deformations, disregarding nonlinear geometric effects in the numerical response of the structure may lead to erroneous and unconservative analyses. It is always advisable to consider them, even for non-slender structures.

When nonlinear geometric effects are considered, the system's stiffness matrix comprises two components, one linked to the material and the other corresponding to the nonlinear geometric effects. This matrix is known as the geometric stiffness matrix (GSM), which considers the effect of formulating equilibrium equations in the deformed configuration. The magnitude of the GSM entries is small compared to those of the material stiffness matrix (MSM) in most structures designed in high and intermediate seismic hazard zones. However, when the system is subjected to extreme loads, the MSM can decrease considerably, causing the geometric stiffness matrix to become proportionally more important than in the elastic range.

These effects can bring unwarranted consequences when they are considered in the definition of a stiffness proportional viscous damping. Especially when a tangent stiffness proportional viscous damping model (TTSPD) is used, which is one of the most common models in commercial and Open-Source software.

The TTSPD maintains the damping forces at low levels even during incursions in the inelastic range with significant changes in deformations and velocities. This is explained by the tangent stiffness matrix decaying in the inelastic range so that the damping forces do not take elevated values. However, when the structure yields and is subjected to large deformations, the damping forces can disappear or even take negative values due to the negative stiffness of the materials under large deformation and the geometric stiffness matrix.

The presence of geometric stiffness in the definition of the damping model has been criticised by Chopra and Mckenna[21], Charney[22], Mondkar and Powell[23], and Charney et al.[24]. Moreover, its presence is sometimes used as a reason for not recommending the TTSPD.

This thesis defines a damping model proportional to the tangent stiffness matrix (TSM) without including the geometric stiffness matrix. The arguments for proposing this model are based on the facts that: (i) the GSM is not a mechanical but a purely geometrical component resulting from formulating the equilibrium equations in the deformed configuration, (ii) the energy dissipation mechanisms modelled through viscous damping models are not affected by the GSM, and (iii) when a damping model proportional to the GSM is defined, the model may introduce energy at high displacement demands when the material stiffness matrix (MSM) decays sufficiently. The possibility of introducing energy into the system through the GSM is a fundamental argument for its removal since it falls outside the realm of conceivable physical and structural phenomena.

1.3.2 High energy dissipation and damping forces on condensed damping models

The stiffness-proportional component of the Rayleigh model has often been criticised since damping forces and moments appear in the massless DoFs when the system enters the inelastic range, which do not exist in the elastic range. Therefore, their appearance is difficult to explain due to their high magnitude, and from a physical point of view, such forces and moments have no justification[21,25].

Some authors[21,25] have proposed to define condensed damping models, where the damping matrix has non-zero values only in the DoFs with mass. The entries of the matrix related with the DoFs without mass are defined with zeros to eliminate these forces and moments, considered "spurious". The condensed models have been scarcely studied since they are difficult to implement in commercial finite element programs. Among all the existing ones, the only one available in some programs is the Wilson and Penzien[11] model, also known as modal damping.

Condensed damping models may be equally inappropriate for nonlinear dynamic analyses since the initial properties of the system define them[26]. This implies that the damping forces can increase without limit, causing a response that may be unconservative. Furthermore, these models are criticised as the damping matrix, defined between the DoFs with mass, is fully populated. The latter condition implies dampers between DoFs that are not physically connected, and it is not ideal for the skyline matrix storage commonly used in finite element programs. Finally, since the massless DoFs have no damping, their velocities exhibit large fluctuations during the analysis.

This thesis reports the performance of all condensed damping models using realistic cases and compares them with global models commonly available in commercial software. The proposed case studies correspond to reinforced concrete and steel structures subjected to ground motion records under high demands. The results clearly show the benefits and disadvantages of these models and their applicability in commercial finite element programs. Additionally, this thesis proposes a damping model proportional to the condensed stiffness matrix - in opposition to the total stiffness matrix - using the tangent stiffness matrix, which has not been explored in the literature.

The implementation of all condensed models in the author's software, the results, and the conclusions presented are relevant contributions to the literature since they are rarely implemented in commercial programs.

1.3.3 Nonlinear viscous damping models

RD was used by analogy in nonlinear dynamic analyses when they were developed. However, the assumptions made by Lord Rayleigh[8] and Wilson and Clough[10] are not fulfilled. In systems with an inelastic resisting system, the damping forces can reach proportionally higher magnitudes compared to the material resisting forces. Therefore, the damping forces are not small, can reach considerable magnitudes, and significantly affect the structure's response. Furthermore, it is well known that the component proportional to the stiffness matrix causes the higher modes to have a larger effective damping ratio.

Traditional damping models such as RD, Mass, and stiffness proportional damping models (MPD and SPD, respectively) define the damping forces through linear models proportional to the velocities of the system. This condition is not a problem during linear dynamic analyses since the material-related resisting forces are also linear and directly proportional to the deformations. Therefore, the ratio between the maximum damping and material resistance forces will be in an acceptable magnitude range. In inelastic systems, the material resisting forces are defined through nonlinear constitutive rules. However, the damping forces are still defined through linear models. When the structure or structural elements reach their yield strength, significant changes in deformations and hence velocities occur. The material resisting forces arrive at a predefined value, while the damping forces increase to magnitude values that are not easy to justify [21,25,27–29]. In some specific cases, the damping forces can reach a magnitude equal to the capacity of the structural members[25].

The limitations of traditional damping models have motivated substantial research over the last decades, where methodologies and new models have been proposed to improve the treatment of the sources of energy dissipation independent of the material's constitutive rules. However, the community has not yet reached a consensus.

Recently, some nonlinear damping models have emerged in the literature. These models guarantee that the damping forces are at reasonable [8,27,29,30] levels and thus solve the main problem of traditional damping models. From the perspective of the author of this thesis, nonlinear damping models are promising since that they provide essential flexibility in modelling damping forces. Nevertheless, existing nonlinear damping models for structural engineering cannot easily be implemented in commercial software. In addition, these models need partial calculations of the inter-storey strength and stiffness.

This thesis studies new nonlinear damping models that solve the numerical difficulties of existing models. These models were developed for systems using elements with distributed plasticity, employing a formulation with certain numerical and mathematical simplifications presented in chapter 5 and another formulation entirely consistent from a numerical and mathematical point of view in chapter 6.

Both models aim to contribute to nonlinear damping modes for frame elements in structural engineering, which have been little studied in the literature. Furthermore, their development seeks to limit the magnitude of the damping forces to reasonable [27,29,30] values compared to the resisting forces of the materials. This is intended to fulfil the initial assumptions Rayleigh[8], Wilson, and Clough[10] used to implement viscous damping models in dynamic analysis.

1.4 Objectives

1.4.1 General objective

To evaluate the performance of newly proposed damping models in relation to the identified problems of existing models in nonlinear dynamic analyses of frame structures.

1.4.2 Specific objectives

- To assess a total tangent stiffness proportional damping model independent of the geometric stiffness matrix for nonlinear dynamic analyses
- To evaluate a condensed tangent stiffness proportional damping model for nonlinear dynamic analyses.
- To analyse an elemental capped damping model applied at the basic reference system for nonlinear dynamic analyses using distributed plasticity elements.
- To examine a fibre-based non-linear damping model for dynamic analyses using distributed plasticity elements.

1.5 Research methodology

This thesis was developed in a single work front that proposed and evaluated new damping models that solve one or more problems of the traditional models.

One main obstacle to develop this project was finding a finite element program to implement the new damping models. Unfortunately, most commercial programs are not open source; hence, modifying them or implementing new damping models is impossible. Some open-source programs like OpenSees were also not created to implement new damping models quickly.

Therefore, before starting this research work, it was necessary to create a finite element program capable of performing nonlinear static and dynamic analysis on 2D and 3D structures from zero. The author of this work almost entirely developed this program to achieve the objectives. The program is presented in the last chapter as a fundamental part of the development of this thesis.

This program was compared with commercial and opensource programs such as Seismostruct and OpenSees using different case studies of static and dynamic nonlinear analysis of concrete and steel structures, presented in the annexes. The program's prediction developed by the author is equivalent to the aforementioned programs. This guarantees the validity of the numerical models needed to perform this type of analysis. The validations of the software results are presented in Annex 10.

The damping models were implemented in the finite element program and tested under dozens of different structures. However, only the most relevant cases are presented in the text, where the advantages of the new models are clearly shown. Subsequently, a detailed numerical and conceptual analysis is presented to justify and further explain the benefits of the new approaches.

The results and performance of the damping models are analysed mainly from a theoretical and numerical behavioural point of view, following the methodology presented in the vast majority of manuscripts on this subject. In addition, some comparisons with experimental information in the literature are shown, but it is emphasised that information from dynamic tests is rarely available. Comparison with experimental data provides considerable scientific support.

1.6 Scientific communication

Journal articles

- Baena-Urrea JF, Almeida JP. Material-tangent-stiffness-proportional viscous damping for nonlinear geometric inelastic frame analysis. *Earthquake Engineering and Structural Dynamics* 2022.
- Baena-Urrea JF. Fibre-based nonlinear viscous damping model defined for dynamic analysis using distributed plasticity elements. **(Submitted to the journal of earthquake engineering)**

Conference articles

- Baena-Urrea JF, Almeida JP. Tangent-stiffness-proportional viscous damping independent of the geometric stiffness matrix. *3rd European Conference on Earthquake Engineering and Seismology*, Bucharest, Romania: 2022.
- Baena-Urrea JF, Almeida JP. Condensed-tangent-stiffness-proportional viscous damping model for nonlinear time history analysis. *3rd European Conference on Earthquake Engineering and Seismology*, Bucharest, Romania: 2022.

2. Literature review of viscous damping models

The use of nonlinear analyses has spread during the last decades among the engineering community due to the availability of more advanced models and software running on increasingly powerful hardware and the growing relevance of performance-based design and assessment of structures[31]. The standard system of equations expressing equilibrium in nonlinear time history analysis (THA) using viscous damping is

$$\begin{bmatrix} \mathbf{M}_{\mathrm{tt}} & 0 \\ 0 & 0 \end{bmatrix} \begin{Bmatrix} \ddot{\mathbf{U}}_{\mathrm{t}}(\mathrm{t}) \\ \ddot{\mathbf{U}}_{0}(\mathrm{t}) \end{Bmatrix} + \begin{bmatrix} \mathbf{C}_{\mathrm{tt}} & \mathbf{C}_{\mathrm{t0}} \\ \mathbf{C}_{\mathrm{0t}} & \mathbf{C}_{00} \end{bmatrix} \begin{Bmatrix} \dot{\mathbf{U}}_{\mathrm{t}}(\mathrm{t}) \\ \dot{\mathbf{U}}_{0}(\mathrm{t}) \end{Bmatrix} + \{\mathbf{f}(\mathbf{U}(\mathrm{t}))\} = \begin{Bmatrix} \mathbf{P}_{\mathrm{Et}}(\mathrm{t}) \\ \mathbf{P}_{\mathrm{E0}}(\mathrm{t}) \end{Bmatrix} + \begin{Bmatrix} \mathbf{P}_{\mathrm{gt}} \\ \mathbf{P}_{\mathrm{g0}} \end{Bmatrix} \quad (2.1)$$

Where **M** and **C** are the mass and damping matrices, respectively, **f** (**U**(t)) is the nonlinear relation between the force and deformation of the system, including nonlinear geometric effects and the materials' nonlinear behaviour. In the case of earthquake loading, the vectors $\mathbf{U}$, $\dot{\mathbf{U}}$, and $\ddot{\mathbf{U}}$ refer to the relative displacement, velocity, and acceleration of the DoFs. The right side of eq. (2.1) contains the static and dynamic loads applied to the system. The vector $\mathbf{P}_{\mathrm{E}}(\mathrm{t})$ is commonly used to express the earthquake forces at the DoFs with mass. For instance, in a 2D system $\begin{Bmatrix} \mathbf{P}_{\mathrm{Et}}(\mathrm{t}) \\ \mathbf{P}_{\mathrm{E0}}(\mathrm{t}) \end{Bmatrix} = \begin{Bmatrix} \mathbf{P}_{\mathrm{Et}}(\mathrm{t}) \\ 0 \end{Bmatrix} = \begin{Bmatrix} -\mathbf{M}_{\mathrm{tt}}\mathbf{J}_{\mathbf{x}}\ddot{\mathrm{u}}_{\mathrm{gx}}(\mathrm{t}) \\ 0 \end{Bmatrix} + \begin{Bmatrix} -\mathbf{M}_{\mathrm{tt}}\mathbf{J}_{\mathbf{z}}\ddot{\mathrm{u}}_{\mathrm{gz}}(\mathrm{t}) \\ 0 \end{Bmatrix}$. where the vector $\mathbf{J}_{\mathbf{x}}$ and $\mathbf{J}_{\mathbf{y}}$ denote the influence vector indicating the DoFs affected by the ground acceleration, $\ddot{u}_{gx}$ and $\ddot{u}_{gy}$, in the horizontal and vertical directions. The gravity and static forces $\begin{Bmatrix} \mathbf{P}_{\mathrm{gt}} \\ \mathbf{P}_{\mathrm{g0}} \end{Bmatrix}$ may be defined in all the DoFs. The subscripts t and 0 represent the mass and massless DoFs.

The energy imparted by an external force on the structure is equal to the sum of the kinetic energy of its mass, the energy permanently and temporarily stored in the hysteretic cycles, and the energy dissipated by other sources such as friction between structural and non-structural elements, micro hysteretic curves in structural and non-structural components, soil-structure interaction, among others[32,33]. Trying to model these sources of energy dissipation directly through mathematical models would make the nonlinear analysis unpragmatic and even unfeasible. Therefore, all these sources of energy dissipation not dependent on hysteretic cycles have been commonly represented by viscous damping models calibrated through experimental data of structures under small-amplitude vibrations. In nonlinear THA, the damping forces are represented by the second term of eq. (2.1).

Lord Rayleigh[8] originally proposed the first viscous damping model under the premise "with a degree of approximation sufficient for acoustics purposes". The Rayleigh damping (RD) model was implemented in linear dynamic analysis of structures since the effect of damping forces on the structure's response is small. For instance, in a linear single degree of freedom (SDoF) using a damping ratio of 5%, the damping force may reach approximately 10% of the inertial or elastic forces of the structure[29,34,35]. Using this argument, Wilson and Clough[11] mentioned that it is justifiable to use RD for step-by-step linear dynamic analyses of multi-degree of freedom (MDoF). Nevertheless, recognizing that the exact form of damping in most structures is unknown.

Rayleigh model has been widely used in different engineering fields since its definition is simple, does not require additional calculations and provides an orthogonal matrix with the modal shapes of the structural system. Due to its simplicity and advantages, RD is probably the most widespread and used damping model in finite element programs.

RD was implemented in nonlinear dynamic analyses of SDoF and MDoF systems by analogy with the linear case. However, RD defines a large effective damping ratio on the higher modes, which leads to a generalised overdamped response of the structure and proportionally high damping forces when the stiffness decays after and during incursions in the inelastic range[22,25,28,36]. For instance, in the case of an inelastic SDoF defined with a damping ratio of 5%, the damping forces reach 20% of the system's resisting and inertial forces and even increase to higher magnitudes in some cases. The latter causes an underestimation of displacements, internal forces, and the amount of energy dissipated by the constitutive rules of the materials[26,30,37]. Furthermore, the stiffness proportional component of RD triggers the appearance of unbalanced or “spurious” damping forces in the massless DoF during and after incursions in the inelastic range[23,25,38] which are difficult to explain physically due to their magnitude. These consequences have been the arguments for proposing and researching new strategies to model the energy dissipation of mechanisms independent of the constitutive rules of the material.

The modelling of damping in nonlinear structural analyses has been intensively studied over the last 35 years, but no methodology is universally accepted. This chapter presents a literature review of the main models to define the damping matrix and damping forces to simulate the sources of energy dissipation independent of the constitutive rules of materials developed in recent years. After the physical and mathematical description of each model and strategy, detailed discussions about the advantages and disadvantages are presented, highlighting the arguments exposed in the scientific field. However, this chapter and this thesis do not include other methodologies, such as numerical damping from some integration methods or approaches that have not been commonly used in the context of nonlinear dynamic analysis of frame MDoF systems. This chapter is divided into two main sub-chapters: linear and nonlinear damping models.

2.1 Linear viscous damping model

This section presents essential linear damping models in the literature. The definition of linear models is considered when a constant matrix relates the vector of forces and velocities throughout the analysis. Additionally, all local formulations with a constant relationship between damping forces and velocities are included. Therefore, all models involving reformulations of the relationship between damping forces and velocities are considered nonlinear, even though they are strictly an ad hoc method to simulate nonlinear behaviour.

2.1.1 Total global viscous damping models

Rayleigh damping model was defined using eq. (2.2) as a combination of mass and stiffness matrix multiplied by two damping parameters.

$$[\mathbf{C}] = \mathrm{a}_0[\mathbf{M}] + \mathrm{a}_1[\mathbf{K}] \tag{2.2}$$

The damping parameters are found through eq. (2.3) using two frequencies and two damping ratios.

$$\begin{Bmatrix} \zeta_i \\ \zeta_j \end{Bmatrix} = \frac{1}{2}\begin{bmatrix} \omega_i^{-1} & \omega_i \\ \omega_j^{-1} & \omega_j \end{bmatrix}\begin{Bmatrix} a_0 \\ a_1 \end{Bmatrix} \tag{2.3}$$

An only mass or stiffness proportional damping model can be defined using the following damping parameters.

$$a_0 = 2\zeta_i\omega_i \quad \text{or} \quad a_1 = \frac{2\zeta_i}{\omega_i} \tag{2.4}$$

The frequencies used for its definition are commonly those of the structure. However, some studies[39,40] choose other frequencies to consider the decay of the natural frequencies after the system enters the inelastic range. Additionally, the damping ratio is generally defined by the type of material, but it may vary according to the building use, height, and other parameters[41–43].

The mass component of RD has a small effective damping ratio in the upper modes. Like the previous component, it can cause high damping forces when the system yields[44,45]. MPD presents an arrangement of dampers challenging to justify, which would physically correspond to air-structure interaction or the masses sliding inside the building. However, some authors[46] indicate that these physical phenomena are negligible. In addition, the damping forces are proportional to the rigid body motion of the structure, which also has no valid physical justification and makes this model undesirable for structural systems with seismic isolators[27,37,47]. Perform3D[48] proposes two options for isolated structures (i) a RD model where the mass-proportional term is connected to the soil, affecting the entire structure, and the damping parameter is defined with the structure's period considering the elastic properties of the isolators. (ii) a RD model where the mass proportional dampers are connected to the level above the isolators, affects only the isolated structure, and the period of the superstructure is used to define the damping parameter. Perform3D[48] highlights that the experience shows little difference between the two methods and suggests using the first option.

The stiffness component of RD has several problems in dynamic analysis: (i) higher modes have large damping ratios[22,36], (ii) the magnitude of the damping forces can be relatively significant, and (iii) when the structure yields, damping forces appear in the massless DoFs[25,28,38]. The latter can cause an overstrength capacity, unconservative analyses, and potential mistakes. For example, Medina and Krawinkler[37] showed that maximum floor drifts and peak resistance demands could be underestimated by about 10% and 30%, respectively, on regular moment-resisting frame structures exposed to far-field ground motions using a damping ratio of 5%. Chrisp[28] and Bernal[25] early described these pathologies. However, Kanaan and Powell[38] also mentioned the problems related to unbalanced moments during incursions in the inelastic range.

Despite all the problems, this component of the Rayleigh model is the most accepted from a physical point of view since the energy dissipated by the damping forces is proportional to the change of internal deformations of the structural element with respect to time. Additionally, this model remains constant through the analysis, which is attractive from a computational cost point of view. Some programs and researchers have chosen to use it but modifying the initial stiffness of the structural elements to avoid problems and numerical pathologies. For instance, Perform3D[48] uses 15% of the area of the fibres in reinforced concrete sections to define the damping matrix. This is done to consider the cracked fibres of RC elements. Still, it uses 100% of the fibres for metallic elements.

OpenSees[49] presents different options for defining the damping matrix described in this chapter. The developers of this program allow to extract and save the stiffness matrix of the last step to be used to define the damping matrix. This methodology can be particularly useful in concrete structures that experience significant stiffness changes due to the early cracking of concrete fibres under substantial seismic or gravity loads. However, this methodology implies that the analysis must be conducted twice, and special care must be taken in defining the damping parameter.

Moreover, it is possible to define a damping matrix by weighting different models in OpenSees[49]. For example, it is feasible to specify a damping matrix that accounts for both the initial stiffness matrix and the tangent to have an intermediate between the two models. Additionally, it is possible to define other combinations with the mass matrix, current stiffness, last converged stiffness, and even the Wilson and Penzien[11] model.

2.1.2 Condensed global viscous damping models

Some authors[25,29,30,50] have proposed defining the viscous damping matrix only between the DoFs with mass to eliminate the “spurious” damping forces appearing during incursions in the inelastic range. Thus, the position related to the massless DoFs will be defined with zero values. In reality, the systems with massless DoFs do not exist; nevertheless, this assumption is customarily used since structural inertia can be well represented without defining the mass in all DoFs of the structure. Additionally, determining each node's mass on large systems is not pragmatic.

The condensed Rayleigh damping model was presented by Bernal[25], who proposed eliminating the spurious damping in the massless DoFs using the condensed initial stiffness matrix. The Rayleigh model is defined in a condensed form with eq. (2.5), where the damping parameters are equally defined using the eq. (2.3).

$$\begin{bmatrix} \mathbf{C}_{tt} & \mathbf{C}_{t0} \\ \mathbf{C}_{0t} & \mathbf{C}_{00} \end{bmatrix} = a_0 \begin{bmatrix} \mathbf{M}_{tt} & 0 \\ 0 & 0 \end{bmatrix} + a_1 \begin{bmatrix} \widehat{\mathbf{K}}_{tt} & 0 \\ 0 & 0 \end{bmatrix} \tag{2.5}$$

where $\widehat{\mathbf{K}}_{tt}$ is the condensed stiffness matrix given by eq. (2.6) in terms of submatrices of the total initial stiffness matrix.

$$\widehat{\mathbf{K}}_{tt} = \mathbf{K}_{tt} - \mathbf{K}_{0t}^{t}\mathbf{K}_{00}^{-1}\mathbf{K}_{0t} \tag{2.6}$$

An only mass (MPD) or stiffness (SPD) proportional damping model can be defined using eqs. (2.7) and (2.8), where the damping parameters are found through eq. (2.4)

$$\begin{bmatrix} \mathbf{C}_{tt} & \mathbf{C}_{t0} \\ \mathbf{C}_{0t} & \mathbf{C}_{00} \end{bmatrix} = \begin{bmatrix} \mathbf{C}_{tt} & 0 \\ 0 & 0 \end{bmatrix} = a_0 \begin{bmatrix} \mathbf{M}_{tt} & 0 \\ 0 & 0 \end{bmatrix} \tag{2.7}$$

$$\begin{bmatrix} \mathbf{C}_{tt} & \mathbf{C}_{t0} \\ \mathbf{C}_{0t} & \mathbf{C}_{00} \end{bmatrix} = \begin{bmatrix} \mathbf{C}_{tt} & 0 \\ 0 & 0 \end{bmatrix} = a_1 \begin{bmatrix} \widehat{\mathbf{K}}_{tt} & 0 \\ 0 & 0 \end{bmatrix} \tag{2.8}$$

Caughey[51,52] proposed a generalisation of the Rayleigh model to define a damping ratio at more than two frequencies employing eq. (2.9).

$$\mathbf{C} = \mathbf{M} \sum_{i=0}^{N-1} a_i [\mathbf{M}^{-1}\mathbf{K}]^i \tag{2.9}$$

Where the damping parameters are defined with the following system of equations

$$\zeta_n = \frac{1}{2} \sum_{i=0}^{N-1} a_i \omega_n^{2i-1} \tag{2.10}$$

In general, structural systems are modelled with massless DoFs, hence eq. (2.9) could not be used since the mass matrix has no inverse. The latter is solved using the mass matrix ($\mathbf{M}_{tt}$) and the condensed stiffness matrix ($\widehat{\mathbf{K}}_{tt}$)[26,53], where the subscript denotes the DoFs with mass. Caughey damping is rarely used in linear and nonlinear dynamic analysis since the series presented in eq. (2.9) are challenging to solve. Additionally, eq. (2.10) is ill-conditioned, and reviewing the damping ratio in all modes, where it is not directly defined, is required to ensure that they take reasonable values [54].

Alternatively, Wilson and Penzien[11] proposed a more efficient model expressed by eq. (2.11)

$$\mathbf{C} = \mathbf{M}\left[\sum_{i=1}^{N} \frac{2\zeta_n \omega_n}{\mathbf{M}_g} \{\boldsymbol{\phi}\} \{\boldsymbol{\phi}\}^T\right] \mathbf{M} \tag{2.11}$$

Modal damping has been recommended for nonlinear dynamic analysis in several studies[21,29,55] since it allows to define the damping ratio at more than two frequencies. Modal damping has been criticised since it involves the computation of all eigenvalues and eigenvectors. However, Chopra and McKenna[21] shows that the model can be defined only with the most important modes of the structure without significantly affecting the system's response.

Condensed damping models eliminate the spurious damping moments at the massless DoFs. Nevertheless, they define a fully populated matrix in the position of the DoFs with mass which goes again the skyline matrix storage format typically used in commercial finite element programs. The latter also implies dampers between DoFs that are not physically connected. Recent studies[30,53,56] show that these models may have similar energy dissipation levels than RD and TISPD; therefore, they may be equally unsuitable for nonlinear dynamic analysis. Finally, Luco and Lanzi[57] highlighted that the massless DoFs present significant oscillations in their velocity.

Physically, energy dissipation of non-directly modelled mechanisms comes from different sources like structural connections, friction between structural and non-structural components, intrinsic damping between the soil in contact with the foundation, and even aerodynamic damping. Most of these mechanisms affect the entire structure; therefore, these models can be widely criticised from a physical point of view.

Finally, during elastic analyses, the response of both models, condensed and total, are identical, but when the structure yields, it is not clear the effect that the condensation has on the global response of the structure[58].

2.1.3 Elemental and localized viscous damping models

The global total damping models discussed above use the stiffness and mass matrix to define the damping matrix. This makes them highly efficient since the stiffness and mass matrix are needed so that the calculation of the damping matrix does not significantly increase the computational cost. However, when a model proportional to the stiffness matrix is used, defining the damping matrix and even the damping forces at the elemental level is possible. This approach is equivalent to the global formulation but provides greater flexibility. For example, different damping values, including zero damping, can be defined on elements likely to yield and cause undesired effects during the analysis. Furthermore, it is possible to consider additional options for defining the damping matrix described in this section.

Most commercial software for non-linear analyses, such as OpenSees[49], Seismostruct[48,59], and Perform3d[48], among others, allow elemental damping to assign different damping ratios or to exclude specific elements.

In elements with concentrated plasticity, it is common to define elastic beams with non-linear springs at the ends. These springs have very high initial stiffness, causing undesired effects when they enter the inelastic range since the damping matrix is defined using the initial stiffness matrix. To avoid this problem, Zareian and Medina [60] proposed assembling the global damping matrix from the elemental damping matrices without considering the contribution of the springs at the ends of the beam. Therefore, the damping matrix is defined only with the elements that remain in the elastic range throughout the analysis. Hall[30] mentions that this model, although practical, has low levels of damping and is equivalent to the model proportional to the tangent stiffness matrix described later. The reason is that with the tangent stiffness proportional model, these springs will have no damping when the structure enters the inelastic range. So, the results between the two models will be very similar.

Recently Puthanpurayil et al.[61] proposed to define several elemental damping models using the elemental frequencies, mass, and stiffness matrix. The difference with existing stiffness proportional elemental models is that this study proposes using elemental frequencies, not global frequencies, to define the damping parameters. To determine the mass of the elements, the authors propose to use either a concentrated or a consistent mass formulation [62]. The main drawback is that a calibration process is required to establish the damping parameters since the global and elemental frequencies differ. Although this calibration is consistent, this may have unexpected consequences and prevent its easy application in finite element software.

In the literature, it has been proposed to replace global damping models with discrete dampers. Jäger and Adam[63] also used this approach to represent the initial-stiffness proportional damping model in near-collapse structures. Most of these approaches use non-linear dampers, so further details are presented in the next section, which concerns non-linear damping models.

2.2 Nonlinear viscous damping models

This section reviews nonlinear viscous damping models developed in the literature. Formulations include global, condensed and elemental models that present reformulations of the damping matrix throughout the analysis. In addition, models that define an elemental damping matrix, use discrete dampers, or other viscous elements whose relationship is given by a nonlinear function depending on velocities.

2.2.1 Total global viscous damping model

Since the development of nonlinear dynamic analyses and the appearance of some of the first software[23,29,38,64,65] to perform them, it was proposed to use the tangent stiffness matrix to define the damping matrix through the following equation.

$$\mathbf{C} = \mathrm{a}_1 \, \mathbf{K}^{\mathrm{Tan}} \tag{2.12}$$

Recent studies[36,66–68] recommend using this method since unbalanced damping forces in the DoFs without mass are significantly reduced but not eliminated. Some authors[57] argue that these damping forces and moments at massless DoFs may be numerical artefacts rather than a deficiency of the damping model. Additionally, this model has better-matched experimental results and performs well[69]. Nevertheless, the results are not convincing since the response of a tangent stiffness proportional damping is remarkably similar to when no damping is accounted for [70].

Specific issues arising from using a tangent SPD were described early in DRAIN2D[38] and ANSI-I[23]. They include possible equilibrium unbalances that need to be accounted for, caused by the fact that the stiffness matrix of the previously converged step is typically used to define the damping matrix for the next step. Therefore, the system is not in equilibrium at the beginning of each step. This model also implies that the system's capacity to dissipate energy differs considerably from one step to the next, depending on whether the system is in the elastic or inelastic range.

Furthermore, when the structure falls into the inelastic range, the damping forces decrease. The latter may be advantageous because the constitutive rules dissipate most of the energy, and no further dissipation through a viscous model would be necessary. However, they may be small if there is a significant decay of the stiffness matrix during or after incursions into the inelastic range. As a result, it has been proposed to update the damping parameters at each step to maintain a constant damping ratio[22,32], which is computationally expensive since the natural frequencies must be calculated at each step.

More recently, Chopra and Mckenna[21,71] argued that the model has several conceptual limitations, including damping force-velocity relations exhibiting hysteresis due to the reformulation of the damping matrix at each step. Moreover, it implies negative damping at large deformations due to the negative slope of the material constitutive rules and the presence of the GSM[21–23]. Hall[27] considers this model as ad hoc to simulate the nonlinear behaviour of the damping forces, and no physical justification exists for proposing it.

As shown in eqs. (2.13) and (2.14), the tangent stiffness matrix can also define RD by maintaining or not updating the damping parameters.

$$\begin{bmatrix} \mathbf{C}_{tt} & \mathbf{C}_{t0} \\ \mathbf{C}_{0t} & \mathbf{C}_{00} \end{bmatrix} = a_0\,\mathbf{M} + a_1\,\mathbf{K}^{Tan} \tag{2.13}$$

$$\begin{bmatrix} \mathbf{C}_{tt} & \mathbf{C}_{t0} \\ \mathbf{C}_{0t} & \mathbf{C}_{00} \end{bmatrix} = a_0^{Tan}\mathbf{M} + a_1^{Tan}\mathbf{K}^{Tan} \tag{2.14}$$

Luco and Lanzi[57,72,73] formulated two alternatives for defining the damping matrix according to the following equations.

$$\tilde{\mathbf{C}} = \mathbf{K}^{Tan}\mathbf{K}^{-1}\mathbf{C}\,\mathbf{K}^{-1}\mathbf{K}^{Tan} \tag{2.15}$$

$$\tilde{\mathbf{C}} = \mathbf{C}\,\mathbf{K}^{-1}\mathbf{K}^{Tan} \tag{2.16}$$

These proposals are proportional to an elastic velocity vector, so the $\mathbf{K}^{-1}\mathbf{K}^{Tan}$ terms appear in the equations. Analogous to the previous model, these formulations are nonlinear since the damping matrix is reformulated, causing a non-constant relationship between the damping forces and velocity vector. Luco and Lanzi[57,72,73] conclude that this approach provides smaller damping forces than traditional linear models. Additionally, the model has slightly larger damping forces than the model proportional to the tangent stiffness matrix in the inelastic range. However, the formulation of this model may be computationally expensive, especially in systems with many DoFs.

2.2.2 Condensed global viscous damping models

The damping ratio has been calibrated through experimental tests of structures under small amplitude vibrations. When the damping model is defined, this damping ratio is imposed on a frequency or frequencies of the structure. The system’s frequencies can vary during and after incursions into the inelastic range during nonlinear analyses. Therefore, the damping ratio defined at the beginning of the analysis can differ appreciably, resulting in a larger or smaller effective damping ratio. This and other factors have caused the damping parameters to be updated to maintain a constant effective damping ratio throughout the analysis.

The modal damping model is usually specified with the modal shapes and frequencies of the system in the first step of the analysis. However, Perform3D's manual mentions that this model could be updated to consider the stiffness decay and to guarantee a constant effective damping ratio, but this process is computationally demanding. Chopra and McKenna[21] show that this model can be defined with the principal modes of the structure without affecting the structure's response, which causes a significant decrease in computational cost. Chambreuil et al.[67] used this model to predict small amplitude vibration tests of reinforced concrete beams. The following expression gives this model:

$$\mathbf{C} = \begin{bmatrix} \mathbf{M}_{tt} & 0 \\ 0 & 0 \end{bmatrix} \left[\sum_{i=1}^{N} \frac{2\zeta_n \omega_n}{\mathbf{M}_g} \begin{Bmatrix} \mathbf{\Phi}_{nt}^{Tan} \\ \mathbf{\Phi}_{n0}^{Tan} \end{Bmatrix} \begin{Bmatrix} \mathbf{\Phi}_{nt}^{Tan,t} & \mathbf{\Phi}_{n0}^{Tan,t} \end{Bmatrix} \right] \begin{bmatrix} \mathbf{M}_{tt} & 0 \\ 0 & 0 \end{bmatrix} \tag{2.17}$$

Condensed models, in general, have been little studied since they are not implemented in most of the commercial and OpenSource software.

This thesis devotes an entire chapter to the study of a new model and existing condensed models.

2.2.3 Elemental viscous damping model

Elemental damping models provide greater flexibility than global or condensed models in defining the sources of energy dissipation independent of the material's constitutive rules. The reason is that depending on the type of formulation, damping may or may not be assigned to specific elements. In certain cases, it is possible to specify non-linear relationships to ensure that the magnitude of damping forces is reasonable [8,27,29,30].

As mentioned above, Puthanpurayil et al. proposed a family of elemental damping models that can be regarded as analogous to global linear and nonlinear models. All models are presented in Figure 2.1. The authors define them using frequencies, mass and elemental stiffness. Subsequently, they derive the models using a diagonal matrix where the mass is defined only in the transverse DoFs and a consistent mass matrix expressing the mass in all DoFs through shape functions. The linear models correspond to those with constant coefficients and damping matrix; the others are nonlinear since the damping matrix and damping parameters are reformulated.

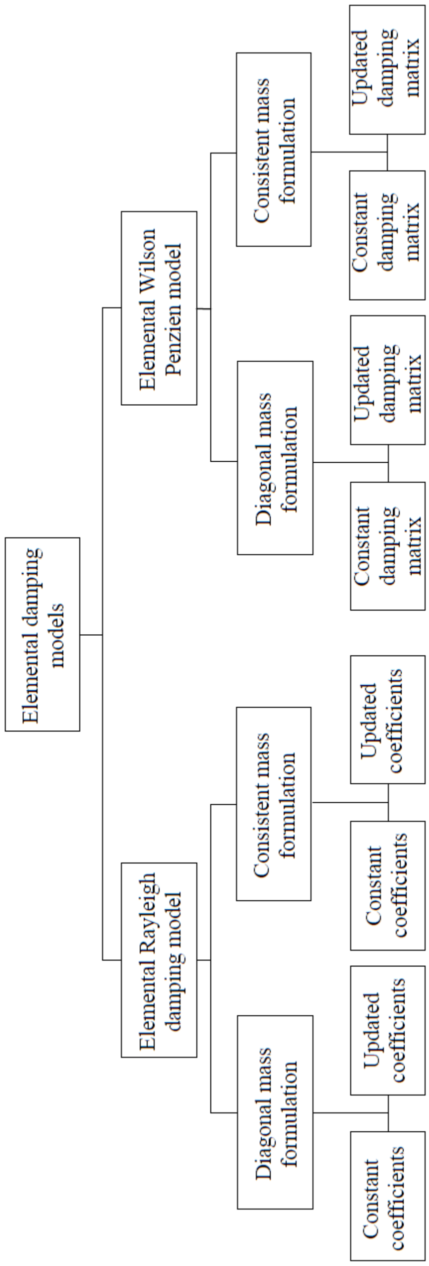

Figure 2.1 Schematic generic classification of the elemental damping models proposed by Puthanpurayil et al.[61]

The main drawback of these models is that the fundamental frequencies differ from the global frequencies. Hence, a calibration process is necessary to define the effective damping ratio at a specific frequency. Even if the authors justify this procedure well, its consequences are unclear. The authors mention that the results of these models are more coherent if a consistent formulation is used. However, this conclusion is a personal assessment.

The model presented by Luco and Lazi can be equally implemented at the elemental level. Unlike the previous models, since no elemental mass matrix is defined, the calibration process performed by Puthanpurayil et al.[61] is not required. Without the calibration process, the results of both models (global and local) are equal, and the only advantage lies in the fact that different damping ratios can be assigned to the structural elements.

Hall[26,27,30] advocates using a nonlinear viscous model to calculate the damping forces since it allows keeping the ratio between the maximum damping and material forces in a tolerable range following the arguments stated by Rayleigh[8] and Wilson and Clough[10].

Hall[27] proposed the definition of nonlinear rectangular viscous elements proportional to the inter-storey stiffness and velocities independent of the rigid body motion, but the damping forces are capped with a predefined limit according to eq. (2.18)

$$R_{d,j}(t) = \pm\min\left(a_1 k_j \left|\dot{x}_{rel,j}(t) - \dot{x}_{rel,j-1}(t)\right|, 2\zeta R_{sy,j}\right) \tag{2.18}$$

The elements proposed by Hall[27] consist of 4 nodes with two transverse DoFs at each node. Therefore, with this type of element, the system has no damping moments in the massless DoFs. This model could be a good alternative for modelling damping forces independent of the constitutive rules of the materials. Nevertheless, the main inconvenience of this model is that the stiffness (k_j) and shear resistance ($R_{sy,j}$) of each floor is required, which may be costly to calculate in large systems with complex architecture. Qian et al.[55] argue that it is unclear which limit should be imposed on the damping forces. Currently, the only relation was proposed by Hall[27] according to the ratio between the maximum damping and material forces in a linear SDoF subjected to a sinusoidal wave.

De Francesco and Sullivan[74] propose to define the dampers at the elemental level rather than at the global level by a viscous damping matrix. Jäger and Adam[63] also used this approach to represent the initial-stiffness proportional damping model when nonlinear geometric effects are considered. The method of De Francesco and Sullivan [74] consists of defining two linear dampers to simulate a nonlinear behaviour. Bowland and Charney[75] also proposed localized level damping models following an evolutionary approach where damping is added from rotational dampers attached to a rigid link ghost element.

In addition, most commercial software can define linear or nonlinear dampers in the rotational DoFs or between two consecutive floors to model, under a specific argument, the sources of energy dissipation independent of the constitutive rules of the materials.

3. Material tangent stiffness proportional viscous damping

3.1 Abstract

This chapter presents a stiffness-proportional viscous damping model based on the material component of the total tangent stiffness matrix. It is developed for nonlinear geometric inelastic frame analysis and implemented with distributed plasticity formulations. The use of a corotational approach allows isolating the nonlinear effects arising from material and geometric sources, hence allowing to preclude the contribution of the latter to simulate non-modelled sources of energy dissipation. Following the presentation of the theoretical framework and a discussion on the physical meaningfulness of the proposed approach, several illustrative case studies are presented. The first is based on the damped free vibration response of a slender cantilever with an elastic response, whereas the second addresses the seismic behaviour of an inelastic reinforced concrete cantilever column. Comparisons with the total-tangent-stiffness-proportional approach showcase the advantages of the current proposal.

3.2 Introduction

Finite element (FE) software packages often use the updated Lagrangian[12–14] or the corotational[15–17] formulations to model nonlinear geometrical effects on beams and other elements. The updated Lagrangian uses the reference configuration of the previous converged step to formulate the FE equations, and it is fixed for a certain period Δt[15], whereas in the corotational formulation, the reference configuration is continuously updated following the displacements and rotation of the element. Even if it is recognized that the corotational formulation is more accurate[18], each formulation has advantages over the others that are not described in this document but can be found elsewhere[18,19].

For extreme loads and systems susceptible to large deformations, disregarding nonlinear geometric effects in the numerical response of the structure may lead to erroneous and unconservative analyses. In general, it is always advisable to take them into account, even for non-slender structures. These effects can bring unwarranted consequences when they are considered in the definition of unmodelled energy dissipation sources for nonlinear analysis.

During ground motion response or other extreme dynamic loadings, the total energy input in a numerically simulated structure is equal to the kinetic energy, the energy dissipated in the material hysteretic rules[76], and the energy dissipated by other mechanisms that are usually not easy to model explicitly: micro-hysteretic curves of the materials in the elastic range, friction between structural and non-structural components, intrinsic damping of the soil in contact with the foundation, among others [32,77]. These non-directly modelled sources of energy dissipation are usually represented through a simplified viscous model known as Rayleigh damping (RD). The numerical simplicity of this model, coupled with the possibility of orthogonalising the system in linear analyses, has made RD ubiquitous in FE software and the most common model for viscous damping in linear and nonlinear dynamic analysis. The corresponding damping matrix is obtained as a linear combination of the mass and stiffness matrices, where the multiplication coefficients are found from specified input damping ratios at two distinct frequencies[54]. This method, inherited from linear analysis, presents deficiencies and inconsistencies when implemented for nonlinear response simulation, as further discussed in the following sections. One of such inconsistencies studied in the present work is the physically meaningless presence of the geometric stiffness matrix (GSM) in the definition of the stiffness-proportional term of the damping matrix – which appears when nonlinear geometric effects are considered.

Nonlinear analyses have become common in everyday structural engineering practice due to the community's growing interest in performance-based design, seismic control systems, and the evaluation of existing structures[31]. During dynamic loading, these analyses present a source of uncertainty related to how other sources of energy dissipation, independent of material hysteretic rules, are modelled[25,28]. Especially during extreme loads events where the system behaves in the inelastic range.

3.3 Material tangent stiffness proportional viscous damping

3.3.1 Motivation

As far as the authors are aware, up until now, RD or stiffness-proportional damping (SPD) models have been defined as proportional to the total stiffness matrix, in particular the total tangent stiffness matrix (TSM), $\mathbf{K}^{\mathrm{Tan}}$. The total stiffness matrix also determines the natural frequencies of the structure, which are in turn typically used to estimate the damping parameters a_0 and a_1 (for RD) or just a_1 (for SPD), see eqs. (2.3) and (2.4).

The current proposal employs a corotational formulation enabling a decomposition of the total tangent stiffness matrix of the structure into a material tangent stiffness matrix $\mathbf{K}^{\mathrm{TanMat}}$ and a geometric tangent stiffness matrix $\mathbf{K}^{\mathrm{TanGeo}}$, denoted respectively as MSM and GSM. The GSM shows up when large displacements are considered and equilibrium is established in the deformed structural configuration. One advantage arising from the above decomposition is that it allows defining the MSM as the proportionality matrix for the damping model. The physical justification to explore such path can be straightforwardly understood by recalling that material hysteretic response is the main source of internal damping. For example, if one considers a detached RC element, dissipative sources occur at the concrete, steel, and concrete-steel interface levels. Since the progressive degradation of these material mechanisms and the associated energy dissipation are simulated during an extreme loading event through the nonlinear relations $\{\mathbf{f}(\mathbf{U}(\mathrm{t}))\}$ in eq. (2.1)), it is rational to define the dissipative contribution from the damping model proportional just to the (decreasing) tangent stiffness of these material mechanisms. It is herein argued that the more accurate way to implement this approach is to leave the GSM out of the damping proportionality matrix, as it does not reflect material damage or plastification. In other words, it is claimed that the damping model should be proportional only to the MSM and not to the GSM. To the best of the authors' knowledge, only Charney[22] briefly suggested not including the GSM to compute the stiffness-proportional term of Rayleigh-based damping models. The extended physical meaningfulness of the herein proposed and investigated material-tangent-stiffness-proportional damping (MTSPD) preserves the advantages of SPD, particularly the sparsity of the proportionality matrix. Additionally, the new MTSPD avoids another physically senseless numerical pathology, namely the introduction of energy in the post-peak response of MDoF systems due to nonlinear geometric effects, which occurs regularly in response simulation of extreme loading events.

Another related aspect that will also be investigated in this work is the definition of the damping parameters a_0 and a_1 – see eqs. (2.3) and (2.4), which are usually computed based on an estimated value of the damping ratio for one or two structural frequencies, typically corresponding to the fundamental frequency or two of the first natural frequencies of the MDoF system. The latter have until now been obtained with the TSM. However, it can be argued that a more physically consequential choice for the purpose of obtaining a_0 and a_1 would be to determine these natural frequencies with the MSM alone. Such approach is again intended to anchor the damping model to the material-related mechanisms that govern energy dissipation. In fact, as it will be recalled in the next section, the GSM depends on the magnitude of the externally applied forces (with predominance to the axial force in each element) and the rotation of each element from its initial position to the current one. There appears to be no persuasive reason why variations of any such two quantities should change the natural frequency or frequencies to which damping ratio(s) are assigned.

The next section recalls nonlinear geometric frame analysis with the corotational approach, including the MSM and GSM derivation. An appraisal of the relative contribution of the latter for an elastic and an inelastic beam element is also carried out before presenting the mathematical formulation of the newly proposed MTSPD model. Finally, the implementation of the authors' program is presented for a transient dynamic analysis.

3.3.2 Material and geometric terms of the stiffness matrix in the corotational formulation

The corotational approach expresses the beam elemental displacements and internal forces in the three reference systems shown in Figure 3.1 for a planar case: global (gl), local (loc), and basic (bsc). The basic system is defined with the current position of the element's nodes and follows the element as it deforms, allowing for a separation between the rigid body motion and the internal deformations. The latter are expressed in eq. (3.1), at the basic reference system, in terms of the local displacements ($\mathbf{u}^{\mathrm{loc}}$) and the corotating angle (β) between the local and the basic reference system.

$$u_1^{\mathrm{bsc}} = l - l_0, \qquad u_2^{\mathrm{bsc}} = u_3^{\mathrm{loc}} - \beta, \qquad u_3^{\mathrm{bsc}} = u_6^{\mathrm{loc}} - \beta \tag{3.1}$$

where l is the deformed length of the element in the current position of the nodes and l_0 is the undeformed length of the element.

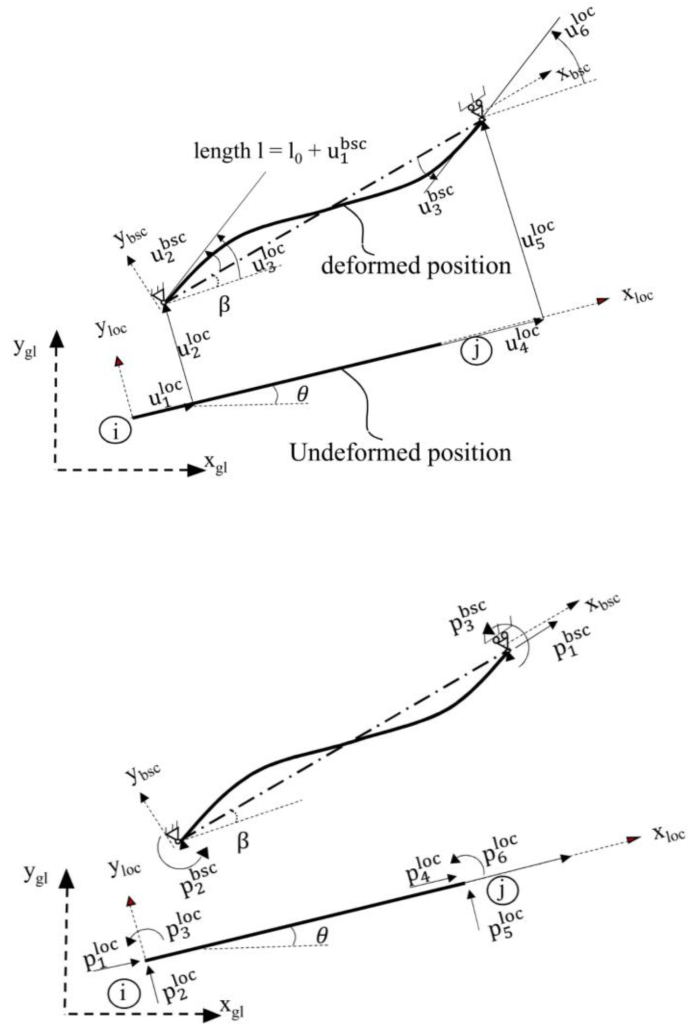

Figure 3.1 Element forces and displacements expressed in the different reference systems.

The incremental compatibility ($\mathbf{\Gamma_C}(\mathbf{u}^{\mathrm{loc}})$) matrix is obtained by differentiation:

$$\frac{\partial \mathbf{u}^{\mathrm{bsc}}}{\partial \mathbf{u}^{\mathrm{loc}}} = \left(\mathbf{\Gamma}_{\mathrm{C}}(\mathbf{u}^{\mathrm{loc}})\right) = \begin{bmatrix} -\cos(\beta) & -\sin(\beta) & 0 & \cos(\beta) & \sin(\beta) & 0 \\ -\sin(\beta)/l & \cos(\beta)/l & 1 & \sin(\beta)/l & -\cos(\beta)/l & 0 \\ -\sin(\beta)/l & \cos(\beta)/l & 0 & \sin(\beta)/l & -\cos(\beta)/l & 1 \end{bmatrix} \tag{3.2}$$

At the basic level, it is possible to obtain the constitutive relations expressing the basic forces as a function of the basic displacements

($\mathbf{p}^{\mathrm{bsc}}(\mathbf{u}^{\mathrm{bsc}})$). Namely, this work uses an Euler-Bernoulli linear elastic beam and an inelastic force-based element.

After the basic forces ($\mathbf{p}^{\mathrm{bsc}}(\mathbf{u}^{\mathrm{bsc}})$) are found, they can be expressed in the local reference system ($\mathbf{p}^{\mathrm{loc}}$) using equilibrium relations derived by equilibrium in the deformed configuration or with the principle of virtual work:

$$\mathbf{p}^{\mathrm{loc}} = \mathbf{\Gamma}_{\mathrm{E}}\left(\mathbf{u}^{\mathrm{loc}}\right) \cdot \mathbf{p}^{\mathrm{bsc}}\left(\mathbf{u}^{\mathrm{bsc}}\right) = \left(\mathbf{\Gamma}_{\mathrm{C}}\left(\mathbf{u}^{\mathrm{loc}}\right)\right)^{\mathrm{T}} \cdot \mathbf{p}^{\mathrm{bsc}}\left(\mathbf{u}^{\mathrm{bsc}}\right) \tag{3.3}$$

The previous expression indicates that the equilibrium matrix is the transpose of the incremental compatibility matrix, which illustrates the principle of contragradiency in structural analysis.

The elemental global forces are then found with a rotation matrix considering the angle (θ) between the global and the local reference systems. The elemental contributions from the composing elements are then assembled to obtain the global resisting forces of the structure. Finally, the latter are compared with the external forces applied to the structure: using numerical methods, convergence in the nonlinear problem is achieved when their difference falls within a specified convergence criterion.

The incremental relation between the global structural forces and displacements is required to solve the nonlinear problem and define a tangent-stiffness-proportional damping (TSPD). Such relationship is found by assembling the global elemental tangent stiffness matrices, obtained from the local ones through rotation (θ), into the tangent stiffness matrix of the global system. At the local reference system, the tangent elemental stiffness ($\mathbf{k}^{\mathrm{TanLoc}}$) is found differentiating eq. (3.3) with respect to the local displacements:

$$\mathbf{k}^{\mathrm{TanLoc}} = \frac{\partial \mathbf{p}^{\mathrm{loc}}}{\partial \mathbf{u}^{\mathrm{loc}}} = \frac{\partial(\mathbf{\Gamma}_{\mathrm{E}}(\mathbf{u}^{\mathrm{loc}}))}{\partial \mathbf{u}^{\mathrm{loc}}} \cdot \mathbf{p}^{\mathrm{bsc}}(\mathbf{u}^{\mathrm{bsc}}) + \mathbf{\Gamma}_{\mathrm{E}}(\mathbf{u}^{\mathrm{loc}}) \cdot \frac{\partial(\mathbf{p}^{\mathrm{bsc}}(\mathbf{u}^{\mathrm{bsc}}))}{\partial \mathbf{u}^{\mathrm{loc}}} \tag{3.4}$$

The application of the chain rule of differentiation to the second term on the right-hand side brings out the incremental relation between the basic forces and the basic displacements, which is obtained according to the specific element formulation as outlined in sections 3.4.1 and 3.4.2. The term ($\frac{\partial \mathbf{u}^{\mathrm{bsc}}}{\partial \mathbf{u}^{\mathrm{loc}}}$) is expressed in eq. (3.2), yielding as final result:

$$\mathbf{k}^{\mathrm{TanLoc}} = \frac{\partial \mathbf{p}^{\mathrm{loc}}}{\partial \mathbf{u}^{\mathrm{loc}}} = \underbrace{\frac{\partial(\boldsymbol{\Gamma}_{\mathrm{E}}(\mathbf{u}^{\mathrm{loc}}))}{\partial \mathbf{u}^{\mathrm{loc}}} \cdot \mathbf{p}^{\mathrm{bsc}}}_{\mathbf{k}^{\mathrm{TanGeoLoc}}} + \underbrace{\boldsymbol{\Gamma}_{\mathrm{E}}(\mathbf{u}^{\mathrm{loc}}) \cdot \frac{\partial(\mathbf{p}^{\mathrm{bsc}}(\mathbf{u}^{\mathrm{bsc}}))}{\partial \mathbf{u}^{\mathrm{bsc}}} \cdot \boldsymbol{\Gamma}_{\mathrm{C}}(\mathbf{u}^{\mathrm{loc}})}_{\mathbf{k}^{\mathrm{TanMatLoc}}} \tag{3.5}$$

The first and second terms on the right side of the equation above are the geometric and material components of the elemental stiffness matrix, respectively, which will give rise to the GSM and MSM at the global structural level. The derivative $\frac{\partial(\boldsymbol{\Gamma}_{\mathrm{E}}(\mathbf{u}^{\mathrm{loc}}))}{\partial \mathbf{u}^{\mathrm{loc}}}$ can be readily expanded in the sum of the following three terms:

$$\mathbf{k}_1^{\mathrm{TanGeoLoc}} = \frac{\mathrm{p}_1^{\mathrm{bsc}}}{\mathrm{l}} \begin{bmatrix} \sin(\beta)^2 & & & & & \\ -\cos(\beta)\sin(\beta) & \cos(\beta)^2 & & \mathrm{sym} & & \\ 0 & 0 & 0 & & & \\ -\sin(\beta)^2 & \cos(\beta)\sin(\beta) & 0 & \sin(\beta)^2 & & \\ \cos(\beta)\sin(\beta) & -\cos(\beta)^2 & 0 & -\cos(\beta)\sin(\beta) & \cos(\beta)^2 & \\ 0 & 0 & 0 & 0 & 0 & 0 \end{bmatrix} \tag{3.6}$$

$$\mathbf{k}_2^{\mathrm{TanGeoLoc}} = \frac{\mathrm{p}_2^{\mathrm{bsc}}}{\mathrm{l}^2} \begin{bmatrix} -2\cos(\beta)\sin(\beta) & & & & & \\ \cos(\beta)^2 - \sin(\beta)^2 & 2\cos(\beta)\sin(\beta) & & \mathrm{sym} & & \\ 0 & 0 & 0 & & & \\ 2\cos(\beta)\sin(\beta) & \sin(\beta)^2 - \cos(\beta)^2 & 0 & -2\cos(\beta)\sin(\beta) & & \\ \sin(\beta)^2 - \cos(\beta)^2 & -2\cos(\beta)\sin(\beta) & 0 & \cos(\beta)^2 - \sin(\beta)^2 & 2\cos(\beta)\sin(\beta) & \\ 0 & 0 & 0 & 0 & 0 & 0 \end{bmatrix} \tag{3.7}$$

$$\mathbf{k}_3^{\mathrm{TanGeoLoc}} = \frac{\mathrm{p}_3^{\mathrm{bsc}}}{\mathrm{l}^2} \begin{bmatrix} -2\cos(\beta)\sin(\beta) & & & & & \\ \cos(\beta)^2 - \sin(\beta)^2 & 2\cos(\beta)\sin(\beta) & & \mathrm{sym} & & \\ 0 & 0 & 0 & & & \\ 2\cos(\beta)\sin(\beta) & \sin(\beta)^2 - \cos(\beta)^2 & 0 & -2\cos(\beta)\sin(\beta) & & \\ \sin(\beta)^2 - \cos(\beta)^2 & -2\cos(\beta)\sin(\beta) & 0 & \cos(\beta)^2 - \sin(\beta)^2 & 2\cos(\beta)\sin(\beta) & \\ 0 & 0 & 0 & 0 & 0 & 0 \end{bmatrix} \tag{3.8}$$

$\mathbf{k}_2^{\mathrm{TanGeoLoc}}$ and $\mathbf{k}_3^{\mathrm{TanGeoLoc}}$ are equal and thus renamed as $\mathbf{k}_{2,3}^{\mathrm{TanGeoLoc}}$. The following expression gives the local elemental geometric tangent stiffness matrix $\mathbf{k}^{\mathrm{TanGeoLoc}}$:

$$\mathbf{k}^{\mathrm{TanGeoLoc}} = \mathbf{k}_1^{\mathrm{TanGeoLoc}} + \mathbf{k}_{2,3}^{\mathrm{TanGeoLoc}} + \mathbf{k}_{2,3}^{\mathrm{TanGeoLoc}} \tag{3.9}$$

The latter expression is restated in eq. (3.10) to expose the axial and shear forces in the basic system, which are more engineer-friendly quantities, where $\mathbf{G}_1^{\mathrm{TanGeoLoc}}$ and $\mathbf{G}_{2,3}^{\mathrm{TanGeoLoc}}$ are the matrices of eqs. (3.7) and (3.8) divided by $\mathrm{p}_1^{\mathrm{bsc}}$ and $\mathrm{p}_2^{\mathrm{bsc}}$, respectively. Since $\mathbf{G}_1^{\mathrm{TanGeoLoc}}$ and $(\mathrm{l}\mathbf{G}_{2,3}^{\mathrm{TanGeoLoc}})$ have a similar order of magnitude, the relative importance of the axial and shear forces will govern the corresponding contribution to the stiffness matrix. For common civil engineering elements subjected to combined bending and compression, such as columns under seismic loading, the magnitude of the axial force is often significantly higher than the shear force, and hence the contribution of the shear-force term can usually be neglected.

$$\mathbf{k}^{\mathrm{TanGeoLoc}} = \underbrace{\mathrm{p}_1^{\mathrm{bsc}}}_{\text{Axial force}} \cdot \mathbf{G}_1^{\mathrm{TanGeoLoc}} + \underbrace{\frac{(\mathrm{p}_2^{\mathrm{bsc}} + \mathrm{p}_3^{\mathrm{bsc}})}{\mathrm{l}}}_{\text{Shear force}} (\mathrm{l}\mathbf{G}_{2,3}^{\mathrm{TanGeoLoc}}) \tag{3.10}$$

The previous expressions in eqs. (3.6) and (3.7) show that the rows and columns corresponding to the rotational degrees of freedom of the local tangent stiffness matrix are null. Therefore, the GSM will affect only the vertical and horizontal DoFs of a planar structure. The relative magnitude of the local geometric stiffness matrix entries are compared to those of the local material stiffness matrix for elastic and inelastic elements in the next section. Further details regarding the corotational formulation can be found in other references[78–81].

3.3.3 Relative contribution of geometric and material stiffness terms

Linear elastic beam element

In the linear elastic case, and assuming a simply supported beam as basic system – represented in Figure (3.1), it is straightforward to derive from fundamental principles of mechanics the incremental constitutive relation required for the material stiffness matrix in eq. (3.5).

$$\mathbf{k}^{\mathrm{bsc}} = \frac{\partial(\mathbf{p}^{\mathrm{bsc}}(\mathbf{u}^{\mathrm{bsc}}))}{\partial \mathbf{u}^{\mathrm{bsc}}} = \begin{bmatrix} \mathrm{EA}/\mathrm{l}_0 & 0 & 0 \\ 0 & 4\mathrm{EI}/\mathrm{l}_0 & 2\mathrm{EI}/\mathrm{l}_0 \\ 0 & 2\mathrm{EI}/\mathrm{l}_0 & 4\mathrm{EI}/\mathrm{l}_0 \end{bmatrix} \tag{3.11}$$

The local material tangent stiffness matrix $\mathbf{k}^{\mathrm{TanMatLoc}}$ can now be expressed, including the compatibility and equilibrium matrices presented in eq. (3.2).

$$
\mathbf{k}^{\mathrm{TanMatLoc}} = \begin{bmatrix}
\frac{EA}{l_0}\cos(\beta)^2 + \frac{12EI}{l_0 l^2}\sin(\beta)^2 & \square & \square & \square & \square & \square \\
\left(\frac{EA}{l_0} - \frac{12EI}{l_0 l^2}\right)\cos(\beta)\sin(\beta) & \left(\frac{EA}{l_0}\sin(\beta)^2 + \frac{12EI}{l_0 l^2}\cos(\beta)^2\right) & \square & \mathrm{sym} & \square & \square \\
-\frac{6EI}{l_0 l}\sin(\beta) & \frac{6EI}{l_0 l}\cos(\beta) & \frac{4EI}{l_0} & \square & \square & \square \\
-\left(\frac{EA}{l_0}\cos(\beta)^2 + \frac{12EI}{l_0 l^2}\sin(\beta)^2\right) & -\left(\frac{EA}{l_0} - \frac{12EI}{l_0 l^2}\right)\cos(\beta)\sin(\beta) & \frac{6EI}{l_0 l}\sin(\beta) & \frac{EA}{l_0}\cos(\beta)^2 + \frac{12EI}{l_0 l^2}\sin(\beta)^2 & \square & \square \\
-\left(\frac{EA}{l_0} - \frac{12EI}{l_0 l^2}\right)\cos(\beta)\sin(\beta) & -\left(\frac{EA}{l_0}\sin(\beta)^2 + \frac{12EI}{l_0 l^2}\cos(\beta)^2\right) & -\frac{6EI}{l_0 l}\cos(\beta) & \left(\frac{EA}{l_0} - \frac{12EI}{l_0 l^2}\right)\cos(\beta)\sin(\beta) & \frac{EA}{l_0}\sin(\beta)^2 + \frac{12EI}{l_0 l^2}\cos(\beta)^2 & \square \\
-\frac{6EI}{l_0 l}\sin(\beta) & \frac{6EI}{l_0 l}\cos(\beta) & \frac{2EI}{l_0} & \frac{6EI}{l_0 l}\sin(\beta) & -\frac{6EI}{l_0 l}\cos(\beta) & \frac{4EI}{l_0}
\end{bmatrix} \tag{3.12}
$$

The matrices $\mathbf{k}^{\text{TanGeoLoc}}$ and $\mathbf{k}^{\text{TanMatLoc}}$, defined in eqs. (3.10) and (3.12), are now compared using a simple cantilever steel column with section properties, as shown in Figure 3.2. The comparison is performed through the ratio between the geometric and material matrices at the same entries [row, column], in particular: [1,1], [2,1] and [2,2]. It can be observed that the ratio for the other matrix entries are repeated (see eqs. (3.6), (3.7), and (3.12)), whereas for the rotational terms it is null, i.e. the GSM does not affect the rotational DoFs. The ratio is evaluated for different cantilever heights, imposed lateral drifts, and axial load ratios (ALRs):

- The height values h are 3, 5, and 10 m, equivalent to a slenderness ratio of 36, 60, and 121, using an element effective length factor of Euler's critical load equal to two. They cover common and high slenderness ratios for steel structural elements.
- The studied drift values fall between 0% and 10%. The upper limit of this range of drifts covers extreme demands that may occur in practice and in experimental tests.
- The following ALRs are considered: -35%, -30%, -20%, -10%, 10%, 20%, 30%, and 40%; where the negative sign stands for compressive load. The largest compressive ALR of -35% is defined considering that the Euler's buckling load for the slenderest case (h = 10 m) is close to -38%. The Euler's buckling loads for the other height values are -152% and -423%.

The GSM and MSM were calculated using the author's program. In the first step, the axial load is imposed on the element, and then a linearly increasing history of lateral displacements is imposed on the top horizontal DoF, corresponding to the drifts mentioned. After reaching convergence at each step, using the Newton-Raphson method, the GSM and MSM were stored. The results are plotted in the graphs of Figure 3.3. Similar line shades represent a specific matrix entry [row, column], whereas similar line styles correspond to similar height values (or slenderness ratios).

Figure 3.3 shows that the matrix entries [1,1] and [2,1] of $\mathbf{k}^{\mathrm{TanLoc}}$ will not be significantly influenced by $\mathbf{k}^{\mathrm{TanGeoLoc}}$, which can be understood by looking at eqs. (3.6), (3.7), and (3.8): (i) on the one hand, the matrix $\mathbf{k}_1^{\mathrm{TanGeoLoc}}$ has in these positions the functions "$\sin^2(\beta)$" and "$\cos(\beta)\sin(\beta)$", which for drifts up to 10% will be small values; (ii) on the other hand, even if the entry [2,1] in the matrix $\mathbf{k}_{2,3}^{\mathrm{TanGeoLoc}}$ has a value close to one, the magnitude of the shear force will in general be small, as mentioned before. By contrast, the position [2,2] can be critically influenced by $\mathbf{k}^{\mathrm{TanGeoLoc}}$ in slender structures, and it increases with absolute values of the axial load ratio.

One other aspect to highlight in the elastic case is that the influence of the $\mathbf{k}^{\mathrm{TanGeoLoc}}$ in the entry [2,2] is more relevant when the imposed drift is low and decreases for higher drifts, which may not be intuitive. It can be explained by the fact that, as the drift increases, the axial stiffness of the element starts contributing decisively to this entry in $\mathbf{k}^{\mathrm{TanMatLoc}}$, see eq. (3.12). Even if this component is multiplied by $\sin(\beta)^{2,}$ the axial stiffness is usually much larger than the bending stiffness, and it thus becomes an important contribution.

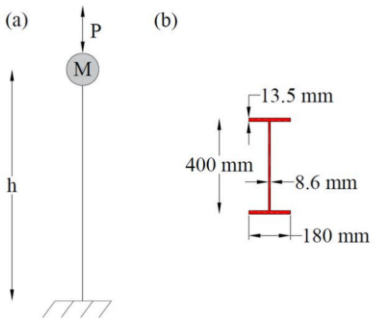

$M_{translation}$	=	3.06 ton (W=30 kN)
$M_{rotation}$	=	0.66 ton.m^2
A	=	8450 mm^2
I	=	231.3e6 mm^4
E	=	200 GPa

Figure 3.2 (a) Cantilever steel column modelled with one corotation elastic element. (b) Geometric and mechanical characterisation: masses, cross-sectional area (A) and second area moment (I), and modulus of elasticity (E).

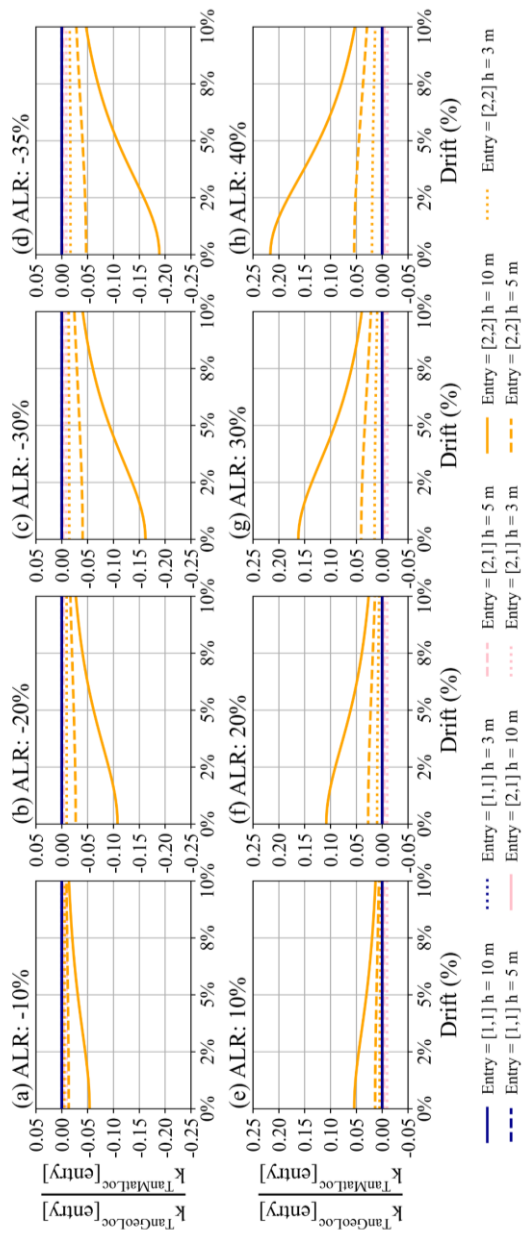

Figure 3.3 (a-h) Evolution, with imposed drift, of the ratio between the same entries (row, column) of the matrices $\boldsymbol{k}^{TanGeoLoc}$ and $\boldsymbol{k}^{TanMatLoc}$ in a elastic beam element, for different cantilever heights and axial load ratios (negative and positive indicate compression and tension, respectively).

Nonlinear beam element using force interpolation functions

Several model formulations of inelastic beams with distributed plasticity have been developed in recent decades. The so-called displacement-based element[82] is based on displacement interpolation functions to find the deformation along the element and sections, which are subsequently used to calculate the cross-sectional forces and basic forces. Commonly, this element uses Hermite polynomials and a Lagrange linear function to interpolate the transverse and axial displacement, respectively, implying a linear curvature and a constant average strain along the element. The displacement-based beam element has been gradually replaced by another model commonly known as force-based beam element[83]. The latter interpolates the nodal forces to find the internal forces strictly in equilibrium along the element, which holds regardless of whether linear or nonlinear constitutive sectional relations are considered. When such a formulation is used, special state determination algorithms, such as those described in[83,84], must be implemented. Due to some of its superior features and increasing use in commercial and open-source software[85], force-based elements are herein employed to compare $\mathbf{k}^{\mathrm{TanGeoLoc}}$ and the $\mathbf{k}^{\mathrm{TanMatLoc}}$ for the case of nonlinear response. The state determination algorithm, presented by Neuenhofer and Filippou[84], was employed in this work because it bypasses an extra loop in the solution algorithm presented by Spacone et al.[83] at the section level.

For the nonlinear case, the integrals along the element length are evaluated numerically as it is not possible, in general, to derive analytical expressions as in the linear elastic case. In the particular case of the force-based element, such integrals refer to the basic displacements and the element flexibility matrix in the basic system, which is inverted to obtain the basic stiffness matrix required for eq. (3.5)

Similarly to the linear elastic beam of the previous section, the ratio between the entries of $\mathbf{k}^{\mathrm{TanGeoLoc}}$ and $\mathbf{k}^{\mathrm{TanMatLoc}}$ is compared using the same cantilever steel column. The same values of axial load, slenderness, and imposed drifts are considered. Inelasticity is taken into account at the sectional level through a fibre discretisation modelling of the web and flanges using 60 and 5 fibres, respectively. The steel fibres have a yield stress of 355 MPa with Young's modulus of 200 GPa and a post-yield hardening parameter of 1e-05; according to the model proposed by Menegotto and Pinto[86], the remaining model parameters are $A_r = 20$, $A_1 = 18.5$, $A_2 = 0.15$, $A_3 = 0$, and $A_4 = 0$.

The results are shown in Figure 3.4, which indicates that the matrix entries [1,1] and [2,1] of $\mathbf{k}^{\mathrm{TanLoc}}$ will not be significantly influenced by $\mathbf{k}^{\mathrm{TanGeoLoc}}$. This result had also been observed for the linear elastic case. Under small drift values, the geometric and material stiffness matrix ratios are similar between the linear and nonlinear cases. Nevertheless, they significantly differ under large drifts. As in the linear elastic case, the position [2,2] is significantly influenced by the $\mathbf{k}^{\mathrm{TanGeoLoc}}$. Under large drifts, the ratio between GSM and MSM is more significant in the inelastic case than the elastic case because the MSM decreases significantly when the element has incursions in the inelastic range. As a consequence, the influence of GSM can become important, even in non-slender elements, with respect to the MSM. The peaks shown in the columns under tension loads are caused by the entry [2,1] of the $\mathbf{k}^{\mathrm{TanMatLoc}}$, which assumes a zero value at specific imposed drifts going from a positive to a negative stiffness value. Finally, at small drifts, the behaviour of the curves in compression and tension are equivalent in absolute terms. However, as the drift increases, the curves differ since the values taken by the material stiffness matrix in the inelastic range differ.

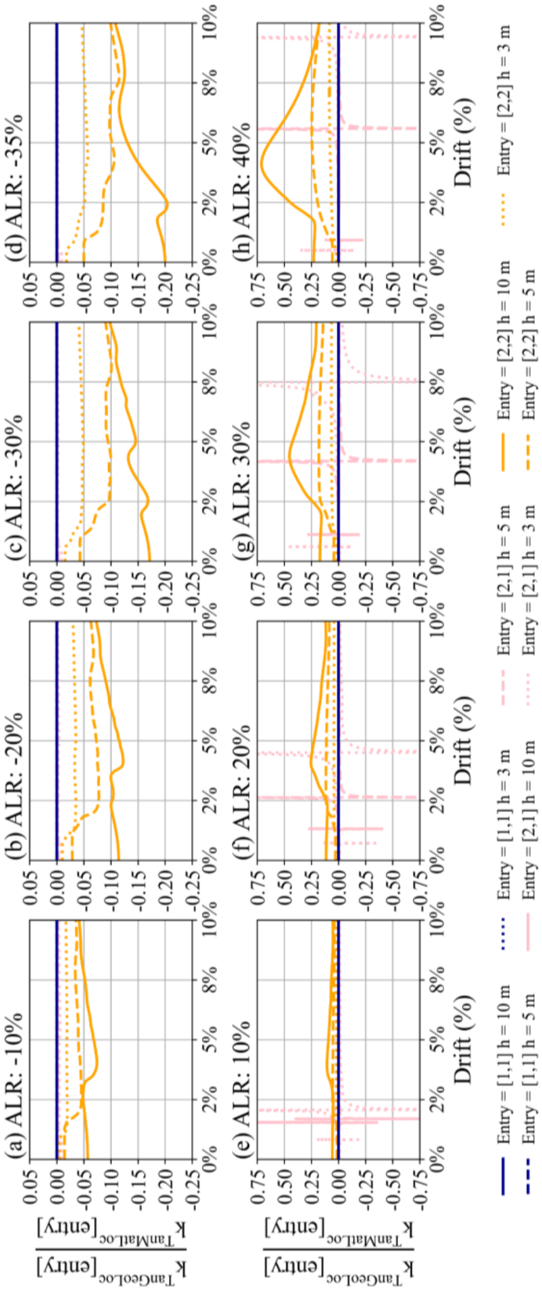

Figure 3.4 (a-h) Evolution, with imposed drift, of the ratio between the same entries (row, column) of the matrices $\boldsymbol{k}^{TanGeoLoc}$ and $\boldsymbol{k}^{TanMatLoc}$ in an inelastic beam element, for different cantilever heights and axial load ratios (negative and positive indicate compression and tension, respectively).

3.3.4 Formulation and implementation

The damping matrix of eq. (2.1) is defined using a MTSPD given as:

$$\begin{bmatrix} \mathbf{C}_{tt}^{Mat} & \mathbf{C}_{t0}^{Mat} \\ \mathbf{C}_{0t}^{Mat} & \mathbf{C}_{00}^{Mat} \end{bmatrix} = a_{1T} \begin{bmatrix} \mathbf{K}_{tt}^{TanMat} & \mathbf{K}_{t0}^{TanMat} \\ \mathbf{K}_{0t}^{TanMat} & \mathbf{K}_{00}^{TanMat} \end{bmatrix} \tag{3.13}$$

or

$$\begin{bmatrix} \mathbf{C}_{tt}^{Mat} & \mathbf{C}_{t0}^{Mat} \\ \mathbf{C}_{0t}^{Mat} & \mathbf{C}_{00}^{Mat} \end{bmatrix} = a_{1M} \begin{bmatrix} \mathbf{K}_{tt}^{TanMat} & \mathbf{K}_{t0}^{TanMat} \\ \mathbf{K}_{0t}^{TanMat} & \mathbf{K}_{00}^{TanMat} \end{bmatrix} \tag{3.14}$$

The damping parameter can be defined using the desired frequency according to eq. (2.3) and (2.4). In this work, the damping parameters a_{1T} and a_{1M} are defined with the fundamental frequency corresponding to the first mode shape $\boldsymbol{\phi}_1$ satisfying eq. (3.15) or eq. (3.16), respectively.

$$\mathbf{K}^{Tan}\boldsymbol{\phi}_1 = \omega_T^2 \mathbf{M}\boldsymbol{\phi}_1 \tag{3.15}$$

$$\mathbf{K}^{TanMat}\boldsymbol{\phi}_1 = \omega_M^2 \mathbf{M}\boldsymbol{\phi}_1 \tag{3.16}$$

where $\mathbf{K}^{Tan}$ and $\mathbf{K}^{TanMat}$ are the total tangent stiffness matrix TSM and the material tangent stiffness matrix MSM at the first step after applying the gravity loads, and ω_T and ω_M are the fundamental frequencies. The response of the structures presented in the following sections is studied using both alternatives for the damping parameters. As discussed in the motivation, defining the MTSPD through the damping parameter a_{1M} is conceivably more physically and mathematically consistent, i.e. based on the frequency obtained with the MSM instead of the TSM. The models investigated and compared in the current work are summarised in Table 3.1.

Table 3.1 Tangent-stiffness-proportional damping models analysed in the current work.

Complete name	Damping parameter	Nomenclature	Expression
Total tangent stiffness-proportional viscous damping model	a_{1T}	TTSPD_a_{1T}	$\mathbf{C} = a_{1T}\,\mathbf{K}^{Tan}$
	a_{1M}	TTSPD_a_{1M}	$\mathbf{C} = a_{1M}\,\mathbf{K}^{Tan}$
Material tangent stiffness-proportional viscous damping model	a_{1T}	MTSPD_a_{1T}	$\mathbf{C}^{Mat} = a_{1T}\,\mathbf{K}^{TanMat}$
	a_{1M}	MTSPD_a_{1M}	$\mathbf{C}^{Mat} = a_{1M}\,\mathbf{K}^{TanMat}$

It is also possible to define a RD proportional to the material tangent stiffness, using eqs. (3.17) and (3.18):

$$\begin{bmatrix} \mathbf{C}_{tt}^{Mat} & \mathbf{C}_{t0}^{Mat} \\ \mathbf{C}_{0t}^{Mat} & \mathbf{C}_{00}^{Mat} \end{bmatrix} = a_{0T} \begin{bmatrix} \mathbf{M}_{tt} & 0 \\ 0 & 0 \end{bmatrix} + a_{1T} \begin{bmatrix} \mathbf{K}_{tt}^{TanMat} & \mathbf{K}_{t0}^{TanMat} \\ \mathbf{K}_{0t}^{TanMat} & \mathbf{K}_{00}^{TanMat} \end{bmatrix} \tag{3.17}$$

$$\begin{bmatrix} \mathbf{C}_{tt}^{Mat} & \mathbf{C}_{t0}^{Mat} \\ \mathbf{C}_{0t}^{Mat} & \mathbf{C}_{00}^{Mat} \end{bmatrix} = a_{0M} \begin{bmatrix} \mathbf{M}_{tt} & 0 \\ 0 & 0 \end{bmatrix} + a_{1M} \begin{bmatrix} \mathbf{K}_{tt}^{TanMat} & \mathbf{K}_{t0}^{TanMat} \\ \mathbf{K}_{0t}^{TanMat} & \mathbf{K}_{00}^{TanMat} \end{bmatrix} \tag{3.18}$$

where the damping parameters are found with two desired frequencies or with the natural frequencies satisfying eq. (3.15) or eq. (3.16). A Wilson and Penzien damping model independent of the GSM could also be defined through eq. (3.19) at the beginning of the analysis or updating it with the current frequencies and modal shapes of the structure at each step, as proposed by Chambreuil et al.[67].

$$\begin{bmatrix} \mathbf{C}_{tt}^{Mat} & \mathbf{C}_{t0}^{Mat} \\ \mathbf{C}_{0t}^{Mat} & \mathbf{C}_{00}^{Mat} \end{bmatrix} = \begin{bmatrix} \mathbf{M}_{tt} & 0 \\ 0 & 0 \end{bmatrix} \left[\sum_{i=1}^{N} \frac{2\zeta_i \omega_i}{M_{g,i}} \begin{Bmatrix} \mathbf{\Phi}_{i,t}^{TanMat} \\ \mathbf{\Phi}_{i,0}^{TanMat} \end{Bmatrix} \left\{ \mathbf{\Phi}_{i,t}^{TanMat,t} \quad \mathbf{\Phi}_{i,0}^{TanMat,t} \right\} \right] \begin{bmatrix} \mathbf{M}_{tt} & 0 \\ 0 & 0 \end{bmatrix} \tag{3.19}$$

Where ω_i and $\mathbf{\Phi}_i^{TanMat}$ are the modal frequencies and shapes satisfying eq. (3.16), respectively. $M_{g,i}$ is the generalized modal mass. The present work only investigates the influence of the geometric stiffness matrix in a TSPD model. In fact, the presence of the mass matrix in the two above-defined models hinders the observation of the effect of the GSM on the component proportional to the TSM.

The damping models were implemented in an objected-oriented software written in python for this research. The program performs 2D and 3D static and dynamic nonlinear analyses. Preliminary software validation was performed using benchmark tests and through comparison with OpenSees[49] and SeismoStruct[59], which are not reported in this chapter due to space constraints. The Newmark-beta integration method and Newton-Raphson scheme are used to solve the nonlinear equations.

3.4 Case studies

3.4.1 Slender cantilevered steel column under elastic damped free vibration

Figure 3.5 presents the first structure that will be used to illustrate the advantages and specificities of the proposed MTSPD. As recalled in the previous section, the influence of the GSM becomes important in slender structures subjected to significant axial loads. Thus, the slenderest cantilever analysed in section 3.3.3 is again employed in this example. Further, it is subdivided into several elements to capture the nonlinear geometric effects inside the member (also known as P-δ effects). This structure undergoes a simple damped free vibration movement. The traditional TTSPD approach and the new MTSPD model are compared, assuming a damping ratio of 2% associated with the fundamental frequency, a value often used for steel structures. The column has a translational mass ($M_{translation}$) and a rotational inertia ($M_{rotation}$) at the top. It is modelled with five elastic corotational beam elements with a compression or tension load at the top expressed in terms of the ALR. In the first step, a horizontal load is imposed at the top node to create a horizontal displacement of 0.8 m, i.e., corresponding to a drift of 8%. The second step removes the horizontal load, and the system oscillates in damped free vibration.

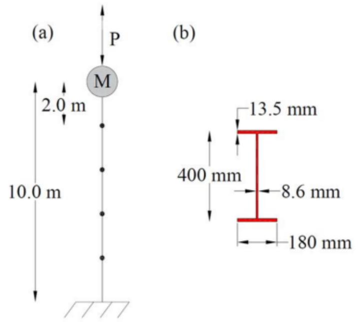

$M_{translation}$	=	3.06 ton (W=30 kN)
$M_{rotation}$	=	0.66 ton*m^2
A	=	8450 mm^2
I	=	231.3e6 mm^4
E	=	200 GPa

Figure 3.5 (a) Cantilever steel column modelled with five corotation elastic elements. (b) Geometric and mechanical characterisation: masses, cross-section area (A) and second area moment (I), and modulus of elasticity (E).

Two cases for each damping model are considered, which differ on how the damping parameter (a_T or a_M) is computed, see section 3.3.4 and eq. (2.4). As discussed in section 5.3.1, the GSM affects the computed natural frequencies of a MDoF system. Such effect may not be negligible for slender structures where the contribution of the GSM to the TSM is significant. This can be observed in Figure 3.6, which shows the variation of the three first structural frequencies as a function of the ALR. The fundamental frequency is influenced the most, approaching a null value near the critical buckling load (i.e., for ALR=-38%), and increases for higher values of the ALR. The following two frequencies are proportionally less affected. Additionally, the geometric stiffness matrix does not affect the rotational DoF of the structures.

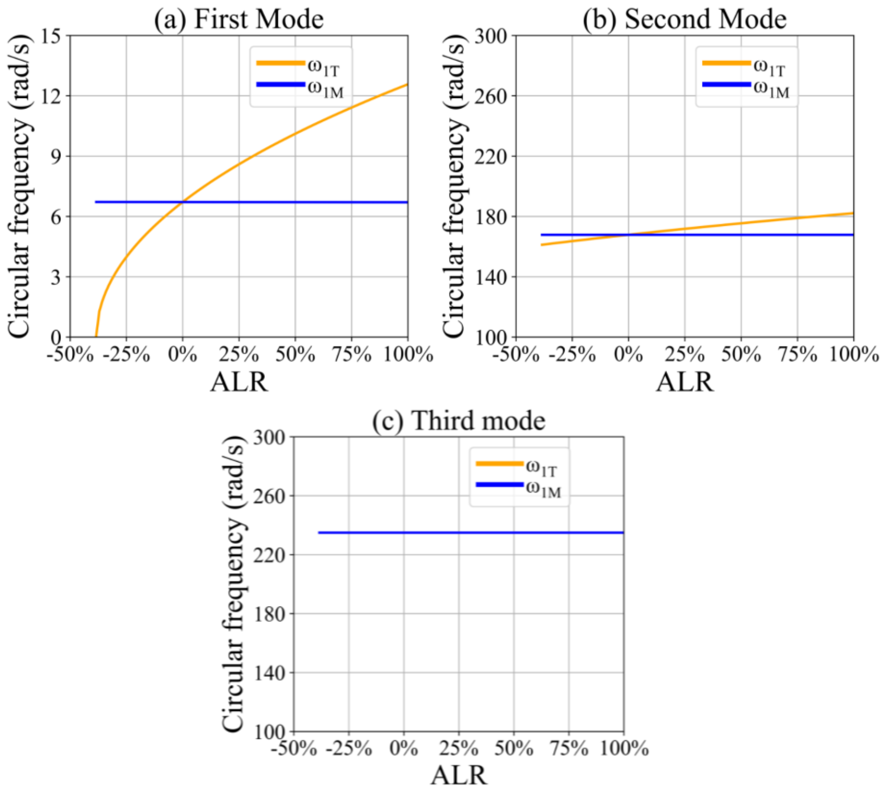

Figure 3.6 (a-c) Influence of the ALR on the natural frequencies of the cantilever column

The variation of the fundamental horizontal frequency will consequently also affect a_1. Figure 3.7 shows that the damping parameter a_{1T} increases sharply for higher compressive ALR. Additionally, there is an opposite less critical effect under increasing ALR in tension, steadily reducing the magnitude of the damping parameter.

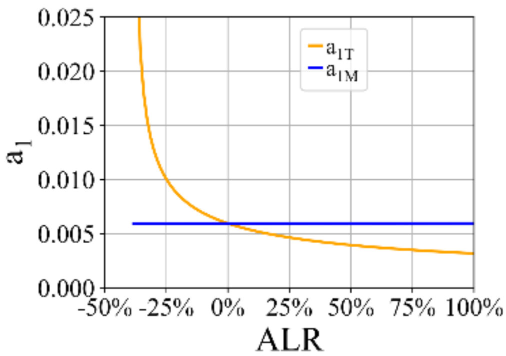

Figure 3.7 Evolution of the damping parameters with the ALR

First case: damping parameter based on TSM

In this first case, the damping parameter a_{1T} is estimated using the system's fundamental frequency computed with the TSM according to eq. (3.15), i.e. considering the influence of the GSM. Two alternative tangent stiffness matrices are used to define the damping matrix: the TSM, comprising the material and geometric terms, and the material-only component, MSM. These two models are denoted respectively as TTSPD_a_{1T} and MTSPD_a_{1T}.

Response to compressive load

Figure 3.8 shows the horizontal displacement at the top of the column under damped free vibration subjected to different compressive ALRs. The motion decay does not change significantly between the TTSPD_a_{1T} and the MTSPD_a_{1T} under low axial load levels. This is expected since, for reduced axial loads, the GSM entries are small in absolute value compared to the ones of the MSM. However, when the slender structure is subjected to intermediate or higher levels of compressive ALR (-20% to -35%), the response of the two models differs drastically. Two effects are involved as the ALR increases in compression: (i) on the one hand, for the model TTSPD_a_{1T}, the higher compressive load produces a significant decrease of $\mathbf{k}^{\mathrm{TanGeoLoc}}$ and hence the tangent TSM used as proportionality damping matrix; such effect is much less pronounced or negligible for the model MTSPD_a_{1T}, since nonlinear geometric effects only affect the equilibrium and incremental compatibility matrices present in $\mathbf{k}^{\mathrm{TanMatLoc}}$, see eq. (3.5), and hence the proportionality matrix MSM; (ii) on the other hand, the fundamental frequency decreases considerably due to the nonlinear geometric effects, causing the parameter a_{1T} to be larger, see eq. (2.4) and Figure 3.7; this effect equally influences both models.

The combination of the two effects above explains the responses depicted in Figure 3.8**.** For the model TTSPD_a_{1T}, it is apparent that as the ALR reduces, i.e. for higher compressive loads, effect (i) is exactly compensated by effect (ii), resulting in the exact effective damping as the initially-defined damping ratio (see below). For the MTSPD_a_{1T}, effect (ii) clearly governs, producing a more damped response for higher compressions.

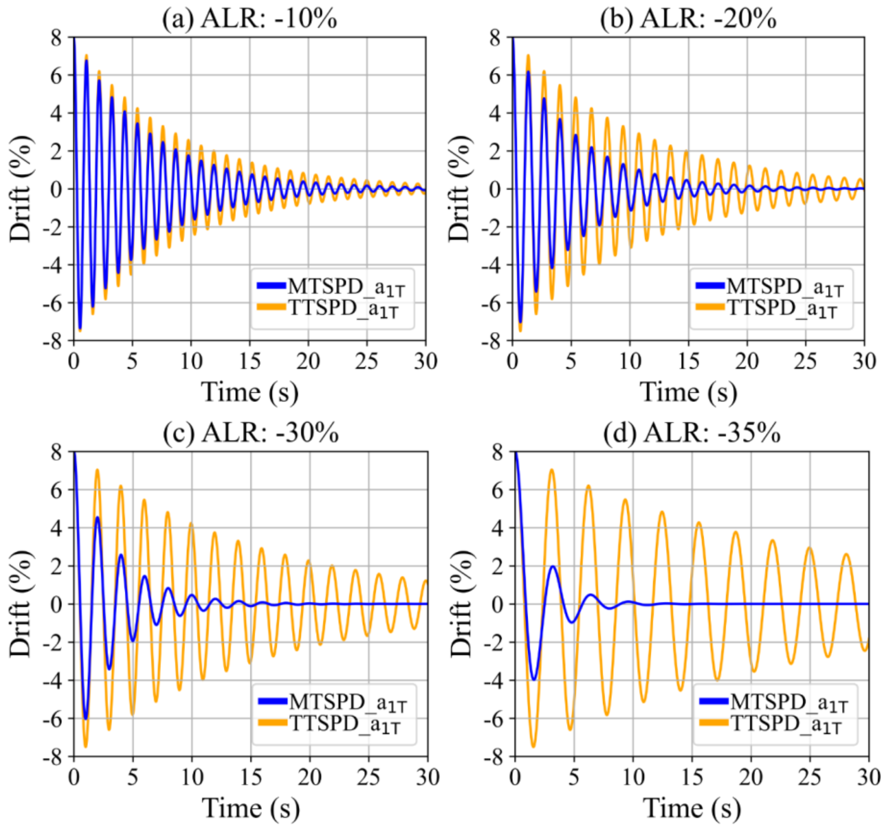

Figure 3.8 (a-d) Time-history response of cantilever top horizontal displacement for damping models MTSPD_a_{1T} and TTSPD_a_{1T} under different compressive ALRs.

The number of cycles to reach a displacement equal to half of the initially imposed one, i.e. of 0.40 m ($J_{50\%}$), the logarithmic decrement (δ) calculated with the natural logarithm of the ratio between two successive peaks, the effective damping ratio, the time ($T_{80\%}$) and number of cycles ($C_{80\%}$) required to dissipate the 80% of the energy input by the horizontal force are shown in Table 3.2 to characterize the decay of motion using both models. The effective damping ratio is found with eq. (3.20), originally derived for elastic single degree of freedom SDoF systems.

$$\delta = \frac{2\pi\zeta}{\sqrt{1-\zeta^2}} \tag{3.20}$$

Table 3.2 shows that, as discussed above, the initially-defined damping ratio of 2% used to compute parameter a_{1T} is kept for TTSPD_a_{1T}, but the effective damping ratio differs for the model MTSPD_a_{1T}. For the latter, the effective damping ratio increases considerably as the compression load increases, reaching a value of 21.8% for the higher ALR.

Table 3.2 shows the energy input required for the horizontal force to impose a displacement of 0.8 m, which decreases under higher axial compression load because the horizontal stiffness is lower. Additionally, the table presents the time required to dissipate 80% of the mentioned energy with both models. When ALRs of -10% and -35% are compared, the TTSPD_a_{1T} takes almost three times longer to dissipate 80% of a total energy input that is nearly eight times smaller. The number of cycles $C_{80\%}$ remains constant with a TTSPD_a_{1T}, implying that the energy dissipated per cycle decreases considerably. The latter is due to GSM and due to smaller velocities. By contrast, the MTSPD_a_{1T} takes less time and cycles, consistent with smaller energy input.

Table 3.2 Decay motion characterisation under compressive ALRs for TTSPD_a_{1T} and MTSPD_a_{1T}.

ALR	ω_T (rad/s)	a_{1T}	E_I (kJ)	TTSPD_a_{1T}					MTSPD_a_{1T}				
				$J_{50\%}$	δ	ζ_{eff}	$T_{80\%}$	$C_{80\%}$	$J_{50\%}$	δ	ζ_{eff}	$T_{80\%}$	$C_{80\%}$
-10%	5.79	0.0069	33.08	5.5	0.128	2.0%	6.86	6.32	4.5	0.169	2.7%	5.16	4.78
-20%	4.67	0.0086	21.52	5.5	0.128	2.0%	8.48	6.30	3.0	0.260	4.1%	4.27	3.19
-30%	3.16	0.0127	9.56	5.5	0.128	2.0%	12.51	6.29	1.5	0.565	8.9%	2.69	1.37
-35%	2.02	0.0198	4.00	5.5	0.128	2.0%	19.61	6.30	0.5	1.400	21.8%	2.05	0.68

The performance of the damping models is also illustrated through the plots of time *vs* cumulative dissipated energy by the damping model shown in Figure 3.9. The cumulative dissipated energy curves present small oscillations caused by the velocity variations in the damped free vibration movement. In all cases, the model MTSPD_a_{1T} has a steeper slope at the beginning of the response, implying that it dissipates energy faster than the system using the TTSPD_a_{1T} under compressive loading.

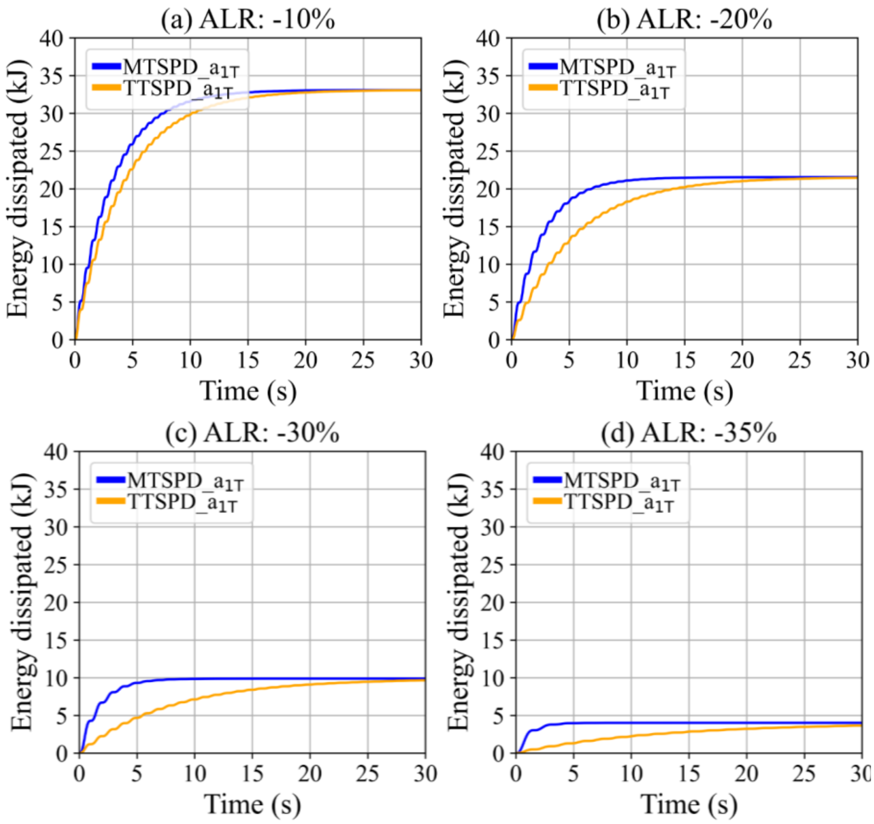

Figure 3.9 (a-d) Cumulative energy dissipated by the damping models MTSPD_a_{1T} and TTSPD_a_{1T} for different compressive ALRs.

This example illustrates a key disadvantage of the widely employed TTSPD_a_{1T}: the model is not tied up to the material-related mechanisms of damping; instead, it assimilates other aspects, such as external loads and the evolution of the deformed configuration. In other words, when an analyst assigns a certain damping ratio for a specific frequency in TTSPD_a_{1T}, it is possible that such energy dissipation arises from mechanisms unrelated to energy dissipation.

Response to tensile load

The presence of external tensile loads causes an opposite but analogous effect with respect to the previous case: the fundamental frequency increases (see Figure 3.7), implying a smaller damping parameter. However, the GSM will increase some values within the TSM, compensating for the reduction in the damping parameter. The influence of the mentioned phenomena can be observed in the history of displacements in Figure 3.10. Contrary to the compression loading, the motion decay is faster in the TTSPD_a_{1T} than in the MTSPD_a_{1T}. This difference increases for higher values of the ALR, but it is proportionally smaller than with compressive loads.

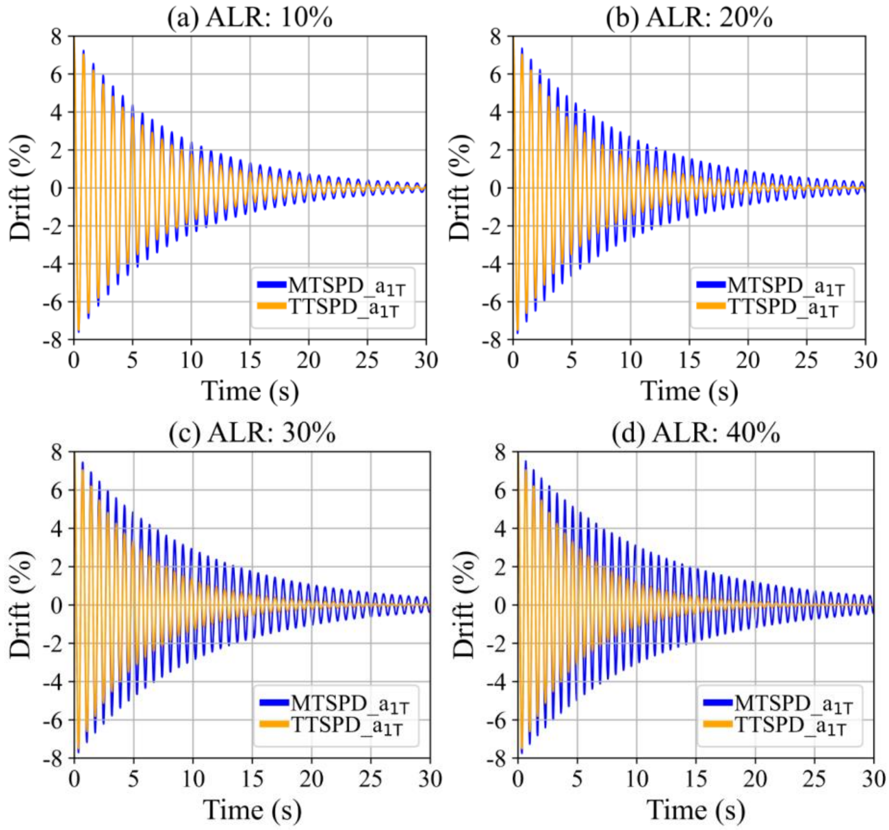

Figure 3.10 (a-d) Time-history response of cantilever top horizontal displacement for damping models MTSPD_a_{1T} and TTSPD_a_{1T} under different tensile ALRs.

Table 3.3 includes several parameters describing the movement decay of the free damped motion. Similarly to the previous case, the effective damping ratio for the TTSPD_a_{1T} corresponds to the assigned value, whereas the effective damping ratio for the MTSPD_a_{1T} is smaller and reduces as the ALR increases. The MTSPD_a_{1T} dissipates energy more slowly than the TTSPD_a_{1T}, and similarly to the previous case, the models show an opposite evolution as the ALR increases: the energy-dissipation time reduces for the TTSPD_a_{1T} – consistent with the reduction of the natural period. The number of cycles $C_{80\%}$ is constant with TTSPD_a_{1T} – even if the energy input is significantly bigger. The time $T_{80\%}$ and number of cycles $C_{80\%}$ increase with the MTSPD_a_{1M} – consistent with the increment of the energy input.

Table 3.3 Decay motion characterisation under tensile ALRs for models TTSPD_a_{1T} and MTSPD_a_{1T}.

ALR	ω_T (rad/s)	a_{1T}	E_I (kJ)	TTSPD_a_{1T}					MTSPD_a_{1T}				
				$J_{50\%}$	δ	ζ_{eff}	$T_{80\%}$	$C_{80\%}$	$J_{50\%}$	δ	ζ_{eff}	$T_{80\%}$	$C_{80\%}$
10%	7.53	0.0053	55.95	5.5	0.128	2.0%	5.26	6.30	7.0	0.100	1.5%	6.78	8.10
20%	8.26	0.0048	67.29	5.5	0.128	2.0%	4.80	6.31	8.5	0.084	1.3%	7.38	9.67
30%	8.92	0.0044	78.55	5.5	0.128	2.0%	4.44	6.30	10.0	0.072	1.1%	7.91	11.19
40%	9.51	0.0042	89.76	5.5	0.128	2.0%	4.16	6.30	11.0	0.064	1.0%	8.40	12.71

The above performance is again observed in the cumulative dissipated energy curves presented in Figure 3.11. The difference between the two models is slight for low axial load levels and becomes more noticeable as the axial load increases.

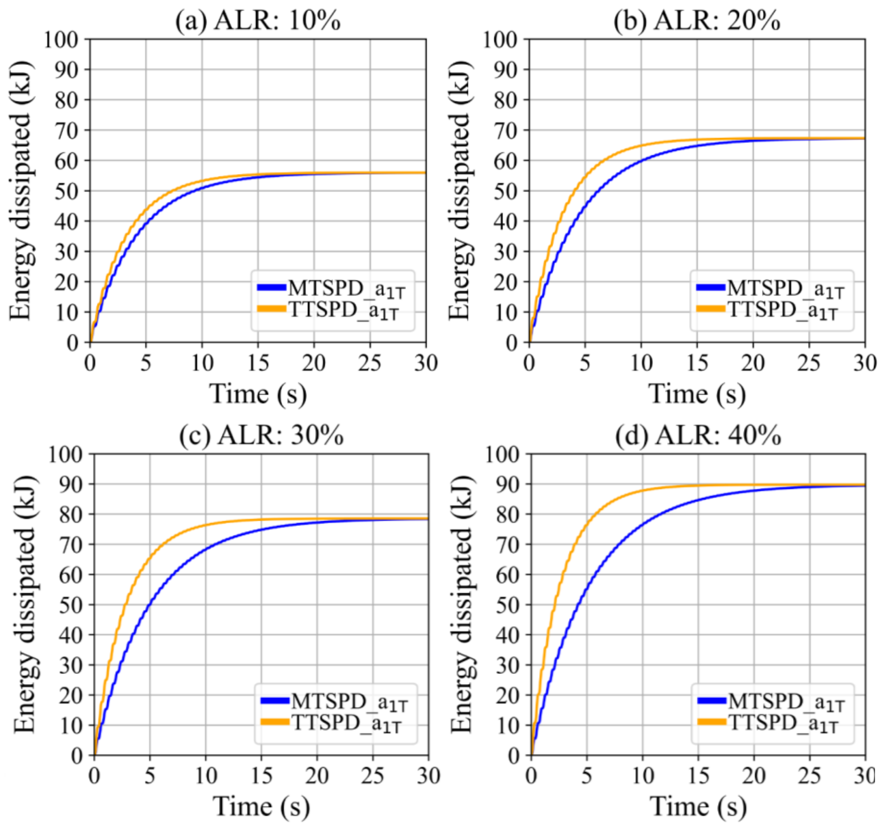

Figure 3.11 (a-d) Cumulative energy dissipated by the damping models MTSPD_a1T and TTSPD_a1T for different tensile ALRs.

Second case: damping parameter based on MSM

In this second case, the damping parameter a_{1M} is estimated using the system's fundamental frequency computed with the MSM according to eq. (3.16), i.e. without considering the influence of the GSM. As in the previous cases, two alternative tangent stiffness matrices are used to define the damping matrix: the TSM, comprising the material and geometric terms, and the MSM alone. These two models are denoted respectively as TTSPD_a_{1M} and MTSPD_a_{1M}.

Response to compressive load

Figure 3.12 shows the free-damped vibration response of both models under compressive ALRs. The response of the MTSPD_a_{1M} is more damped than that of TTSPD_a_{1M}. Nevertheless, it is less damped than the response of MTSPD_a_{1T} presented in Figure 3.8

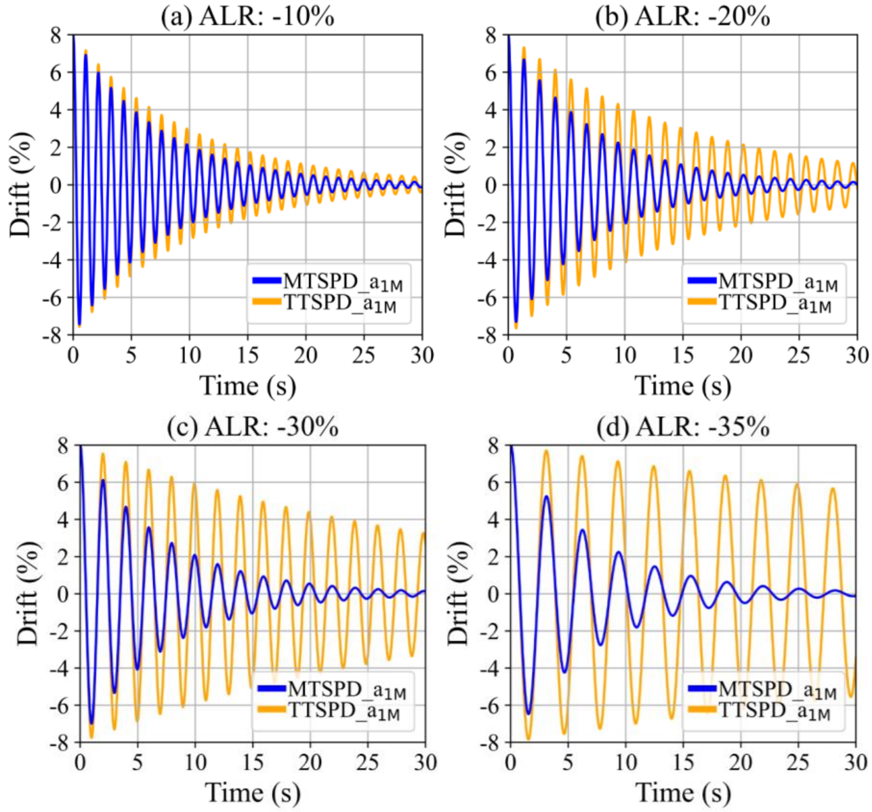

Figure 3.12 (a-d) Time-history response of cantilever top horizontal displacement for damping models MTSPD_a_{1M} and TTSPD_a_{1M} under different compressive ALRs.

The quantified characterization of the response shown in Table 3.4 can be contrasted with the values presented in Table 3.2. For instance, note that the maximum effective damping ratio with MTSPD_a_{1M}, found with eq. (3.20) for an ALR of -35%, is 6.8%; this compares with the 21.4% obtained with the model MTSPD_a_{1T}. It results directly of the much smaller damping parameter: 0.006 instead of 0.0198. It is noteworthy that the model MTSPD_a_{1M} takes the same time $T_{80\%}$ for all the selected ALRs. Since the parameter a_{1M} and the proportionality matrix remain unchanged for the different ALRs, and the energy input is smaller for more compressive loads, one could reason that the dissipative time $T_{80\%}$ and number of cycles $C_{80\%}$ should also be smaller. However, concerning the time, it should not be forgotten that for higher compressions, the natural frequency reduces, and consequently, the velocities also decrease, in turn implying smaller damping forces.

Table 3.4 Decay motion characterisation under compressive ALRs for TTSPD_a_{1M} and MTSPD_a_{1M}.

ALR	ω_M (rad/s)	a_{1M}	E_I (kJ)	TTSPD $T_{80\%}$_a_{1M}					MTSPD_a_{1M}				
				$J_{50\%}$	δ	ζ_{eff}	$T_{80\%}$	$C_{80\%}$	$J_{50\%}$	δ	ζ_{eff}	$T_{80\%}$	$C_{80\%}$
-10%	6.72	0.006	33.08	6.5	0.111	1.8%	8.0	7.41	5.0	0.147	2.3%	5.9	5.47
-20%	6.72	0.006	21.52	8.0	0.089	1.4%	12.4	9.28	4.0	0.182	2.9%	5.9	4.41
-30%	6.72	0.006	9.56	12.0	0.061	1.0%	26.7	13.60	3.0	0.269	4.2%	5.8	2.95
-35%	6.72	0.006	4.00	18.0	0.039	0.6%	66.3	21.84	2.0	0.422	6.8%	5.8	1.91

Regarding the cumulative dissipated energy as a function of time, see Figure 3.13, the initial slope of TTSPD_a_{1M} and MTSPD_a_{1M} is less steep than the TTSPD_a_{1T} and MTSPD_a_{1T} presented in Figure 3.9, respectively.

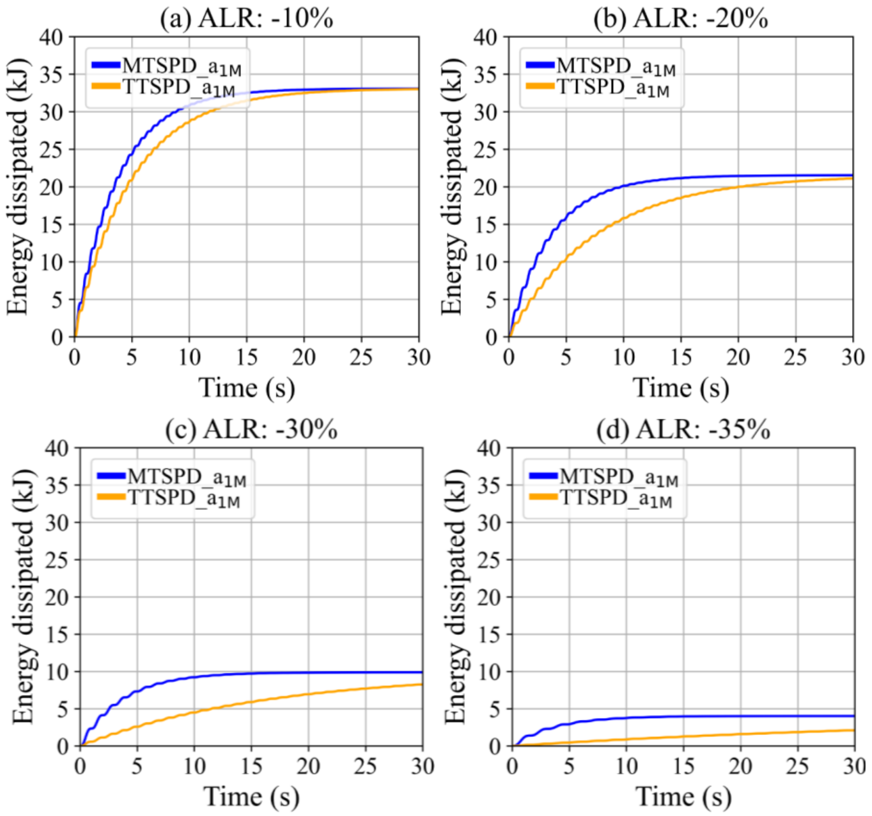

Figure 3.13 (a-d) Cumulative energy dissipated by the damping models MTSPD_a_{1M} and TTSPD_a_{1M} for different compressive ALRs.

Response to tensile load

Figure 3.14 shows the vibratory response under tensile ALRs. The response of the TTSPD_a_{1M} is more damped than that of MTSPD_a_{1M}. The movement decay of TTSPD_a_{1M} and MTSPD_a_{1M} decays faster than TTSPD_a_{1T} and MTSPD_a_{1T}, presented in Figure 3.10, which is a direct consequence of the damping parameter used.

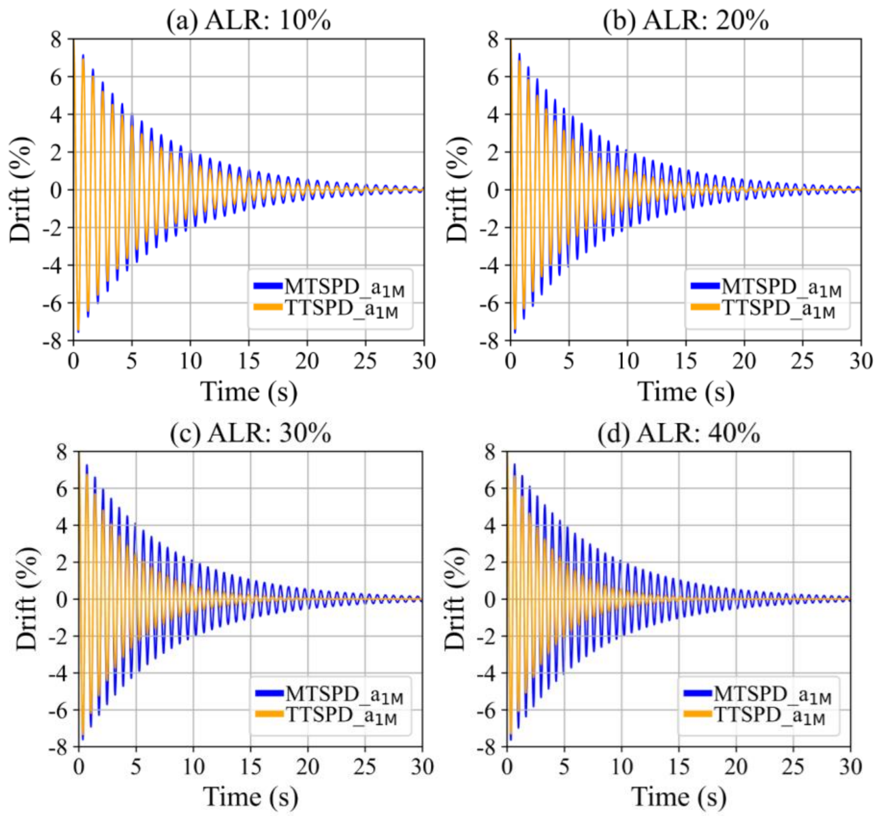

Figure 3.14 (a-d) Time-history response of cantilever top horizontal displacement for damping models MTSPD_a_{1M} and TTSPD_a_{1M} under different tensile ALRs.

The number of cycles needed to reach a peak displacement of 0.40 m for MTSPD_a_{1T} and MTSPD_a_{1M} is respectively, 11 and 8, under an ALR of 40%. Comments analogous to the previous compressive loading cases are applicable. Namely, regarding the time $T_{80\%}$, it is again similar for the different ALRs with the model MTSPD_a_{1M}. Moreover, it corresponds to the same amount of dissipative time required for compressive loads. In terms of $C_{80\%}$, the MTSPD_a_{1M} needs a larger number of cycles for increasing axial load, which is in agreement with the increase of the input energy.

Table 3.5 Decay motion characterisation under tensile ALRs for models TTSPD_a_{1M} and MTSPD_a_{1M}.

ALR	ω_M (rad/s)	a_{1M}	E_I (kJ)	TTSPD_a_{1M}					MTSPD_a_{1M}				
				$J_{50\%}$	δ	ζ_{eff}	$T_{80\%}$	$C_{80\%}$	$J_{50\%}$	δ	ζ_{eff}	$T_{80\%}$	$C_{80\%}$
10%	6.72	0.006	55.95	5.0	0.144	2.3%	4.79	5.73	6.5	0.113	1.8%	6.0	7.17
20%	6.72	0.006	67.29	4.5	0.159	2.5%	3.98	5.21	7.0	0.104	1.6%	6.0	7.86
30%	6.72	0.006	78.55	4.5	0.171	2.7%	3.34	4.73	7.5	0.096	1.5%	5.9	8.35
40%	6.72	0.006	89.76	4.0	0.183	2.9%	2.91	4.40	8.0	0.091	1.4%	5.9	8.93

The aforementioned is also observed in the curves of cumulative energy dissipated by the damping model. The TTSPD_a_{1M} and MTSPD_a_{1M} dissipate energy faster than TTSPD_a_{1T} and MTSPD_a_{1T}, which can be seen in Figure 3.15 and Figure 3.11. However, it is recalled that the damping parameter a_{1T} changes less under increasing tension loads with respect to compressive loads. Thus, the difference between the models using a damping parameter a_{1M} or a_{1T} is more noticeable under compression.

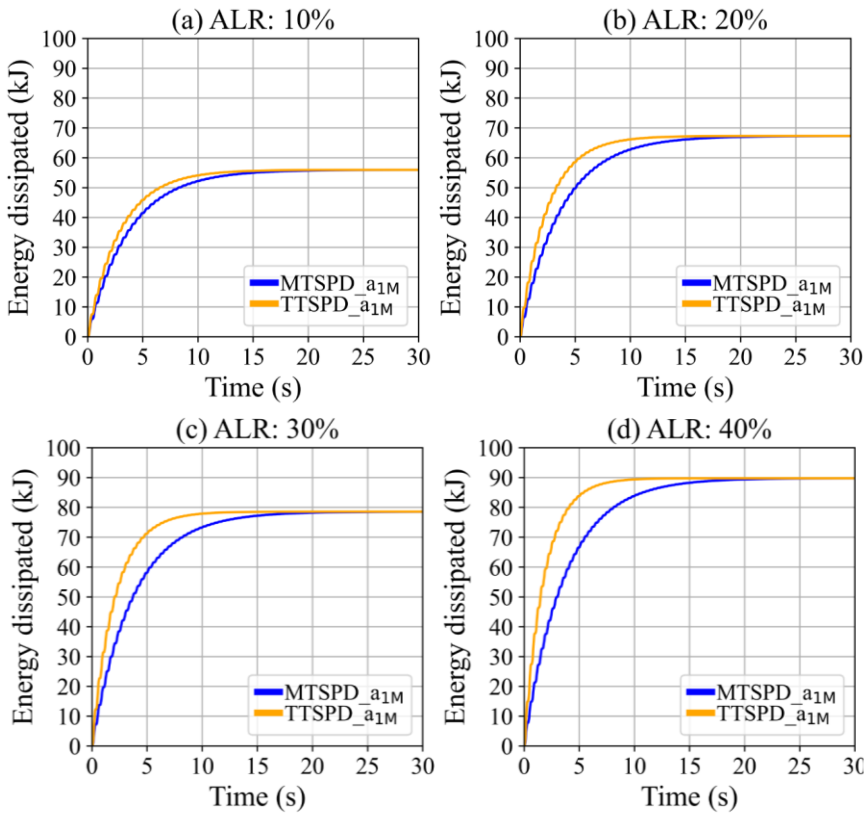

Figure 3.15 (a-d) Cumulative energy dissipated by the damping models MTSPD_a_{1M} and TTSPD_a_{1M} for different tensile ALRs.

The current case study illustrates the significance of the damping ratio for the model recommended in the current work, MTSPD_a_{1M}. The specified loading implies that the total energy input in the column is a function of the nonlinear geometric effects, observable by the distinct asymptotic values in the plots of Figure 3.13 and Figure 3.15. The physically relevant point to note is that all such structures with different ALRs take the same amount of time to dissipate the imparted energy, which confirms that the new damping model is tied up to material-deformation mechanisms (identical to all the cantilevers). Therefore, the intended insensitivity to nonlinear geometric contributions for energy dissipation simulation is confirmed.

3.4.2 Seismic response of a slender inelastic concrete column

This section analyses the inelastic response of a slender reinforced concrete column, represented in Figure 3.17. The structure is subjected to a horizontal component of the ground motion record of the Loma Prieta earthquake, downloaded from the PEER Strong Motion Database[87] and shown in Figure 3.16 (1989, M_w=6.2, station: APEEL 10 – Skyline), under different axial loads.

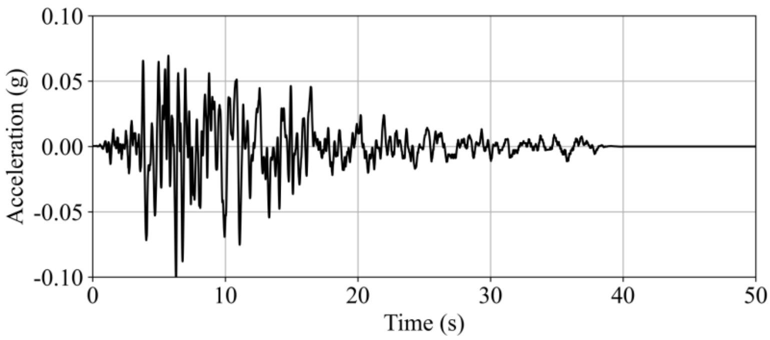

Figure 3.16 Ground motion record from the Loma Prieta earthquake (1989) used for the case study.

The numerical simulations were performed according to the following modelling hypotheses for the uniaxial models: (i) the concrete fibres were modelled using the proposal by Mander et al.[88] with the modifications suggested in Martinez-Rueda and Elnashai[89]; (ii) the confinement factors were computed as 1.49 and 1.15 for the fibres confined at the base of the column and above, respectively; (iii) the unconfined compressive strength of the concrete fibres is 28 MPa, and the Young's modulus is 25 GPa; no tensile strength was assumed; (iv) the steel fibres have a yield stress of 514 MPa with Young's modulus of 210 GPa and a post-yield hardening parameter of 0.005; according to the model proposed by Menegotto and Pinto[86], the remaining model parameters are: A_r = 20, A_1 = 18.5, A_2 = 0.15, A_3 = 0, and A_4 = 0.

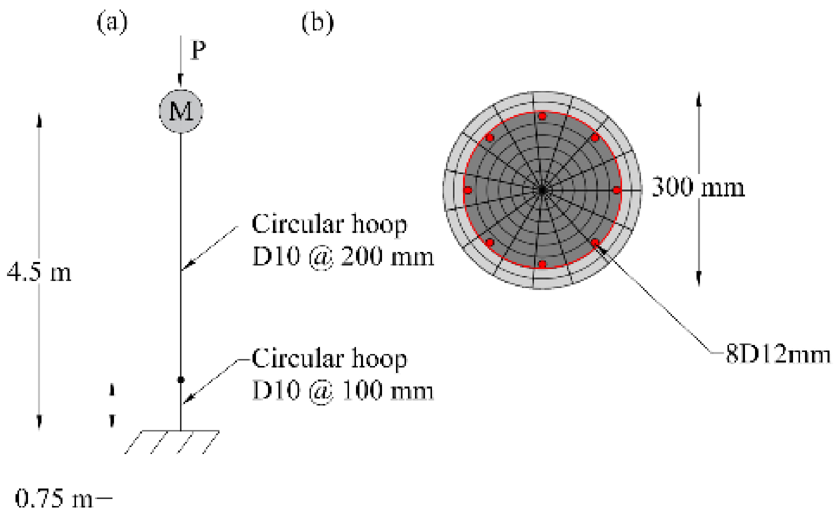

Figure 3.17 (a) Geometric dimensions of the column, transverse reinforcement, and identification of two beam elements, (b) cross-section discretisation.

Two force-based elements of 0.75 m (at the base) and 3.75 m, with three integration points each, were used to model the structure. At the top, the column has a translational mass of 7.65 ton and rotational inertia of 0.90 ton·m^2. A vertical static load imposing a compressive ALR of -10%, -20%, -30%, and -40% is applied at the first step of the analysis.

Three of the damping models presented in previous sections, namely MTSPD_a_{1M}, MTSPD_a_{1T}, and TTSPD_a_{1T}, are defined with a damping ratio of 2%. The Newmark integration method (β = 0.25 and γ = 0.5) combined with the Newton Raphson scheme are used to find the time-history response of the structure. The damping parameters and natural frequencies used to define the models are presented in 3.6.

Table 3.6 Natural frequencies and damping parameters obtained with the total and material stiffness matrix.

ALR	ω_T (rad/s)	a_{1T}	ω_M (rad/s)	a_{1M}
-10%	6.91	0.00579	7.36	0.00544
-20%	6.33	0.00632	7.27	0.00550
-30%	5.65	0.00708	7.16	0.00559
-40%	4.83	0.00828	7.01	0.00571

The lateral displacement response at the top of the column for increasing axial loads is presented in Figure 3.18. It can be observed that the TTSPD_a_{1T} shows higher displacements and a slower amplitude decay. By contrast, MTSPD_a_{1T} has the smallest displacements and the fastest amplitude decay, causing a more damped response compared to MTSPD_a_{1M}. The response of the latter model occurs between the other two, which is a direct consequence of using a_{1M} instead of a_{1T}. This behaviour can be further confirmed in the moment and curvature time-histories at the base cross-section presented in Figure 3.19 and Figure 3.20, respectively. The moment and curvature demands are seen to be higher with the model TTSPD_a_{1T} than with MTSPD_a_{1T} and MTSPD_a_{1M}.

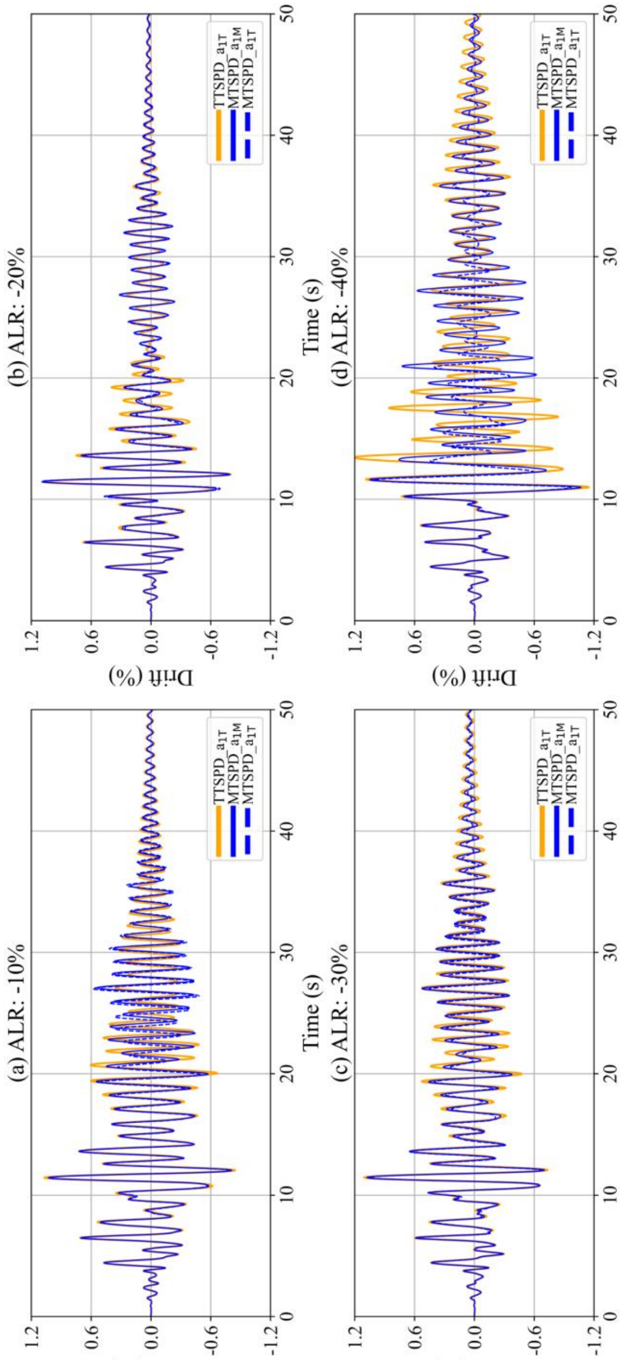

Figure 3.18 (a-d) Time-history response of cantilever top horizontal displacement under different compressive ALRs for TTSPD_a1T, MTSPD_a1M, and MTSPD_a1T models.

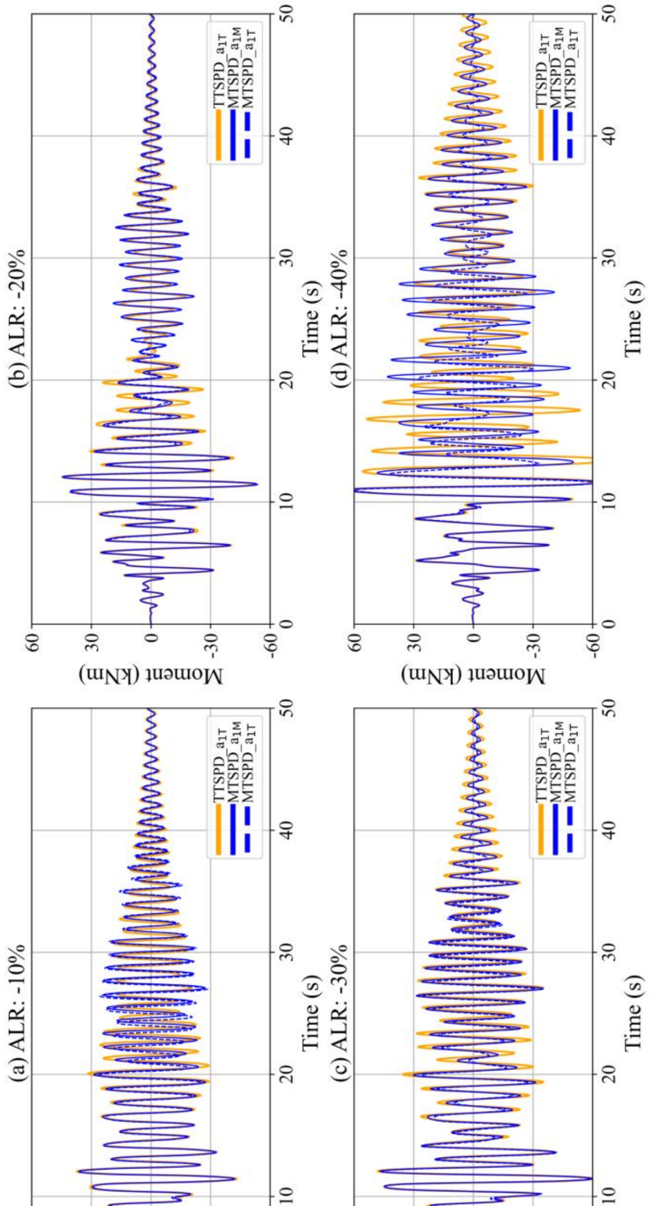

Figure 3.19 (a-d) Time-history of base cross-section bending moment under different compressive ALRs for TTSPD_a_{1T}, MTSPD_a_{1M}, and MTSPD_a_{1T} models.

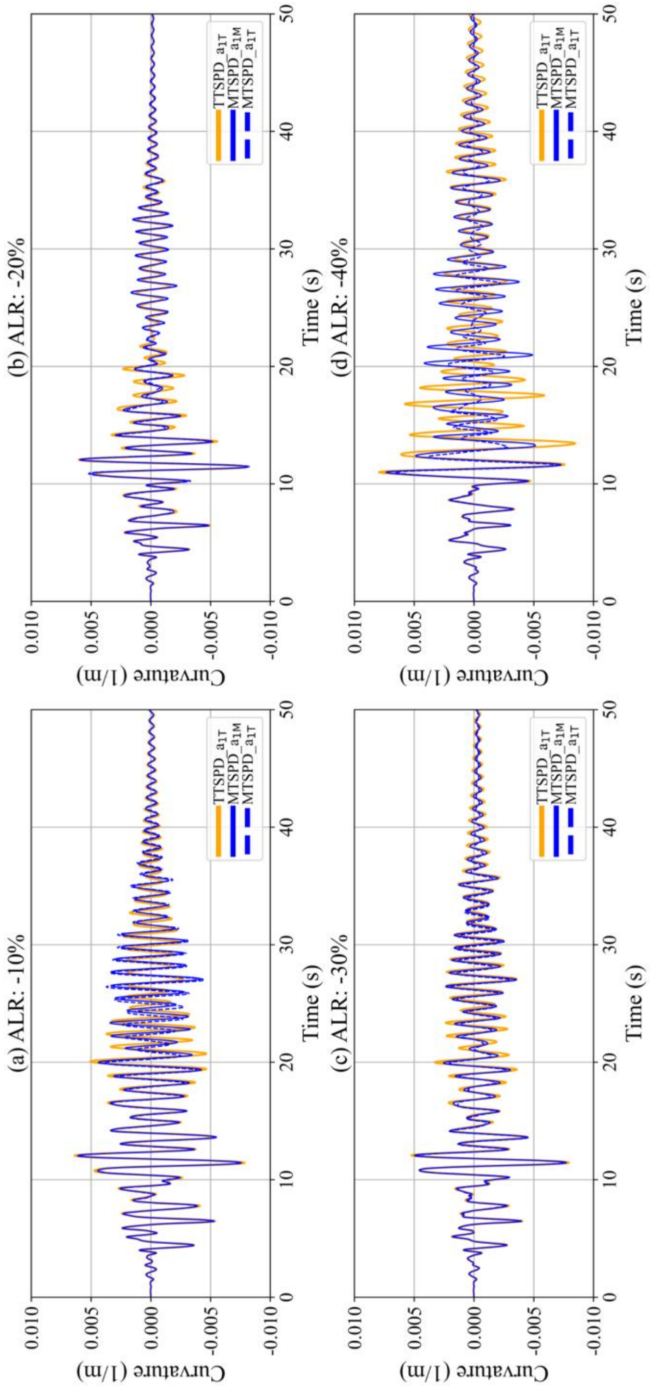

Figure 3.20 (a-d) Time-history of base cross-section curvature under different compressive ALRs for TTSPD_a1T, MTSPD_a1M, and MTSPD_a1T models.

The damage index in one structural element depends on the reached maximal deformation response and the hysteretic rules' total energy[90]. The total energy dissipated by the damping model and the hysteretic material response are presented in Figure 3.21 and Figure 3.23. In general, both versions of the model MTSPD dissipate more energy than TTSPD_a_{1T}. Under an ALR of -40%, the energy dissipated by the MTSPD_a_{1T} is similar to the energy dissipated by TTSPD_a_{1T}. The latter is caused by a more damped response of the MTSPD_a_{1T}, which reduces the total energy input to the system. Even if this model dissipated less energy than the others (particularly MTSPD_a_{1M}) for an ALR of -40%, the total energy dissipated by the rules of the materials is smaller, as shown in Figure 3.23.

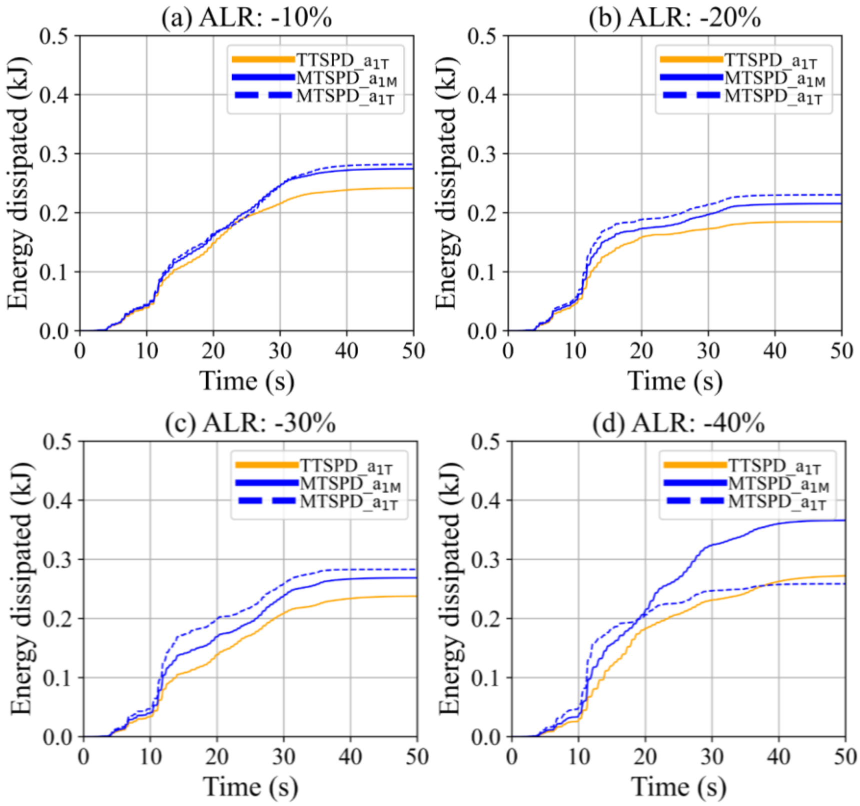

Figure 3.21 (a-d) Dissipation of energy by the different damping models under increasingly compressive ALRs.

In order to visualise clearly the influence of the geometric stiffness matrix in terms of energy dissipation, the energy dissipated by TTSPD_a1T model is separated in Figure 3.22 (a-d) into the energy dissipated by the material-related component (E_D^{Mat}) and the energy introduced by the component proportional to the GSM (E_D^{Geo}). Adding both curves in Figure 3.22 (a-d) gives the same curves presented in Figure 3.21 (a-d), respectively. The introduction of energy by the damping model through the GSM justifies its elimination because no such physical mechanism exists in reality.

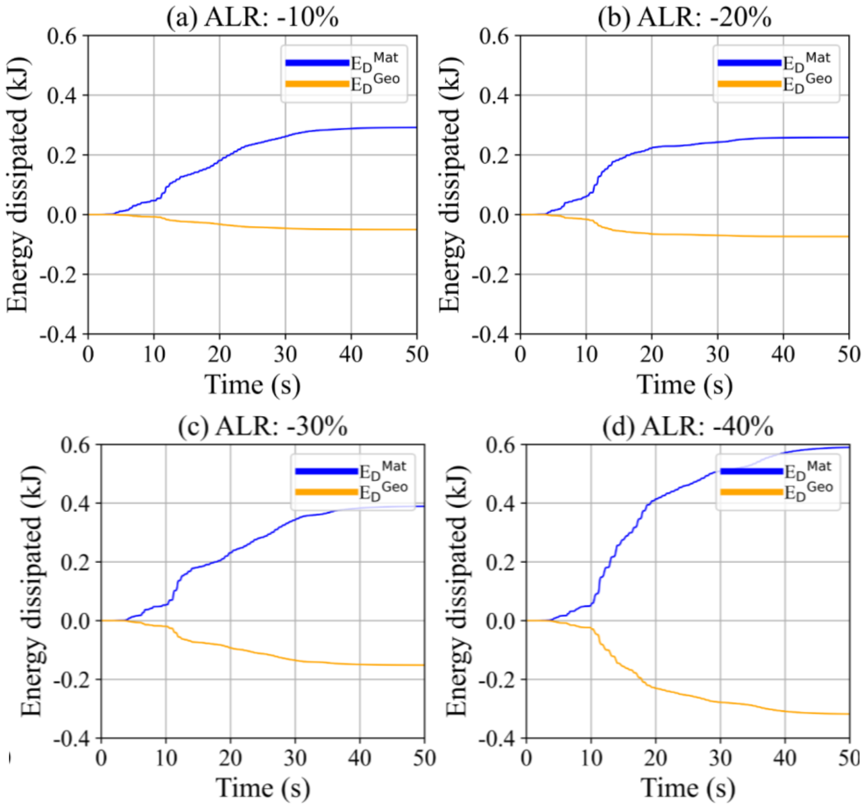

Figure 3.22 (a-d) Cumulative energy dissipated by TTSPD_a1T model divided into the energy dissipated by component proportional to the MSM and GSM

For small ALRs, the difference between the cumulative energy dissipated by the materials – shown in Figure 3.23 (a-d) – is generally small and similar for the different models. As the compression load increases, the total energy dissipated by the materials using the three models diverges. The column modelled with TTSPD_a_{1T} dissipated more energy through the hysteretic rules of the material, which is a direct consequence of its smaller capacity to dissipate energy through the damping term. It is noted that the oscillations in Figure 3.23 (a-d) are due to the fact that the curves represent not only the energy permanently stored but also the recoverable elastic energy.

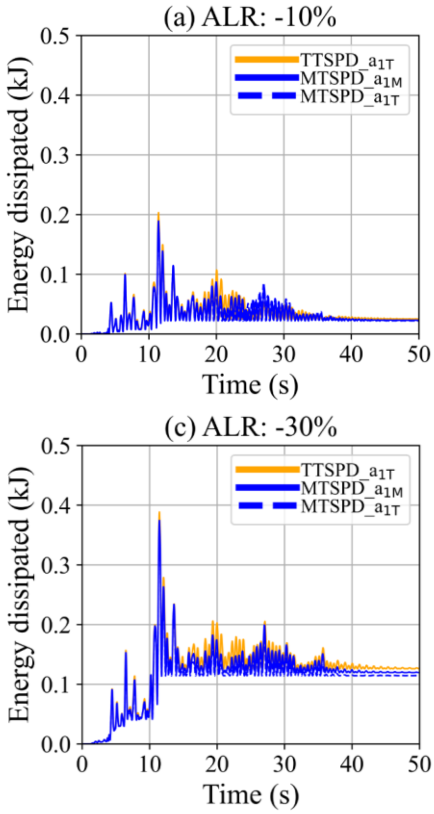

Figure 3.23 (a-d) Cumulative energy dissipated by the hysteretic rules of the materials under different compressive ALRs.

This example demonstrates that the influence of the GSM in the definition of damping models is noteworthy, even in reinforced concrete elements that are typically less slender than steel elements. The structure's response varies significantly in terms of deformations and internal forces if a damping model dependent, partially dependent or independent of the GSM is considered under important gravity loads. In nonlinear dynamic analyses of structures, the importance of the GSM can increase as the MSM decays due to lowering stiffness in the materials under increasing inelastic deformation demands. The above is observed in this case study: initially, all the models tend to follow a similar response, but the response changes noticeably after the highest deformation demand is attained. This observation is aligned with the discussion in section 3.3.

3.5 Conclusions

Most nonlinear time-history analyses employ the initial or, more commonly, the tangent stiffness proportional term of Rayleigh damping using the total stiffness matrix (TSM). The latter can be obtained as a sum of the material stiffness matrix (MSM) and the geometric stiffness matrix (GSM) when nonlinear geometric effects are considered. This chapter presents the derivation and implementation of a novel damping viscous model proportional just to the MSM, i.e., independent of the GSM, for beam elements. Physically, no conceivable energy-dissipation mechanisms can justify the inclusion of the GSM in the definition of the damping model, which is the rationale for developing the present model. The mathematical derivation and the nonlinear dynamic analyses in this manuscript, performed using elastic and inelastic elements, elucidate the main theoretical and physical features of the proposed damping model. This investigation shows that the GSM can contribute appreciably to the TSM in slender elastic structures under moderate to high axial load ratios; additionally, its relative importance is more significant in inelastic structures due to the MSM decay under large displacement demands.

A second aspect investigated in this work is the definition of the damping parameters, which are usually computed based on an estimated value of the damping ratio for one or two structural frequencies. The latter are commonly found with the TSM, taking significantly varying values according to the gravity loads applied on the structure due to the contribution of the GSM. This study suggests that a more physically consequential choice for obtaining the damping parameters would be to determine them using the natural frequencies found with the MSM, which remain constant regardless of the gravity loads applied to the structure.

The results show that the response of structural systems are affected due to the inclusion of the GSM in the definition of a stiffness proportional damping model, especially under significant gravity loads. The differences were highlighted in terms of energy dissipation, displacements, and internal forces. The work demonstrates that using the traditional total tangent stiffness-proportional damping model, the magnitude of the damping matrix changes considerably depending on the gravity forces applied. This affects the model's physical basis to simulate non-directly modelled energy-dissipation mechanisms, which are not linked to the GSM. It is argued that the damping model herein proposed, which is anchored just to material-related mechanisms, has a more physically consistent response, as illustrated in several case studies. The development of this model should also be considered as an evolution and response to previous concerns from other researchers, who have expressed concern about the presence of the GSM in the definition of stiffness proportional damping models.

4. Condensed tangent stiffness proportional viscous damping

4.1 Abstract

This chapter presents a condensed tangent stiffness proportional viscous damping model independent of the geometric stiffness matrix. It is developed for nonlinear dynamic analysis and implemented with distributed plasticity formulations. Following the theoretical derivation and its implementation, several case studies are presented. The first deals with the free vibration response of an inelastic bridge pier after being subjected to a history of static displacements, and the second is based on the seismic response of a multi-story reinforced concrete frame. Comparisons with existing total and condensed formulations show that the new proposal eliminates the spurious damping forces, avoids high levels of energy dissipation presented by damping models defined with the initial properties, and has numerical problems related to the geometric stiffness matrix during extreme loads and deformations.

4.2 Introduction

Nonlinear analyses have become common in everyday structural engineering practice due to the community's growing interest in performance-based design, seismic control systems, and the evaluation of existing structures[31]. During dynamic loading, these analyses present a source of uncertainty related to how other sources of energy dissipation, independent of material hysteretic rules, are modelled[25,28]. Especially during extreme loads events where the system behaves in the inelastic range.

The energy imparted by an external force on the structure is equal to the sum of the kinetic energy of its mass, the energy permanently and temporarily stored in the hysteretic cycles, and the energy dissipated by mechanisms not directly modelled. All these sources of energy dissipation not dependent on hysteretic cycles have been commonly represented by viscous damping models calibrated through experimental data of structures under small-amplitude vibrations.

Lord Rayleigh[8] originally proposed the first model under the premise "with a degree of approximation sufficient for acoustics purposes". The Rayleigh damping (RD) model was implemented in linear dynamic analysis of structures because the effect of damping forces on the structure's response is small. For instance, in a linear SDoF using a damping ratio of 5%, the damping force may reach approximately 10% of the inertial or elastic forces of the structure[29]. Using this argument, Wilson and Clough[11] mentioned that it is justifiable to use RD for step-by-step linear dynamic analyses of MDoF. Nevertheless, recognizing that the exact form of damping in most structures is unknown. Additionally, RD creates a damping matrix orthogonal to the modal shapes of the structural system. Due to its simplicity and advantages, RD is probably the most widespread and used damping model in finite element programs.

The main arguments for using RD in linear analyses are no longer valid for nonlinear analysis. The damping force for an inelastic SDoF defined with the 5% critical damping may reach 20% of the system's other forces but increase much more at times[29]. It can lead to an overall increase in the effective damping ratio of the system during the analysis[22], which is challenging to justify physically. Additionally, during incursions in the inelastic range on MDoF, the orthogonality of the system is lost, and RD triggers significant damping moments in the massless DoFs that can reach a magnitude equal to the yield moment of the structural element[25].

Some research projects[25,29,30,50] have proposed defining the viscous damping matrix only between the DoFs with mass to eliminate the spurious damping forces appearing during incursions in the inelastic range. Thus, the position related to the massless DoFs will be defined with zero values. These models eliminate the spurious damping moments at the massless DoFs. Nevertheless, they trigger overall changes in the effective damping ratio of the structure that may imply high energy dissipation levels because the system's initial properties define them.

This chapter proposes a damping model proportional to the condensed stiffness matrix – in opposition to the total stiffness matrix – using the tangent stiffness matrix, which has not been explored in the literature. The chapter also compares the behaviour of existing total and condensed damping models using realistic structures subjected to nonlinear dynamic analysis, where the numerical deficiencies of existing condensed damping models are highlighted. The next section will theoretically describe the existing models and the new proposed. Subsequently, two numerical examples highlight the difficulties and advantages of the different models in nonlinear dynamic analyses using distributed plasticity formulations. Finally, the last part sums up the main conclusions.

4.3 Condensed-tangent-stiffness-proportional viscous damping model

4.3.1 Motivation

The main advantages of existing condensed damping models lie in the elimination of the spurious damping forces in the massless DoFs and in the fact that the damping matrix must be calculated once, which is preferable from a computational cost perspective.

Although condensed initial stiffness proportional damping and modal damping eliminate spurious damping forces, they can cause an overdamped response in the structure due to the stiffness decay. These models may imply levels of energy dissipation similar to the counterpart proportional to the total initial stiffness matrix or RD, which are generally considered inappropriate by the engineering community.

They can also present additional problems related to underestimating internal forces and displacements.

The model proportional to the tangent stiffness matrix has been commonly used to reduce traditional models' high energy dissipation levels. Additionally, this model reduces the damping forces in the massless DoFs. However, they are not entirely eliminated and can have significant magnitudes, as mentioned by Chopra and McKenna[21].

This chapter proposes defining a condensed SPD model using the condensed tangent stiffness matrix to avoid high levels of energy dissipation and eliminate the spurious damping forces. As far as the author is aware, condensed damping models proportional to stiffness have been defined with the initial properties of the system. Additionally, the GSM is excluded from the definition of the damping matrix and damping parameters, as proposed in the last chapter. This will avoid the potential consequences of the geometric stiffness matrix during extreme loads and deformations.

Condensed models have been little studied, considering that they are not implemented in most commercial and open-source software. Therefore, another motivation for this chapter is to provide a detailed study of the existing condensed models implemented in the author's program. The latter is a significant contribution to the literature.

4.3.2 Formulation

The tangent stiffness matrix of the structure in nonlinear analysis at the local level can be found at each step using the following equation:

$$\mathbf{K}^{\mathrm{TanLoc}} = \mathbf{K}^{\mathrm{TanGeoLoc}} + \mathbf{K}^{\mathrm{TanMatLoc}} \tag{4.1}$$

Where, $\mathbf{K}^{\mathrm{TanMatLoc}}$ is the material-related component and $\mathbf{K}^{\mathrm{TanGeoLoc}}$ is the geometric stiffness matrix.

The global material stiffness matrix $\mathbf{K}^{\mathrm{TanMat}}$ is found assembling all the local material stiffness matrices. Therefore, it is proposed to define the damping matrix using eq. (4.2) with a damping parameter found at the beginning of the analysis or updating them as indicated in eq. (4.3).

$$\mathbf{C}^{\mathrm{MatTan}} = \mathrm{a}_{0\mathrm{M\,initial}} \cdot \begin{bmatrix} \mathbf{M}_{\mathrm{tt}} & 0 \\ 0 & 0 \end{bmatrix} + \mathrm{a}_{1\mathrm{M\,initial}} \begin{bmatrix} \widehat{\mathbf{K}}_{\mathrm{tt}}^{\mathrm{MatTan}} & 0 \\ 0 & 0 \end{bmatrix} \tag{4.2}$$

$$\mathbf{C}^{\mathrm{MatTan}} = \mathrm{a}_{0\mathrm{M\,updated}} \cdot \begin{bmatrix} \mathbf{M}_{\mathrm{tt}} & 0 \\ 0 & 0 \end{bmatrix} + \mathrm{a}_{1\mathrm{M\,updated}} \begin{bmatrix} \widehat{\mathbf{K}}_{\mathrm{tt}}^{\mathrm{MatTan}} & 0 \\ 0 & 0 \end{bmatrix} \tag{4.3}$$

Where $\widehat{\mathbf{K}}_{\mathrm{tt}}^{\mathrm{MatTan}}$ is the condensed tangent stiffness matrix found through eq. (4.4)

$$\widehat{\mathbf{K}}_{\mathrm{tt}}^{\mathrm{MatTan}} = \mathbf{K}_{\mathbf{tt}}^{\mathrm{MatTan}} - \mathbf{K}_{\mathrm{t0}}^{\mathrm{MatTan}} \mathbf{K}_{00}^{\mathrm{MatTan}-1} \mathbf{K}_{0\mathrm{t}}^{\mathrm{MatTan}} \tag{4.4}$$

The damping parameters a_{0M} and a_{1M} are found through eq. (2.3) using the frequencies without considering the GSM. Moreover, a model proportional only to the condensed material tangent stiffness matrix can be defined using eqs. (4.5) and (4.6).

$$\mathbf{C}^{\mathrm{MatTan}} = \mathrm{a}_{1\mathrm{M\,initial}} \begin{bmatrix} \widehat{\mathbf{K}}_{\mathrm{tt}}^{\mathrm{MatTan}} & 0 \\ 0 & 0 \end{bmatrix} \tag{4.5}$$

$$\mathbf{C}^{\mathrm{MatTan}} = \mathrm{a}_{1\mathrm{M\,updated}} \begin{bmatrix} \widehat{\mathbf{K}}_{\mathrm{tt}}^{\mathrm{MatTan}} & 0 \\ 0 & 0 \end{bmatrix} \tag{4.6}$$

As mentioned above, condensed models eliminate spurious damping forces since the entries of the submatrices $\mathbf{C}_{00}$, $\mathbf{C}_{0t,}$ and $\mathbf{C}_{t0}$ are defined with zeros. In contrast, the submatrix $\mathbf{C}_{tt}$ is fully populated since it is proportional to the matrix $\widehat{\mathbf{K}}_{\mathrm{tt}}^{\mathrm{MatTan}}$ which has this condition.

4.4 Case studies

This section presents two case studies showing the advantages of the proposed model and the pathologies of existing condensed damping models with distributed plasticity elements. The damping models implemented are defined according to Table 4.1. As mentioned above, even if the nonlinear geometric effects are considered, the geometric stiffness matrix is removed from the definition of all damping models, as indicated in the previous chapter. The damping models defined with the initial damping parameter are defined after imposing the gravity loads and using a damping ratio of 3%. The analyses are performed in a program developed by the author.

Table 4.1 Damping models analysed and implemented

Name damping model	Abbreviation	Stiffness used for computing the damping matrix	Stiffness used for computing the damping parameters
Total initial stiffness proportional damping	TISPD	$\mathbf{K}^{\mathrm{InitMat}}$	$\mathbf{K}^{\mathrm{InitMat}}$
Total initial Rayleigh damping	TIRD	$\mathbf{K}^{\mathrm{InitMat}}$	$\mathbf{K}^{\mathrm{InitMat}}$
Condensed initial stiffness proportional damping	CISPD	$\mathbf{K}^{\mathrm{InitMat}}$	$\mathbf{K}^{\mathrm{InitMat}}$
Condensed initial Rayleigh damping	CIRD	$\mathbf{K}^{\mathrm{InitMat}}$	$\mathbf{K}^{\mathrm{InitMat}}$
Modal damping	MD	N/A	N/A
Total tangent stiffness proportional damping	TTSPD	$\mathbf{K}^{\mathrm{TanMat}}$	$\mathbf{K}^{\mathrm{InitMat}}$
Total tangent Rayleigh damping	TTRD	$\mathbf{K}^{\mathrm{TanMat}}$	$\mathbf{K}^{\mathrm{InitMat}}$
Condensed tangent stiffness proportional damping	CTSPD	$\mathbf{K}^{\mathrm{TanMat}}$	$\mathbf{K}^{\mathrm{InitMat}}$
Condensed tangent Rayleigh damping	CTRD	$\mathbf{K}^{\mathrm{TanMat}}$	$\mathbf{K}^{\mathrm{InitMat}}$
Updated condensed tangent stiffness proportional damping	UCTSPD	$\mathbf{K}^{\mathrm{TanMat}}$	$\mathbf{K}^{\mathrm{TanMat}}$
Updated modal damping	UMD	N/A	N/A
Mass proportional damping	MPD	N/A	$\mathbf{K}^{\mathrm{InitMat}}$

4.4.1 Dynamic response of an inelastic concrete bridge pier

Reinforced concrete (RC) structures have significant changes in their stiffness because concrete has good compressive and low tensile strength properties. Under tensile demands, concrete fibres provide stiffness for minimal loads. Thus, RC sections will crack quickly under higher loads causing significant changes in the computed stiffness of the structure. Additionally, RC sections have confined and unconfined concrete fibres; even during small-magnitude earthquakes, the unconfined fibres at the edges of the cross-sections can quickly reach their ultimate strains. The above causes a relevant decrease in the structure's stiffness, affecting the damping models shown in Table 4.1.

This study case compares the structural response of the damping models presented in Table 4.1 and finds the effective damping ratio after incursions in the inelastic range. The cantilevered bridge pier column, depicted in Figure 4.1 (a), is modelled using two force-based elements[83–85] defined with three Gauss-Lobatto integration points and a corotational formulation to consider nonlinear geometric effects[78,79,81]. At the top, the pier has a translational and rotational mass of 100 tons and 2.0 ton.m^2, respectively.

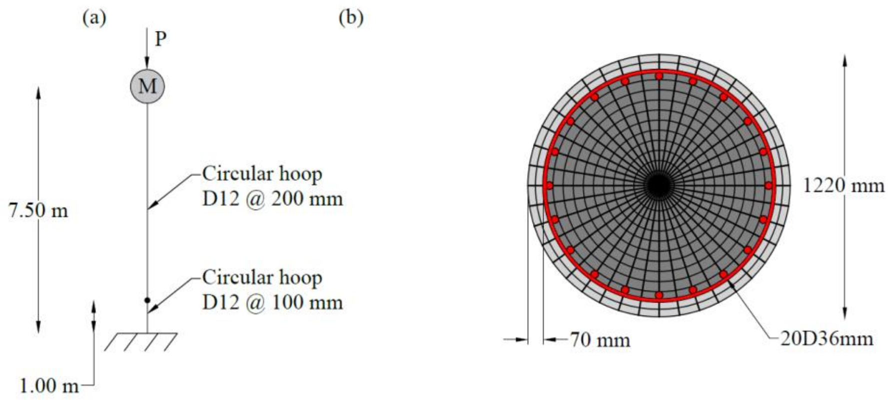

Figure 4.1 (a) Geometric dimensions, transverse reinforcement, and identification of two-beam elements of the bridge pier, (b) cross-section discretisation.

The monitored sections are discretised at the integration points, as shown in Figure 4.1 (b). The steel and concrete fibres are modelled using the uniaxial constitutive laws presented by Menegotto and Pinto[86] and Mander et al.[88]. The confined concrete properties are defined using the procedure described in the EN 1998-2[6]. The input parameters of the uniaxial constitutive laws are presented in Table 4.2.

Table 4.2 Input parameters of the uniaxial constitutive models used to model the steel and concrete fibres.

Steel Fibres	**f_y (MPa)**	**E (GPa)**	**b**	**R_0**	**A_1**	**A_2**	**A_3**	**A_4**	**ε_{su}**
Steel bars	518.5	200.0	0.005	20.0	18.5	0.25	0.0	1.0	0.11
Concrete Fibres	**f_c (MPa)**	**E (GPa)**	**ε_c**	**ε_{cu}**	**f_t (MPa)**	**ε_t**	**beta**		
Concrete cover	-38.0	26.4	-0.0025	-0.004	3.0	0.00015	0.9		
Column's concrete core at the base	-44.5	26.4	-0.0037	-0.012	3.0	0.00015	0.9		
Column’s concrete core at the top	-41.0	26.4	-0.0028	-0.008	3.0	0.00015	0.9		

The beta parameter is assumed to be 0.9 in the concrete constitutive law to avoid a very high negative stiffness after the models reach the tension peak stress. The program developed uses an original Newton-Rapson scheme to solve the nonlinear problem; thus, this negative stiffness can cause convergence problems and even pathologies in the damping models that are not studied in this chapter. The strain-stress relations of the material models are plotted in Figure 4.2 (a-c), where the main features of the uniaxial constitutive laws are highlighted.

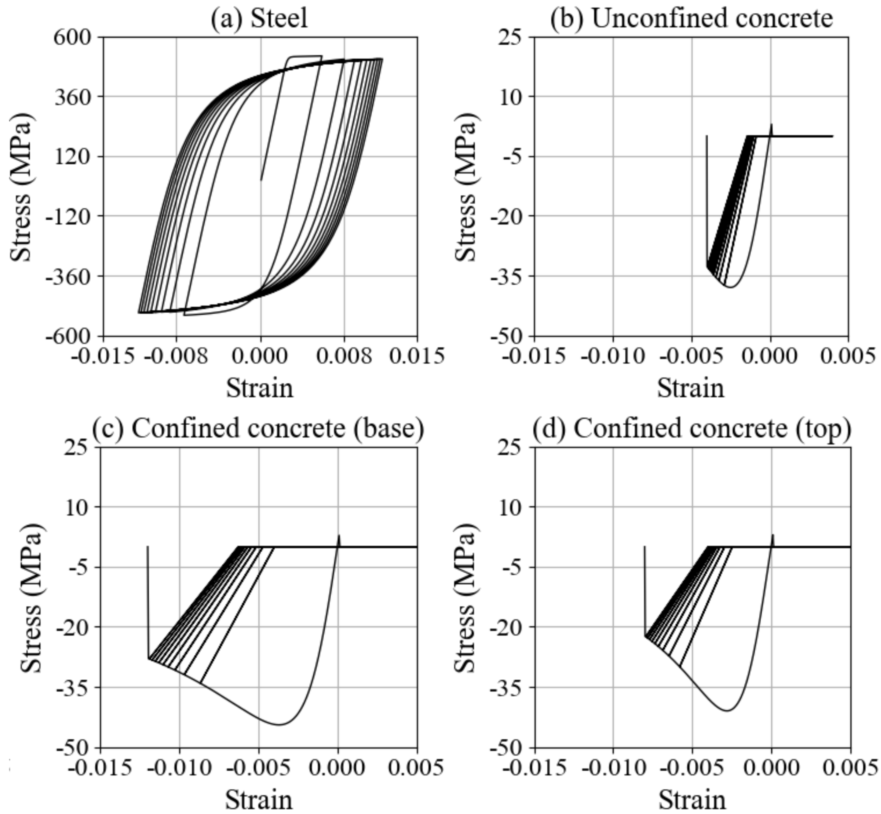

Figure 4.2 Uniaxial constitutive laws used for modelling the steel and concrete fibres: (a) Menegotto and Pinto[86]*, (b-d) Mander et al.*[88].

The structure is initially subjected to a static history of displacements at the top, shown in Figure 4.3. The main purpose is to cause a controlled stiffness degradation in the element and observe the structure's response using the different damping models, specifically to identify the effective damping ratio of the structure after incursions in the inelastic range. During the history of displacement, the nonlinear problem is solved using a displacement control method and a Newton-Raphson scheme. At the end of it, the column is brought to 0% drift, which does not necessarily imply zero force, and the problem is switched from a static analysis to a dynamic analysis using Newmark ($\beta = 0.25$ and $\gamma = 0.5$) and a Newton-Raphson scheme to find the solution of the nonlinear problem. The latter means that the top node, where the displacement was imposed, is released, and the column is in a damped free vibration response.

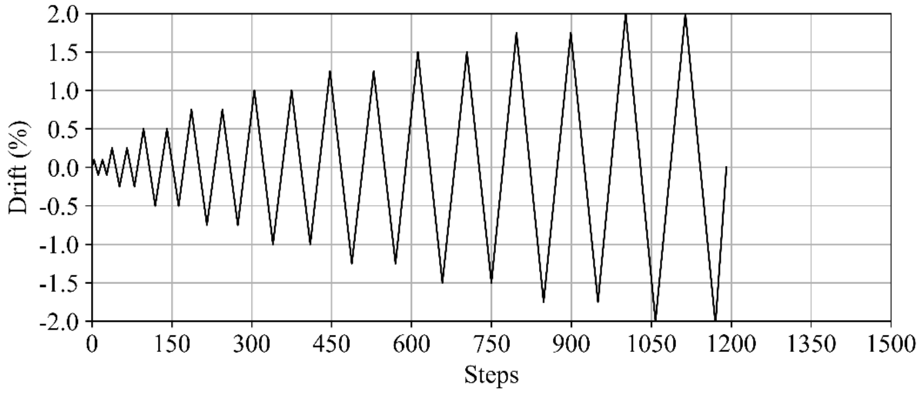

Figure 4.3 History of statically imposed drifts at the top horizontal DoF of the bridge pier.

Figure 4.4 (a) presents the force-displacement response at the top of the bridge pier. The moment curvature and centroid strain at the base are exhibited in Figure 4.4 (b-c). These plots show the stiffness decay and material damage on the structure, which will be required to understand the behaviour of the damping models when moving from a nonlinear static to a nonlinear dynamic analysis.

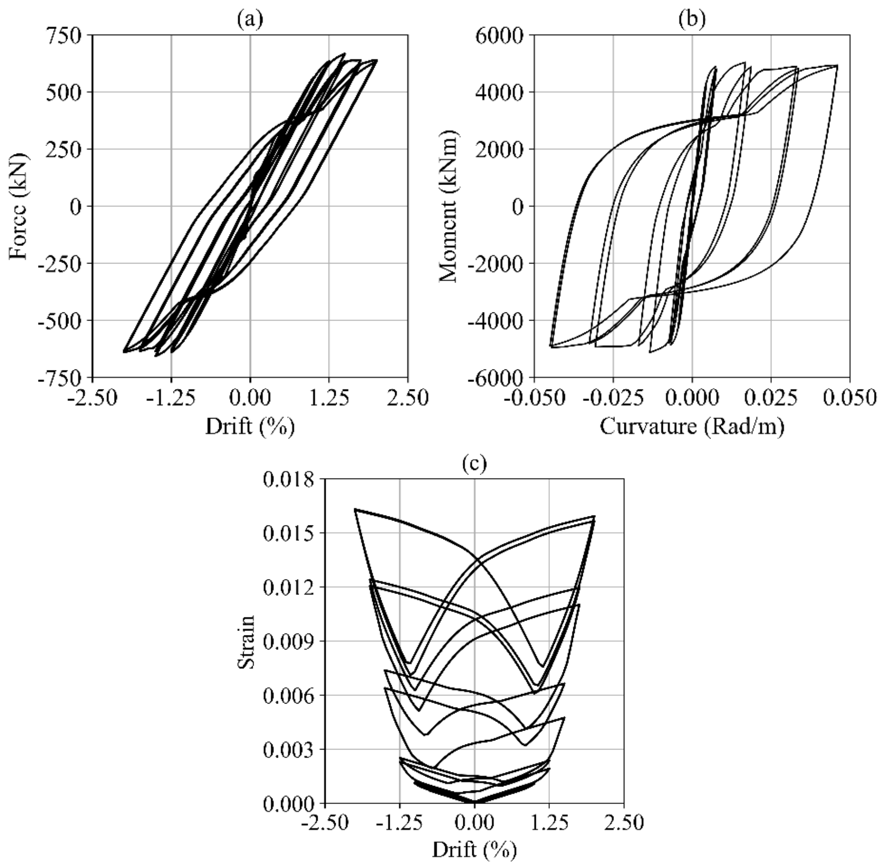

Figure 4.4 (a) force drift curve of the bridge pier, (b) moment-curvature curve of the cross-section at the base, (c) strain at the centroid of the section at the base versus drift of the bridge pier.

Figure 4.5 presents the complete response of the structure using the CISPD and CTSPD damping models, i.e., including the static displacement at the beginning and dynamic response at the end. The structure's response is equal when the displacement history is applied because damping is not considered in static analysis. The models differ when the analysis is switched from nonlinear static to nonlinear dynamic, where damping influences the structural response.

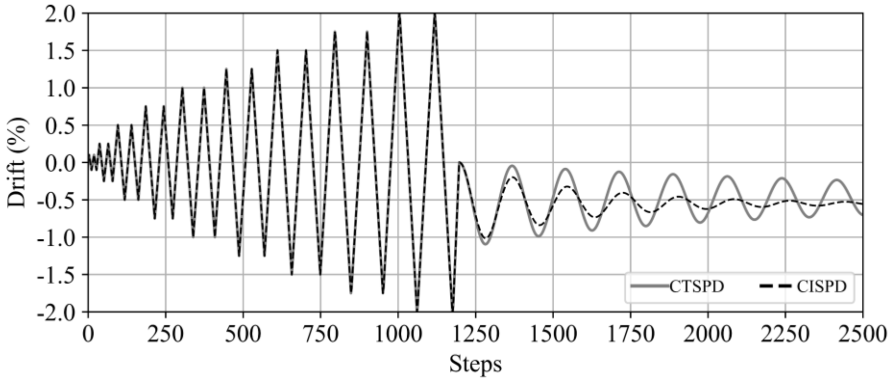

Figure 4.5 History of the cantilever bridge pier drifts using CISPD and CTSPD.

The free vibration response of the dynamic analysis is taken to calculate the logarithmic decrement of the structure and find the effective damping ratio of the different damping models using the following equation initially derived for a SDoF.

$$\delta = \frac{2\pi\zeta}{\sqrt{1-\zeta^2}} \tag{4.7}$$

Figure 4.6 presents only the free vibration response of the structure using the different damping models. The imposed static displacements are not shown for clarity and considering the static response is equal in all cases. The CIRD, CISPD, CTRD, and CTSPD models show a similar response to the analogue models proportional to the total stiffness matrix: TIRD, TISPD, TTRD, and TTSPD, respectively. The models defined from the initial properties (CIRD, CISPD, TIRD, TISPD, MD, MPD) have a similar response and all present an overdamped response compared to the other models based on the current properties in this specific case. This is a direct consequence of the decay of the structural stiffness, shown in Figure 4.4 (a-b), after the history of displacement. Although no experimental tests were performed in this study, this decay in the damping capacity to dissipate energy when using the current properties of the system may have a physical sense because the element will crack significantly along its length. The latter will cause an effective loss in energy dissipation capacity through the materials' micro-hysteretic curves; see the strain increment at the centroid in Figure 4.4 (c). Models based on the current system properties have been criticized because the damping forces decrease considerably during incursions into the inelastic range; however, during these incursions, the material constitutive laws are expected to take most of the energy.

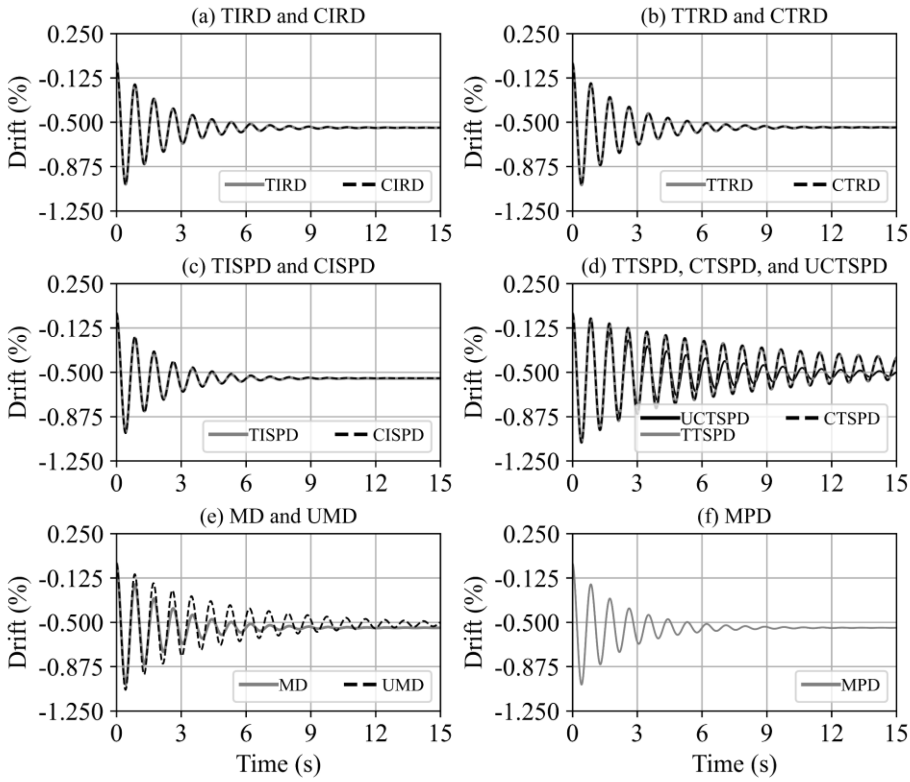

Figure 4.6 (a-f) Time-history response of cantilever top horizontal displacement for the damping models presented in Table 4.1 after the statically imposed drifts.

Table 4.3 presents the effective damping ratio found through equation (4.7). The damping models based on the initial properties have an effective damping ratio at least two times bigger than the initially defined ones, including MD. The effective damping ratio is smaller in the TTSPD and CTSPD models, whereas the TTRD and CTRD have an increment in the damping ratio due to the presence of the mass matrix in the definition of the damping matrix. Finally, the UMD and UCTSPD models retain the initially defined damping ratio since the damping parameters are updated. All models depicted with the total stiffness matrix had a higher effective damping ratio than those based on the condensed stiffness matrix, but the difference is small.

Table 4.3 Effective damping ratio of the different damping models after the statically imposed drifts.

Abbreviation	Defined damping ratio	Effective damping ratio
TISPD	3.0%	7.2%
TIRD	3.0%	6.3%
CISPD	3.0%	6.9%
CIRD	3.0%	6.2%
MD	3.0%	6.2%
TTSPD	3.0%	1.7%
TTRD	3.0%	5.9%
CTSPD	3.0%	1.7%
CTRD	3.0%	5.9%
UCTSPD	3.0%	3.1%
UMD	3.0%	3.1%
MPD	3.0%	6.2%

This case study shows that condensed models based on the initial properties of the system exhibit, like the total models, a significant increase in the effective damping ratio. Total damping models based on initial system properties are usually considered inadequate. By analogy, the condensed models TISPD, TIRD, CISPD, CIRD, MPD, and MD are equally inappropriate in this case.

4.4.2 Dynamic response of an inelastic concrete frame structure

Figure 4.7 presents an ideal multi-story RC structure used to compare the damping models presented in Table 4.1. The building comprises two frames and six storeys with the dimensions shown. Masses of 12.8 tons and 25.5 tons are considered lumped at the central and edge nodes, respectively, in the vertical and horizontal directions. The structural members are modelled with force-based elements considering distributed plasticity and using three integration points[83–85]. Also, a corotational formulation[78,79,81] was employed to account for nonlinear geometric effects. The rigid length offsets of the elements were defined according to the full dimensions of the cross-sections. For simplicity, "Cross-section 1" is used for all the columns, while "Cross-section 2" is assigned to all the beams. Both cross-sections have a cover width of 50 mm and steel bars of 20 mm distributed according to Figure 4.1.

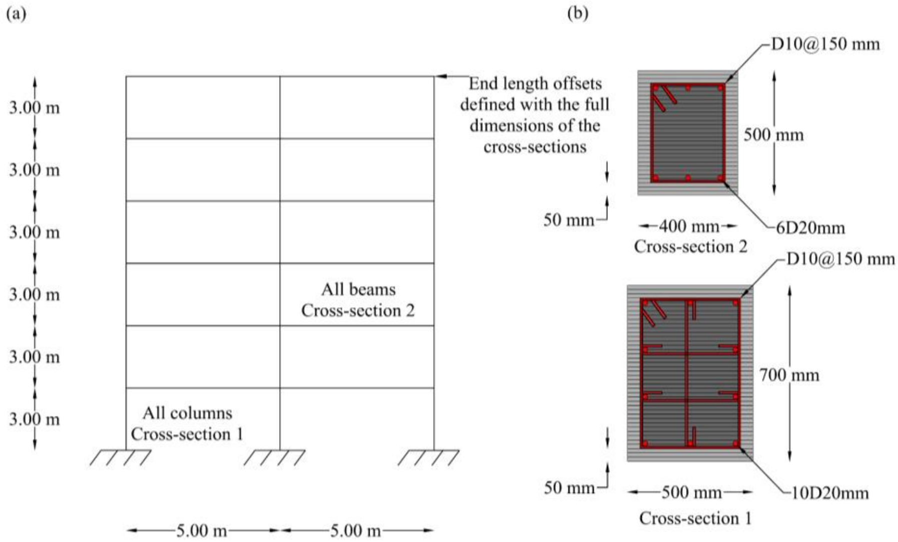

Figure 4.7 (a) Geometric dimensions and identification of the column and beam elements of the concrete frame, (b) cross-section discretisation and longitudinal and transverse reinforcement.

The concrete fibres use the model by Mander et al.[88], considering different input parameters to model the unconfined and confined concrete fibres. The confined concrete in the beams is less confined than the concrete core of the columns, represented in the ultimate strain and peak strength. The uniaxial model of Menegotto and Pinto [86] was employed to simulate the steel bars of the cross-sections. The input parameters of the material constitutive laws are presented in Table 4.4.

Table 4.4 Input parameters of the uniaxial constitutive models used to model the steel and concrete fibres.

Steel Fibres	**f_y (MPa)**	**E (GPa)**	**b**	**R_0**	**A_1**	**A_2**	**A_3**	**A_4**
Steel bars	518.5	200.0	0.005	20.0	18.5	0.25	0.0	1.0
Concrete Fibres	**f_c (MPa)**	**E (GPa)**	**ε_c**	**ε_{cu}**	**f_t (MPa)**	**ε_t**	**beta**	
Concrete cover	-38.0	26.4	-0.0025	-0.004	3.0	0.00015	0.9	
Column's concrete core	-45.8	26.4	-0.0040	-0.019	3.0	0.00015	0.9	
Beam's concrete core	-41.2	26.4	-0.0028	-0.018	3.0	0.00015	0.9	

The strain-stress relations of the material models are plotted in Figure 4.2 (a-d), where the main features of the uniaxial constitutive laws are shown.

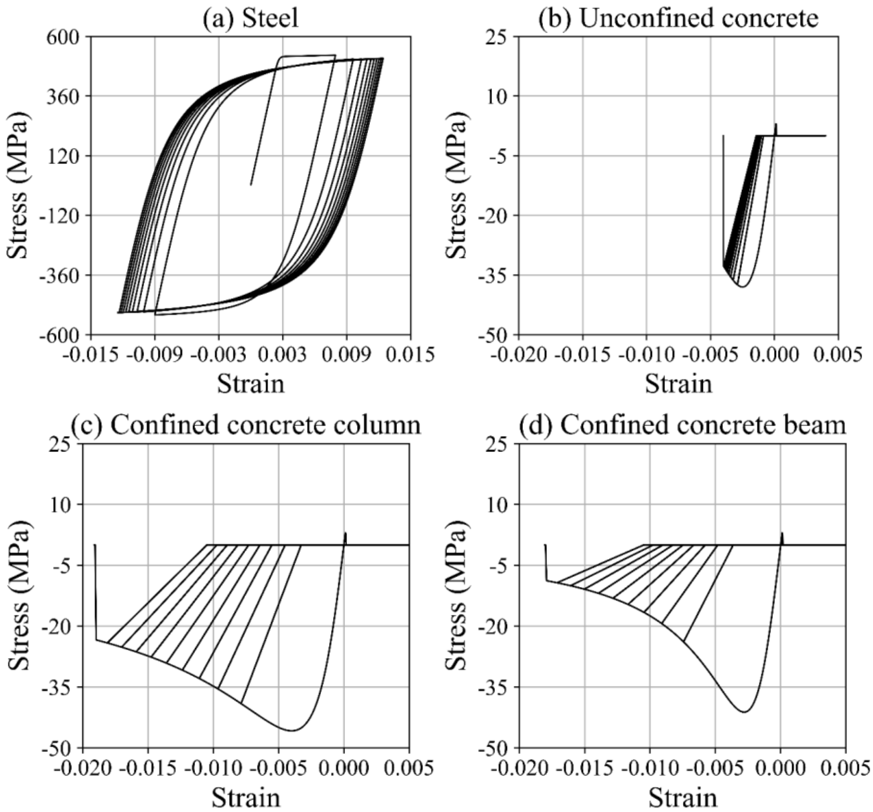

Figure 4.8 Uniaxial constitutive laws used for modelling the steel and concrete fibres: (a) Menegotto and Pinto[86]*, (b-d) Mander et al.*[88].

The scaled horizontal ground motion of the Morgan Hill earthquake (1984, Halls Valley, Mw = 6.2), shown in Figure 4.9, was imposed on the structure. The nonlinear dynamic analysis employs the Newmark integration method ($\beta = 1/4$ and $\gamma = ½$) and a Newton-Raphson scheme to find the solution at each step. The damping models are defined with a damping ratio of 3%.

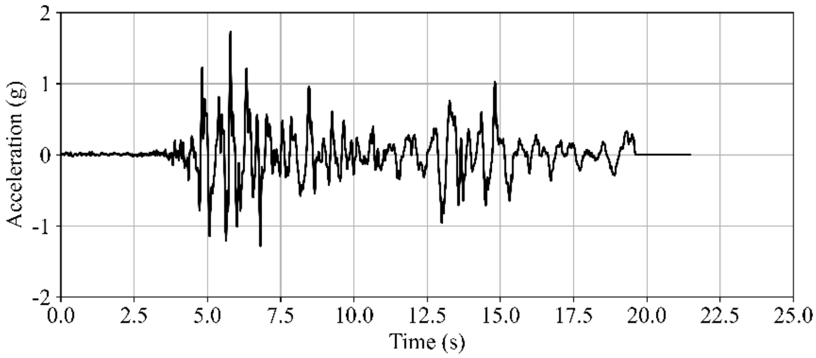

Figure 4.9 Ground motion record from the Morgan earthquake (1984) used for the case study

The structure presents a highly nonlinear response caused by the magnitude of the imposed ground motion record. The system's response is presented through different figures and tables showing the response at the global level structure in terms of energy dissipation, spurious damping forces, maximum displacements, and drifts.

Figure 4.10 (a-f) presents the energy introduced to the system by the ground motion record (E_I), the energy dissipated by the damping models (E_D), and the energy dissipated by the material constitutive laws (E_M). For clarity, the results are plotted in two figures, and the legends are given in descending order. In this case, the damping models considerably influenced the energy entering the system. Additionally, the energy dissipated by each damping model and structural members can radically differ.

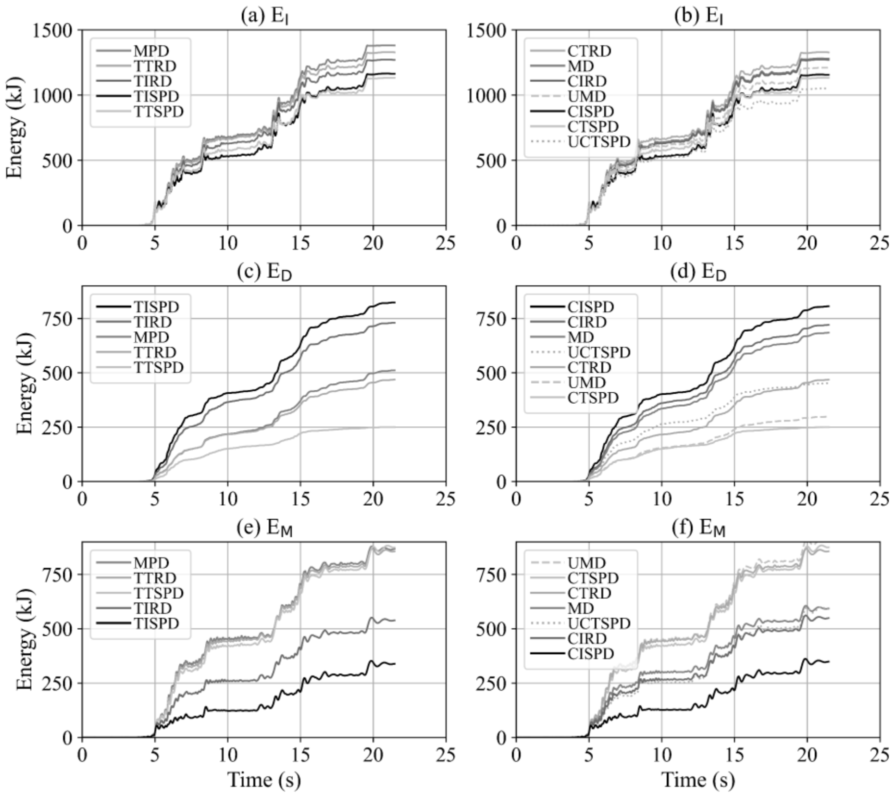

Figure 4.10 (a-b) Cumulative energy input by the ground motion record, (c-d) cumulative energy dissipated by the damping models, and (e-f) cumulative energy dissipated by material constitutive laws.

The TISPD, CISPD, TIRD, and CIRD dissipate more energy than the other models. Additionally, the energy dissipated by the material constitutive laws is smaller than the models using the current properties of the structure. The energy dissipated by the material constitutive laws is an indicator directly linked with the structural damage[90]. MD also dissipates a relevant amount of energy, however, the amount of energy dissipated by the materials is not as low as the models mentioned above. MPD dissipates less energy than the previous models, implying that the material constitutive laws absorb more energy.

The models defined with the current system properties TTSPD, CTSPD and UMD dissipate less energy through the damping model and more through the material constitutive rules. The TTRD and

CTRD models show moderate levels of energy dissipation; however, the amount of energy dissipated by the material constitutive laws is high. Finally, UTSPD has average levels of energy dissipation through the damping model and material constitutive laws.

Table 4.5 presents the final cumulative energy introduced by the ground motion record and the energy dissipated by the damping models and material constitutive laws. It is also shown the percentage of the input energy dissipated by both mechanisms. The table is presented with a conditional layout to facilitate data visualization. Except for MPD, all models defined with the initial properties dissipate over 50% of the input energy. The TISPD and CISPD models dissipated more than 70% of the energy introduced by the ground motion record and about 30% through the material constitutive rules. MD, CIRD, and TIRD dissipated proportionally less energy than TISPD and CISPD. Nevertheless, the percentage of energy dissipated is still high compared to the models using the current properties of the system.

The TTSPD and CTSPD models dissipate about 22% of the energy and the materials 77%. The missing 1% is represented in the kinetic energy of structural mass that the damping model will finally absorb. The remaining models dissipate less energy through the material constitutive laws, but this percentage is higher than the TISPD, TIRD, CISPD, CIRD, and MD.

The different levels of energy dissipation through the material constitutive laws mean that the elements with higher demands are in the structures with damping models defined with the current properties of the system. As explained above, TISPD and TIRD are considered inappropriate in nonlinear dynamic analysis. For this case, the high levels of energy dissipation of CISPD, MD, and CIRD may suggest that these models are equally inappropriate for nonlinear dynamic analysis.

Table 4.5 Total energy input, dissipated by the material constitutive laws and dissipated by the damping model.

Abbreviation	E_I (kJ)	E_M (kJ)	E_M/E_I (%)	E_D (kJ)	E_D/E_I (%)
TISPD	1163	339	29%	824	71%
TIRD	1270	539	42%	730	58%
CISPD	1155	349	30%	806	70%
CIRD	1270	549	43%	720	57%
MD	1279	594	46%	685	54%
TTSPD	1132	874	77%	250	22%
TTRD	1328	856	65%	469	35%
CTSPD	1132	875	77%	250	22%
CTRD	1327	856	65%	468	35%
UCTSPD	1049	592	56%	452	43%
UMD	1209	905	75%	298	25%
MPD	1380	868	63%	512	37%

Figure 4.11 shows spurious damping moments occurring at the top left node of the structure. Only the models defined with the total stiffness matrix present spurious damping moments in the massless DoFs. The models depicted with the initial properties (TISPD and TIRD) have the highest damping moments, remaining after the structure enters the inelastic range since the orthogonality of the system is lost.

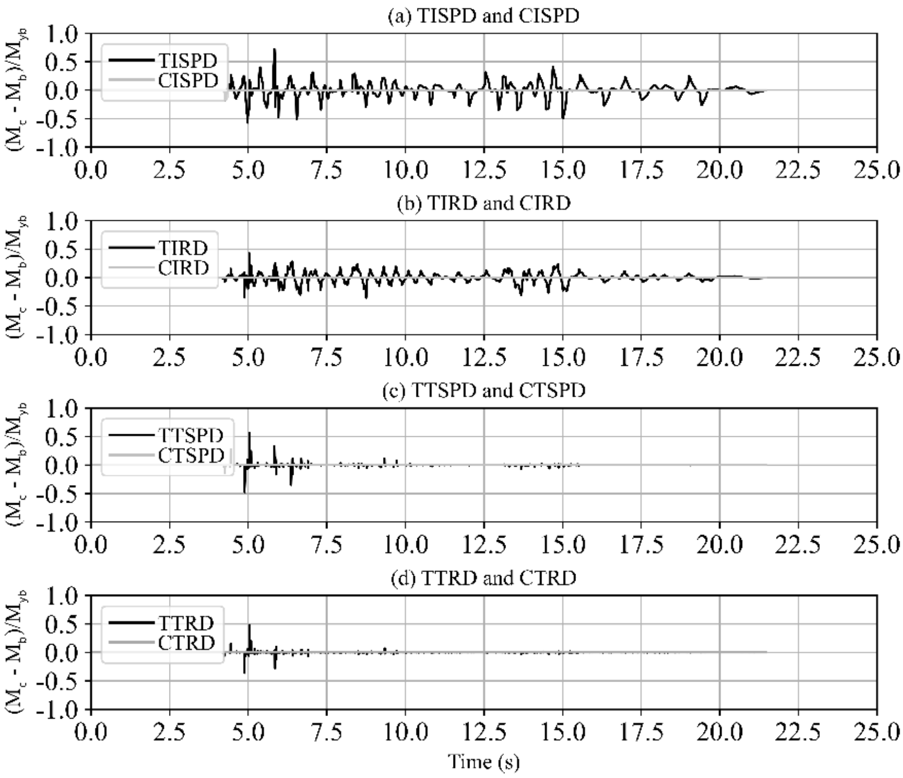

Figure 4.11 Damping moments at the top left node of the RC frame for the different damping models

Models defined with the total tangent stiffness matrix significantly reduce the spurious damping moments but are not entirely eliminated. Commercial software usually employs an approximative tangent stiffness to solve the nonlinear problem; if this approximate matrix defines the damping model, the spurious damping moments are expected to have a higher magnitude. Condensed models eliminate spurious damping moments since the entries of the damping matrix related to the massless DoFs are defined with zeros. The damping model proposed in this work allows using a model proportional to the tangent stiffness matrix without having spurious damping forces. The elimination of damping moments has generally been the main argument for using condensed damping models.

Tables 4.6 and Table 4.7 present the maximum drifts and displacements at each story of the structure with a conditional layout for better interpretation and comprehension. The damping models can significantly influence the drifts and displacements of the structure. For example, the CISPD model presents a maximum drift at the last floor, less than half of that presented by CTSPD. This difference between the models based on the initial properties will generate divergent results when estimating the damage of structural elements.

Table 4.6 Maximum drift per storey

	Maximum drift per storey					
Model	1a	2a	3a	4a	5a	6a
TISPD	1.13%	1.77%	2.02%	1.96%	1.67%	1.23%
TIRD	1.41%	1.51%	1.82%	1.99%	2.09%	2.00%
CISPD	1.11%	1.76%	2.01%	1.96%	1.69%	1.28%
CIRD	1.41%	1.52%	1.81%	1.99%	2.11%	2.02%
MD	1.51%	1.68%	1.76%	1.98%	2.21%	2.21%
TTSPD	1.68%	1.83%	1.93%	2.42%	2.96%	3.19%
TTRD	1.68%	1.91%	1.68%	2.20%	2.78%	3.02%
CTSPD	1.68%	1.83%	1.93%	2.42%	2.97%	3.19%
CTRD	1.68%	1.91%	1.68%	2.20%	2.78%	3.02%
UCTSPD	1.38%	1.61%	1.81%	2.05%	2.21%	2.16%
UMD	1.76%	1.98%	1.85%	2.37%	2.96%	3.23%
MPD	1.81%	1.99%	1.96%	2.19%	2.56%	2.76%

Table 4.7 Maximum displacement per storey

	Maximum displacement per storey (m)					
Model	1a	2a	3a	4a	5a	6a
TISPD	0.034	0.087	0.147	0.205	0.251	0.281
TIRD	0.042	0.088	0.123	0.174	0.229	0.274
CISPD	0.033	0.086	0.146	0.204	0.250	0.281
CIRD	0.042	0.088	0.124	0.173	0.228	0.274
MD	0.045	0.096	0.136	0.166	0.223	0.270
TTSPD	0.050	0.105	0.148	0.185	0.246	0.322
TTRD	0.051	0.108	0.152	0.171	0.216	0.284
CTSPD	0.051	0.105	0.148	0.185	0.246	0.322
CTRD	0.051	0.108	0.152	0.171	0.216	0.284
UCTSPD	0.041	0.085	0.135	0.183	0.224	0.275
UMD	0.053	0.112	0.160	0.190	0.236	0.311
MPD	0.054	0.114	0.164	0.205	0.253	0.296

4.5 Conclusion

This chapter investigates the response of a proposed viscous damping model based on a condensed tangent stiffness proportional matrix independent of the geometric stiffness matrix. The latter eliminates spurious damping forces, avoids the high levels of energy dissipation, and increases the effective damping ratio of the structure compared with the condensed damping model defined with the initial properties. This approach also preserves solid physical meaningfulness related to a reduction of the damping energy when the hysteretic material response is activated and eliminates the potential consequences of the presence of the geometric stiffness matrix in the definition of the damping matrix under extreme loads and displacements.

Through one bridge pier subjected to a combined nonlinear static and dynamic analysis, it was shown that all the condensed damping models defined with the original properties of the structure caused an overdamped response after incursions in the inelastic range. Additionally, a second case study of a multi-storey reinforced concrete frame shows that the condensed damping models defined with the original properties of the structure can present similar levels of energy dissipation, drift and displacements than the total initial stiffness proportional damping and Rayleigh damping models. These are generally considered inappropriate for nonlinear dynamic analysis due to increments in the effective damping ratio, high levels of energy dissipation through the damping model and spurious damping forces in the massless DoFs. The first two considerably affect the total energy absorbed by the constitutive rules of the material, which is linked to structural damage. As illustrated in two study cases, the proposed damping model is anchored in a material-related mechanism and avoids the mentioned problematics.

5. Capped elemental damping ratio for distributed plasticity elements

5.1 Abstract

This chapter presents a capped elemental damping model for nonlinear dynamic analysis using distributed plasticity elements. The damping forces are defined in the basic reference system using an initial stiffness proportional damping matrix and basic velocities independent of the rigid body motion. The basic damping forces are capped to a percentage of the bending and axial capacity before being expressed in the local and global reference system. Viscous damping models were implemented in dynamic analyses because damping forces are expected to be small compared to material-resisting forces. Hence any inaccuracies in the model would not significantly affect the structure's response. Generally, traditional damping models do not satisfy this initial assumption; thus, this limit is justified. Following the theoretical framework, implementation, and further justification, several study cases are presented using the proposed model. The study cases correspond to realistic steel and RC structures subjected to different ground motion records. Comparison with traditional models implemented in the basic and global reference system shows the advantage of the current proposal.

5.2 Introduction

Over the last years, significant research has been devoted to modify traditional global models to solve the problems of Rayleigh damping and other existing models. Although improvements have been made and specific issues have been solved, many researchers consider them insufficient[58,61,75].

The reason is that many of the new models propose to modify the damping matrix through a particular methodology. The above may perform adequately in specific cases, yet they lead to side effects or other commonly criticised pathologies. All damping models defined through a constant damping matrix do not guarantee that the damping forces have reasonable [8,27,29,30] magnitudes when the system enters the inelastic range. Additionally, having a nonlinear material resisting system while still using linear damping does not meet the initial assumptions for implementing viscous damping models in dynamic analyses. Therefore, a switch to nonlinear damping models should be made to progress in this field and solve the problems of existing models.

This chapter and the following one present nonlinear damping models implemented on elements with distributed plasticity during dynamic analysis. The approaches presented appeal to intuition and physical sense and respecting the initial assumption used to implement viscous damping models in dynamic analysis related to the magnitude of the damping forces compared to the material resisting force.

The model proposed in this chapter is defined at the element level using the initial stiffness matrix. Unlike others in the literature, this model and damping forces are defined and calculated at the basic reference system, independent of the rigid body motion. At this reference system, the basic damping forces are capped to a percentage of the bending and axial capacity of the structural element to avoid the proportionally high damping forces with respect to the material resisting forces. Then these forces are expressed in the local and global reference system.

The proposal has a mathematical simplification which is detailed later. This simplification implies that going to the fibre or section is unnecessary to define a nonlinear relationship between damping forces and velocities. However, the penalty is paid when the Jacobian is determined since it is not wholly consistent. This implies that more iterations are needed to converge into the inelastic range during incursions. This model is presented since, from the author's perspective, it can be a valuable and interesting contribution to the literature. However, the last chapter of this thesis presents a fully mathematically consistent fibre-implemented model.

The following section describes the new model theoretically, presents the required modifications to Newmark's method, and a pseudo-algorithm indicating the steps needed for its implementation in finite element programs. Subsequently, four numerical examples of steel and RC structures subjected to nonlinear dynamic analysis are presented, evaluating and comparing the new and existing models. Finally, the last section sums up the main conclusions.

5.3 Capped elemental viscous damping defined at the basic reference system

5.3.1 Motivation

The motivation of this chapter is to study a new capped elemental damping model defined at the basic reference system for distributed plasticity elements to limit the magnitude of the damping forces. Since the advent of nonlinear dynamic analysis until the last decade, the energy dissipation of mechanisms independent of the constitutive rules of the material has been considered mainly through viscous damping models defined at the global level.

The problems associated with global models have led several authors to define the damping of a structural system rather at the elemental level. Recent studies, such as Puthanpurayil et al.[61] and Francesco and Sullivan[74], show that damping models depicted at the elemental level have numerical advantages and appear more reliable than damping models defined at the global level. This justifies pursuing the study of new elemental damping models, which have a broad physical meaning and a formulation more consistent with reality.

SPD has been more accepted than MPD since it corresponds to the energy dissipated by the internal deformations of the elements. This means that the magnitude of the damping forces using an SPD is implicitly defined independently of the rigid body motion, but the forces are expressed taking it into account. Whereas, with an MPD, the magnitude of the damping forces is proportional to the rigid body motion and the deformations of the system, which is less appealing from a physical point of view. For instance, the rigid body motion does not activate the micro-hysteretic curves of the materials, the connections between structural elements, or other internal mechanisms. Therefore, the MPD should not be considered to define the viscous damping forces.

The elemental and global SPD damping models are equivalent if the same damping parameter is used and nonlinear geometric effects are not considered. When nonlinear geometric effects are considered, the elemental model has an additional advantage since the basic stiffness matrix depends only on the stiffness of the material and does not include the contribution of the geometric stiffness matrix.

Damping models in nonlinear dynamic analyses must respect basic premises used by Lord Rayleigh[8] and Wilson and Clough[10] to implement viscous damping in dynamic analysis. One of them states that damping forces are expected to be small compared to the material-resisting forces of the structure; hence any inaccuracies in the model should not significantly affect the results. Most damping models do not assure the latter when the structure enters the inelastic range, especially under high demands.

The proposed model follows the principle of Hall[26,27] where the damping forces are kept within a certain limit that has traditionally been considered reasonable[8,27,29,30]. This limit is imposed at each element in the basic reference system instead of defining the capped viscous rectangular element proposed by Hall[26,27] according to the inter-storey shear capacity.

The herein proposed model inherits some problems of a SPD. For instance, the model does not present deterioration in the capacity to dissipate energy, which is a realistic phenomenon according to Smyrou et al.[46] and higher modes of vibration will be equally overdamped. The limits or caps imposed to the damping forces compensate for the latter, especially when the structure is under high demands. These problems are discussed later.

The following sections present an overview of the geometric transformation used in nonlinear analyses of framed structures, where the derivation of the basic deformations and velocities independent of rigid body motion are shown. Subsequently, the definition of the new damping model at the basic level is described and further details are discussed. Finally, necessary modifications to the Newmark-beta method and a pseudo-algorithm are presented.

5.3.2 Review of the corotational formulation and linear approximation

This section presents an Euler-Bernoulli beam's deformations, velocities and internal forces, shown in Figure 5.1, using a corotational and linear geometric transformation. Some of the equations and figures have been reported in previous sections. However, due to the size of the document and for the sake of clarity, some of them are reproduced.

The internal deformation using a corotational geometric transformation is expressed in eqs. (5.1), (5.2), and (5.3) at the basic reference system, in terms of the local displacements ($\mathbf{u}^{loc}$) and the corotating angle (β) between the local and basic reference system.

$$u_1^{bsc} = l - l_0 \tag{5.1}$$

$$u_2^{bsc} = u_3^{loc} - \beta \tag{5.2}$$

$$u_3^{bsc} = u_6^{loc} - \beta \tag{5.3}$$

where l is the deformed length of the element in the current position of the nodes and l_0 is the undeformed length. The corotating angle (β) is defined by the following expression.

$$\beta = \tan^{-1}\left(\frac{u_5^{loc} - u_2^{loc}}{l_0 + u_4^{loc} - u_1^{loc}}\right) = \tan^{-1}\left(\frac{l_y}{l_x}\right) \tag{5.4}$$

l_x and l_y are the current distance between the nodes expressed in both axes of the local reference system.

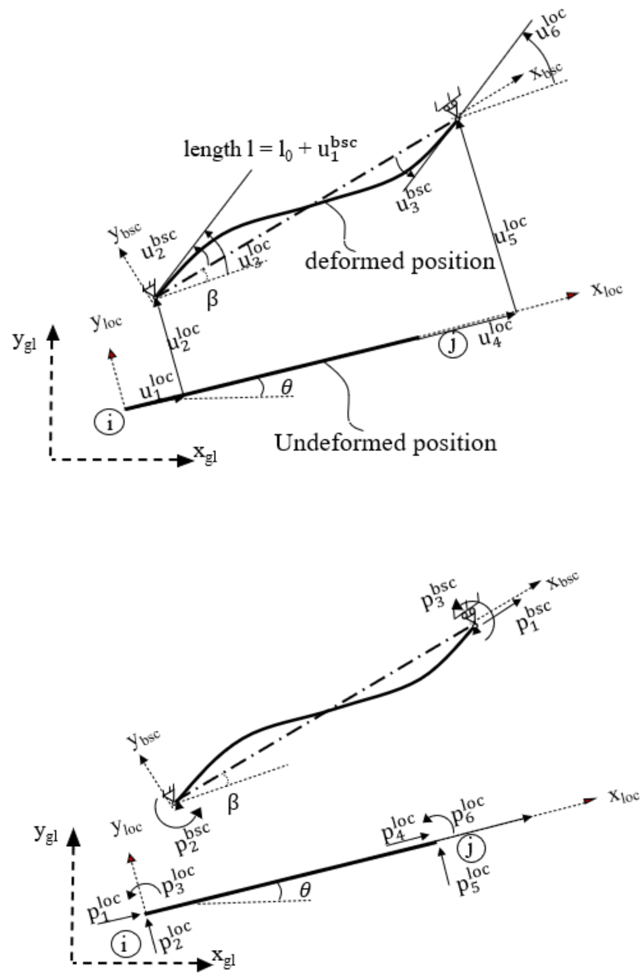

Figure 5.1 Element forces and displacements expressed in the different reference systems.

The incremental compatibility ($\mathbf{\Gamma}_{\mathrm{C}}^{\mathrm{loc-bsc}}$) matrix is obtained by differentiation:

$$\frac{\partial \mathbf{u}^{\mathrm{bsc}}}{\partial \mathbf{u}^{\mathrm{loc}}} = \begin{bmatrix} -\cos(\beta) & -\sin(\beta) & 0 & \cos(\beta) & \sin(\beta) & 0 \\ -\sin(\beta)/l & \cos(\beta)/l & 1 & \sin(\beta)/l & -\cos(\beta)/l & 0 \\ -\sin(\beta)/l & \cos(\beta)/l & 0 & \sin(\beta)/l & -\cos(\beta)/l & 1 \end{bmatrix} \tag{5.5}$$

The basic velocities are found through a corotational formulation deriving the basic displacements with respect to time. These deformation rates are also independent of rigid body motion and indicate how fast deformations occur in the system.

$$\mathbf{v}^{bsc} = \dot{\mathbf{u}}^{bsc} = \frac{d(\mathbf{u}^{bsc})}{dt} \tag{5.6}$$

Eqs. (5.1), (5.2) and (5.3) are derived with respect to time and eqs. (5.7), (5.8), and (5.9) are found

$$\frac{d(u_1^{bsc})}{dt} = v_1^{bsc} = \frac{l_x\dot{l}_x + l_y\dot{l}_y}{l} \tag{5.7}$$

$$\frac{d(u_2^{bsc})}{dt} = v_2^{bsc} = \dot{u}_3^{loc} - \frac{l_x\dot{l}_y - l_y\dot{l}_x}{l^2} \tag{5.8}$$

$$\frac{d(u_3^{bsc})}{dt} = v_3^{bsc} = \dot{u}_6^{loc} - \frac{l_x\dot{l}_y - l_y\dot{l}_x}{l^2} \tag{5.9}$$

Where $\mathbf{v}^{loc}$ represents the velocities of the DoFs expressed in the local reference system. $\dot{l}_x$ y $\dot{l}_y$ correspond to the derivative of l_x and l_y with respect to time, expressed by eqs. (5.10) and (5.11).

$$\dot{l}_x = \frac{d(l_x)}{dt} = \frac{d(l_0 + u_4^{loc} - u_1^{loc})}{dt} = v_4^{loc} - v_1^{loc} \tag{5.10}$$

$$\dot{l}_y = \frac{d(l_y)}{dt} = \frac{d(u_5^{loc} - u_2^{loc})}{dt} = v_5^{loc} - v_2^{loc} \tag{5.11}$$

Employing a linear approximation, eqs. (5.1), (5.2), and (5.3) become eqs. (5.12), (5.13) and (5.14), respectively, when a Taylor expansion is performed to u_1^{bsc} and β, and just the first term is conserved.

$$u_1^{bsc} = u_4^{loc} - u_1^{loc} \tag{5.12}$$

$$u_2^{bsc} = u_3^{loc} - \frac{u_5^{loc} - u_2^{loc}}{l_0} \tag{5.13}$$

$$u_3^{bsc} = u_6^{loc} - \frac{u_5^{loc} - u_2^{loc}}{l_0} \tag{5.14}$$

The incremental compatibility ($\boldsymbol{\Gamma}_C^{loc-bsc}$) matrix is obtained by differentiation:

$$\frac{\partial \mathbf{u}^{\mathrm{bsc}}}{\partial \mathbf{u}^{\mathrm{loc}}} = \mathbf{\Gamma}_{\mathrm{C}}^{\mathrm{loc-bsc}} = \begin{bmatrix} -1 & 0 & 0 & 1 & 0 & 0 \\ 0 & 1/\mathrm{l}_0 & 1 & 0 & -1/\mathrm{l}_0 & 0 \\ 0 & 1/\mathrm{l}_0 & 0 & 0 & -1/\mathrm{l}_0 & 1 \end{bmatrix} \tag{5.15}$$

Eqs. (5.12), (5.13), and (5.14) are derived with respect to time to get the basic velocities using a linear approximation expressed by eqs. (5.16), (5.17), and (5.18).

$$\mathrm{v}_1^{\mathrm{bsc}} = \mathrm{v}_4^{\mathrm{loc}} - \mathrm{v}_1^{\mathrm{loc}} \tag{5.16}$$

$$\mathrm{v}_2^{\mathrm{bsc}} = \mathrm{v}_3^{\mathrm{loc}} - \frac{\mathrm{v}_5^{\mathrm{loc}} - \mathrm{v}_2^{\mathrm{loc}}}{\mathrm{l}_0} \tag{5.17}$$

$$\mathrm{v}_3^{\mathrm{bsc}} = \mathrm{v}_6^{\mathrm{loc}} - \frac{\mathrm{v}_5^{\mathrm{loc}} - \mathrm{v}_2^{\mathrm{loc}}}{\mathrm{l}_0} \tag{5.18}$$

Eqs. (5.16), (5.17), and (5.18) can also be obtained, using a linear approximation, through eq. (5.19), which is invalid when a corotational formulation is used.

$$\mathbf{v}^{\mathrm{bsc}} = \mathbf{\Gamma}_{\mathrm{C}}^{\mathrm{loc-bsc}} \cdot \mathbf{v}^{\mathrm{loc}} \tag{5.19}$$

$\mathbf{v}^{\mathrm{loc}}$ is the vector of elemental velocities at the local reference system found with a rotation matrix as a function of the angle θ between the local and global reference systems $\mathbf{\Gamma}_{\mathrm{C}}^{\mathrm{gl-loc}}(\theta)$ and the vector of elemental global velocities $\mathbf{v}^{\mathrm{gl}}$.

$$\mathbf{v}^{\mathrm{loc}} = \mathbf{\Gamma}_{\mathrm{C}}^{\mathrm{gl-loc}}(\theta) \cdot \mathbf{v}^{\mathrm{gl}} \tag{5.20}$$

The basic forces as a function of the basic displacements ($\mathbf{p}^{\mathrm{bsc}}$) are found using an inelastic force-based element, which is not explained in this chapter but can be found elsewhere[83–85]. The basic forces are expressed in the local reference system ($\mathbf{p}^{\mathrm{loc}}$) using equilibrium relations derived from rigid body equilibrium or with the principle of virtual work:

$$\mathbf{p}^{\mathrm{loc}} = \mathbf{\Gamma}_{\mathrm{E}}^{\mathrm{bsc-loc}} \cdot \mathbf{p}^{\mathrm{bsc}} = \left(\mathbf{\Gamma}_{\mathrm{C}}^{\mathrm{loc-bsc}}\right)^{\mathrm{T}} \cdot \mathbf{p}^{\mathrm{bsc}} \tag{5.21}$$

The previous expression indicates that the equilibrium matrix is the transpose of the incremental compatibility matrix, which illustrates the principle of contragradiency in structural analysis.

The elemental global forces are then found with a rotation matrix considering the angle (θ) between the global and the local reference systems. The elemental contributions from the elements are assembled to obtain the global resisting forces of the structure. During nonlinear analysis, the latter are compared with the external forces applied to the structure: using numerical methods, convergence in the nonlinear problem is achieved when their difference falls within a specified convergence criterion.

The incremental relation between the global structural forces and displacements is required to solve the nonlinear problem. Such relationship is found by assembling the global elemental tangent stiffness matrices into the tangent stiffness matrix of the global system. At the local reference system, the tangent elemental stiffness ($\mathbf{k}^{\mathrm{TanLoc}}$) is found differentiating eq. (5.21) with respect to the local displacements:

$$\mathbf{k}^{\mathrm{TanLoc}} = \frac{\partial \mathbf{p}^{\mathrm{loc}}}{\partial \mathbf{u}^{\mathrm{loc}}} = \frac{\partial (\mathbf{\Gamma}_{\mathrm{E}}^{\mathrm{bsc-loc}})}{\partial \mathbf{u}^{\mathrm{loc}}} \cdot \mathbf{p}^{\mathrm{bsc}} + \mathbf{\Gamma}_{\mathrm{E}}^{\mathrm{bsc-loc}} \cdot \frac{\partial (\mathbf{p}^{\mathrm{bsc}})}{\partial \mathbf{u}^{\mathrm{loc}}} \tag{5.22}$$

The application of the chain rule of differentiation to the second term on the right-hand side brings out the incremental relation between the basic forces and the basic displacements, which is obtained according to the specific element formulation. The term $\left(\frac{\partial \mathbf{u}^{\mathrm{bsc}}}{\partial \mathbf{u}^{\mathrm{loc}}}\right)$ is expressed in eq. (5.5) and (5.15), yielding as final result:

$$\mathbf{k}^{\mathrm{TanLoc}} = \frac{\partial \mathbf{p}^{\mathrm{loc}}}{\partial \mathbf{u}^{\mathrm{loc}}} = \underbrace{\frac{\partial (\mathbf{\Gamma}_{\mathrm{E}}^{\mathrm{bsc-loc}})}{\partial \mathbf{u}^{\mathrm{loc}}} \cdot \mathbf{p}^{\mathrm{bsc}}}_{\mathbf{k}^{\mathrm{TanGeoLoc}}} + \underbrace{\mathbf{\Gamma}_{\mathrm{E}}^{\mathrm{bsc-loc}} \cdot \frac{\partial (\mathbf{p}^{\mathrm{bsc}})}{\partial \mathbf{u}^{\mathrm{bsc}}} \cdot \mathbf{\Gamma}_{\mathrm{C}}^{\mathrm{loc-bsc}}}_{\mathbf{k}^{\mathrm{TanMatLoc}}} \tag{5.23}$$

The first and second terms on the right side of the equation above are the geometric and material components of the elemental stiffness matrix, respectively, which will give rise to the GSM and material stiffness matrix (MSM) at the global structural level. The derivative $\frac{\partial (\mathbf{\Gamma}_{\mathrm{E}}^{\mathrm{bsc-loc}}(\mathbf{u}^{\mathrm{loc}}))}{\partial \mathbf{u}^{\mathrm{loc}}}$ and further details regarding the corotational formulation can be found in other references[78–81]. The GSM disappears using a linear approximation since $\frac{\partial (\mathbf{\Gamma}_{\mathrm{E}}^{\mathrm{bsc-loc}}(\mathbf{u}^{\mathrm{loc}}))}{\partial \mathbf{u}^{\mathrm{loc}}}$ is a matrix filled with zeros.

5.3.3 Formulation of a capped elemental viscous damping model for nonlinear dynamic analysis using distributed plasticity elements

The damping matrix is defined using an SPD in the basic reference system, depicted by eq. (5.24).

$$\mathbf{c}^{\mathrm{bsc}} = \mathrm{a}_1 \mathbf{k}^{\mathrm{bsc}} \tag{5.24}$$

The procedure to find the basic stiffness matrix $\mathbf{k}^{\mathrm{bsc}}$ in distributed plasticity elements like force-based and displacement-based elements is described in the annexe, but the formulation can be found in the following manuscripts[82–85]. The damping parameter a_1 is found using eq. (5.25).

$$\mathrm{a}_1 = \frac{2\zeta_0}{\omega_{\mathrm{i}}} \tag{5.25}$$

Where, ω_{i} is the frequency of the first mode of vibration at the global level and not the elemental frequency as recommended by Puthanpurayil et al.[61]. The model proposed uses an SPD model, but does not define an elemental mass matrix. The latter implies that the calibration process defined by Puthanpurayil et al.[61] is not required using these assumptions.

5.3.4 Elemental vs global viscous damping model for nonlinear dynamic analysis using an SPD model

The elemental and global models are compared when an SPD is used for illustrative purposes. The damping forces are defined by eq. (5.26) without imposing limits on the damping forces.

$$\mathbf{p}_{\mathrm{d}}^{\mathrm{bsc}} = \mathbf{c}^{\mathrm{bsc}} \cdot \mathbf{v}^{\mathrm{bsc}} \tag{5.26}$$

Where $\mathbf{v}^{\mathrm{bsc}}$ is the vector of basic velocities defined by eqs. (5.7), (5.8), and (5.9) and eqs. (5.16), (5.17), and (5.18), using a corotational formulation and linear approximation, respectively. Eq. (5.27) expresses the basic damping forces in the local reference system using equilibrium relations.

$$\mathbf{p}_{\mathrm{d}}^{\mathrm{loc}} = \mathbf{\Gamma}_{\mathrm{E}}^{\mathrm{bsc-loc}}(\mathbf{u}^{\mathrm{loc}}) \cdot \mathbf{p}_{\mathrm{d}}^{\mathrm{bsc}} \tag{5.27}$$

The elemental damping forces are expressed in the global reference system using eq. (5.28)

$$\mathbf{p}_{\mathrm{d}}^{\mathrm{gl}} = \mathbf{\Gamma}_{\mathrm{E}}^{\mathrm{loc-gl}}(\theta) \cdot \mathbf{p}_{\mathrm{d}}^{\mathrm{loc}} \tag{5.28}$$

Where $\mathbf{\Gamma}_{\mathrm{E}}^{\mathrm{loc-gl}}(\theta)$ is the rotation matrix as a function of the angle between the local and global reference system.

Replacing eqs. (5.24), (5.26), and (5.27) in eq. (5.28) the following expression is obtained.

$$\mathbf{p}_{\mathrm{d}}^{\mathrm{gl}} = \mathrm{a}_1 \mathbf{\Gamma}_{\mathrm{E}}^{\mathrm{loc-gl}}(\theta) \cdot \mathbf{\Gamma}_{\mathrm{E}}^{\mathrm{bsc-loc}}(\mathbf{u}^{\mathrm{loc}}) \cdot \mathbf{k}^{\mathrm{bsc}} \cdot \mathbf{v}^{\mathrm{bsc}} \tag{5.29}$$

Considering a linear approximation eqs. (5.19) and (5.20) are replaced in eq. (5.29)

$$\mathbf{p}_{\mathrm{d}}^{\mathrm{gl}} = \mathrm{a}_1 \mathbf{\Gamma}_{\mathrm{E}}^{\mathrm{loc-gl}}(\theta) \cdot \mathbf{\Gamma}_{\mathrm{E}}^{\mathrm{bsc-loc}} \cdot \mathbf{k}^{\mathrm{bsc}} \cdot \mathbf{\Gamma}_{\mathrm{C}}^{\mathrm{loc-bsc}} \cdot \mathbf{\Gamma}_{\mathrm{C}}^{\mathrm{gl-loc}}(\theta) \cdot \mathbf{v}^{\mathrm{gl}} \tag{5.30}$$

Using eq.(5.23), eq. (5.30) becomes eq. (5.31) after expressing the local stiffness matrix in the global reference system

$$\mathbf{p}_{\mathrm{d}}^{\mathrm{gl}} = \mathrm{a}_1 \mathbf{k}^{\mathrm{gl}} \cdot \mathbf{v}^{\mathrm{gl}} \tag{5.31}$$

Therefore, after assembling the elemental damping global forces, the elemental and global damping models are equivalent using a linear approximation and the same damping parameter. When a corotational formulation is considered eqs. (5.19) and (5.20) are invalid, and the models would present different results. Nevertheless, it is expected that the differences would be small for common civil engineering structures, according to chapter 3.

The definition of the damping forces at the elemental level implies that the global damping matrix is only needed to form the Jacobian matrix used in iterative methods, such as Newton-Raphson.

5.3.5 Capped elemental viscous damping model

The magnitude of the damping forces must be capped to reasonable [27,29,30] values. Hall[26,27] uses limits on the axial damping forces of beam and column elements. Additionally, it proposes a rectangular viscous element to simulate the lateral damping forces, which is capped according to the interstorey shear capacity. Therefore, there are no damping forces in the rotational DoFs. Unlike the model proposed by Hall[26,27], this study defines those limits to the basic damping forces of each element before expressing them in the local reference system. Those limits are defined as the product of $2\zeta_0$ and the axial (P_y) and bending moment capacity (M_{yi} and M_{yj}) of the sections at both element ends. The latter value was proposed by Hall[26,27] considering the relation between the material-resisting and damping forces in a linear SDoF. Even if this limit has been historically considered reasonable[27,29,30], any limit can be imposed.

Eqs. (5.32) and (5.37) show how the damping forces are defined in the proposed damping model. Initially, the damping forces $p_{d,1}^{bsc}$, $p_{d,2}^{bsc}$ y $p_{d,3}^{bsc}$ are defined with eq. (5.26) using the initial basic stiffness matrix after applying the gravity loads, then these values are compared with the capacity of the element in the basic DoFs multiplied by $2\zeta_0$.

$$\mathbf{p}_{d,capped}^{bsc} = \begin{bmatrix} p_{d,capped,1}^{bsc} \\ p_{d,capped,2}^{bsc} \\ p_{d,capped,1}^{bsc} \end{bmatrix} = \begin{bmatrix} \pm\min\left(\left|p_{d,1}^{bsc}\right|, \left| P_y \cdot 2\zeta_0\right|\right) \\ \pm\min\left(\left|p_{d,2}^{bsc}\right|, \left| M_{yi} \cdot 2\zeta_0\right|\right) \\ \pm \min\left(\left|p_{d,3}^{bsc}\right|, \left| M_{yj} \cdot 2\zeta_0\right|\right) \end{bmatrix} \tag{5.32}$$

The object-oriented program developed by author for this research facilitates the calculation of the cross-sections' capacity composing each structural element. The latter can be done when the instance of the cross-section class is initialized or after applying the gravity loads on the structure to consider the axial-bending interaction.

It is important to note that the rotational DoFs are coupled in the basic stiffness matrix. This work assumes that when one end reaches the maximum damping moment, the relation to define the damping forces in the other rotational DoF is unaffected. The damping model must be defined at the sectional or fibre level to be fully mathematically consistent. This model is presented in the next chapter. Therefore, this assumption hinders finding a consistent damping matrix to form the Jacobian when the limits are reached, and an original Newton-Raphson method is used.

When the damping model and forces are defined at the element level, the rotational DoFs have damping moments, even in the elastic range. However, they will have a magnitude between the limits proposed. Additionally, when the basic damping forces are expressed at the local reference system, it can be demonstrated that the maximum shear-damping force of the element is $\frac{2\zeta(M_{yi}+M_{yj})}{l_0}$ when both ends reach the maximum damping moment.

This model and the capped damping model of Hall [26,27] have the disadvantage that the higher modes of the structure will be overdamped since they are defined with a SPD. This is continuously criticized by several author[21,22,29,36,54,61]. Hall[26,27] and this study argue that the overdamping in the higher modes will be partially compensated by the limits imposed on the damping forces. Nevertheless, it is also possible to adjust the damping ratio imposed on the first mode by multiplying it by a factor found through a weighted average considering the equivalent damping ratio of higher modes.

$$f = \frac{\zeta_0 m_T}{\sum \zeta_i m_i} \tag{5.33}$$

Where m_T is the total mass of the structure, m_i is the effective shear modal mass of each mode, and ζ_i is the damping ratio of each mode associated with the initial definition. This factor can be found using all the modes of the structure or until the mass considered reaches a significant percentage of the total mass. Therefore, the damping parameter a_1 on eq. (5.26), and the limits are found with a damping ratio equal to $\zeta_0 f$.

The capped elemental damping model has numerous advantages. For instance, it does not affect the skyline matrix storage commonly used in commercial finite element programs. The damping forces will have reasonable [27,29,30] values through the analysis when an initial SPD is used. Finally, the damping force will not disappear when the elements yield.

5.3.6 Implementation of capped elemental viscous damping model using the Newmark-beta numerical integration method

The damping model is implemented using the Newmark method with several modifications presented below. Newmark[91] developed a general procedure for solving any dynamic problem given by eqs. (5.34) and (5.35).

$$\dot{\mathbf{U}}_{n+1} = \frac{\gamma}{\beta\Delta}(\mathbf{U}_{n+1} - \mathbf{U}_n) + \left(1 - \frac{\gamma}{\beta}\right)\dot{\mathbf{U}}_n + \Delta t\left(1 - \frac{\gamma}{2\beta}\right)\ddot{\mathbf{U}}_n \tag{5.34}$$

$$\ddot{\mathbf{U}}_{n+1} = \frac{1}{\beta\Delta t^2}(\mathbf{U}_{n+1} - \mathbf{U}_n) + \frac{1}{\beta\Delta t}\dot{\mathbf{U}}_n - \left(\frac{1}{2\beta} - 1\right)\ddot{\mathbf{U}}_n \tag{5.35}$$

This procedure aims to find the displacements, velocities, and accelerations at time step n + 1 satisfying eq. (5.36)

$$\widehat{\mathbf{P}}_{s,n+1} = \mathbf{F}_{n+1} \tag{5.36}$$

$\mathbf{F}_{n+1}$ is the vector of external applied forces and $\widehat{\mathbf{P}}_{s,n+1}$ is the vector of resisting forces of the system defined by eq. (5.37), including the inertial, damping, and material components.

$$\widehat{\mathbf{P}}_{s,n+1} = \mathbf{M} \cdot \ddot{\mathbf{U}}_{n+1} + \mathbf{P}_{d,n+1} + \mathbf{P}_{r,n+1} \tag{5.37}$$

The eq. (5.37) is expanded using Taylor's series, interpreting the resistant forces as a function of $\mathbf{U}_{n+1}$ and considering only the first two terms.

$$\widehat{\mathbf{P}}^{k+1}_{s,n+1} = \widehat{\mathbf{P}}^{k}_{s,n+1} + \frac{\partial \widehat{\mathbf{P}}_s}{\partial \mathbf{U}_{n+1}} \cdot \Delta \mathbf{U}^k = \mathbf{F}_{n+1} \tag{5.38}$$

$\widehat{\mathbf{P}}_s$ is differentiated at the known displacements $\mathbf{U}_{n+1}$

$$\frac{\partial \widehat{\mathbf{P}}_s}{\partial \mathbf{U}_{n+1}} = \mathbf{M} \cdot \frac{\partial \ddot{\mathbf{U}}}{\partial \mathbf{U}_{n+1}} + \frac{\partial \mathbf{P}_d}{\partial \mathbf{U}_{n+1}} + \frac{\partial \mathbf{P}_r}{\partial \mathbf{U}_{n+1}} \tag{5.39}$$

$$\widehat{\mathbf{K}}_{t,n+1}^{k} \equiv \frac{\partial \mathbf{P}_s}{\partial \mathbf{U}_{n+1}} = \frac{1}{\beta(\Delta t)^2}\mathbf{M} + \mathbf{K}_{d,n+1}^{k,Tan} + \mathbf{K}_{r,n+1}^{k,Tan} \tag{5.40}$$

Where the derivative in the inertia term is found with eq. (5.35). The $\frac{\partial \mathbf{P}_d}{\partial \mathbf{U}_{n+1}}$ is derived by eq. (5.41) according to the following procedure at the local reference system.

$$\frac{\partial \mathbf{p}_d^{loc}}{\partial \mathbf{u}_{n+1}^{loc}} = \frac{\partial\left(\boldsymbol{\Gamma}_E^{bsc-loc} \cdot \mathbf{p}_d^{bsc}\right)}{\partial \mathbf{u}_{n+1}^{loc}} = \frac{\partial \boldsymbol{\Gamma}_E^{bsc-loc}}{\partial \mathbf{u}_{n+1}^{loc}} \cdot \mathbf{p}_d^{bsc} + \boldsymbol{\Gamma}_E^{bsc-loc} \cdot \frac{\partial \mathbf{p}_d^{bsc}}{\partial \mathbf{u}_{n+1}^{loc}} \tag{5.41}$$

The chain rule is used to find the unknown relation $\frac{\partial \mathbf{p}_d^{bsc}}{\partial \mathbf{u}_{n+1}^{loc}}$ yielding to eq. (5.39)

$$\frac{\partial \mathbf{p}_d^{loc}}{\partial \mathbf{u}_{n+1}} = \frac{\partial \boldsymbol{\Gamma}_E^{bsc-loc}}{\partial \mathbf{u}_{n+1}^{loc}} \cdot \mathbf{p}_d^{bsc} + \boldsymbol{\Gamma}_E^{bsc-loc} \cdot \frac{\partial \mathbf{p}_d^{bsc}}{\partial \mathbf{v}^{bsc}} \cdot \frac{\partial \mathbf{v}^{bsc}}{\partial \mathbf{v}^{loc}} \cdot \frac{\partial \mathbf{v}^{loc}}{\partial \mathbf{u}_{n+1}^{loc}} \tag{5.42}$$

where $\frac{\partial \mathbf{v}^{loc}}{\partial \mathbf{u}_{n+1}^{loc}}$ is derived from eq. (5.34).

$$\frac{\partial \mathbf{p}_d^{loc}}{\partial \mathbf{u}_{n+1}} = \frac{\partial \boldsymbol{\Gamma}_E^{bsc-loc}}{\partial \mathbf{u}_{n+1}^{loc}} \cdot \mathbf{p}_d^{bsc} + \boldsymbol{\Gamma}_E^{bsc-loc} \cdot \mathbf{c}^{bsc} \cdot \boldsymbol{\Gamma}_C^{loc-bsc} \frac{\Upsilon}{\beta \Delta t} \tag{5.43}$$

The Jacobian $\frac{\partial \mathbf{P}_d}{\partial \mathbf{U}_{n+1}}$ is assembled at the global level from the contribution of each element of the structure. Finally, $\frac{\partial \mathbf{P}_r}{\partial \mathbf{U}_{n+1}}$ is found using eq. (5.23).

Replacing the definition of $\widehat{\mathbf{K}}_{t,n+1}^{k}$ on eq. (5.38), the following expression is obtained.

$$\widehat{\mathbf{K}}_{t,n+1}^{k} \cdot \Delta \mathbf{u}^k = \mathbf{F}_{n+1} - \mathbf{P}_{d,n+1}^{k} - \mathbf{P}_{r,n+1}^{k} - \mathbf{M} \cdot \ddot{\mathbf{U}}_{n+1}^{k} = \widehat{\mathbf{R}}_{n+1}^{k} \tag{5.44}$$

Where $\ddot{\mathbf{U}}_{n+1}^{k}$ is found substituting eq. (5.34) in the right side of eq. (5.44). Eqs. (5.38) and (5.44) present the basis for the Newton-Raphson iteration method. In eq. (5.44), $\mathbf{F}_{n+1}$ and the other terms without superscript k remain constant during the time step, while the other terms with superscript k must be updated at each iteration. The described procedure is summarized by Figure 5.2 using a pseudocode diagram.

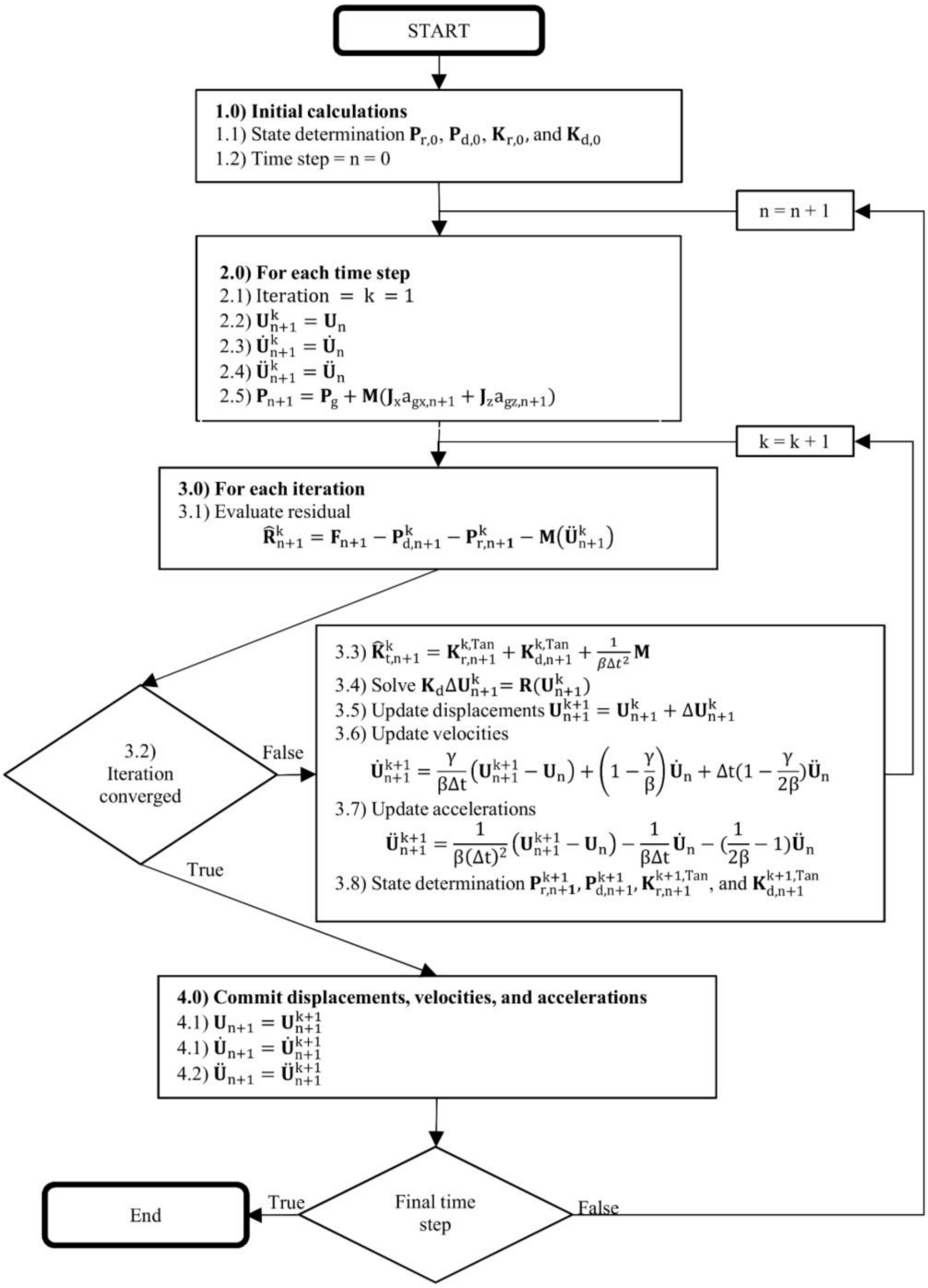

Figure 5.2 Newmark integration method using an elemental viscous damping model.

5.4 Case studies

This section presents four case studies showing the performance of the proposed model. The first two cases are simple steel and RC frames subjected to an incremental sinusoidal ground motion record where only the three elemental models depicted in Table 5.1 are used. The EISPD and EISPD_capped are defined with the basic initial stiffness, and the ETSPD is proportional to the basic tangent stiffness. Section 5.3.4 demonstrated that EISPD and ETSPD give the same results as TISPD and TTSPD when nonlinear geometric effects are not considered. Therefore, the EISPD and ETSPD are used to compare the damping forces at the elemental level with the EISPD_capped since the TISPD and TTSPD are well-known models.

The last two cases correspond to conventional steel and RC MDoF subjected to real ground motion records. Like the first two cases, the elemental models are compared. Furthermore, at the global level, all the other models in Table 5.1 are evaluated in terms of dissipated energy, displacements, and drifts. All analyses were performed in a program developed by the author during his doctoral studies.

Table 5.1 Damping models analysed and implemented in the current work.

Name damping model	Abbreviation	Stiffness used for computing the	
		damping matrix	damping parameters
Elemental initial stiffness proportional damping	EISPD	$\mathbf{k}^{\mathrm{Initbsc}}$	$\mathbf{K}^{\mathrm{Init}}$
Elemental tangent stiffness proportional damping	ETSPD	$\mathbf{k}^{\mathrm{Tanbsc}}$	$\mathbf{K}^{\mathrm{Init}}$
Capped elemental initial stiffness proportional damping	EISPD_capped	$\mathbf{k}^{\mathrm{Initbsc}}$	$\mathbf{K}^{\mathrm{Init}}$
Total initial stiffness proportional damping	TISPD	$\mathbf{K}^{\mathrm{Init}}$	$\mathbf{K}^{\mathrm{Init}}$
Total tangent stiffness proportional damping	TTSPD	$\mathbf{K}^{\mathrm{Tan}}$	$\mathbf{K}^{\mathrm{Init}}$
Total initial Rayleigh damping	TIRD	$\mathbf{K}^{\mathrm{Init}}$	$\mathbf{K}^{\mathrm{Init}}$
Condensed initial stiffness proportional damping	CISPD	$\mathbf{K}^{\mathrm{Init}}$	$\mathbf{K}^{\mathrm{Init}}$
Modal damping	MD	N/A	N/A
Total tangent Rayleigh damping	TTRD	$\mathbf{K}^{\mathrm{Tan}}$	$\mathbf{K}^{\mathrm{Init}}$
Mass proportional damping	MPD	N/A	$\mathbf{K}^{\mathrm{Init}}$

5.4.1 Nonlinear dynamic analyses of a simple inelastic steel frame

To illustrate the behaviour of the capped damping model, consider the simple steel frame depicted in Figure 5.3. The structure consists of two steel columns with a HEA280 cross-section and an upper beam with an IPE360 cross-section. Both structural elements are modelled with distributed plasticity elements known as force-based elements, using four integration points where the cross-sections above are defined.

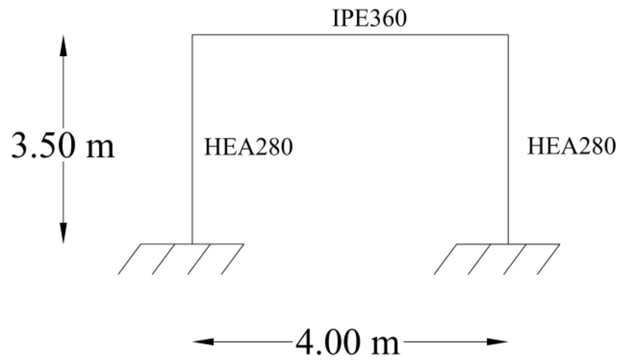

Figure 5.3 Geometric dimensions of a simple steel frame and identification of steel cross-sections.

The flanges and web of the cross-sections are modelled using 3 and 60 fibres, respectively, where the constitutive rule shown in Figure 5.4 (a) is defined. The moment-curvature diagram of both cross-sections is presented in Figure 5.4 (b) and (c). For simplicity, nonlinear geometrical effects and rigid length offsets are not considered. The structure has two masses concentrated in the upper degrees of freedom, equivalent to 10 tons.

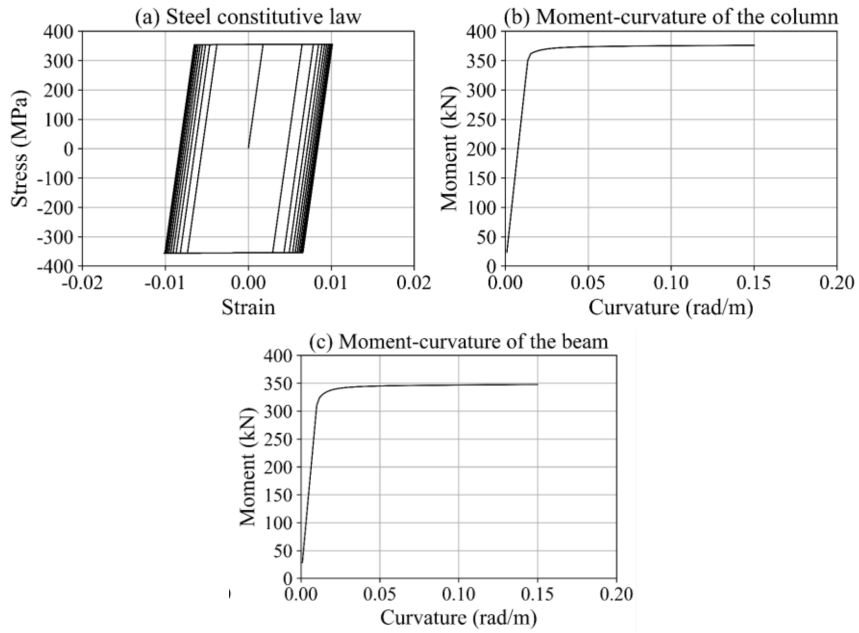

Figure 5.4 (a) Uniaxial constitutive law used for modelling the steel fibres, (b) Moment-curvature of the HEA280 cross-section used in the columns, and (c) Moment-curvature of the IPE360 cross-section used in the beams.

The frame is subjected to the incremental harmonic signal presented in Figure 5.5. This case study aims to show the structure's response in terms of elemental damping forces, "spurious" damping moments in the massless DoFs, and energy dissipation using the EISPD_capped. The response is compared with the EISPD and ETSPD.

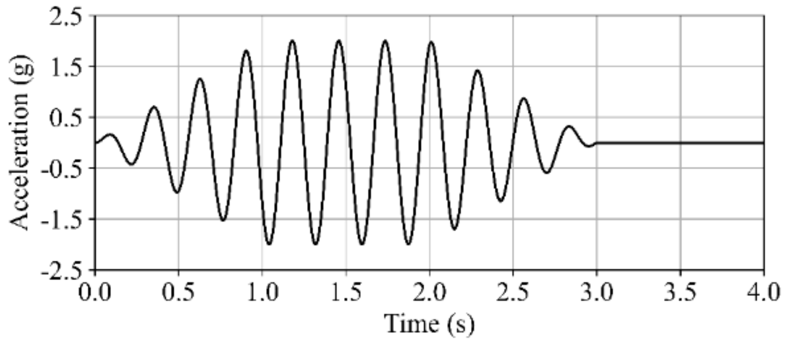

Figure 5.5 Sinusoidal ground motion record

Figure 5.5 shows the elemental damping moment and shear using EISPD, ETSPD and EISPD_capped at the left node of the frame's beam. The elemental damping moments of the EISPD and ETSPD models reach a magnitude close to 6.5%, which is high considering that the damping ratio is 2%. Although the ETSPD model also reaches this magnitude, the damping forces decrease when the element reaches the yield moment of the element. The EISPD_capped model keeps the magnitude of the damping moments to a value equal to 2ζ times the yield moment of the cross-section and the shear forces to a value equal to $4\zeta M_y/l_0$. Viscous damping models were implemented in dynamic analysis because the damping forces are expected to be minor, so any inaccuracies in the model will not significantly influence the structure's global or local response. The model presented in this chapter is the only of the three where this initial assumption is satisfied.

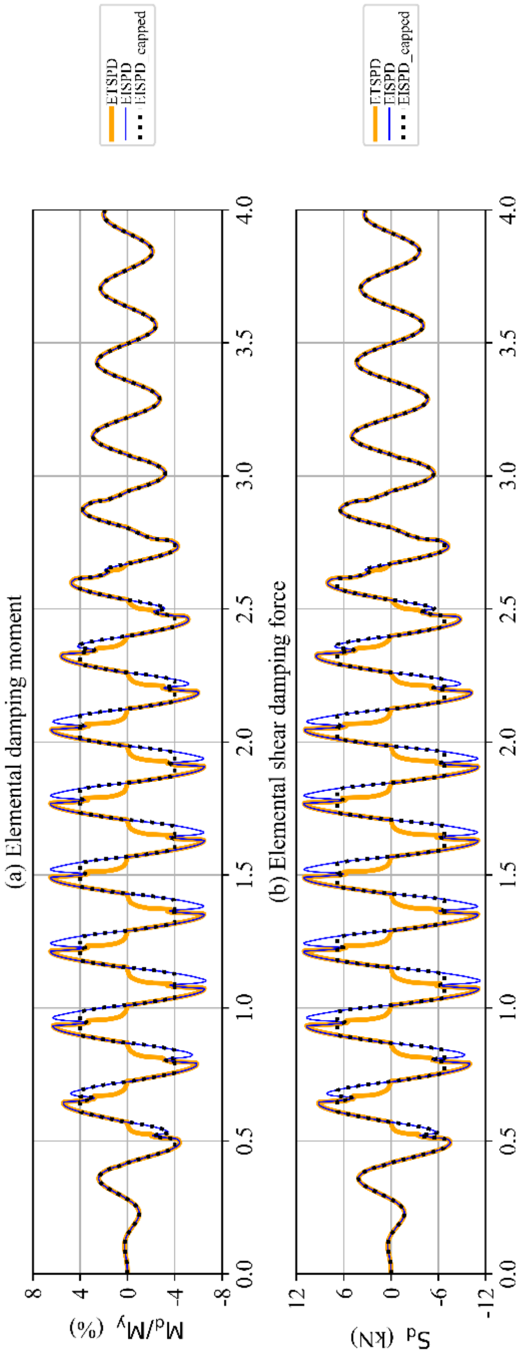

Figure 5.6 (a) elemental damping moment, and (b) shear damping force at node i of the beam.

In the elastic range, the damping forces do not exist in the massless DoFs at the global level, but when the structure yields, damping forces, and moments appear in those DoFs. The main problem with the "spurious" damping moments is that they can have an important magnitude, even reaching the capacity of the structural elements in specific cases such as the steel frame presented by Bernal[25].

The elemental damping forces are in all DoFs at any time step with the elemental models shown in Table 5.1. The latter has a physical justification since the damping forces influence all DoFs in reality. Thus, the “spurious” damping moments and forces in the massless DoFs do not disappear when the damping forces are assembled in the global vector. The model presented in this chapter avoids the concern of the “spurious” damping moments since the elemental damping forces are limited to reasonable [27,29,30] magnitudes.

Figure 5.7 presents the “spurious” damping moments in the rotational DoF of the upper left node. EISPD has the largest moments among the three models, followed by EISPD_capped and ETSPD. In addition, Figure 5.7 (b) and (c) show the spurious damping moments presented by a system using a TISPD and TTSPD, respectively. It is observed that the elemental and global damping models give equivalent results when nonlinear geometric effects are neglected.

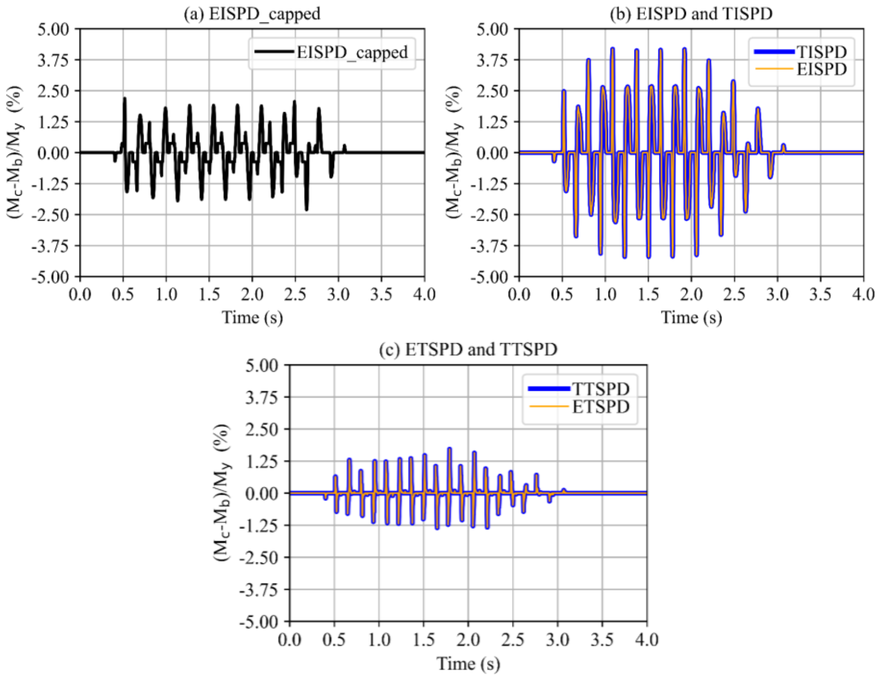

Figure 5.7 History of "spurious" damping moments in the rotational DoF of the frame top left node for (a) EISPD_capped, (b) EISPD and TISPD, and (c) ETSPD and TTSPD.

Figure 5.8 (a-c) presents an energy analysis where the cumulative energy introduced by the ground motion record (E_I), the cumulative energy dissipated by the damping forces (E_D), and the cumulative energy dissipated by the material (E_M) are shown, respectively. By limiting the damping forces, the amount of energy dissipated by the damping model decreases considerably compared to an EISPD, see Figure 5.8 (b). The ETSPD dissipates less energy since the damping forces decay when the structural elements enter the inelastic range. However, the model EISPD_capped dissipates the most energy through the constitutive rules of the materials with a slight difference compared to the others.

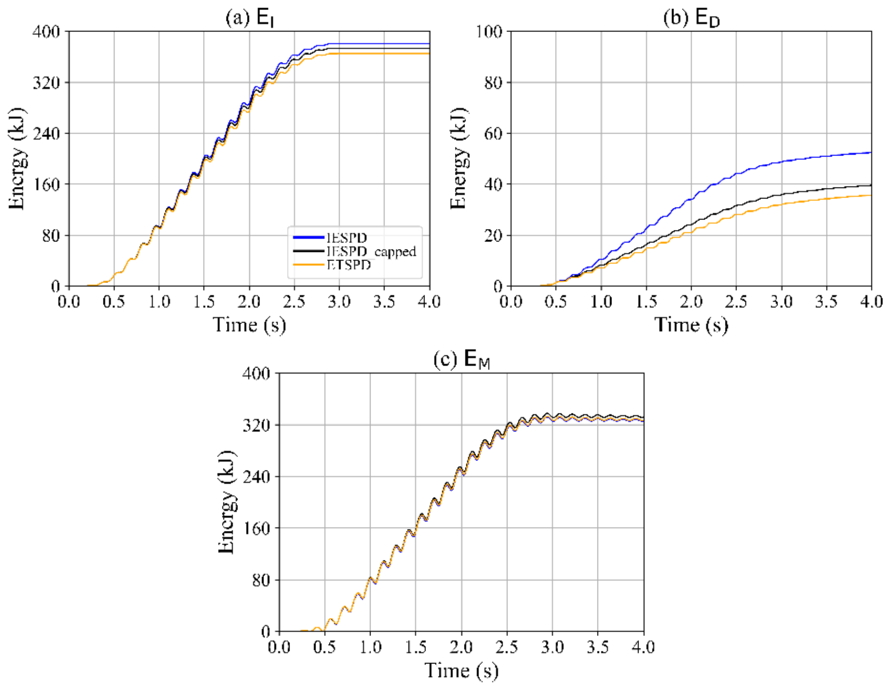

Figure 5.8 (a) Cumulative energy input by the ground motion record (E_I), (b) cumulative energy dissipated by the damping models (E_D), and (c) cumulative energy dissipated by material constitutive laws (E_M).

5.4.2 Nonlinear dynamic analyses of a simple RC frame

This case study presents nonlinear dynamic analyses of a simple RC frame with the geometry and cross-sections shown in Figure 5.9 (a-c). The frame has a distributed load of 31 kN/m on the beam, but the total mass of 15 tons is concentrated at the top transversal DoFs.

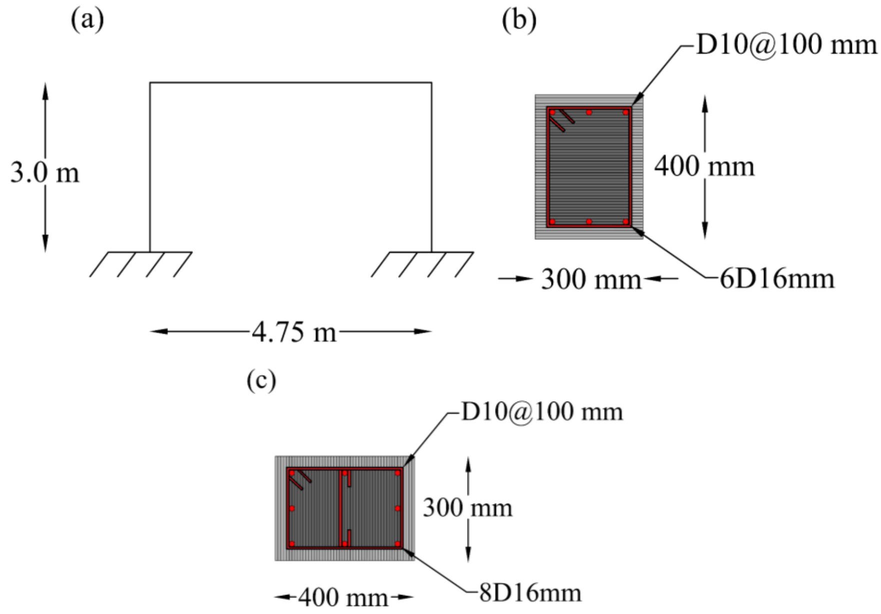

Figure 5.9 (a) Geometric dimensions of a simple RC frame, (b) cross-section of the beam, and (c) cross-section of columns.

The response of RC structures can vary more than steel structures depending on the damping model used due to significant stiffness changes caused by cracking of the concrete fibres and early loss of cover fibres. The latter is the principal reason to study this kind of structure.

The structural members of the frame are modelled using force-based elements[83,84] with four integration points. The steel fibres of the sections are represented with the Menegotto and Pinto[86] constitutive rule presented in Figure 5.10 (a), and the concrete fibres of the cover and confined core are modelled using the Mander et al.[88] constitutive rule shown in Figure 5.10 (a) and (b), respectively. The tensile strength of the concrete is not considered.

The elemental damping models, presented in Table 5.1, are defined after applying gravity loads which partially crack the structure since the tensile strength is not considered. In this case, the elemental damping models were determined with a damping ratio of 3%.

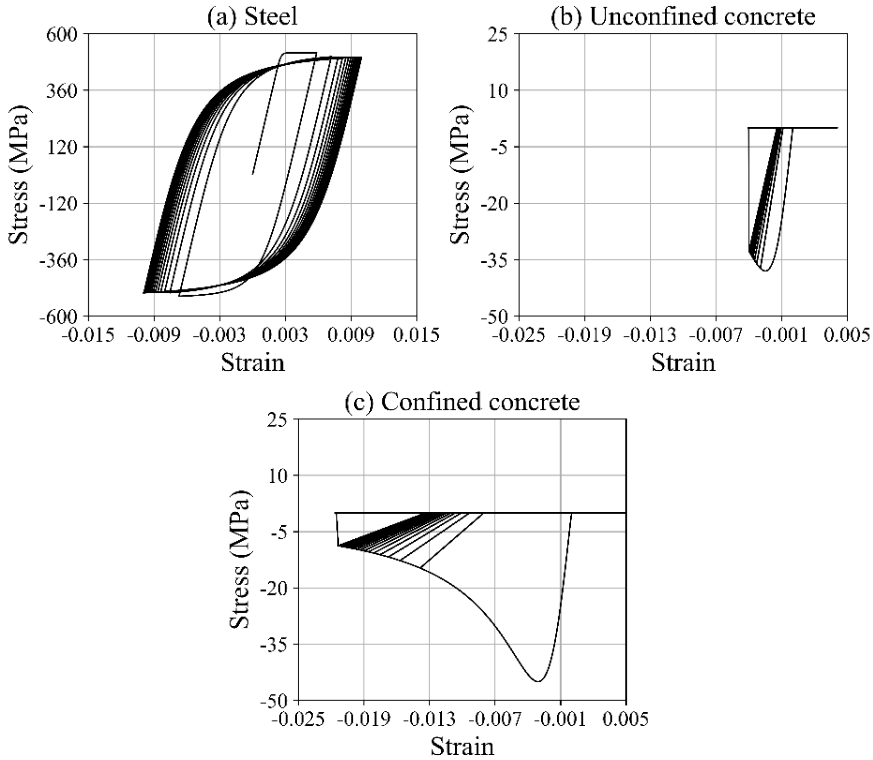

Figure 5.10 Uniaxial constitutive laws used for modelling the steel and concrete fibres: (a) Menegotto and Pinto[86], (b-c) Mander et al.[88].

Figure 5.11 (a) and (b) present the moment-curvature diagram of the cross-sections that conform the structural elements of the frame up to failure. The bending moment diagram shown in Figure 5.11 (a) considers an axial load of -75 kN due to the distributed load on the beam.

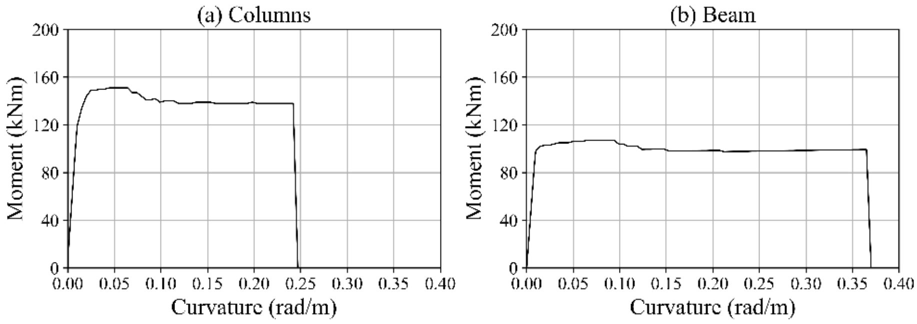

Figure 5.11 (a) Moment-curvature of the columns, and (b) Moment-curvature of the beam.

The concrete frame is subjected to the incremental sinusoidal ground motion record presented in Figure 5.12 to observe the behaviour of the damping models.

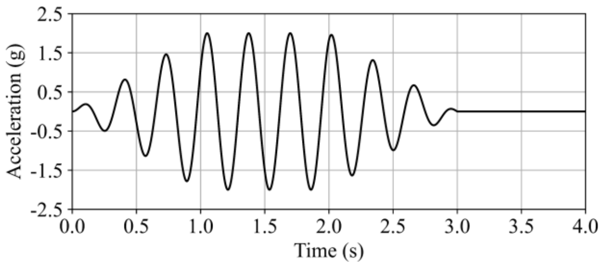

Figure 5.12 Incremental sinusoidal ground motion record

Figure 5.13 (a-b) presents the history of the damping moment and shear force at the left node of the beam, respectively. Figure 5.13 (a) shows that the damping moments reach values close to 15% of the yield moment of the cross-section presented in Figure 5.11 (b) when an EISPD is used. The ETSPD model presents smaller magnitudes that fall within a reasonable range. However, the damping forces decay rapidly when the element yields, causing the curve to present triangular shapes. Equally, the damping forces with EISPD_capped have reasonable limits, but the damping forces do not decay when the structure enters the inelastic range. This is advantageous since one of the major criticisms of the model proportional to the tangent stiffness matrix is the decay of the damping forces during incursions in the inelastic range.

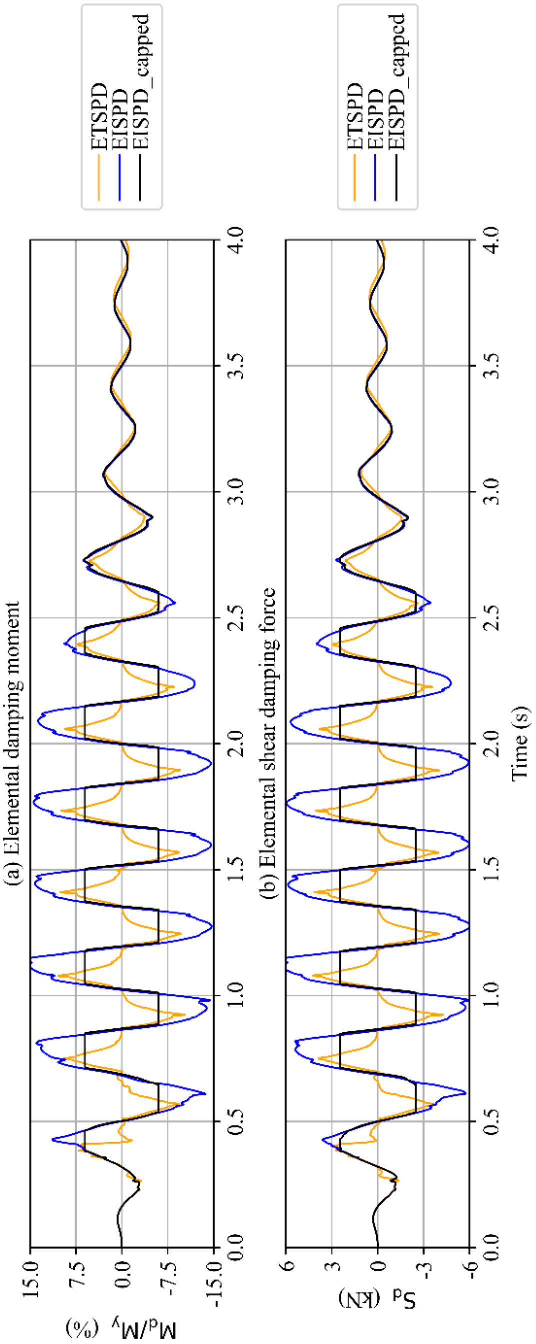

Figure 5.13 (a) elemental damping moment and (b) shear damping force at the left node of the beam.

Figure 5.14 (a-c) presents the “spurious” damping moments at the upper left node using the elemental models in Table 5.1, TISPD, and TTSPD. This figure shows that the EISPD has larger magnitudes of spurious damping moments than the other elemental models. The EISPD_capped is the second in magnitude, presenting a significant decrease compared to the EISPD. Finally, the ETSPD model has the lowest magnitude. These results agree with those shown in the previous case study.

Figure 5.14 (b) and (c) compare the magnitude of the "spurious" damping moments in the rotational DoF using a global and elemental damping model. As in the previous case, both models are equivalent when nonlinear geometric effects are not considered, and the same damping parameter is used.

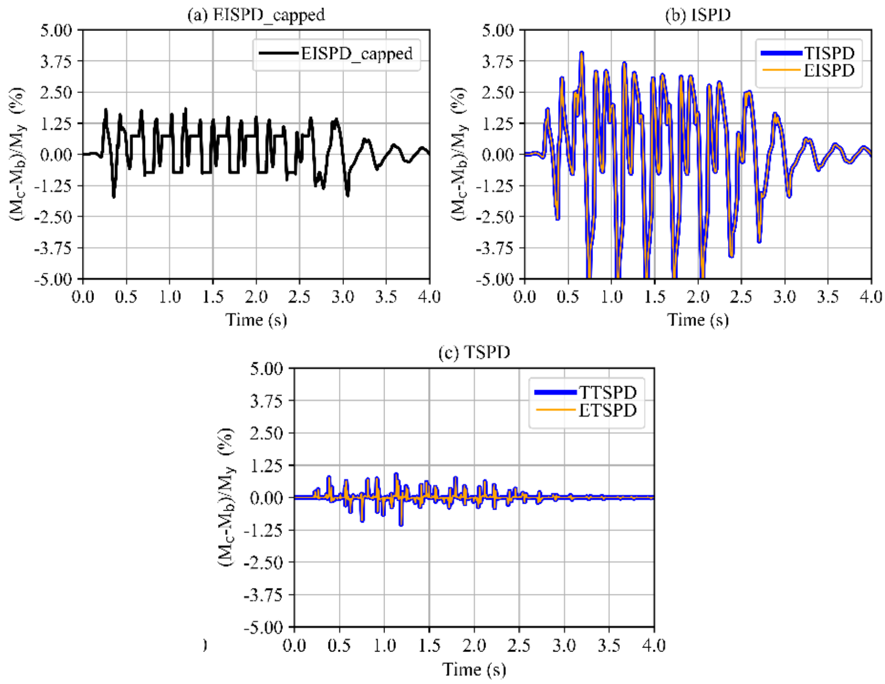

Figure 5.14 History of “spurious” damping moments in the rotational DoF of the frame top left node for (a) EISPD_capped, (b) EISPD and TISPD, and (c) ETSPD and TTSPD.

Figure 5.15 (a-c) presents an energy analysis where the cumulative energy introduced by the ground motion record (E_I), the cumulative energy dissipated by the damping forces (E_D), and the cumulative energy dissipated by the material (E_M) are shown, respectively. The EISPD is the model that dissipates more energy, which implies that the structural system dissipates less energy through the constitutive rules of the materials. The EISPD_capped and ETSPD dissipate less energy than EISPD, which is reflected in the energy dissipated by the constitutive rules.

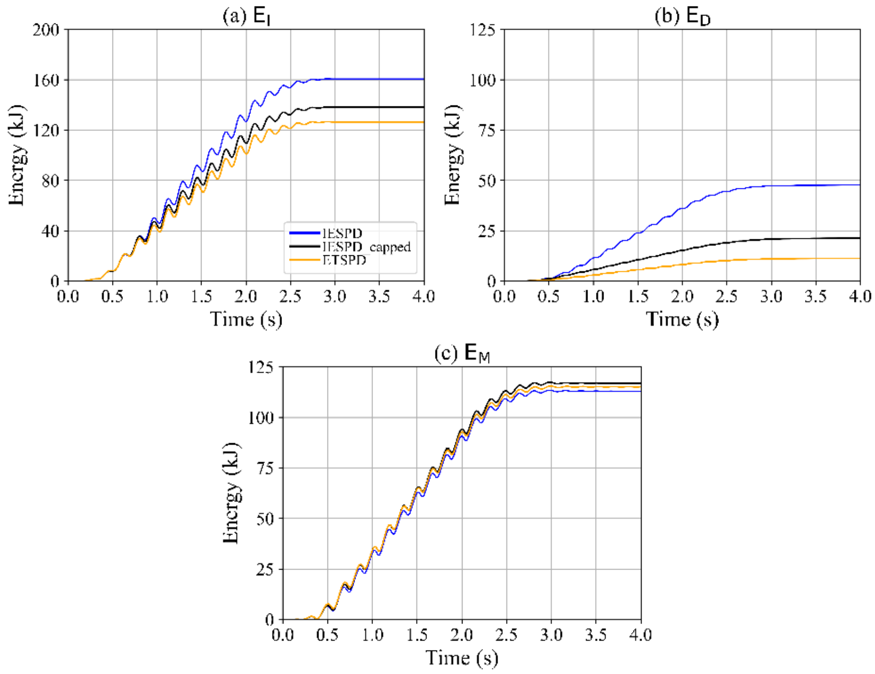

Figure 5.15 (a) Cumulative energy input by the ground motion record, (b) cumulative energy dissipated by the damping models, and (c) cumulative energy dissipated by material constitutive laws.

5.4.3 Nonlinear dynamic analyses of a realistic steel frame

This case study presents a realistic steel frame to compare the damping models in Table 5.1. The building comprises three frames and six storeys, with the dimensions shown in Figure 5.16. The structure is modelled with force-based elements using four integration points. All beams have a cross-section W610X94, and all columns have a cross-section W690X170. The beams have a distributed load of -78 kN/m. The masses corresponding to this distributed load of 28.9 and 57.8 ton are imposed at the outer and central nodes, respectively, only in the horizontal direction. For simplicity, nonlinear geometrical effects and rigid length offsets are not considered. This case study was taken from an OpenSees[49] academic problem.

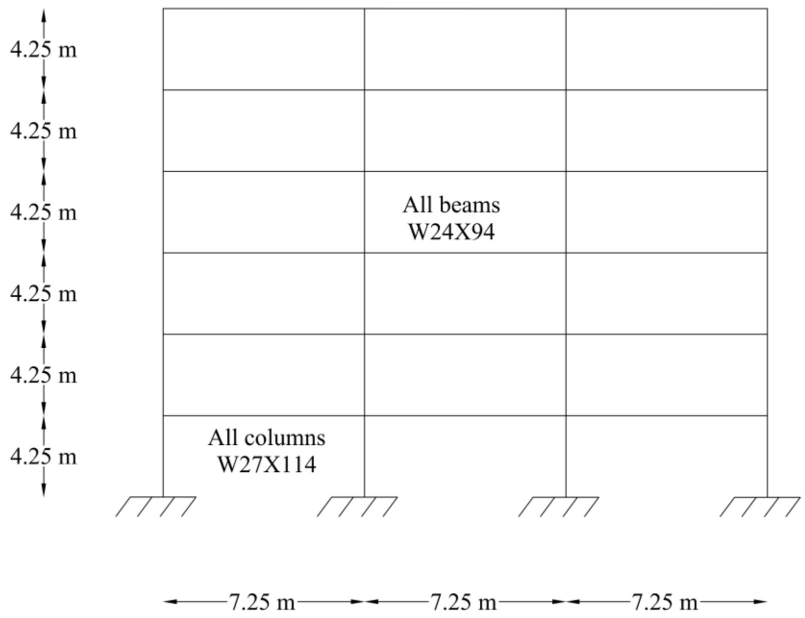

Figure 5.16 Geometric dimensions of a realistic steel frame taken from OpenSees[49] and identification of steel cross-sections.

The cross-sections have 12 and two fibres in the web and flanges, where the constitutive rule of Menegotto and Pinto[86], presented in Figure 5.17 (a), is defined. Figure 5.17 (b) and Figure 5.17 (c) show the moment-curvature diagrams of the cross-sections.

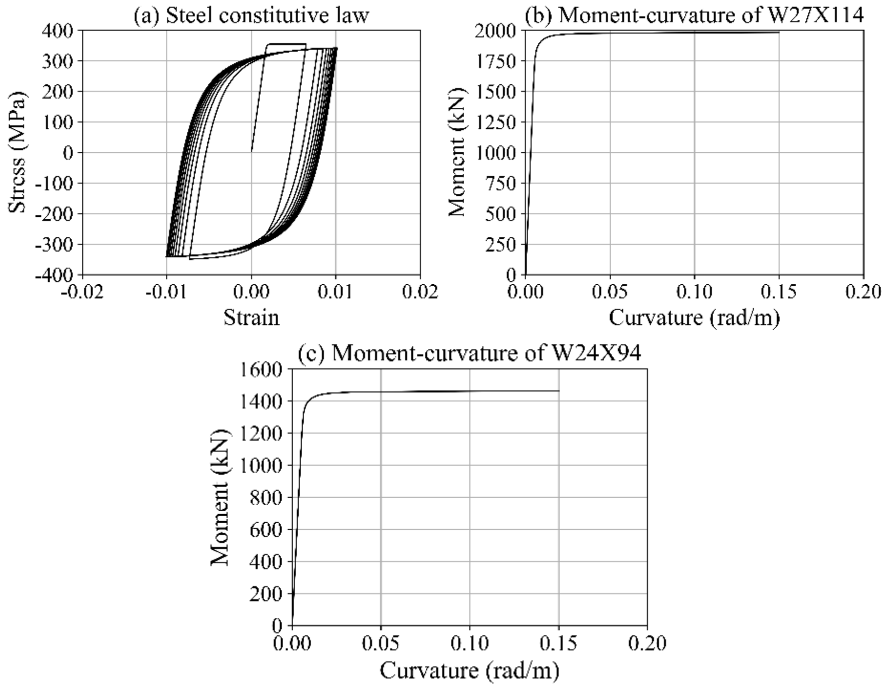

Figure 5.17 (a) Uniaxial constitutive law of Menegotto and Pinto[86] *used for modelling the steel fibres, (b) Moment-curvature of the W27X114 cross-section used in the columns, and (c) Moment-curvature of the W24X94 cross-section used in the beams.*

The structure is subjected to the horizontal component of the ground motion record of the Denali earthquake, downloaded from the PEER Strong Motion Database[87] and shown in Figure 5.18 (2002, station: TAPS Pump Station #10). All the damping models presented in Table 5.1 were defined with a damping ratio of 3% to observe the difference between the models better.

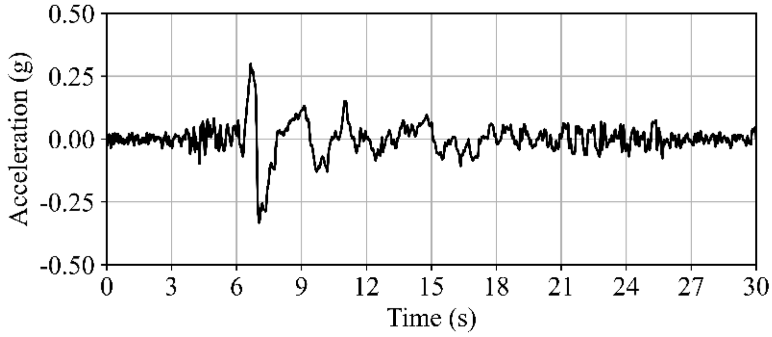

Figure 5.18 Ground motion record from the Denali earthquake

Figure 5.19 presents the history of elemental damping moments and shear forces at the left end of the first-floor beam of the left frame. When the structure is in the elastic range, all the elemental damping models present a coincident response since the loading and unloading stiffness of the constitutive rule, presented in Figure 5.17 (a), is similar to the initial, especially under low demands. Therefore, the damping forces between the three elemental models differ when the element enters the inelastic range or the damping moments overpass the imposed limit in the EISPD_capped.

For instance, at 7.5 seconds, the damping moment using the EISPD reaches a magnitude close to 12% of the yield moment of the section. During this time interval, the damping moment using the ETSPD decreases rapidly after reaching a magnitude of 7.5% of the yield moment of the cross-section due to the stiffness matrix decay. Both moments are high, considering the defined damping ratio. The EISPD_capped limits the damping moments to a value of 6%, and the damping moments and shear forces do not decay when the structure enters the inelastic range.

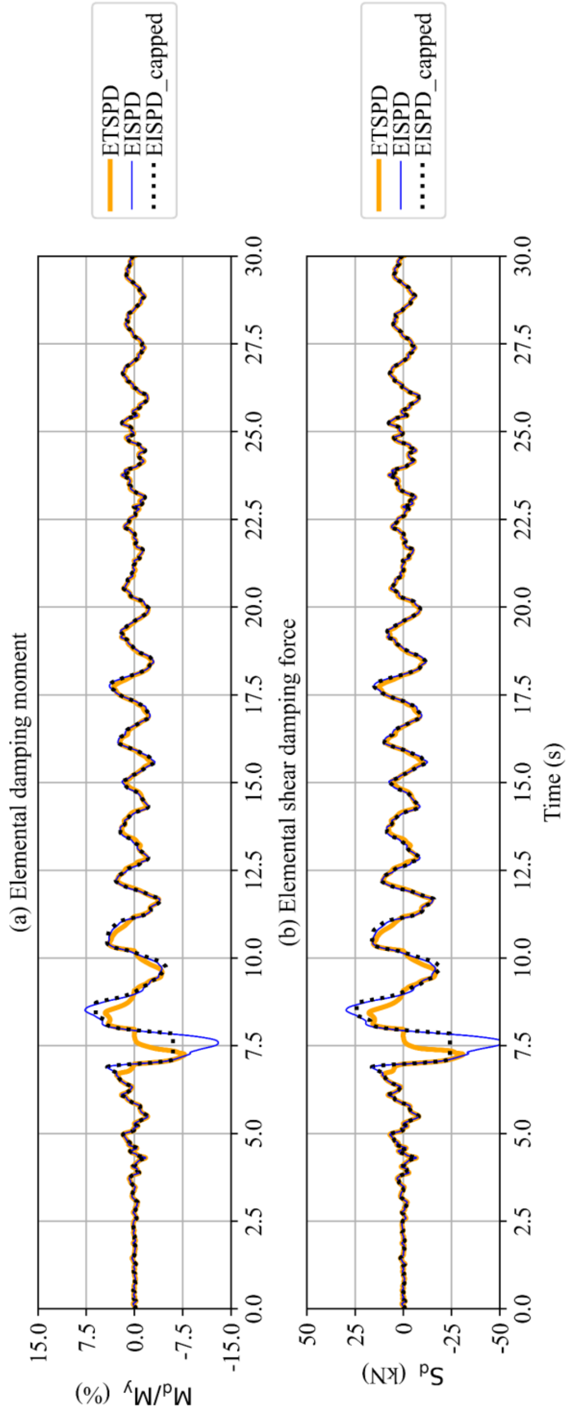

Figure 5.19 (a) Elemental damping moment and (b) Shear damping force at the left end of the first-floor beam of the left frame

Figure 5.20 (a-c) presents an energy analysis where the cumulative energy introduced by the ground motion record (E_I), the cumulative energy dissipated by the damping forces (E_D), and the cumulative energy dissipated by the material (E_M) are shown, respectively. Figure 5.20 (b) indicates that the EISPD model dissipates the most energy, followed by EISPD_capped and ETSPD. Therefore, the structural elements that dissipate the most energy belong to the structural system using an ETSPD, followed by EISPD_capped and EISPD.

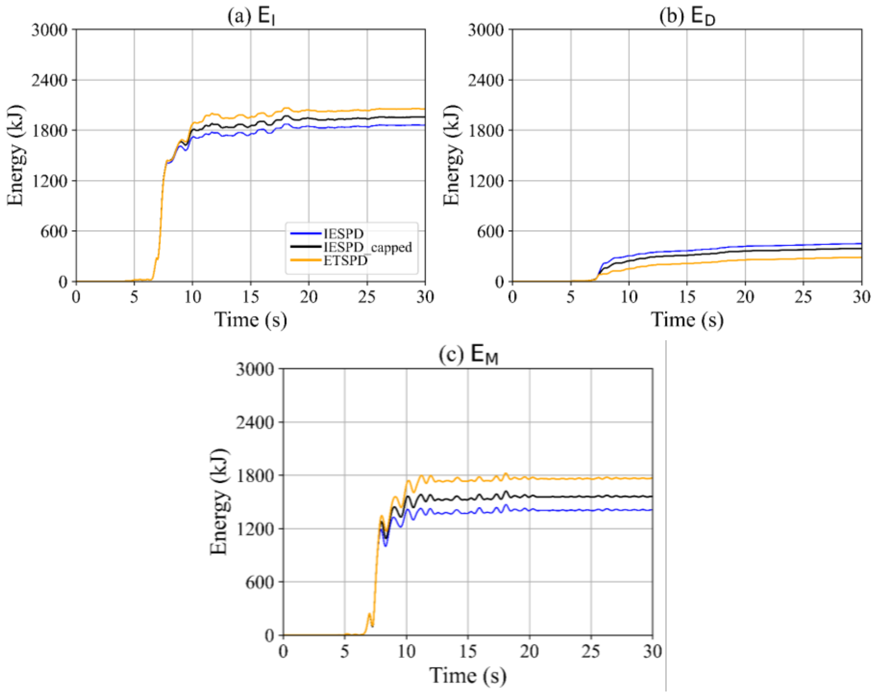

Figure 5.20 (a) Cumulative energy input by the ground motion record, (b) cumulative energy dissipated by the damping models, and (c) cumulative energy dissipated by material constitutive laws.

Table 5.2 presents the energy dissipation analyses for all the damping models shown in Table 5.1. Among all, the structural systems using ETSPD and TTSPD dissipate the most energy through the constitutive rules of the materials. When these models are used, the damping forces decrease significantly as the elements enter the inelastic range so that the elements will have more demands. By contrast, the systems using

EISPD, TISPD, and CISPD dissipate the least energy through the constitutive rules of the materials.

All SPD models have a high effective damping ratio in the upper modes. In the models proportional to the TSM, this is partially compensated by the damping forces decay when the system enters the inelastic range, and in the proposed model, by the imposed limits. However, this is not compensated in the EISPD, TISPD, TIRD, and CISPD; additionally, the damping model is linear, while the resistance system is nonlinear. Therefore, the damping becomes proportionally more important in the inelastic range.

The EISPD_capped dissipates 80% of the energy introduced through the material constitutive rules, which is the average of all the models presented in Table 5.1. However, it is higher than the percentage of energy dissipated by the constitutive rules of the structural systems using EISPD, TISPD, and CISPD. As in the two previous case studies, it can be observed that the EISPD and TISPD, and ETSPD and TTSPD models have the same results since nonlinear geometric effects are not accounted for.

Table 5.2 Cumulative energy introduced by the ground motion record, cumulative energy dissipated by the damping model, and cumulative energy dissipated by the material constitutive rules.

Abbreviation	E_I (kJ)	E_M (kJ)	E_M/E_I (%)	E_D (kJ)	E_D/E_I (%)
EISPD	1865	1410	76%	452	24%
ETSPD	2052	1760	86%	289	14%
EISPD_capped	1958	1560	80%	395	20%
TISPD	1865	1410	76%	452	24%
TTSPD	2052	1760	86%	289	14%
TIRD	1906	1493	78%	410	21%
CISPD	1873	1429	76%	441	24%
MD	1908	1506	79%	399	21%
TTRD	1949	1583	81%	363	19%
MPD	1906	1524	80%	378	20%

Table 5.3 presents the maximum inter-storey drift and the maximum horizontal displacements per floor at the nodes on the left side of the

building, using a conditional format for easier comprehension. The models with the largest drifts and displacements are ETSPD and TTSPD, while those with the smallest drifts and displacements are EISPD, TISPD, and CISPD. The other models are in between the values of the models, including the model proposed in this work. Nevertheless, in terms of displacement, the EISPD_capped are after the ETSPD and TTSPD.

Table 5.3 Maximum drift per storey

	Maximum drift per storey					
Model	1a	2a	3a	4a	5a	6a
EISPD	4.0%	3.9%	2.7%	1.6%	1.0%	0.6%
ETSPD	5.1%	4.6%	2.4%	1.4%	0.9%	0.6%
EISPD_capped	4.6%	4.3%	2.7%	1.5%	0.9%	0.6%
TISPD	4.0%	3.9%	2.7%	1.6%	1.0%	0.6%
TTSPD	5.1%	4.6%	2.4%	1.4%	0.9%	0.6%
TIRD	4.5%	4.1%	2.4%	1.5%	0.9%	0.6%
CISPD	4.2%	4.0%	2.7%	1.6%	0.9%	0.6%
MD	4.6%	4.2%	2.4%	1.5%	0.9%	0.6%
TTRD	4.8%	4.3%	2.3%	1.4%	0.9%	0.6%
MPD	4.8%	4.2%	2.4%	1.5%	1.0%	0.6%

Table 5.4 Maximum displacement per storey

	Maximum displacement per storey (m)					
Model	1a	2a	3a	4a	5a	6a
EISPD	0.17	0.34	0.45	0.52	0.55	0.57
ETSPD	0.22	0.41	0.51	0.57	0.60	0.62
EISPD_capped	0.20	0.38	0.49	0.55	0.59	0.60
TISPD	0.17	0.34	0.45	0.52	0.55	0.57
TTSPD	0.22	0.41	0.51	0.57	0.60	0.62
TIRD	0.19	0.37	0.47	0.53	0.56	0.58
CISPD	0.18	0.35	0.46	0.52	0.56	0.57
MD	0.20	0.37	0.47	0.53	0.56	0.58
TTRD	0.21	0.39	0.49	0.54	0.57	0.59
MPD	0.20	0.38	0.48	0.53	0.56	0.58

The values of cumulative energy, drift and maximum displacement change as a function of the damping models. However, in both steel structures the influence of the damping models is not extremely large. This is not new and has been mentioned and explained in other studies[92]. The reasons behind are (i) the steel constitutive rules do not have large stiffness decay after incursions into the inelastic range and (ii) elements with distributed plasticity present a more consistent formulation than elements with concentrated plasticity where inelastic springs with high initial stiffnesses are placed. In contrast, concrete structures have large stiffness decays after incursions in the inelastic range since concrete fibres crack, unconfined concrete fibres easily reach the ultimate strain, and the loading and unloading slope of the constitutive rule of the materials decrease considerably with respect to the initial stiffness. Therefore, the choice of the damping model has a more significant influence.

5.4.4 Nonlinear dynamic response of Arede's RC frame

This case study shows the results of nonlinear dynamic analyses performed on the realistic RC structure in Figure 5.21. This 2D structural system corresponds to the internal frame of the real 3D structure of Arede[93]. This structure was designed according to Eurocode to have a high ductility capacity. The structural system studied comprises two frames and four floors with the dimensions shown.

The beams and columns are numbered, and the cross-sections are identified with the codes “CX” and “BX”, respectively. The detailing of the reinforcement is not described in this article but is well documented in Arede[93].

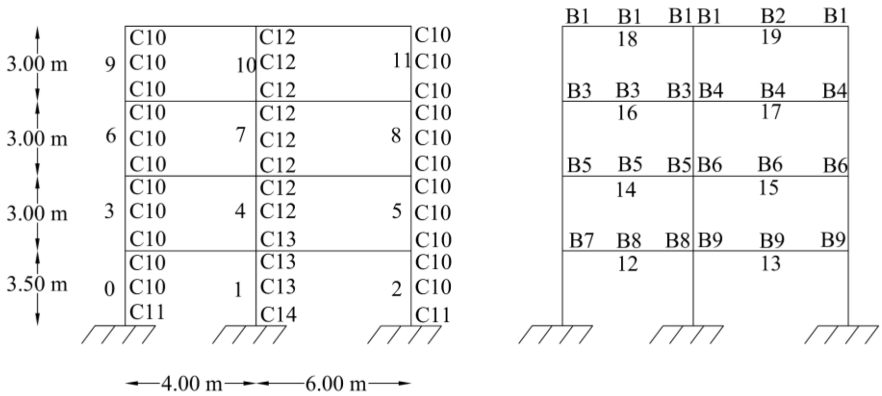

Figure 5.21 (a) Geometric dimensions of the Arede´s frame, identification of elements and column cross-sections, and (b) identification of elements and beams cross-sections.

The beams of the top and first three floors have a distributed load of 35 and 34 kN/m, respectively. The mass corresponding to these distributed loads is considered lumped in the transverse directions, i.e., no mass is defined in the rotational DoFs. All columns and beams are modelled using forced-based elements[83,84] with three integration points, where the three sections per element presented in Figure 5.21 are defined. For simplicity, nonlinear geometric effects and rigid length offsets are not considered in these analyses.

Figure 5.22 (a) shows the Menegotto and Pinto[86] constitutive rule used to model the steel bars. Figure 5.22 (b) and (c) show the constitutive rule presented by Mander[88] to model the unconfined and confined concrete, respectively. All the steel bars and concrete used to build this structure presented slightly different strengths, and the degree of confinement of the concrete varies depending on each beam and column.

For simplicity, the constitutive rules in Figure 5.22 (a-c) are used for all structural elements.

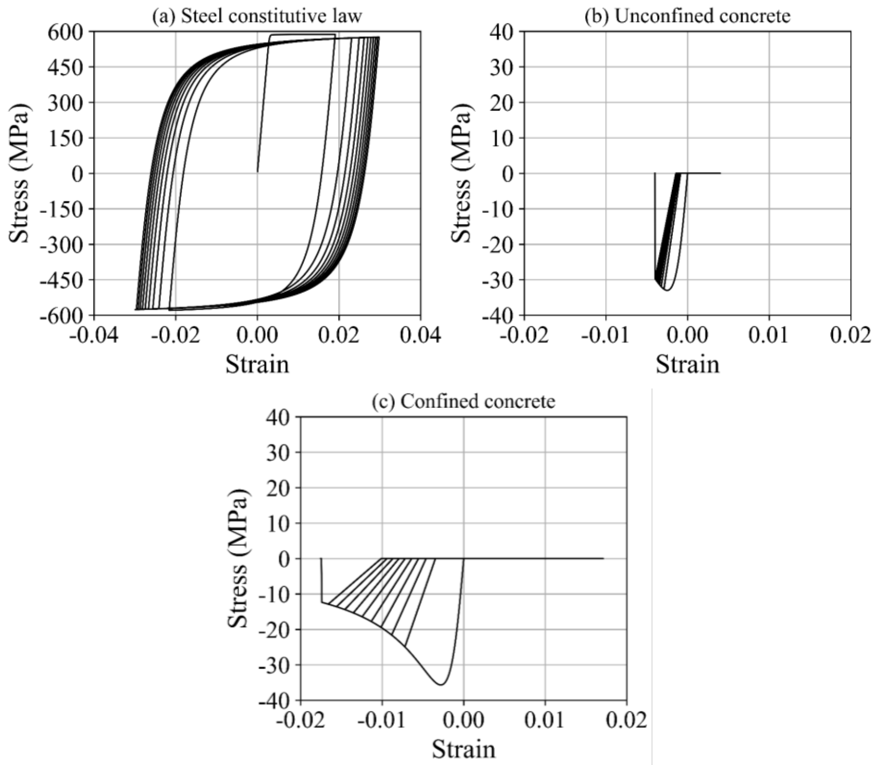

Figure 5.22 Uniaxial constitutive laws used for modelling the steel and concrete fibres: (a) Menegotto and Pinto[86], (b-c) Mander et al.[88].

Table 5.5 presents the maximum resisting moment of the column cross-sections considering the axial load on the elements. The values of resisting moments shown are used to define the limit of the damping moment at the basic reference system.

Table 5.5 Maximum resistant moment of the sections composing the columns

Member	Section ID	Axial Load (kN)	My- (kNm)	My+ (kNm)	Member	Section ID	Axial Load (kN)	My- (kNm)	My+ (kNm)
0	C10	-275.9	239.2	239.2	4	C13	-513.0	363.4	363.4
0	C11	-275.9	337.8	337.8	5	C10	-309.9	245.3	245.3
1	C13	-681.8	377.6	377.6	6	C10	-137.5	214.0	214.0
1	C14	-681.8	509.0	509.0	7	C12	-345.8	297.3	297.3
2	C10	-412.2	263.4	263.4	8	C10	-206.7	226.9	226.9
2	C11	-412.2	360.7	360.7	9	C10	-69.7	201.3	201.3
3	C10	-207.1	227.0	227.0	10	C12	-179.9	268.0	-268.0
4	C12	-513.0	325.1	325.1	11	C10	-104.5	207.8	207.8

Table 5.6 presents the maximum moments of the beam cross-sections. The difference between the positive and negative moments is a limitation of the model proposed in this work. An average between both moments defines the limit at each end to simplify the process.

Table 5.6 Maximum resistance moment of the sections composing the beams

Section ID	My+	My-
B1	99.9	99.9
B2	150.5	100.0
B3	99.9	134.4
B4	100.0	184.7
B5	143.6	177.8
B6	109.1	177.7
B7	143.6	228.0
B8	143.6	202.9
B9	143.6	228.0

The structure is subjected to the scaled horizontal component of the ground motion record of the Northridge earthquake, downloaded from the PEER Strong Motion Database [87] and shown in Figure 5.23 (1994, station: Jensen Filter Plant Administrative Building, 22). For simplicity, geometric effects and rigid length offsets are not considered in this analysis. All damping models were defined with a damping ratio of 3% after applying the gravity loads on the structure.

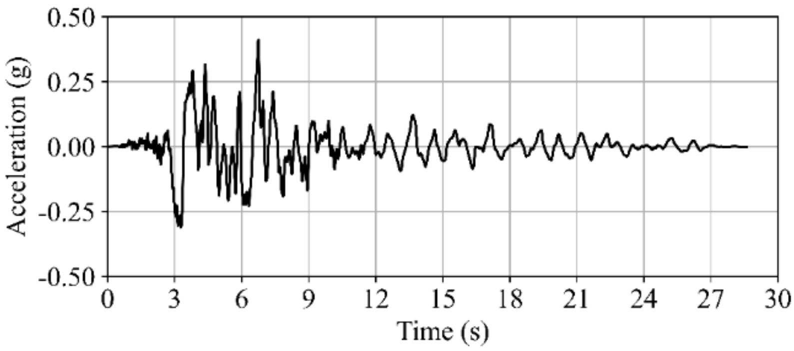

Figure 5.23 Ground motion record from the Northridge earthquake

Figure 5.24 depicts the damping moments and shear forces at the elemental level. As in the previous cases, the damping forces with the EISPD model reach significant magnitudes considering the damping ratio of 3% defined. The EISPD_capped limits these damping moments and forces to reasonable levels.

In contrast to the previous RC case, there are important differences between the EISPD and ETSPD in the elastic range, as the loading and unloading stiffness differs considerably from the initial stiffness. The difference is caused by additional cracking of the concrete fibres and permanent loss of the cover concrete fibres when the ultimate strain is reached. The ETSPD decays to zero at the peak of high demands and presents small damping forces afterwards.

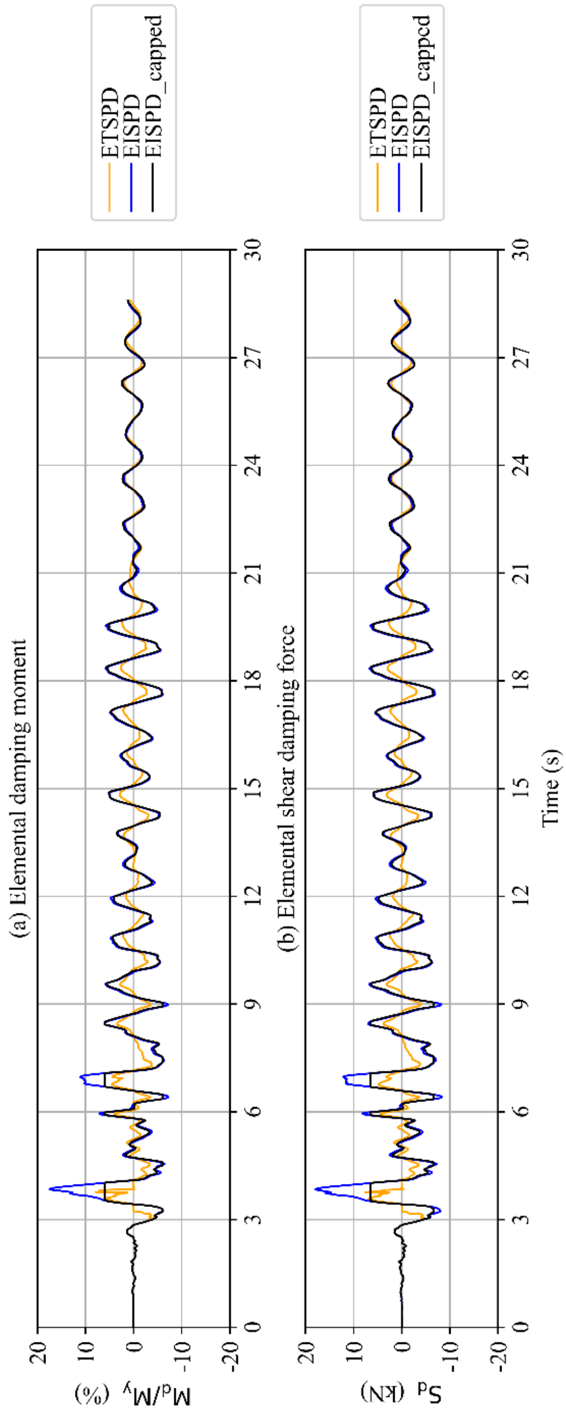

Figure 5.24 (a) Elemental damping moment and (b) Shear damping force at the left end of member 12

Figure 5.25 (a-c) present the cumulative energy introduced by the ground motion record, the energy dissipated by the damping model, and the constitutive rules of the materials, respectively, in the systems using elemental damping models. The IESPD dissipates the most energy, followed by IESPD_capped and ETSPD. The latter is reflected in the cumulative energy dissipated by the constitutive rules in Figure 5.25 (c), where the order is inversed. The difference between the IESPD and IESPD_capped and ETSPD models is significant, which is caused by a substantial decay of the tangent stiffness matrix.

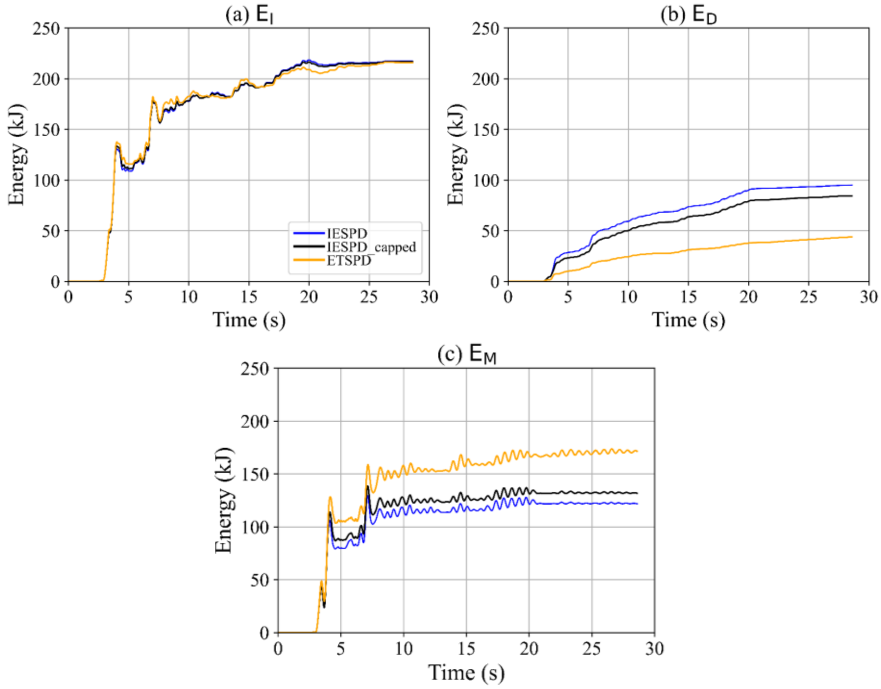

Figure 5.25 (a) Cumulative energy input by the ground motion record, (b) cumulative energy dissipated by the damping models, and (c) cumulative energy dissipated by material constitutive laws.

Table 5.7 shows the results of an energy analysis with all the damping models presented in Table 5.1. As in the previous case, the ETSPD and TTSPD dissipate the most energy through the constitutive rules of the materials. Similarly, EISPD, CISPD and TISPD dissipate less energy than the rest. The other models lie in between these two groups. However, EISPD_capped is closer to the second group than to the first. Additionally, the amount of energy E_M is below the average. This is caused by an increase in the effective damping ratio after the peak of the demand when the stiffness matrix decays permanently.

Table 5.7 Cumulative energy introduced by the ground motion record, cumulative energy dissipated by the damping model, and cumulative energy dissipated by the material constitutive rules.

Abbreviation	E_I (kJ)	E_M (kJ)	E_M/E_I (%)	E_D (kJ)	E_D/E_I (%)
EISPD	217	122	56%	95	44%
ETSPD	216	172	79%	44	20%
EISPD_capped	217	132	61%	85	39%
TISPD	217	122	56%	95	44%
TTSPD	216	172	79%	44	20%
TIRD	220	135	61%	85	39%
CISPD	217	124	57%	93	43%
MD	220	138	63%	82	37%
TTRD	221	149	67%	72	32%
MPD	223	144	65%	78	35%

Tables 5.8 and 5.9 show the maximum drift and displacement per storey using the models presented in Table 5.1. The results indicate that the highest displacements occur in the systems using an ETSPD and TTSPD. Subsequently, the system, using the EISPD_capped, has the most significant displacements in the last three levels; the latter is due to the limits imposed on the damping forces at the time step of the highest demands. The systems using EISPD, TISPD and CISPD have the lowest displacements and drifts. Finally, the systems using the other models are in an intermediate range.

Table 5.8 Maximum drift per storey

	Maximum drift per storey			
Model	1a	2a	3a	4a
EISPD	2.88%	3.02%	2.54%	1.46%
ETSPD	3.47%	3.31%	2.64%	1.59%
EISPD_capped	3.13%	3.21%	2.67%	1.53%
TISPD	2.88%	3.02%	2.54%	1.46%
TTSPD	3.47%	3.31%	2.64%	1.59%
TIRD	3.18%	3.04%	2.33%	1.37%
CISPD	2.88%	3.03%	2.57%	1.48%
MD	3.21%	3.04%	2.34%	1.37%
TTRD	3.39%	3.06%	2.35%	1.41%
MPD	3.33%	2.96%	2.39%	1.46%

Table 5.9 Maximum displacement per storey

	Maximum displacement per storey (m)			
Model	1a	2a	3a	4a
EISPD	0.086	0.177	0.253	0.297
ETSPD	0.104	0.203	0.282	0.325
EISPD_capped	0.094	0.190	0.270	0.316
TISPD	0.086	0.177	0.253	0.297
TTSPD	0.104	0.203	0.282	0.325
TIRD	0.095	0.186	0.256	0.291
CISPD	0.087	0.177	0.254	0.299
MD	0.096	0.188	0.256	0.290
TTRD	0.102	0.193	0.260	0.293
MPD	0.100	0.188	0.254	0.288

5.5 Conclusions

Dynamic analyses use viscous damping models to simulate sources of energy dissipation independent of the constitutive rules of the materials. These models are commonly defined with Rayleigh, modal, mass proportional, or stiffness proportional damping using the initial or tangent stiffness matrix. The damping models were defined under the assumption that damping forces are small compared to the material and inertial resisting forces, so any inaccuracies will not significantly affect the structure's response. Nonetheless, in nonlinear dynamic analyses, this assumption is not satisfied.

This chapter defines in the basic reference system the elemental damping forces using a damping model proportional to the initial stiffness matrix (EISPD), tangent stiffness (ETSPD) and the change of the deformations with respect to time independent of the rigid body motion. These models and the case studies presented demonstrate that the elemental damping forces reach significant magnitudes compared to the maximum capacity of the structural elements. The EISPD and ETSPD give the same as the global models when nonlinear geometric effects are not considered. However, the models differ when nonlinear geometric effects are considered, as demonstrated in this article.

To remedy the proportionally high magnitudes of the elemental damping forces with respect to the capacity of the structural elements, a new elemental level damping model is proposed, which limits the elemental damping forces to a certain percentage of their capacity. This model is defined in the basic reference system, where the damping forces are expressed through the initial stiffness matrix and the basic velocities of each element. When the basic damping forces exceed a certain percentage of the capacity of the structural element, this maximum is imposed before expressing the damping forces in the local and global reference system. The mathematical formulation and various case studies on steel and RC structures elucidate the properties of this model. This new capped model ensures that the damping forces in the structure are within reasonable limits.

6. Fibre-based nonlinear viscous damping model defined for dynamic analysis using distributed plasticity elements

6.1 Abstract

This chapter presents a new nonlinear viscous damping model implemented in the fibre where a constitutive rule is defined between the strain rates and the damping stresses. This model is developed for nonlinear dynamic analyses using distributed plasticity frame elements with fibre cross-sections. The model is proportional to the initial stiffness of the fibre material, but the maximum damping stress is limited to avoid local and global high damping forces and prevent them from decaying or taking negative values when the structure is in the inelastic range. The manuscript details the formulation used to find the fibre strain rates, the damping forces at each level of the structure and its implementation using the Newmark method. The predictions of the model are compared with the real response of a reinforced concrete structure tested on a seismic table under high demands. Additionally, a numerical case study is presented addressing the inelastic response of a steel structure.

6.2 Introduction

Viscous damping was used by analogy in nonlinear dynamic analyses when they were developed. However, the assumptions made by Lord Rayleigh[8] and Wilson and Clough[10] are not fulfilled. In systems with an inelastic resisting system, the damping forces can reach proportionally higher magnitudes compared to the material resisting forces. Therefore, the damping forces are not small, can reach considerable magnitudes, and significantly affect the structure's response.

Traditional damping models such as RD, Mass, and stiffness proportional damping models (MPD and SPD, respectively) define the damping forces through linear models proportional to the velocities of the system. This condition is not a problem during linear dynamic analyses since the material-related resisting forces are also linear and directly proportional to the deformations. Therefore, the ratio between the maximum damping and material resistance forces will be in an acceptable magnitude range. In inelastic systems, the material resisting forces are defined through nonlinear constitutive rules. However, the damping forces are still defined through linear models. When the structure or structural elements reach their yield strength, significant changes in deformations and hence velocities occur. The material resisting forces arrive at a predefined value, while the damping forces increase to magnitude values that are not easy to justify [21,25,27–29]. In some specific cases, the damping forces can reach a magnitude equal to the capacity of the structural members[25].

This chapter presents a new viscous damping model defined in the fibre through a nonlinear constitutive rule between the strain rates and damping stresses. This approach provides essential flexibility and allows extracting information about damping forces existing in each fibre, section, element, and structure, which are unavailable with traditional global models. The above implies having full control over the analysis and understanding the response of every component of the structural system. The performance of this approach is compared with an experimental test available in the literature, existing global damping models, and other illustrative fibre models presented. Finally, the last section summarises the main conclusions.

6.3 Viscous damping model implemented at the fibre level for distributed plasticity elements

6.3.1 Motivation

Significant progress and compression of damping models have been achieved in the last decades. However, the community has no consensus on how to model damping forces. Hence, new models must be developed to advance in this field. Nonlinear damping models are promising, despite the numerical complexities. For instance, the model proposed by Hall[27] requires initial calculations that may be difficult to perform, especially in large systems with complex architecture. Qian et al.[55] reports that Hall's and other existing nonlinear models cannot be easily implemented in commercial finite element programs. The motivation of this chapter is to propose a nonlinear damping model which allows (i) to have a mathematically consistent formulation, (ii) to limit the damping forces, and (iii) to be easily implemented in existing software using distributed plasticity elements.

Consequently, defining the damping model at the fibre level is suggested following a uniaxial constitutive relation between the damping stress and the strain rates. This constitutive rule is defined according to the initial assumptions made for implementing viscous damping models in dynamic analysis. This section describes the mathematical details of the model.

6.3.2 Derivation of the strain rates using displacement-based elements

The internal deformation of a 2D beam using a linear geometric transformation is expressed in eqs. (6.1), (6.2), and (6.3) at a basic reference system independent of the rigid body motion, in terms of the local displacements (u^{loc}).

$$u_1^{bsc} = u_4^{loc} - u_1^{loc} \tag{6.1}$$

$$u_2^{bsc} = u_3^{loc} - \frac{u_5^{loc} - u_2^{loc}}{l_0} \tag{6.2}$$

$$u_3^{bsc} = u_6^{loc} - \frac{u_5^{loc} - u_2^{loc}}{l_0} \tag{6.3}$$

The subscript numbers are the DoFs in each reference system (gl, loc, and bsc) shown in Figure 6.1. It should be noted that the geometric transformation employs a simply support basic reference system.

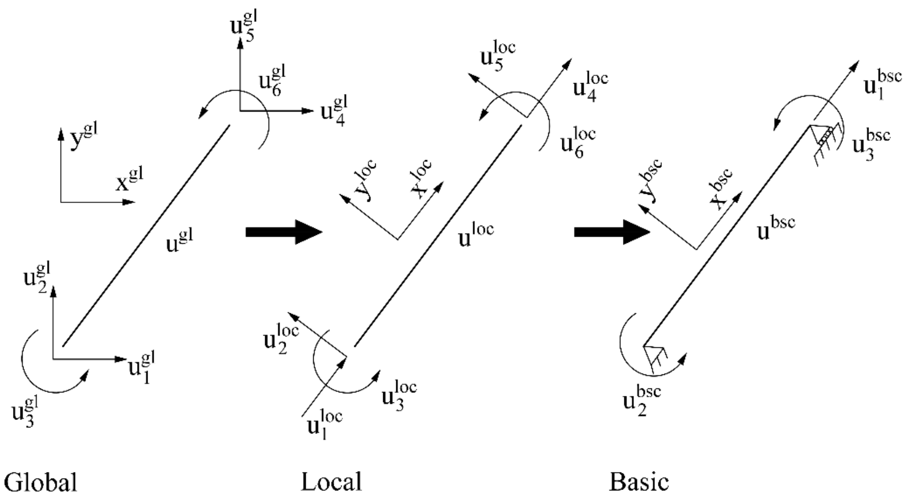

Figure 6.1. Internal deformation of a beam using a linear geometric transformation.

Using a 2D Euler-Bernoulli beam and a displacement-based formulation, the deformations inside the beam are found, assuming that the axial deformation is constant, and the curvature varies linearly.

$$\begin{bmatrix} \varepsilon_0(x) \\ \chi_z(x) \end{bmatrix} = \begin{bmatrix} \frac{1}{l_0} & 0 & 0 \\ 0 & \frac{2x}{l_0^2} + \frac{4\left(\frac{x}{l_0} - 1\right)}{l_0} & \frac{4x}{l_0^2} + \frac{2\left(\frac{x}{l_0} - 1\right)}{l_0} \end{bmatrix} \begin{bmatrix} u_1^{bsc} \\ u_2^{bsc} \\ u_3^{bsc} \end{bmatrix} \tag{6.4}$$

The deformation in the fibre located at a position (x,y) of the cross-section is found from eq. (6.5)

$$\boldsymbol{\varepsilon}(x, y) = [1 \quad -y] \begin{bmatrix} \varepsilon_0(x) \\ \chi_z(x) \end{bmatrix} = \mathbf{B}(y)\mathbf{e}(x) \tag{6.5}$$

The basic velocities are found deriving the basic displacements with respect to time. These deformation rates are also independent of rigid body motion and indicate how fast the basic deformations occur in the system.

$$\dot{\mathbf{u}}^{bsc} = \frac{d(\mathbf{u}^{bsc})}{dt} \tag{6.6}$$

Therefore, eqs. (6.7), (6.8), and (6.9) are found

$$\dot{u}_1^{bsc} = \dot{u}_4^{loc} - \dot{u}_1^{loc} \tag{6.7}$$

$$\dot{u}_2^{bsc} = \dot{u}_3^{loc} - \frac{\dot{u}_5^{loc} - \dot{u}_2^{loc}}{l_0} \tag{6.8}$$

$$\dot{u}_3^{bsc} = \dot{u}_6^{loc} - \frac{\dot{u}_5^{loc} - \dot{u}_2^{loc}}{l_0} \tag{6.9}$$

Eqs. (6.7), (6.8), and (6.9) can also be obtained, using a linear approximation, through eq. (6.10), which is not valid when a corotational geometric transformation is used.

$$\dot{\mathbf{u}}^{bsc} = \boldsymbol{\Gamma}_C^{loc-bsc}\dot{\mathbf{u}}^{loc} \tag{6.10}$$

Where, the compatibility ($\boldsymbol{\Gamma}_C^{loc-bsc}$) and equilibrium relations $\left(\boldsymbol{\Gamma}_E^{bsc-loc}\right)^T$ are expressed by eq. (6.11).

$$\boldsymbol{\Gamma}_C^{loc-bsc} = \left(\boldsymbol{\Gamma}_E^{bsc-loc}\right)^T = \begin{bmatrix} -1 & 0 & 0 & 1 & 0 & 0 \\ 0 & 1/l_0 & 1 & 0 & -1/l_0 & 0 \\ 0 & 1/l_0 & 0 & 0 & -1/l_0 & 1 \end{bmatrix} \tag{6.11}$$

The change of the section deformations with respect to time is obtained by differentiating eq. (6.4)

$$\begin{bmatrix} \dot{\varepsilon}_0(x) \\ \dot{\chi}_z(x) \end{bmatrix} = \begin{bmatrix} \dfrac{1}{l_0} & 0 & 0 \\ 0 & \dfrac{2x}{l_0^2} + \dfrac{4\left(\dfrac{x}{l_0} - 1\right)}{l_0} & \dfrac{4x}{l_0^2} + \dfrac{2\left(\dfrac{x}{l_0} - 1\right)}{l_0} \end{bmatrix} \begin{bmatrix} \dot{u}_1^{bsc} \\ \dot{u}_2^{bsc} \\ \dot{u}_3^{bsc} \end{bmatrix} \tag{6.12}$$

Finally, the strain rates are obtained by differentiating eq. (6.5) with respect to time.

$$[\dot{\varepsilon}(x,y)] = [1 \quad -y] \begin{bmatrix} \dot{\varepsilon}_0(x) \\ \dot{\chi}_z(x) \end{bmatrix} = \mathbf{B}(y)\dot{\mathbf{e}}(x) \tag{6.13}$$

6.3.3 Nonlinear constitutive rule between strain rates and damping stress

In a viscoelastic Kelvin-Voigt beam, the stress in the fibre is defined by eq. (6.14). This model depends on two components: one proportional to young's modulus (E) and one proportional to the viscosity (η) modulus for a linear elastic material and a linear viscous model.

$$\sigma_x(x, y) = E\varepsilon(x, y) + \eta\dot{\varepsilon}(x, y) \quad (6.14)$$

However, this chapter proposes to define the stress in the fibre using two different constitutive rules depending on the strains and strain rates expressed by eq. (6.15), which is the generalisation for nonlinear analysis.

$$\sigma_x(x, y) = f(\varepsilon(x, y)) + g\big(\dot{\varepsilon}(x, y)\big) \quad (6.15)$$

The strain-dependent function is defined with ordinary constitutive rules such as the curves proposed by Kent and Park[94], Mander et al.[88] or Menegotto and Pinto[86]. Due to the lack of experimental evidence, the constitutive rules between strain rates and damping stresses must follow the initial hypotheses to define a viscous damping model in linear SDoF systems. Therefore, a model proportional to the fibre stiffness is defined according to Figure 6.2, the initial slope of the curve is proportional to the young's modulus (E) and the damping parameter (a_1) found using eq. (2.4). Nevertheless, this curve is capped with the limit proposed by Hall[26,27,30], using the yield stress of the material (σ_y) and a damping ratio (ζ) to avoid high damping forces and moments during incursions in the inelastic range, where the strain rates increase dramatically. This limit performs well for homogeneous materials such as steel since it has the same properties in compression and traction. However, in concrete fibres, this limit does not guarantee that the damping forces and moments will be relatively small compared to the material resisting component given that it has different mechanical properties in tension and compression. Therefore, this value must be adjusted, by a factor λ, to consider that under tensile load the concrete fibres will crack and do not contribute to the material resisting forces.

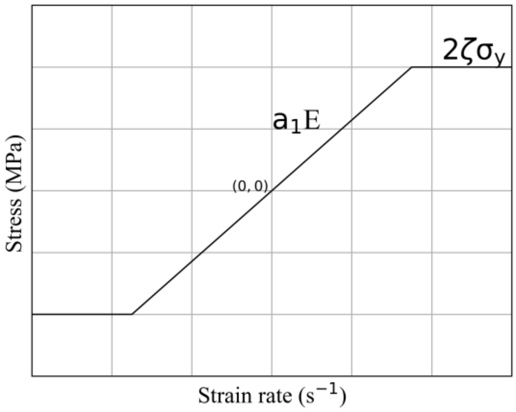

Figure 6.2 Constitutive rule between strain rate and stress

The definition of this curve is performed to keep the damping forces within a reasonable magnitude range and follow the initial premises used by Rayleigh[8] and Wilson and Clough[10] to implement viscous damping models in linear SDoF and MDoF. Besides the constitutive rule presented in Figure 6.2, this chapter also studies two illustrative constitutive rules without limits where the slope is defined with the damping parameter a_1 and the initial modulus of elasticity (FISPD) or the tangent modulus of elasticity of the fiber (FTSPD). The results using these constitutive rules are the same as the global models proportional to the initial stiffness matrix and the tangent stiffness matrix, respectively, when nonlinear geometric effects are not considered. The latter is demonstrated further below. Therefore, the FISPD and FTSPD allow to compare the bilinear constitutive rule proposed with well know models.

6.3.4 Derivation of damping forces and damping matrix at section and element level

Following the determination of the damping stress in the fibres, the damping section forces can be calculated by summing up the contribution of each fibre using eq. (6.16)

$$\mathbf{s}_{\mathrm{d}}(\mathrm{x}) = \int_{\Omega} \mathbf{B}^{\mathrm{T}}(\mathrm{y})\mathrm{g}\big(\dot{\varepsilon}(\mathrm{x},\mathrm{y})\big)\mathrm{d}\Omega \tag{6.16}$$

The element damping forces in the basic reference frame are derived employing the following equation.

$$\mathbf{p}_{\mathrm{d}}^{\mathrm{bsc}} = \int_{0}^{\mathrm{l}_0} \mathbf{H}_{\mathrm{e}}^{\mathrm{t}}(\mathrm{x})\mathbf{s}_{\mathrm{d}}(\mathrm{x})\mathrm{dx} \tag{6.17}$$

The basic damping forces depicted by eqs. (6.17) can be expressed in the local reference system using eq. (6.18)

$$\mathbf{p}_{\mathrm{d}}^{\mathrm{loc}} = \mathbf{\Gamma}_{\mathrm{E}}^{\mathrm{bsc-loc}}\mathbf{p}_{\mathrm{d}}^{\mathrm{bsc}} \tag{6.18}$$

Where $\mathbf{\Gamma}_{\mathrm{E}}^{\mathrm{bsc-loc}}$ is the equilibrium relations presented in eq. (6.11)

$$\frac{\partial \mathbf{u}^{\mathrm{bsc}}}{\partial \mathbf{u}^{\mathrm{loc}}} = \mathbf{\Gamma}_{\mathrm{C}}^{\mathrm{loc-bsc}} = \left(\mathbf{\Gamma}_{\mathrm{E}}^{\mathrm{bsc-loc}}\right)^{\mathrm{T}} \tag{6.19}$$

The element global forces are then found with a rotation matrix ($\mathbf{\Gamma}_{\mathrm{C}}^{\mathrm{gl-loc}} = \left(\mathbf{\Gamma}_{\mathrm{E}}^{\mathrm{loc-gl}}\right)^{\mathrm{T}}$) considering the angle (θ) between the global and the local reference systems.

The damping matrix is derived to define the Jacobian used in numerical methods such as Newton-Raphson. The relationship $\frac{\partial \mathbf{p}_{\mathrm{d}}^{\mathrm{bsc}}}{\partial \dot{\mathbf{u}}^{\mathrm{bsc}}}$ is expressed by eq. (6.20).

$$\mathbf{c}^{\mathrm{bsc}}(\mathrm{x}) = \frac{\partial \mathbf{p}_{\mathrm{d}}^{\mathrm{bsc}}}{\partial \dot{\mathbf{u}}^{\mathrm{bsc}}} = \int_{\mathrm{l}_0} \mathbf{H}_{\mathrm{e}}^{\mathrm{T}}(\mathrm{x})\mathbf{c}^{\mathrm{sec}}\mathbf{H}_{\mathrm{e}}(\mathrm{x})\mathrm{dx} \tag{6.20}$$

Where the damping matrix of the sections ($\mathbf{c}^{\mathrm{sec}}$) is calculated according to eq. (6.21)

$$\mathbf{c}^{\mathrm{sec}}(\mathrm{x}) = \frac{\partial \mathbf{s}_{\mathrm{d}}(\mathrm{x})}{\partial \dot{\mathbf{e}}(\mathrm{x})} = \int_{\Omega} \mathbf{B}^{\mathrm{T}}(\mathrm{y}) \frac{\partial \mathrm{g}(\dot{\varepsilon}(\mathrm{x},\mathrm{y}))}{\partial \dot{\mathbf{e}}(\mathrm{x})} \mathrm{d}\Omega \tag{6.21}$$

The relationship $\frac{\partial \mathrm{g}(\dot{\varepsilon}(\mathrm{x},\mathrm{y}))}{\partial \dot{\mathbf{e}}(\mathrm{x})}$ is unknown, so the chain rule is applied.

$$\mathbf{c}^{sec}(x) = \int_{\Omega} \mathbf{B}^T(y) \frac{\partial g(\dot{\varepsilon}(x,y))}{\partial \dot{\varepsilon}(x,y)} \frac{\partial \dot{\varepsilon}(x,y)}{\partial \dot{\mathbf{e}}(x)} d\Omega \tag{6.22}$$

$\frac{\partial \dot{\varepsilon}(x,y)}{\partial \dot{\mathbf{e}}(x)}$ correspond to the matrix $\mathbf{B}(y)$

6.3.5 Implementation of the fibre damping model using the Newmark beta numerical integration method

The damping model is implemented using the Newmark method (Newmark 1959), which established a generic procedure to solve any dynamic problem provided by eqs. (6.23) and (6.24).

$$\dot{\mathbf{U}}_{n+1} = \frac{\gamma}{\beta\Delta}(\mathbf{U}_{n+1} - \mathbf{U}_n) + \left(1 - \frac{\gamma}{\beta}\right)\dot{\mathbf{U}}_n + \Delta t\left(1 - \frac{\gamma}{2\beta}\right)\ddot{\mathbf{U}}_n \tag{6.23}$$

$$\ddot{\mathbf{U}}_{n+1} = \frac{1}{\beta\Delta t^2}(\mathbf{U}_{n+1} - \mathbf{U}_n) + \frac{1}{\beta\Delta t}\dot{\mathbf{U}}_n - \left(\frac{1}{2\beta} - 1\right)\ddot{\mathbf{U}}_n \tag{6.24}$$

Where $\mathbf{U}, \dot{\mathbf{U}}, \text{and } \ddot{\mathbf{U}}$ are the relative displacement, velocity and acceleration vectors, respectively. This method aims to find these vectors at time step n + 1 that satisfy eq. (6.25).

$$\widehat{\mathbf{P}}_{s,n+1} = \mathbf{F}_{n+1} \tag{6.25}$$

$\mathbf{F}_{n+1}$ is the vector of applied external forces and $\widehat{\mathbf{P}}_{s,n+1}$ is the vector of resisting forces of the system defined by eq. (6.26), including the inertia, damping and material components.

$$\widehat{\mathbf{P}}_{s,n+1} = \mathbf{M} \cdot \ddot{\mathbf{U}}_{n+1} + \mathbf{P}_{d,n+1} + \mathbf{P}_{m,n+1} \tag{6.26}$$

Eq. (6.26) is expanded, utilising the Taylor series interpreting the resisting forces as a function of $\mathbf{U}_{n+1}$ and only the first two terms are considered[54].

$$\widehat{\mathbf{P}}_{s,n+1}^{k+1} \approx \widehat{\mathbf{P}}_{s,n+1}^{k} + \frac{\partial \widehat{\mathbf{P}}s}{\partial \mathbf{U}_{n+1}} \cdot \Delta\mathbf{U}^k = \mathbf{F}_{n+1} \tag{6.27}$$

$\widehat{\mathbf{P}}_s$ is differentiated at global displacements $\mathbf{U}_{n+1}$

$$\frac{\partial \mathbf{P}_d}{\partial \mathbf{U}_{n+1}} = \mathbf{M} \cdot \frac{\partial \ddot{\mathbf{U}}_n}{\partial \mathbf{U}_{n+1}} + \frac{\partial \mathbf{P}_d}{\partial \mathbf{U}_{n+1}} + \frac{\partial \mathbf{P}_m}{\partial \mathbf{U}_{n+1}} \tag{6.28}$$

Where the derivative in the inertia term is found deriving eq. (6.24) with respect to $\mathbf{U}_{n+1}$. The $\frac{\partial \mathbf{P}_d}{\partial \mathbf{U}_{n+1}}$ is found in eq. (6.29) at the local reference system.

$$\frac{\partial \mathbf{p}_d^{loc}}{\partial \mathbf{u}_{n+1}^{loc}} = \frac{\partial \mathbf{\Gamma}_E^{bsc-loc}}{\partial \mathbf{u}_{n+1}^{loc}} \cdot \mathbf{p}_d^{bsc} + \mathbf{\Gamma}_E^{bsc-loc} \cdot \frac{\partial \mathbf{p}_d^{bsc}}{\partial \mathbf{u}_{n+1}^{loc}} \tag{6.29}$$

The chain rule is used in eq. (6.30) to find the unknown relation $\frac{\partial \mathbf{p}_d^{bsc}}{\partial \mathbf{u}_{n+1}^{loc}}$

$$\frac{\partial \mathbf{p}_d^{bsc}}{\partial \mathbf{u}_{n+1}^{loc}} = \frac{\partial \mathbf{p}_d^{bsc}}{\partial \dot{\mathbf{u}}^{bsc}} \cdot \frac{\partial \dot{\mathbf{u}}^{bsc}}{\partial \dot{\mathbf{u}}^{loc}} \cdot \frac{\partial \dot{\mathbf{u}}^{loc}}{\partial \mathbf{u}_{n+1}^{loc}} \tag{6.30}$$

where $\frac{\partial \dot{\mathbf{u}}^{loc}}{\partial \mathbf{u}_{n+1}^{loc}}$ is derived from eq. (6.23). The other terms were derived before.

$$\frac{\partial \dot{\mathbf{u}}^{loc}}{\partial \mathbf{u}_{n+1}^{loc}} = \frac{\Upsilon}{\beta \Delta t} \tag{6.31}$$

The $\frac{\partial \mathbf{P}_m}{\partial \mathbf{U}_{n+1}}$ is expressed by eq. (6.32) in the local reference system

$$\frac{\partial \mathbf{p}_m^{loc}}{\partial \mathbf{u}_{n+1}^{loc}} = \frac{\partial (\mathbf{\Gamma}_E^{bsc-loc})}{\partial \mathbf{u}_{n+1}^{loc}} \cdot \mathbf{p}_m^{bsc} + \mathbf{\Gamma}_E^{bsc-loc} \cdot \frac{\partial (\mathbf{p}_m^{bsc})}{\partial \mathbf{u}_{n+1}^{loc}} \tag{6.32}$$

The chain rule is used to find the relation $\frac{\partial (\mathbf{p}_m^{bsc})}{\partial \mathbf{u}_{n+1}^{loc}}$

$$\frac{\partial \mathbf{p}_m^{bsc}}{\partial \mathbf{u}_{n+1}^{loc}} = \frac{\partial \mathbf{p}_m^{bsc}}{\partial \mathbf{u}_{n+1}^{bsc}} \cdot \frac{\partial \mathbf{u}_{n+1}^{bsc}}{\partial \mathbf{u}_{n+1}^{loc}} \tag{6.33}$$

The first and second terms on the right side of eqs. (6.29) and (6.32) are the geometric and material components, respectively. The geometric component is a matrix filled with zeros with a linear geometric transformation since equilibrium is formulated in the undeformed configuration.

6.3.6 Global vs fibre based initial and tangent stiffness proportional damping

The main objective of this chapter is to show that a bilinear constitutive rule between damping stress and strain rate can be defined. This is advantageous since it avoids to have high damping forces or prevents them from decaying when the structure yields. The problems mentioned are the main disadvantages of the damping models proportional to the initial and tangent stiffness matrix, respectively. However, it should be clarified that the models implemented in the fibre using a constitutive rule proportional to the initial and tangent modulus of elasticity are equivalent to the models proportional to the initial and tangent stiffness matrix when nonlinear geometric effects are not considered. This is demonstrated mathematically in this section. Numerically, the damping forces in the section expressed by eq. (6.16) are calculated using the Newton-Cotes method based on the following sum that considers a linear constitutive rule with a slope equal to the initial or tangent modulus of elasticity (E_v) and a damping parameter a_1 for each fiber i.

$$\mathbf{s}_d(x) = \sum_{i=1}^{n} A_i \mathbf{B_i^T}(y) g\big(\dot{\varepsilon}_i(x,y)\big) = \sum_{i=1}^{n} A_i \mathbf{B_i^T}(y) a_1 E_{Vi} \mathbf{B_i}(y) \dot{\mathbf{e}}(x) \tag{6.34}$$

The damping matrix of the section presented by eq. Figure 6.21 is evaluated numerically by means of the following expression.

$$\mathbf{c}_v^{sec}(x) = a_1 \mathbf{k}_v^{sec} = \sum_{\mathbf{i=1}}^{\mathbf{n}} A_i \mathbf{B_i^T}(y) a_1 E_{Vi} \mathbf{B_i}(y) \tag{6.35}$$

The $\mathbf{k}_v^{sec}$ is the initial or tangent stiffness matrix of the section. Therefore, the section damping forces are defined by eq. (6.36)

$$\mathbf{s}_d(x) = a_1 \mathbf{k}_v^{sec} \dot{\mathbf{e}}(x) \tag{6.36}$$

Similarly, the element damping forces presented in eq. Figure 6.20 are evaluated using the Gauss-Legendre quadrature according to the following equation, assuming a linear constitutive relation between damping stress and strain rate

$$\mathbf{p}_{\mathrm{d}}^{\mathrm{bsc}} = \sum_{\mathrm{j=1}}^{\mathrm{n}} \mathrm{w_j} \frac{\mathrm{l_0}}{2} \mathbf{H}_{\mathrm{j}}^{\mathrm{T}} \mathbf{s}_{\mathrm{d,j}}(\mathrm{x}) = \sum_{\mathrm{j=1}}^{\mathrm{n}} \mathrm{w_j} \frac{\mathrm{l_0}}{2} \mathbf{H}_{\mathrm{j}}^{\mathrm{T}} \mathrm{a_1} \mathbf{k}_{\mathrm{v,j}}^{\mathrm{sec}} \mathbf{H}_{\mathrm{j}} \dot{\mathbf{u}}^{\mathrm{bsc}} \tag{6.37}$$

Where the $\mathrm{w_j}$ are the weights of the gaussian quadrature. The damping matrix at the element level is evaluated numerically from the following eq. (6.38)

$$\mathbf{c}^{\mathrm{bsc}} = \mathrm{a_1} \mathbf{k}_{\mathrm{v}}^{\mathrm{bsc}} = \sum_{j=1}^{n} \mathrm{w_j} \frac{\mathrm{l_0}}{2} \mathbf{H}_{\mathrm{j}}^{\mathrm{T}} \mathrm{a_1} \mathbf{k}_{\mathrm{v,j}}^{\mathrm{sec}} \mathbf{H}_{\mathrm{j}} \tag{6.38}$$

The $\mathbf{k}_{\mathrm{v}}^{\mathrm{bsc}}$ is the initial or tangent stiffness matrix at the basic reference system. Therefore, the damping forces at the basic level are calculated with eq. (6.39)

$$\mathbf{p}_{\mathrm{d}}^{\mathrm{bsc}} = \mathrm{a_1} \mathbf{k}_{\mathrm{v}}^{\mathrm{bsc}} \dot{\mathbf{u}}^{\mathrm{bsc}} \tag{6.39}$$

Next, the damping forces at the global level are found from the following expression using the equilibrium relations.

$$\mathbf{p}_{\mathrm{d}}^{\mathrm{gl}} = \mathbf{\Gamma}_{\mathrm{E}}^{\mathrm{loc-gl}} \mathbf{\Gamma}_{\mathrm{E}}^{\mathrm{bsc-loc}} \mathbf{p}_{\mathrm{d}}^{\mathrm{bsc}} \tag{6.40}$$

When a linear geometric transformation is used the following expressions are valid, however, when a corotational geometric transformation is used eq. (6.42) is not valid. Therefore, the models proportional to the global initial or tangent stiffness and defined in the fiber are not the same.

$$\dot{\mathbf{u}}^{\mathrm{loc}} = \mathbf{\Gamma}_{\mathrm{c}}^{\mathrm{gl-loc}} \dot{\mathbf{u}}^{\mathrm{gl}} \tag{6.41}$$

$$\dot{\mathbf{u}}^{\mathrm{bsc}} = \mathbf{\Gamma}_{\mathrm{c}}^{\mathrm{loc-bsc}} \dot{\mathbf{u}}^{\mathrm{loc}} \tag{6.42}$$

Replacing eqs. (6.39), (6.41), and (6.42) in eq. (6.40), the next equation is obtained

$$\mathbf{p}_{\mathrm{d}}^{\mathrm{gl}} = \mathbf{\Gamma}_{\mathrm{E}}^{\mathrm{loc-gl}} \mathbf{\Gamma}_{\mathrm{E}}^{\mathrm{bsc-loc}} \mathrm{a_1} \mathbf{k}_{\mathrm{v}}^{\mathrm{bsc}} \mathbf{\Gamma}_{\mathrm{c}}^{\mathrm{loc-bsc}} \mathbf{\Gamma}_{\mathrm{c}}^{\mathrm{gl-loc}} \dot{\mathbf{u}}^{\mathrm{gl}} = \mathrm{a_1} \mathbf{k}_{\mathrm{v}}^{\mathrm{gl}} \dot{\mathbf{u}}^{\mathrm{gl}} \tag{6.43}$$

Where $\mathbf{\Gamma}_{\mathrm{E}}^{\mathrm{loc-gl}} \mathbf{\Gamma}_{\mathrm{E}}^{\mathrm{bsc-loc}} \mathrm{a_1} \mathbf{k}_{\mathrm{v}}^{\mathrm{bsc}} \mathbf{\Gamma}_{\mathrm{c}}^{\mathrm{loc-bsc}} \mathbf{\Gamma}_{\mathrm{c}}^{\mathrm{gl-loc}} \dot{\mathbf{u}}^{\mathrm{gl}}$ is the initial or tangent element stiffness matrix at the global reference system ($\mathbf{k}_{\mathrm{v}}^{\mathrm{gl}}$), when a linear geometric transformation is used. The later means that the global and fiber models proportional to the initial or tangent stiffness are equivalent. Therefore, the FISPD and FTSPD are used to compare the performance of the model using the constitutive rule presented in Figure 6.2.

6.4 Case studies

This section presents two case studies where the proposed model is tested and compared with existing models in the literature. They correspond to the reinforced concrete column tested by Petrini et al.[66] and a steel column subjected to a ground motion record. Each case study comprises several nonlinear dynamic analyses using the damping models listed in Table 6.1 The first corresponds to the approach proposed in this paper, the next two are defined proportional to the initial and tangent stiffness of the fibre for illustrative purposes. As explained before, the FISPD and FTSPD are equivalent to TISPD and TTSPD when nonlinear geometric effects are not considered. Therefore, the FISPD and FTSPD allow to compare the performance of the first damping model proposed at the section level. At the end of this subchapter, a sensitivity analysis is presented where different damping stress limits are imposed to observe their influence on the response of the structure.

The numerical simulations were carried out in the finite element program developed by the author. This program was developed in Python using object-oriented programming and a singleton pattern structure. The program is capable of performing static and dynamic nonlinear analysis of 2D and 3D structures. The software has been compared with experimental tests and programs such as Seismostruct[59] and Open-Sees[49], which are not reported due to space constraints.

Table 6.1 Damping models analysed and implemented in this chapter.

Name damping model	Abbreviation
Fibre initial stiffness proportional damping bilinear	FISPD_bilinear
Fibre initial stiffness proportional damping	FISPD
Fibre tangent stiffness proportional damping	FTSPD
Total initial stiffness proportional damping	TISPD
Total tangent stiffness proportional damping	TTSPD

6.4.1 RC column tested by Petrini et al.[66]

This section compares the proposed damping model with the experimental test conducted by Petrini et al.[66] at EUCENTRE. The parameters of the numerical simulation were defined following the description of Petrini et al.[66]

The specimen was originally built with the dimensions and hollow circular cross-section presented in Figure 6.3. The bridge pier had a mass at the top of 7.8 Tons. The column was modelled with six frame elements: the yield penetration in the foundation is considered using a 110 mm elastic element, the following four members are modelled using inelastic displacement-based elements and the top part is modelled as a rigid zone through a 440 mm elastic element. The mass of the column is neglected since it does not represent a significant percentage of the upper mass. Nonlinear geometrical effects are not considered, thus a linear geometric transformation is used. The cross-section of the inelastic elements was discretised, as shown in Figure 6.3. The concrete constitutive rule corresponds to the model of Mander et al.[88] with the following properties for unconfined concrete: $f'c = 39$ MPa and $\varepsilon_c = 0.0025$. The confinement factor is taken as 1.35 at the base, which has more stirrups and 1.18 for the upper part. The steel fibres were defined with the model of Menegotto and Pinto [86]. The following parameters were measured experimentally: $f_y = 514$ MPa, $E = 210$ GPa, and $b = 0.004$. The remaining parameters defined by Menegotto and Pinto[86] are: $A0 = 20$, $A1 = 18.5$, $A2 = 0.15$, and $A3 = A4 = 0$.

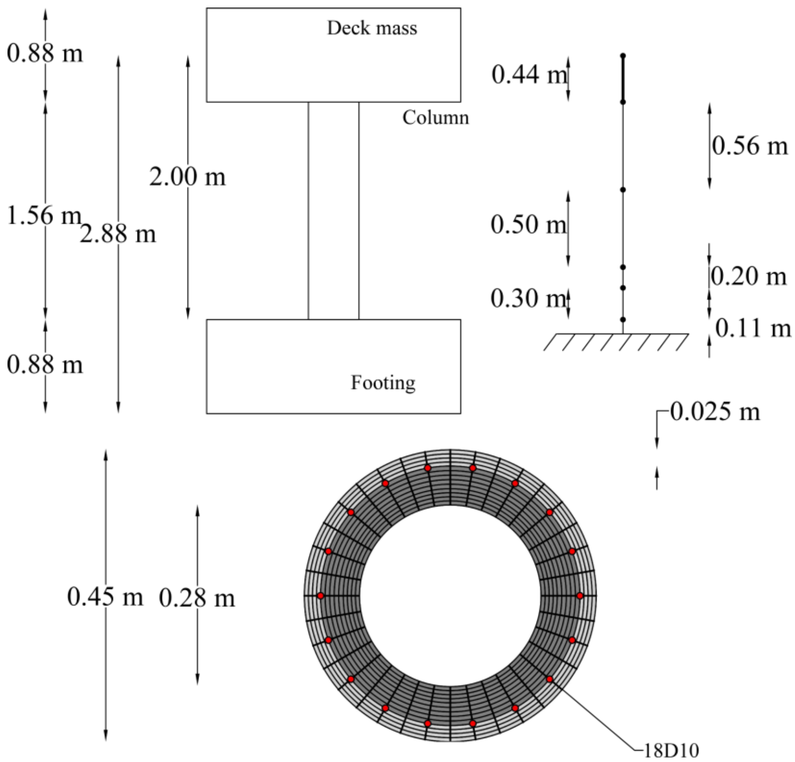

Figure 6.3. Geometric dimensions and schematic detail of the experimental test presented in Petrini et al. (2008)

The column is subjected to the scaled horizontal component of the ground motion record of the Morgan Hill earthquake, downloaded from the PEER Strong Motion Database[87] and shown in Figure 6.4 (1984, station: Halls Valley). All the damping models presented in Table 6.1 were defined with a damping ratio of 5%, which is the value proposed by Petrini et al. [66].

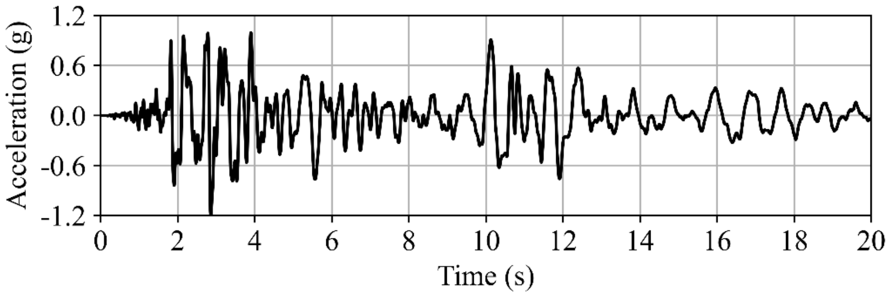

Figure 6.4. Ground motion record of the Morgan Hill earthquake (1984, Halls Valley, M = 6.2, PGA = 0.15g) amplified up to a PGA = 1.2 g

The moment-curvature diagram of the cross-section is presented in Figure 6.5 (a), where the maximum moment reached is 160 kNm considering the axial load of the column. The damping moment vs curvature rate diagram can also be found using fibre models. For instance, Figure 6.5 (b) introduces two curves showing these diagrams. One uses a limit of damping stresses in the fibres equal to $2\zeta\sigma_y$, see the legend. However, this curve has a maximum damping moment of 60 kN.m which is high compared to the section capacity shown in Figure 6.5 (a). As explained before, the latter is caused by the fact that concrete is a non-homogeneous material and does not have the same compressive and tensile strength. Therefore, the maximum damping stress is limited to $2\lambda\zeta\sigma_y$ in all fibres to guarantee that the damping moment will be in an acceptable range of magnitude compared to the material capacity. The lambda value is found by multiplying the maximum material moment of the section (160 kN.m) by 2ζ and dividing the value by the maximum damping moment of the first curve (60 kN.m). Thus, the lambda gives 0.267. Finally, the other curve is obtained, which presents a damping moment equal to 2ζ the yield moment of the cross-section. Again, this calibration is done to avoid high damping forces since all fibres contribute to the damping moment since they are proportional to strain rates.

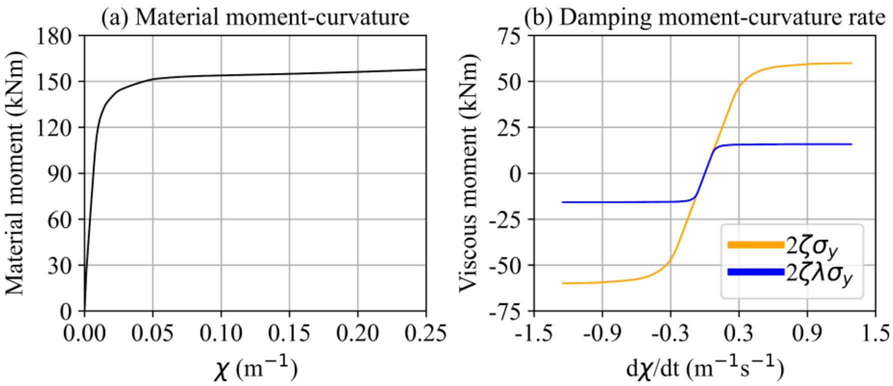

Figure 6.5. (a) Moment-curvature and (b) damping moment-curvature rate of the cross-section.

The history of horizontal displacement, using the damping models indicated in Table 6.1, is shown in Figure 6.6. The FTSPD and FISPD_bilinear models predict the experimental results better than FISPD, as they do not exhibit disproportionately large damping forces when the structure yields. However, the FISPD_bilinear model has a larger residual deformation than the FTSPD, which is more plausible.

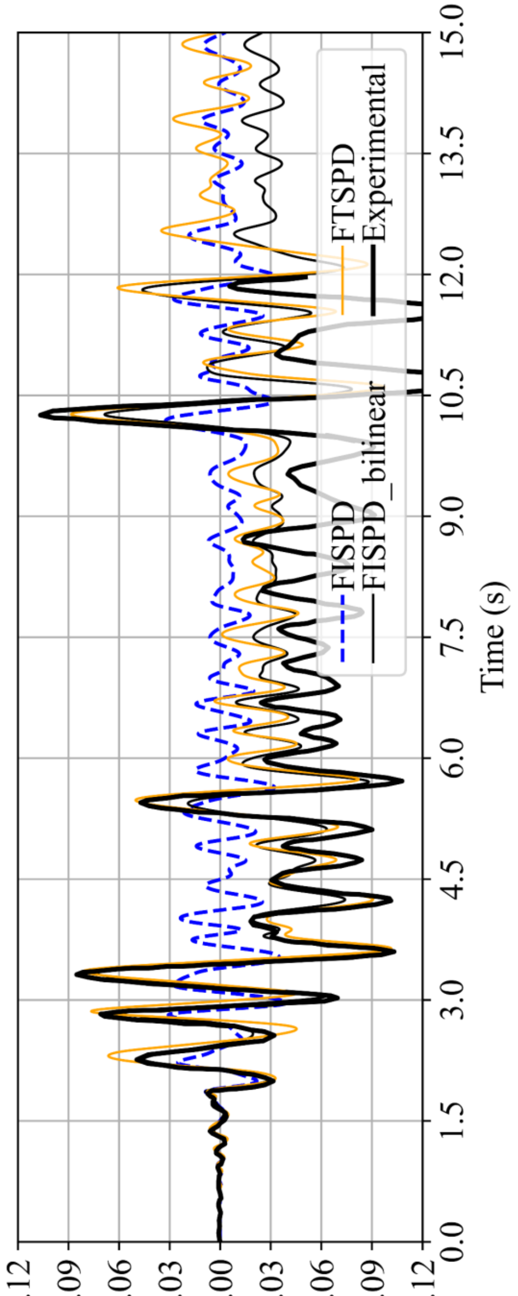

Figure 6.6. Experimental comparison and predicted displacement using the fibre damping models

The viscous moment vs curvature rate and the history of viscous moments are presented in Figure 6.7 and Figure 6.8. The results show that the FISPD_bilinear has damping moments in acceptable ranges, while the FISPD or FTSPD models have high or low values, respectively. The FISPD achieves viscous damping moments close to 80% of the yield moment. Therefore, the structure would present an overstrength that has no justification and causes the displacements to be relatively small. The FTSPD model shows low damping moments after the structure yields or sections crack because the constitutive rule is proportional to the tangent modulus of elasticity. In reinforced concrete structures, the models proportional to the tangent stiffness present serious disadvantages and losses in energy dissipation capacity since the damping parameter is commonly defined with the system's initial frequency, which is high compared to the frequency of the cracked structure. This causes the damping forces to be meagre after incursions into the inelastic range, where cracking and cover loss occur. When the structure yields, the damping forces disappear or are negative since the stiffness is close to or less than zero. For instance, Figure 6.7 (b) shows negative viscous damping moments for positive curvature rates, and Figure 6.8 shows that the magnitude of the damping moments are relatively small. The FISPD_bilinear model presents a mostly bilinear behaviour, as shown in Figure 6.7 (b) and Figure 6.8. Still, it is not perfect, especially at the beginning of the analysis, for several reasons (i) the section is composed of two materials with different mechanical properties, (ii) the concrete cracks in the section, and (iii) the influence of axial load. Nevertheless, all fibres were checked and behaved according to the defined constitutive rule; this information is not shown due to space constraints. The main advantage of this model in comparison with the other two lies in the fact that the damping forces have reasonable values throughout the analysis, do not take on extreme values and do not disappear when the structure enters the inelastic range.

In terms of energy dissipation, Figure 6.9 presents the cumulative energy introduced by the ground motion record (E_I), the cumulative energy dissipated by the damping forces (E_D), and the cumulative energy dissipated by the material (E_M), respectively. Figure 6.9 (b) indicates that the FISPD model dissipates the most energy, followed by FISPD_bilinear and FTSPD. Therefore, the order in Figure 6.9 (c) is the opposite.

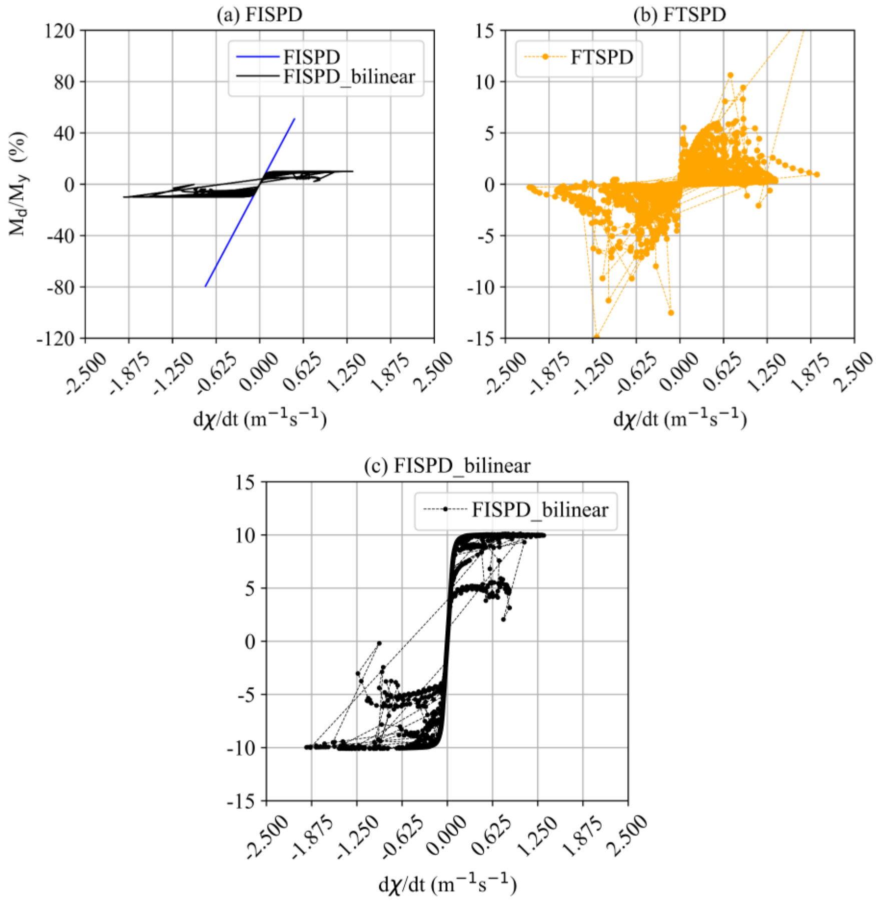

Figure 6.7. Viscous moment vs curvature rate for the different fibre damping models: (a) FISPD and FISPD_bilinear, (b) FTSPD, and (c) FISPD_bilinear

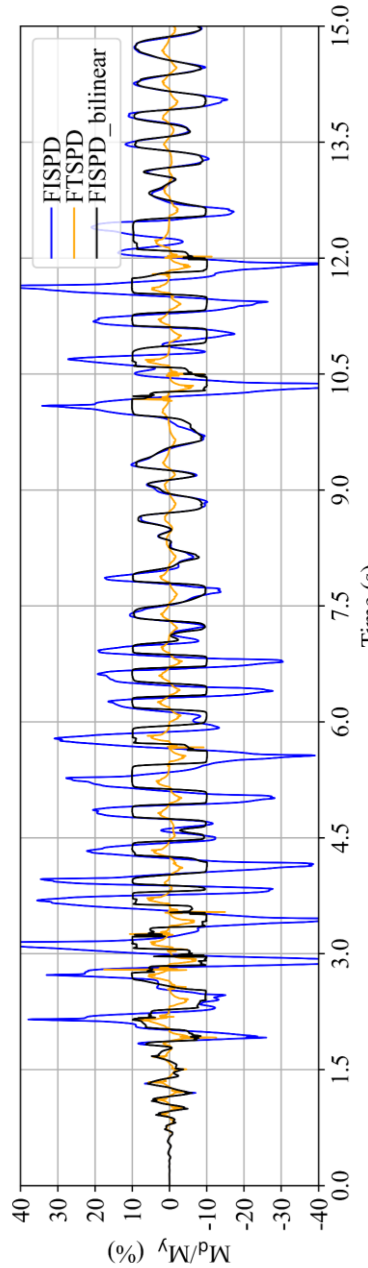

Figure 6.8. history of viscous moments for the different damping models

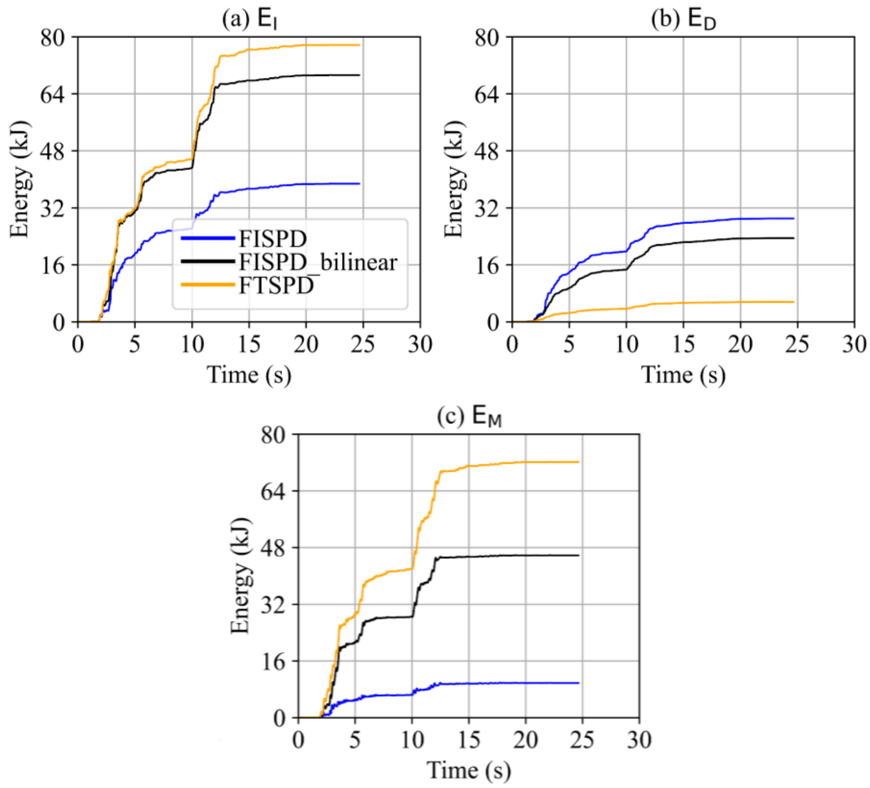

Figure 6.9. (a) Cumulative energy input by the ground motion record, (b) cumulative energy dissipated by the damping models and (c) cumulative energy dissipated by constitutive rules of the material.

The history of displacements using the global and fibre damping models is exhibited in Figure 6.10. As demonstrated before, the fibre models proportional to the initial and tangent modulus of elasticity present the same results as their global counterparts proportional to the initial and tangent stiffness matrix, precisely when a linear geometric transformation is used. This equivalence is not applicable when a corotational geometric transformation is used because eq. (6.42) is invalid. This is important since the models proportional to the initial and tangent stiffness matrix are widely known by the community and serve to compare the performance of the bilinear constitutive rule presented in this work.

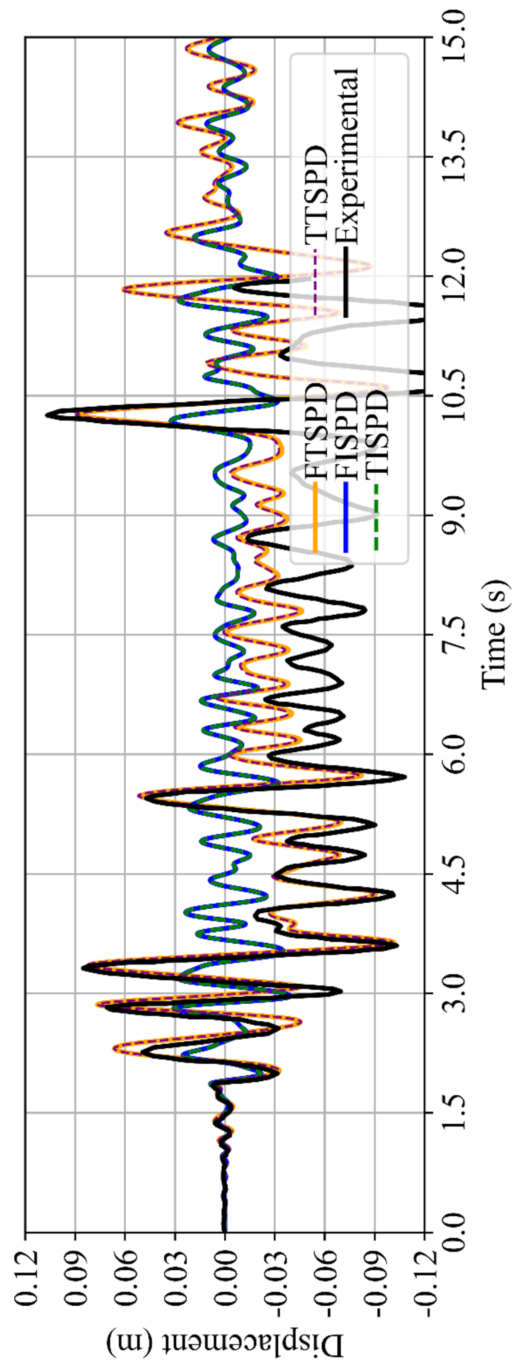

Figure 6.10. Experimental comparison and predicted displacement of the time history test using the global and fibre models.

The models implemented in the fibre have a higher computational cost since they require the calculation of strain rates and the integration of the response of each fibre to obtain the damping forces at the global level. The rationale for using fibre models is that they allow greater flexibility and control, given that a nonlinear constitutive rule can be defined. Thus, the high damping forces presented by the damping model proportional to the initial stiffness matrix can be limited and prevents the damping forces from dropping or becoming negative when the structure yields, as in the case of the damping model proportional to the tangent stiffness matrix. Table 6.2 shows that these models significantly increase the computational cost; however, during the last decades, this has ceased to be a significant limitation due to computing and hardware availability advances. Finally, it should be noted that the author's program was developed in Python, which is slower than other programming languages such as C++ and Pascal, where OpenSees [49] and Seismostruct [59] were developed, respectively.

Table 6.2. Computational analysis for the reinforced concrete structure

Model	Computational time (s)	Average iterations per step
FISPD_bilinear	3183	2.9
FISPD	2695	2.5
FTSPD	2502	2.0
TISPD	1006	1.6
TTSPD	1113	1.7

6.4.2 Nonlinear dynamic analysis of a simple inelastic steel column

This case study corresponds to a steel column with the geometrical properties and cross-section shown in Figure 6.11. The column has a concentrated mass at the top equivalent to 5 tons in the vertical and horizontal DoFs. The structure is modelled using four displacement-based elements with the distribution presented. Each element is defined with two integration points where the cross-section presented in Figure 6.11 is depicted. The cross-section is discretised into two fibres in the flanges and 40 in the web. The fibres have the constitutive rule of Menegotto and Pinto[86], using the following parameters: fy = 355 MPa, E = 200 GPa, b=1e^{-7}, A0 = 20, A1=18.5, A2=0.15, and A3 = A4 = 0.

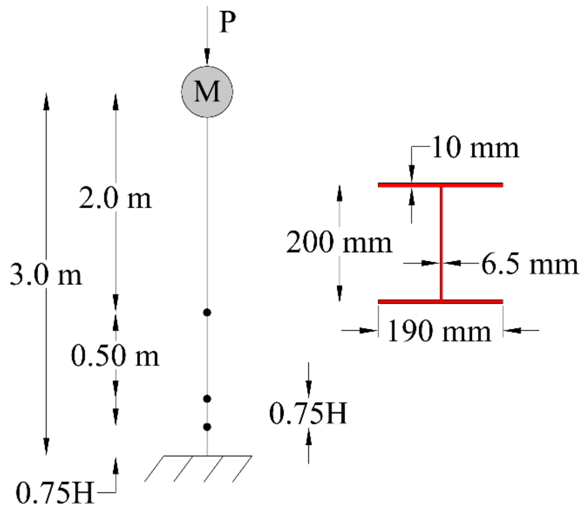

Figure 6.11. Geometric dimensions of a simple steel column with its cross-section

The column is subjected to an incremental sinusoidal ground motion record presented in Figure 6.12; the frequency of the signal corresponds to the horizontal natural frequency of the system. All damping models were defined with a damping ratio of 2%.

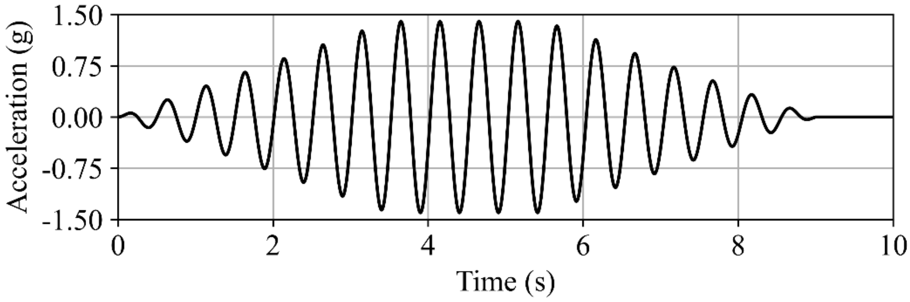

Figure 6.12. Incremental sinusoidal ground motion record

The moment-curvature diagram of the steel section composing the structure is presented in Figure 6.13 (a). The maximum moment reached by the cross-section is 145 kNm, considering the axial load due to the mass at the top. Furthermore, the viscous moment vs rate of curvature is shown in Figure 6.13 (b). Unlike the previous case, the section uses a homogeneous material with the same properties in tension as in compression. Therefore, it is unnecessary to calibrate the limit of the fibre-damping stress. Consequently, the maximum damping moment of the cross-section is equal to $2\zeta M_y$.

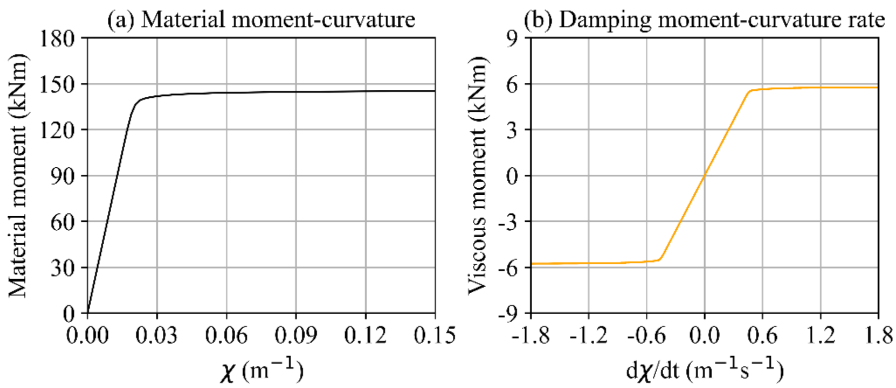

Figure 6.13. (a) Moment-curvature and (b) damping moment-curvature rate of the cross-section.

Figure 6.14 depicts the displacement predicted using the models defined in the fibre. The difference between the displacements is not as significant as in the previous case since steel is a homogeneous material, has lower stiffness losses after inelastic incursions, and the damping ratio is significantly smaller. However, FTSPD has the largest residual displacements, followed by FISPD_bilinear and FISPD models.

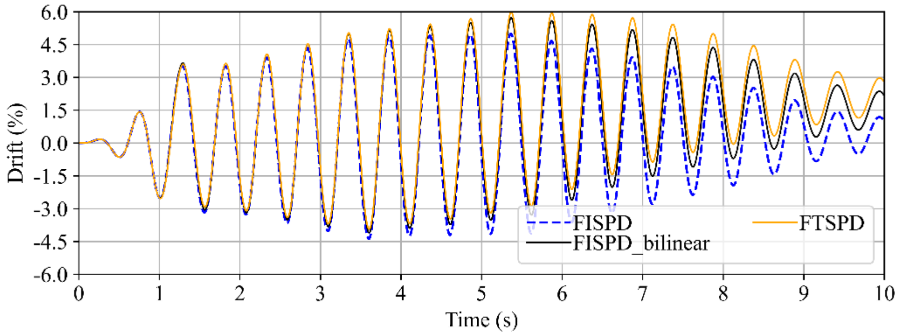

Figure 6.14. Numerical comparison of predicted displacement using the fibre damping models

The damping moment and curvature rate of the section at the base using the three fibre-based models are presented in Figure 6.15. Also, the history of viscous damping moments is shown in Figure 6.16. The FISPD achieves damping moments close to 20% of the yielding moment of the section, which are difficult to justify considering the damping ratio defined. Nonetheless, these damping moments are proportionally smaller than those the previous study case achieved. The FTSPD model exhibits hysteresis, and the magnitude of the damping moments reaches 8% of the yielding moment, which is moderate considering the defined damping ratio, but they decay immediately when the structure yields. Therefore, the history of damping moments has a triangular shape response that has been constantly criticized from a conceptual point of view. Finally, the proposed FISPD_bilinear model presents damping moments in a reasonable magnitude range and does not decay when the structure yields. The latter is the main rationale to justify this model.

In terms of cumulative energy dissipated, it is noted in Figure 6.17 (b) that the model which dissipates the most energy is FISPD, followed by FISPD_bilinear and FTSPD. The latter is reflected in the cumulative energy dissipated by the constitutive rules of the material where the order is inverted. The difference in terms of energy dissipation between the FTSPD and FISPD_bilinear models is smaller than in the first case study since the section uses a homogeneous material that does not present significant stiffness changes after incursions into the inelastic range. Additionally, as shown in Figure 6.16, the area under the curve of the history of damping moments is similar due to the fact that the FTSPD presents higher damping forces than the FISPD_bilinear, but when the structure yields the FTSPD moments disappear, while the FISPD_bilinear moments remain constant.

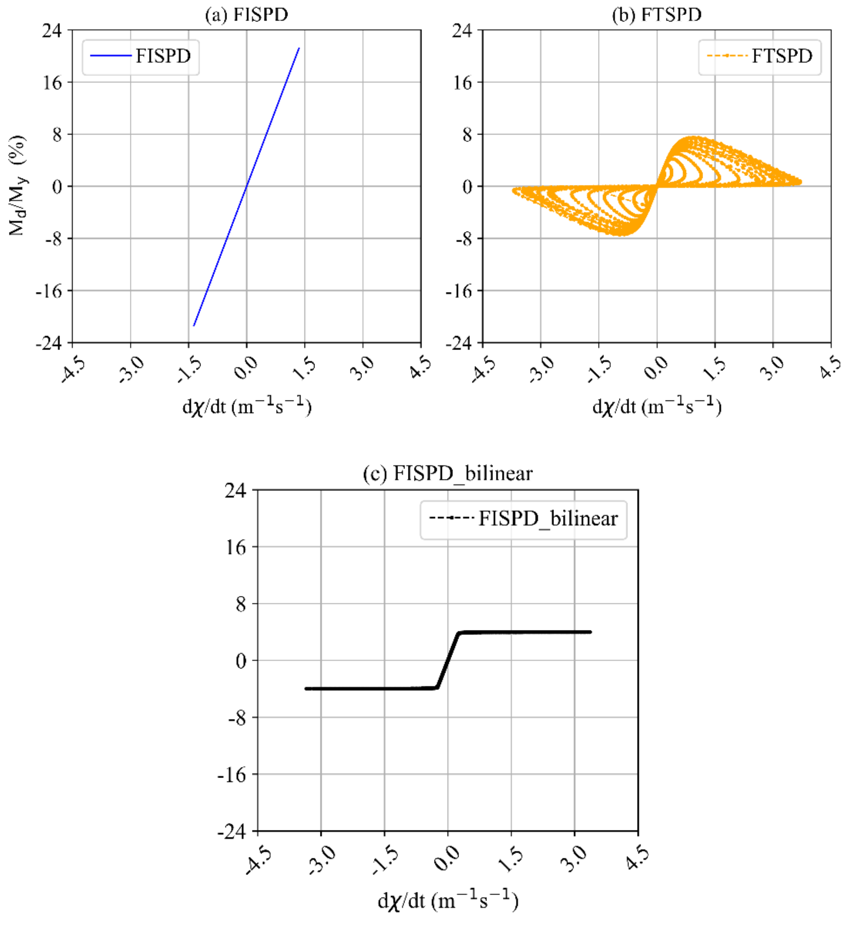

Figure 6.15. Viscous moments vs curvature rates for the different fibre damping models: (a) FISPD, (b) FTSPD, and (c) FISPD_bilinear

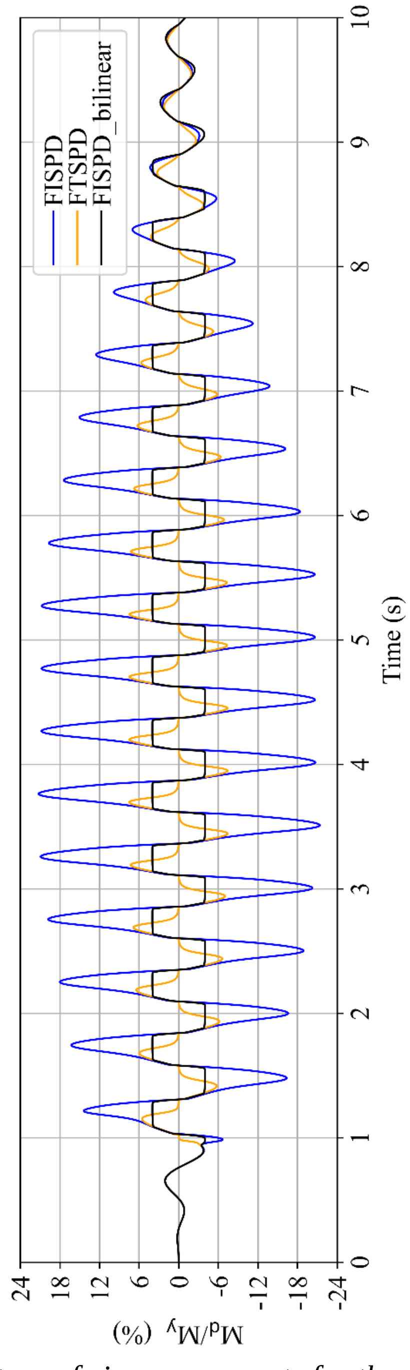

Figure 6.16. History of viscous moments for the different fibre viscous damping models

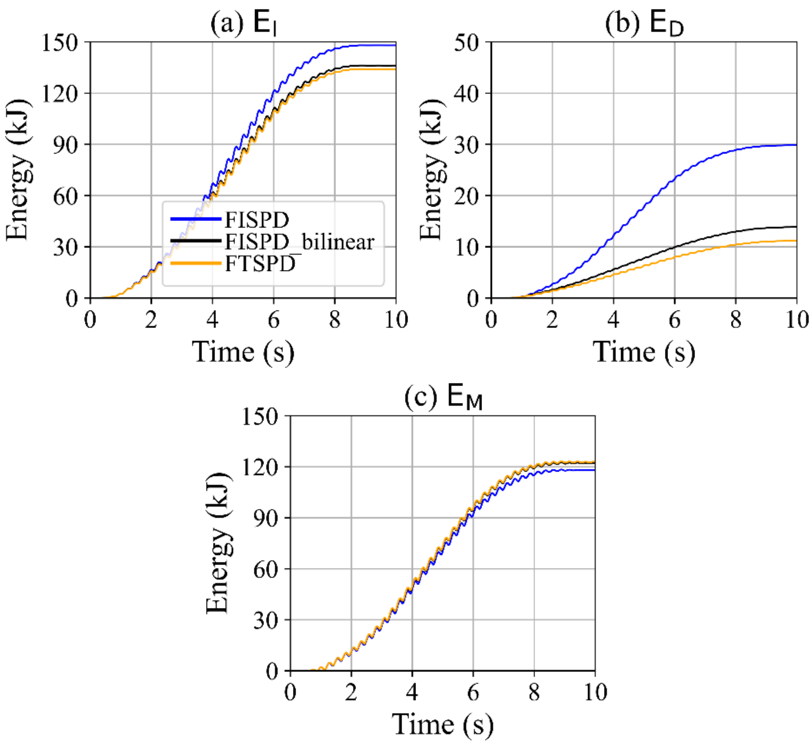

Figure 6.17. (a) Cumulative energy input by the ground motion record, (b) cumulative energy dissipated by the damping models and (c) cumulative energy dissipated by material constitutive laws

As in the previous case, the models implemented in the fibre have a higher computational cost since it is necessary to calculate the strain rates and integrate the response of all the fibres to obtain the response. However, this approach with the bilinear constitutive rule allows to have damping forces in an acceptable range of magnitude, prevents the damping forces from decaying and finally enables to implement any constitutive rule between the damping forces and the strain rates.

Table 6.3 Computational analysis for the steel structure

Model	Computational time (s)	Average number of iterations per step
FISPD_bilinear	166.7	2.88
FISPD	127.7	2.50
FTSPD	125.4	1.98
TISPD	62.4	1.88
TTSPD	76.1	2.17

6.4.3 Sensitivity analysis of the maximum value of the damping stress in the fibre

The bilinear damping models used in the case studies present a limit on the damping forces such that the maximum damping moment of the section is equivalent to $2\zeta M_y$. As mentioned above, Hall[27] proposed this limit, considering the relationship between the damping forces and the resisting forces of the material in an SDoF subjected to a sinusoidal wave. Furthermore, different authors[29,54] consider this relationship between the damping forces and the resisting forces of the material as reasonable in the linear case. However, this sub-chapter presents a sensitivity analysis where other limits on the damping moments are taken to observe the change in the response of the previously shown case studies. Among all the existing damping models, the one with the largest damping forces is proportional to the initial stiffness matrix. Therefore, the structure's response using different damping limits will be between this model and when no damping is considered.

RC column tested by Petrini et al.[66]

The damping stresses of the fibres of the cross-section shown in the Figure 6.3 are limited by the values in Table 6.4, where σ_y and M_y are yield stress and moment linked to fibre and cross-section, respectively.

Table 6.4 limits imposed on the damping stress.

Lambda	Maximum damping stress $2\zeta\lambda\sigma_y$	Maximum damping moment
0	$0\sigma_y$	$0.000M_y$
0.125	$0.0125\sigma_y$	$0.045M_y$
0.25	$0.025\sigma_y$	$0.091M_y$
0.5	$0.05\sigma_y$	$0.182M_y$
0.75	$0.075\sigma_y$	$0.273M_y$
1	$0.1\sigma_y$	$0.364M_y$
1.25	$0.125\sigma_y$	$0.455M_y$
1.5	$0.15\sigma_y$	$0.545M_y$
1.75	$0.175\sigma_y$	$0.636M_y$
2	$0.2\sigma_y$	$0.727M_y$

Figure 6.18 presents the history of damping moments in the lower cross-section of the concrete structure using the limits given in Table 6.4. The damping model formulated in this chapter limits the moments and damping forces to predetermined levels, thus allowing control over the analysis. However, the model presented is proportional to the initial stiffness of the material, so by allowing high values of damping stress in the fibre, the behaviour will be similar to the FISPD. Furthermore, if minimal limits are imposed, the structure's response will be similar to when no viscous damping is considered. The response in terms of displacements is shown in Figure 6.19, where the structure's response using different limits is between the FISPD and FTSPD models, except for the last segment, where the systems using the bilinear models have larger residual displacements. However, the latter converges to the FISPD displacement with very high limits.

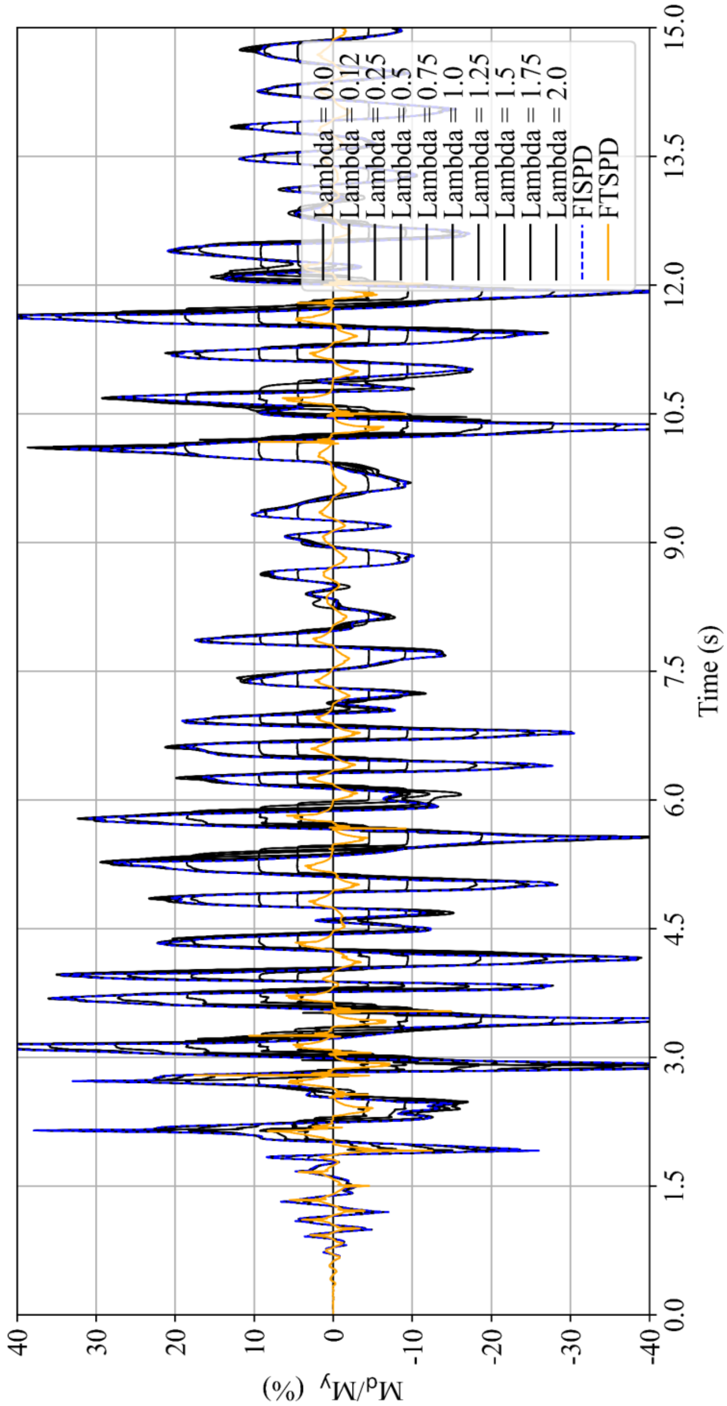

Figure 6.18 History of viscous moments for the different limits imposed at the fiber level.

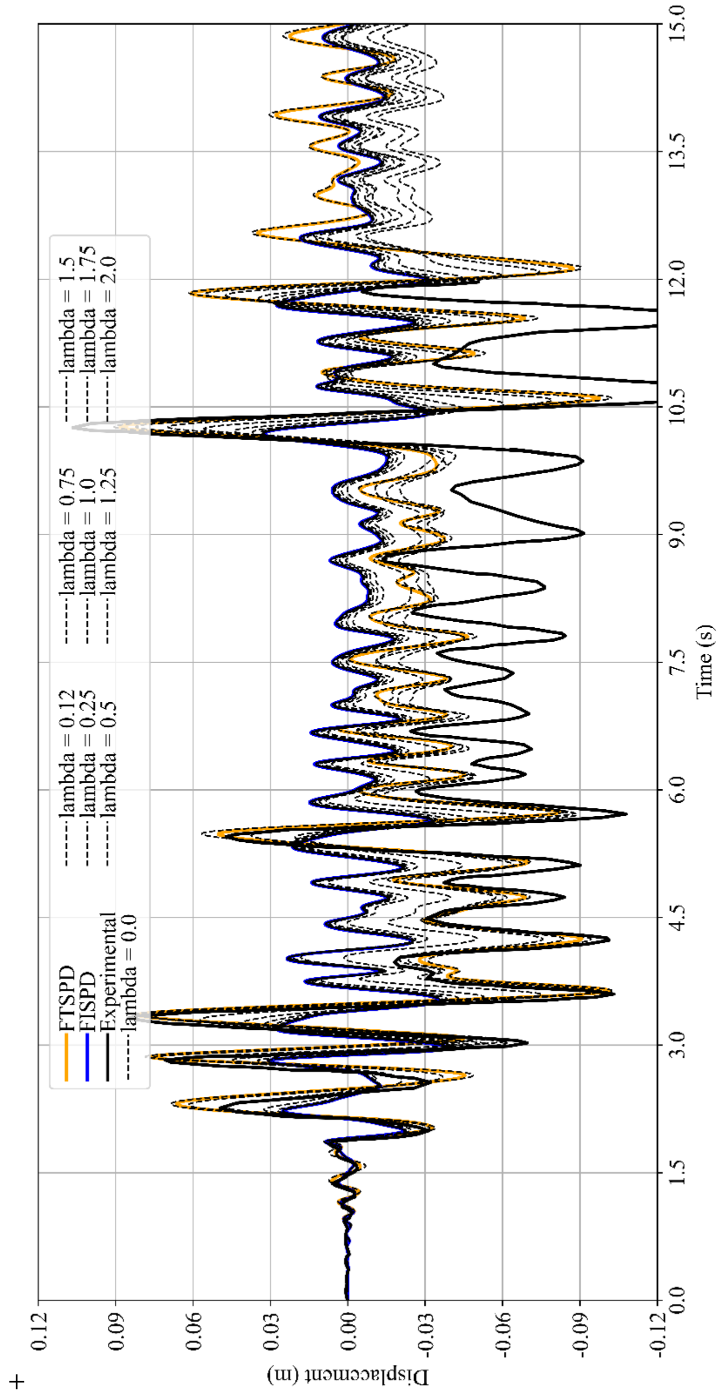

Figure 6.19 Numerical comparison of predicted displacement for the different limits imposed at the fibre level.

Unlike the previous case and for the axial loading conditions of the structure, by imposing a limit on the damping stresses with respect to the yield stress of the material, the maximum damping moment with respect to the yield moment of the material will be limited in the same proportion since steel is a homogeneous material with the same compressive and tensile properties.

Table 6.5 limits imposed on the damping stress

Lambda	Maximum damping stress in the fibre $2\zeta\lambda\sigma_y$	Maximum damping moment in the cross-section
0.0	$0.00\sigma_y$	$0.00M_y$
0.5	$0.02\sigma_y$	$0.02M_y$
1.0	$0.04\sigma_y$	$0.04M_y$
1.5	$0.06\sigma_y$	$0.06M_y$
2.0	$0.08\sigma_y$	$0.08M_y$
2.5	$0.10\sigma_y$	$0.10M_y$
3.0	$0.12\sigma_y$	$0.12M_y$
3.5	$0.14\sigma_y$	$0.14M_y$
4.0	$0.16\sigma_y$	$0.16M_y$
4.5	$0.18\sigma_y$	$0.18M_y$
5.0	$0.20\sigma_y$	$0.20M_y$

The proposed bilinear model is proportional to the initial stiffness of the fibre; thus, when imposing very high damping stress limits, the bilinear model will behave similarly to FISPD. However, by setting low limits, it is possible to have even smaller moments and damping forces approaching a structure where no viscous damping is defined, see Figure 6.20. The main advantage of this model over existing models lies in the control of the damping forces. The engineer decides the range of forces and damping moments he wishes to have in his analysis, something that is impossible to define with traditional models. Similarly, the response in terms of displacements, presented in Figure 6.21, is equivalent to the model proportional to the initial stiffness matrix when very high damping limits are imposed. Furthermore, when very small damping limits are imposed, the response will be analogous to a structure without viscous damping.

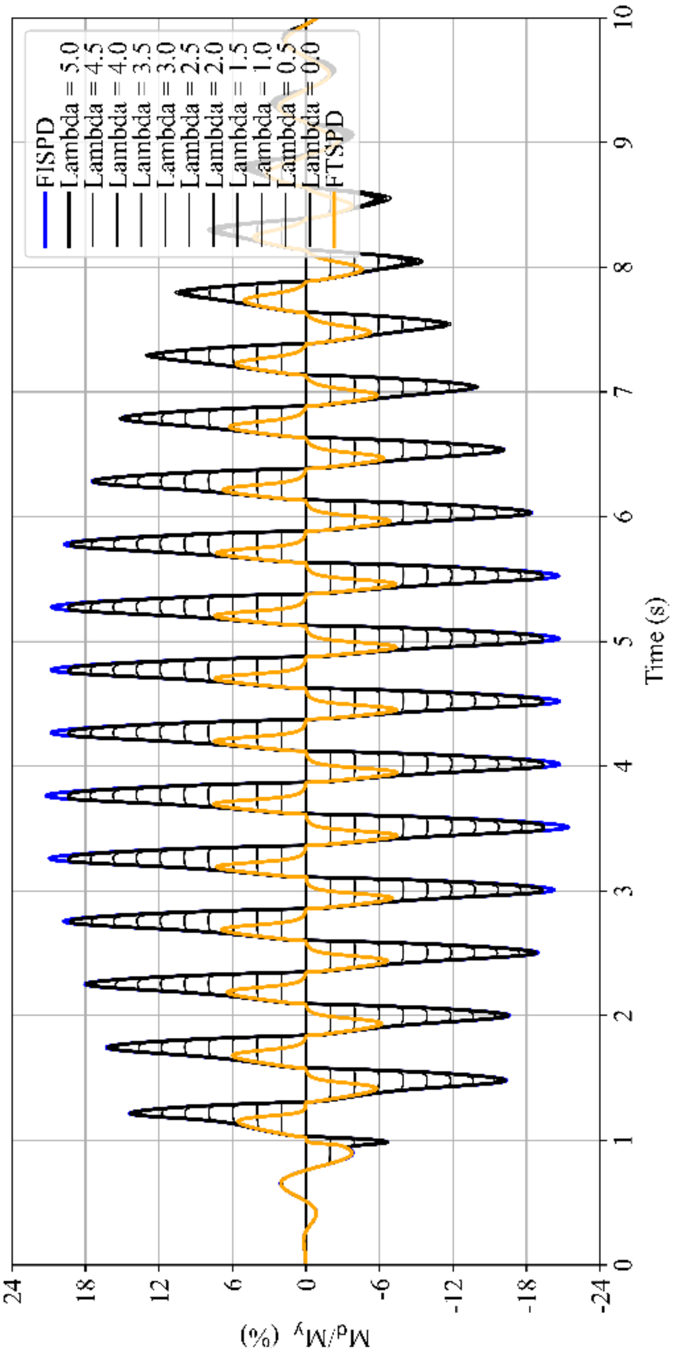

Figure 6.20 History of viscous moments for the different limits imposed at the fiber level.

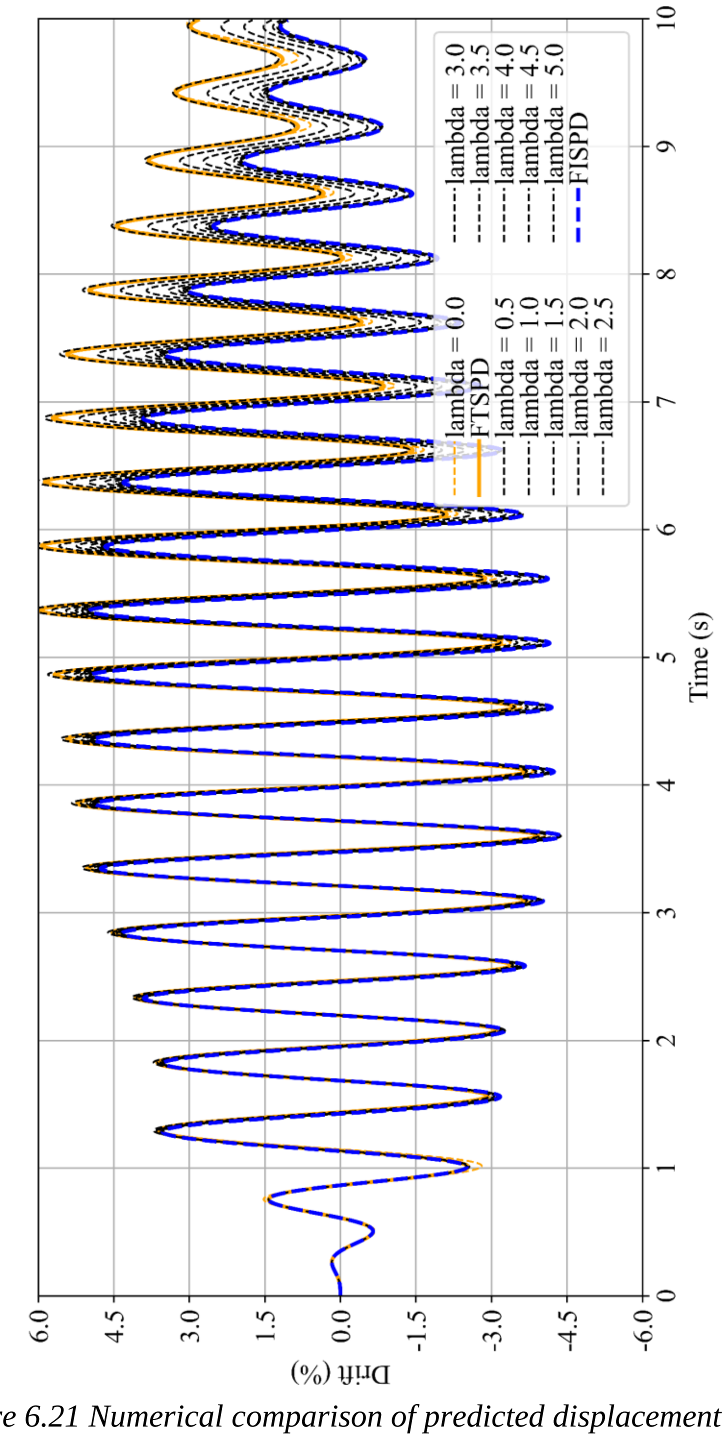

Figure 6.21 Numerical comparison of predicted displacement for the different limits imposed at the fibre level.

6.5 Conclusions

During the last decades, much research has been done to determine how to model energy dissipation sources independent of the materials' constitutive rules in nonlinear dynamic analyses. Significant progress has been made; however, no consensus exists on which model should be used. Most commercial and open-source software uses traditional models proportional to the initial and tangent stiffness matrix, the mass matrix or modal damping. All these models have deficiencies, mainly because the basic assumptions used to implement such models in linear dynamic analyses are not fulfilled. This chapter provides a new non-linear viscous model implemented in the fibre, where a constitutive rule between strain rates and damping stresses is defined. The model is mathematically consistent and easy to implement in commercial programs using distributed plasticity elements. This approach provides damping forces within reasonable magnitude ranges or avoid them from decaying and taking negative values during incursions in the inelastic range. The latter are the main drawback of traditional models proportional to the initial and tangent stiffness, including Rayleigh damping. Additionally, the proposed approach allows satisfying the original fundamental premises to use viscous damping models in dynamic analysis. This manuscript presents a step-by-step mathematical description of the model. Subsequently, the model is used to predict the experimental test available in the literature, where it is shown that the model's predictions closely match the structure's real response. This model ensures that the damping forces are in acceptable magnitude ranges during the entire analysis and that the damping model does not dissipate excessive energy. This model was also used to predict the inelastic dynamic response of a steel structure. In both cases, the prediction of the proposed model was compared with traditional models and other illustrative models implemented in the fibre. This work is a first contribution since further research is required to extrapolate this approach to other formulations of elements with distributed plasticity and better define the constitutive rules between the strain rates and damping stresses.

7. Conclusions

This dissertation presents new viscous damping models to simulate sources of energy dissipation independent of the constitutive rules of materials in nonlinear dynamic analysis of buildings and infrastructure. The contributions of the four chapters that make up this thesis present an introduction to the problem, the mathematical formulation, case studies and detailed conclusions. The first two chapters (3-4) present modifications of the traditional models with the aim of solving some of their problems. The last two chapters (5-6) present two nonlinear models, one implemented at the elemental level with a mathematical simplification and the other one implemented at the fibre level consistently. These nonlinear models are the most valuable contributions of this dissertation from the author's perspective.

7.1 Summary and main conclusions

Chapter 3 of this dissertation presents a tangent stiffness proportional (TSPD) viscous damping model independent of the geometric stiffness matrix (GSM). Additionally, it suggests a more physically consequential choice for obtaining the damping parameters independent of the GSM.

The stiffness proportional damping models use the total stiffness matrix, the sum of the material stiffness (MSM) and the GSM appearing when the equilibrium equations are formulated in the deformed configuration. The presence of the GSM in the definition of a TSPD has been a persistent argument for not recommending this formulation in nonlinear dynamic analysis. The reasons are (i) the GSM is not a mechanical but a purely geometrical component resulting from formulating the equilibrium equations in the deformed configuration, (ii) the energy dissipation mechanisms modelled through viscous damping models are not affected by the GSM, and (iii) when a damping model proportional to the GSM is defined, the model may introduce energy at high displacement demands when the material stiffness matrix

(MSM) decays sufficiently; the possibility of introducing energy into the system through the GSM is a fundamental argument for its removal since it falls outside the realm of conceivable physical, structural phenomena. The latter can be seen in Figure 3.22, where the cumulative energy dissipated by the GSM component of the damping model is negative.

The results suggest that the response of structural systems is influenced by the inclusion of GSM in the definition of a stiffness-proportional damping model, especially under significant gravity loads and slender structures. Differences in terms of energy dissipation, displacements and internal forces were revealed. The chapter demonstrates that, using the traditional damping model proportional to the total tangent stiffness, the magnitude of the damping matrix changes considerably as a function of the applied gravity forces in slender structures.

Chapter 4 examines the condensed damping models that different authors have recommended and proposes a new model proportional to the tangent stiffness matrix. Condensed models have not been widely studied since they are not implemented in most commercial or open-source software. Therefore, for the development of this chapter, all the existing condensed damping models were implemented in the author's software. Afterwards, case studies are presented in which it is clearly demonstrated that these models present high levels of energy dissipation and can present non-conservative results. Furthermore, this chapter illustrates that the response of structures using the condensed models and their analogue total models differ slightly. Hence, if the global models are considered inappropriate for non-linear analysis, they are, by analogy, equally inappropriate.

Intending to avoid the high levels of energy dissipation of existing condensed damping models, this chapter proposes to define a damping model proportional to the condensed tangent stiffness matrix. This model keeps the damping forces relatively small with respect to the material resisting forces and prevents the presence of damping forces in the massless degrees of freedom that have been a prominent argument against total models. This approach also preserves a solid physical meaningfulness related to a reduction of the damping energy when hysteretic material response is activated and eliminates the potential consequences of the presence of the geometric stiffness matrix in the definition of the damping matrix under extreme loads and displacements. Nevertheless, the formulation of a tangent condensed matrix can be computationally expensive for structures with many DoFs.

The viscous damping models were implemented assuming that the damping forces are small compared to the material resisting forces and will not considerably affect the structure's response. In other words, any impressions in the model will not significantly affect the results. However, in analyses where the material resisting system is nonlinear, the baseline assumptions are not fulfilled since the damping model is linear. Consequently, the resisting forces of the material will have a predefined limit, while the damping forces could reach any value and would no longer be proportionally small, affecting the structure's response. This has led to the development of nonlinear models, but the existing ones cannot be easily implemented in commercial software for structural engineering. Therefore, this thesis presents two new contributions in chapters 5 and 6 implemented at the elemental and fibre level.

Chapter 5 determines the elemental damping forces in the basic reference system, employing a damping model proportional to the initial stiffness matrix (EISPD), the tangent stiffness (ETSPD), and the change of deformations with respect to time independent of the motion of the rigid body. These models and the case studies presented demonstrate that the elemental damping forces reach significant magnitudes compared to the maximum capacity of the structural elements. To correct the proportionally high magnitudes of the elemental damping forces with respect to the capacity of the structural elements, a new elemental level damping model is proposed, which limits the elemental damping forces to a certain percentage of their capacity. This model is defined in the basic reference system, where the damping forces are defined through the initial stiffness matrix and the basic velocities of each element. When the basic damping forces exceed a certain percentage of the capacity of the structural element, this maximum is imposed before expressing the damping forces in the local and global reference system. The mathematical formulation and several case studies on steel and RC structures elucidate the properties of this model. This new capped model ensures that the damping forces of the structure are within reasonable limits. This model has a mathematical simplification that allows defining a nonlinear model without going to the fibre, reducing the computational cost. However, this simplification means that the Jacobian used in generic methods such as Newton Raphson is not entirely consistent, which implies a higher number of iterations when the structure is in the inelastic range.

Chapter 6 introduces a completely consistent model from a mathematical point of view where a constitutive relationship between strain rates and damping stresses is defined. The formula presented in this chapter can be easily implemented in commercial and open-source programs. The principle of this mode is that limiting the damping stress in the fibre will ensure that the damping forces are at reasonable levels and that the damping model does not dissipate excessive energy. This chapter presents a step-by-step mathematical description of the model. Subsequently, the model was used to predict the experimental test available in the literature. The results show that this model's predictions closely match the structure's real response. This model was also used to predict the inelastic dynamic response of a steel structure. In both cases, the prediction of the proposed model was compared with traditional models and other illustrative models implemented in the fibre. The results clearly show the flexibility and numerical superiority of this approach, which allows to have full control over damping forces in nonlinear dynamic analysis of frame structures.

7.2 Perspectives and challenges

The modelling of energy dissipation mechanisms independent of the constitutive rules of the materials is a problem which exists practically since the development of nonlinear dynamic analysis. Several researchers have studied this topic; however, there is no consensus on how to model these sources of energy dissipation.

From the author's perspective, the future of this field of research does not lie in traditional global models since they have been extensively studied, and several manuscripts show the performance of conventional models in many case studies. Additionally, all these models are inflexible, given that they are proportional to the global matrices. Nonetheless, the author considers that the model proportional to the tangent stiffness matrix is the only one that fulfils relatively well the basic assumptions used to implement damping models. In other words, it is the only one that keeps the damping forces at low levels, but it is emphasized that this has conceptual implications.

The future of this research topic lies in nonlinear models or other approaches different from traditional viscous damping models. This work presents a simple formulation that can be easily implemented in commercial programs and benefits from tremendous flexibility. This thesis could be continued on several fronts, which are mentioned below.

- ❖ The model presented in the fibre was implemented in displacement-based elements. However, several types of elements with distributed plasticity exist, such as those using force interpolation functions. The strain rates are found directly with displacement-based elements; however, they cannot be found directly when using force-based elements. Therefore, a state-determination algorithm must be implemented, combining the material and damping models. The next step in this thesis would be to extrapolate the formulation presented here to these elements.

- The FISPD_bilinear was developed for Euler-Bernoulli beams. Steel and concrete elements with distributed plasticity defined with a Timoshenko beam can represent a non-linear behaviour for the shear demands at the cross-section level. Another front of the thesis could be to extrapolate the bilinear damping model formulation to Timoshenko beams.
- Additionally, the formulation could be deduced to 3D problems. The main issue with the corotation formulation in 3D problems is that the rotations cannot be added vectorially, but quaternions must be used to find the rotations at the ends of the element. Therefore, studying how the strain rates can be found with this 3D formulation is necessary.
- The constitutive rules of concrete do not have the same compressive and tensile strength, and therefore the limit set on the fibres must be calibrated so that the section does not exhibit high damping moments. From the author's perspective, one could define the constitutive rules between the strain rates and damping stress in another way so that this calibration does not have to be done. However, this needs to be investigated.

8. References

1. Bolt BA. *Earthquakes*. 4th edition. New York: W.H. Freeman and Company; 1999.

2. Kulhanek. *Anatomy of seismograms*. Amsterdam, The Netherlands: Elsevier Science Publishers; 1990.

3. Coburn A, Spence R. *Earthquake protection*. West Sussex, England: Jonh Wiley & Sons Ltd; 2003.

4. Ellingwood BR, Kinali K. Quantifying and communicating uncertainty in seismic risk assessment. *Structural Safety* 2009; **31**(2): 179–187.

5. Liel AB, Haselton CB, Deierlein GG, Baker JW. Incorporating modeling uncertainties in the assessment of seismic collapse risk of buildings. *Structural Safety* 2009; **31**(2): 197–211.

6. EN 1998-2. *Eurocode 8: design of structures for earthquake resistance – part 2: bridges*. Brussels: European committee for standardization; 2011.

7. AISC. *Specification for structural steel buildings*. Chicago, Illinois: American Institute of Steel Construction; 2016.

8. Rayleigh L. *The theory of sound*. Second Edition. New York, USA: Dover Publications; 1877.

9. Berg G. *Report N. IP-291. The analysis of structural response to earthquake forces*. University of Michigan industry program of the college of engineering; 1958.

10. Wilson E, Clough R. Dynamic response by step by step matrix analysis. *Symposium on the use of computers in civil engineering*, 1962.

11. Wilson E, Penzien J. Evaluation of orthogonal damping matrices. *International Journal for Numerical Methods in Engineering* 1972; **4**: 5–10.

12. Chen H, Blandford G. Thin-walled space frames. I: Large deformation analysis theory. *Journal OfStructural Engineering* 1991; **117**: 2499–2520.

13. Gattass M, Abel J. Equilibrium considerations of the Updated Lagrangian formulation of beam-columns with natural concepts. *International Journal for Numerical Methods in Engineering* 1987; **24**: 2119–2141.

14. Bathet K, Bolourchit S. Large displacement analysis of three-dimensional beam structures. *International Journal for Numerical Methods in Engineering* 1979; **14**: 961–986.

15. Crisfield MA. A consistent corotational formulation for nonlinear three-dimensional beam element. *Comp Meths Appl Mech Eng* 1990; **81**: 131–150.

16. Argyris J. An excursion into large rotations. *Comp Meths Appl Mech Eng* 1982; **32**: 85–155.

17. Belytschko T, Hsieh BJ. Non-linear transient finite element analysis with convected coordinates.International Journal for Numerical Methods in Engineering. *International Journal for Numerical Methods in Engineering* 1973; **7**: 255–271.

18. Teh LH, Clarke MJ. *Co-rotational and Lagrangian formulations for elastic three-dimensional beam finite elements*. vol. 48. 1998.

19. Felippa CA. *A systematic approach to the element-independent corotational dynamics of finite elements*. 2000.

20. Hardyniec A, Charney F. An investigation into the effects of damping and nonlinear geometry models in earthquake engineering analysis. *Earthquake Engineering and Structural Dynamics* 2015; **44**: 2695–2715.

21. Chopra A, Mckenna F. Modeling viscous damping in nonlinear response history analysis of buildings for earthquake excitation. *Earthquake Engineering and Structural Dynamics* 2016; **45**(2): 193–211.

22. Charney F. Unintended consequences of modeling damping in structures. *Journal of Structural Engineering* 2008; **134**(4): 581–592.

23. Mondkar D, Powell G. *ANSR-I General purpose program for analysis of nonlinear structural response*. Berkeley, California: University of California; 1975.

24. Hall J. Discussion on ‘an investigation into the effects of damping and nonlinear geometry models in earthquake analysis’ by Andrew Hardyniec and Finley Charney. *Earthquake Engineering and Structural Dynamics* 2017; **46**(2): 341–342.

25. Bernal D. Viscous damping in inelastic structural response. *Journal of Structural Engineering* 1994; **120**(4): 1240–1254.

26. Hall J. Performance of viscous damping in inelastic seismic analysis of moment-frame buildings. *Earthquake Engineering and Structural Dynamics* 2018; **47**(14): 2756–2776.

27. Hall J. Problems encountered from the use (or misuse) of Rayleigh damping. *Earthquake Engineering and Structural Dynamics* 2006; **35**(5): 525–545.

28. Chrisp D. Master’s thesis damping models for inelastic structures. University of Canterbury, New Zealand, 1980.

29. Carr A. *Ruaumoko Theory Manual*. Christchurch, New Zealand: University of Canterbury; 2007.

30. Hall JF. *Report No. EERL 2018-01: performance of viscous damping in inelastic seismic analysis of moment-frame buildings*. Pasadena, California, USA: California Institute of Technology; 2018.

31. Golesorkhi R, Joseph LM, Klemencic R, Shook D, Viise J. *Performance-based seismic design for tall buildings : an output of the CTBUH Performance-Based Seismic Design Working Group*. Chicago,: 2017.

32. Leger P, Dussault S. Seismic-energy dissipation in MDOF structures. *Journal of Structural Engineering* 1992; **118**(5): 1251–1269.

33. Kareem A, Gurley K. *Damping in structures: its evaluation and treatment of uncertainty*. vol. 59. 1996.

34. Blandon CA, Priestley MJN. Equivalent viscous damping equations for direct displacement based design. *Journal of Earthquake Engineering* 2005; **9**(SPEC. ISS. 2): 257–278.

35. Blandon CA, Priestley MJN. Equivalent viscous damping equations for direct displacement based design. *Journal of Earthquake Engineering* 2005; **9**(SPEC. ISS. 2): 257–278.

36. Jehel P. A critical look into Rayleigh damping forces for seismic performance assessment of inelastic structures. *Engineering Structures* 2014; **78**: 28–40.

37. Medina RA, Krawinkler H. *Seismic demands for nondeteriorating frame structures and their dependence on ground motions*. 2003.

38. Kanaan A, Powell G. *Drain 2D A general purpose computer program for dynamic analysis of inelastic plane structures with*

user's guide and supplement. Berkeley, California: University of California; 1973.

39. Simpson B. Higher-mode force response in multi-story strong-back-braced frames. *Earthquake Engineering and Structural Dynamics* 2020; **49**(14): 1406–1427.

40. Björnsson A, Krishnan S. Low-Complexity candidate for benchmarking collapse prediction of steel braced structures. *Journal of Structural Engineering* 2014; **140**(8).

41. Satake N, Suda K, Arakawa T, Sasaki A, Tamura Y. Damping evaluation using full-scale data of buildings in Japan. *Journal of Structural Engineering* 2003; **129**(4): 470–477.

42. Satake N, Suda K, Arakawa T, Sasaki A, Tamura Y, Asce M. Damping Evaluation Using Full-Scale Data of Buildings in Japan.

43. Gibson RF, Plunkett R. A forced-vibration technique for measurement of material damping. *Experimental Mechanics* 1977; **17**(8): 297–302.

44. Erduran E. Hysteretic energy demands in multi-degree-of-freedom systems subjected to earthquakes. *Buildings* 2020; **10**(12): 1–17.

45. Erduran E. Evaluation of Rayleigh damping and its influence on engineering demand parameter estimates. *Earthquake Engineering and Structural Dynamics* 2012; **41**: 1905–1919.

46. Smyrou E, Priestley M, Carr A. Modelling of elastic damping in nonlinear time-history analyses of cantilever RC walls. *Bulletin of Earthquake Engineering* 2011; **9**(5): 1559–1578.

47. Ryan K, Polanco J. Problems with rayleigh damping in base-isolated buildings. *Journal of Structural Engineering* 2008; **134**: 1780–1784.

48. Computers and Structures. *PERFORM-3D nonlinear analysis and performance assessment for 3D structures*. Berkeley, California: 2006.

49. McKenna F, Fenves G, Scott M. *Open system for earthquake engineering simulation (OpenSees)*. Berkeley, USA: Pacific Earthquake Engineering Center; 2000.

50. Chopra A, Mckenna F. Modeling viscous damping in nonlinear response history analysis of buildings for earthquake excitation. *16th World Conference on Earthquake, 16WCEE 2017* 2016; **45**(2): 193–211.

51. Caughey T. Classical normal modes in damped linear dynamic systems. *Journal of Applied Mechanics* 1960; **27**: 269–271.

52. Caughey T, O'kelly M. Classical normal modes in damped linear dynamic systems. *Journal of Applied Mechanics* 1965; **32**(3).

53. Baena-Urrea J, Almeida J. Condensed-tangent-stiffness-proportional viscous damping model for nonlinear time history analysis. *3rd European Conference on Earthquake Engineering and Seismology* 2022.

54. Chopra A. *Dynamics of structures theory and applications to earthquake engineering*. Fourth edition. Boston, USA: Prentice Hall; 2015.

55. Qian X, Chopra A, McKenna F. Modeling viscous damping in nonlinear response history analysis of steel moment-frame buildings: Design-plus ground motions. *Earthquake Engineering and Structural Dynamics* 2021; **50**(3): 903–915.

56. Hall J. Performance of viscous damping in inelastic seismic analysis of moment-frame buildings 2018.

57. Luco J, Lanzi A. Numerical artifacts associated with Rayleigh and modal damping models of inelastic structures with massless coordinates. *Earthquake Engineering and Structural Dynamics* 2019; **48**(13): 1491–1507.

58. Charney F, Lopez-Garcia D, Hardyniec A, Ugalde D. Modeling inherent damping in nonlinear dynamic analysis. *16th World Conference on Earthquake Engineering* 2017.

59. Antoniou S, Pinho R. *Seismostruct - a computer program for static and dynamic nonlinear analysis of framed structures*. Pavia, Italy: SeismoSoft; 2021.

60. Zareian F, Medina R. A practical method for proper modeling of structural damping in inelastic plane structural systems. *Computers and Structures* 2010; **88**(1–2): 45–53.

61. Puthanpurayil A, Lavan O, Carr A, Dhakal R. Elemental damping formulation: an alternative modelling of inherent damping in nonlinear dynamic analysis. *Bulletin of Earthquake Engineering* 2016; **14**: 2405–2434.

62. Logan DL. *A first course in the finite element method*. Wisconsin Platteville: Thomson; 2007.

63. Jäger C, Adam C. Influence of collapse definition and near-field effects on collapse capacity spectra. *Journal of Earthquake Engineering* 2013; **17**(6): 859–878.

64. Powell G. *Drain-2D User's guide*. Berkeley, California: University of California; 1973.

65. Sharpe RD. *The seismic response of inelastic structures*. Christchurch, New Zealand: University of Canterbury; 1974.

66. Petrini L, Maggi C, Priestley N, Calvi G. Experimental verification of viscous damping modeling for inelastic time history

analyzes. *Journal of Earthquake Engineering* 2008; **12**(1): 125–145.

67. Chambreuil C, Giry C, Ragueneau F, Léger P. Seismic energy dissipation in reinforced concrete beam: investigating damping formulations. *European Journal of Environmental and Civil Engineering* 2021: 1–27.

68. Otani S. Nonlinear dynamic analysis of reinforced concrete building structures. *Canadian Journal of Civil Engineering* 1980; **7**: 333–344.

69. Jehel P, Léger P, Ibrahimbegovic A. Initial versus tangent stiffness-based Rayleigh damping in inelastic time history seismic analyses. *Earthquake Engineering and Structural Dynamics* 2014; **43**(3): 467–484.

70. Hall J. Discussion of "A new inherent damping model for inelastic time-history analyses" by Enrique Luco and Armando Lanzi. *Earthquake Engineering and Structural Dynamics* 2018; **47**(10): 2137–2139.

71. Chopra A, McKenna F. Response to John Hall's Discussion (EQE-16-0008) to Chopra and McKenna's paper, 'Modeling viscous damping in nonlinear response history analysis of buildings for earthquake excitation.' *Earthquake Engineering and Structural Dynamics* 2016; **45**(13): 2235–2238.

72. Luco J, Lanzi A. A new inherent damping model for inelastic time-history analyses. *Earthquake Engineering and Structural Dynamics* 2017; **46**(12): 1919–1939.

73. Lanzi A, Luco J. Elastic Velocity Damping Model for Inelastic Structures. *Journal of Structural Engineering* 2018; **144**(6): 04018065.

74. Francesco G, Sullivan TJ. Formulation of localized damping models for large displacement analysis of single-degree-of-freedom inelastic systems. *Journal of Earthquake Engineering* 2020.

75. Bowland A, Charney F. New concepts in modeling damping in structures. *19th Analysis & Computation Specialty Conference*, 2010.

76. Khashaee P, Mohraz B, Sadek F, Lew HS, Gross JL. *Distribution of earthquake input energy in structures*. Gaithersburg, MD: 2003.

77. Kareem A, Gurley K. Damping in structures: Its evaluation and treatment of uncertainty. *Journal of Wind Engineering and Industrial Aerodynamics* 1996; **59**: 131–157.

78. Crisfield MA. *Non-linear Finite Element Analysis of Solids and Structures: Volume 1*. West Sussex, England: 2000.

79. Crisfield MA. *Non-linear Finite Element Analysis of Solids and Structures Volume 2: Advanced Topics*. West Sussex, England: 2000.

80. Magalhães De Souza R. *Ph.D.'s thesis: force-based finite element for large displacement inelastic analysis of frames*. Berkeley, California, USA: University of California; 2000.

81. Filippou Filip C, Fenves Gregory L. Methods of Analysis for Earthquake-Resistant Structures. *Earthquake Engineering - From Engineering Seismology to Performance-Based Engineering*, 2004.

82. Alemdar BN, White DW. Displacement, flexibility, and mixed beam-column finite element formulations for distributed plasticity analysis. *Journal of Structural Engineering* 2005; **131**: 1811–1819.

83. Spacone E, Ciampi V, Filippou F. Mixed formulation of nonlinear beam finite element. *Computers and Structures* 1996; **58**(1): 71–83.

84. Neuenhofer A, Filippou FC. Evaluation of nonlinear frame finite-element models. *Journal of Structural Engineering* 1997; **123**(7): 958–966.

85. Calabrese A, Almeida JP, Pinho R. Numerical issues in distributed inelasticity modeling of RC frame elements for seismic analysis. *Journal of Earthquake Engineering* 2010; **14**(S1): 38–68.

86. Menegotto M, Pinto P. Method of analysis for cyclically loaded R.C. plane frames including changes in geometry and non-elastic behaviour of elements under combined normal force and bending. *IABSE Reports of the Working Commissions* 1973; **13**: 15–22.

87. Pacific Earthquake Engineering Research Center. PEER strong motion database on line. *Https://PeerBerkeleyEdu/Peer-Strong-Ground-Motion-Databases* 2005.

88. Mander J, Priestley M, Park R. Theoretical stress-strain model for confined concrete. *Journal of Structural Engineering* 1988; **114**(8): 1804.

89. Enrique Martlnez-Rueda J, Elnashai AS. *Confined concrete model under cyclic load*. vol. 30. 1997.

90. Park Y, Ang A, Wen Y, Eeri M. Damage-limiting aseismic design of buildings. *Earthquake Spectra* 1987; **3**: 1–26.

91. Newmark N. A method of computation for structural dynamics. *Journal of the Engineering Mechanics Division* 1959: 67–94.

92. Chopra A, Mckenna F. Modeling viscous damping in nonlinear response history analysis of buildings for earthquake excitation.

Earthquake Engineering and Structural Dynamics 2016; **45**(2): 193–211.

93. Arede A.J. Seismic assessment of reinforced concrete frame structures with a new flexibility based element. *Universidade Do Porto* 1997.

94. Kent D, Park R. Flexural members with confined concrete. *Journal of the Structural Division Proceedings of the American Society of Civil Engineers* 1971: 1969–1990.

95. Hjelmstad KD, Taciroglu E. Mixed methods and flexibility approaches for nonlinear frame analysis. *Journal of Constructional Steel Research* 2002; **58**: 967–993.

96. Tarquini D, Almeida JP, Beyer K. Axially equilibrated displacement-based beam element for simulating the cyclic inelastic behaviour of RC members. *Earthquake Engineering and Structural Dynamics* 2017; **46**(9): 1471–1492.

97. Flugge Wilhelm. *Viscoelasticity*. Palo Alto: Springer-Verlag; 1975.

98. Saito T. *STERA 3D Structural earthquake response analysis 3D technical manual, technical manual version 5.8*. Japan: 2017.

99. Uang CM, Bertero V. Evaluation of seismic energy in structures. *Earthquake Engineering and Structural Dynamics* 1990; **19**: 77–90.

100. Reinhorn A, Roh H, Sivaselvan M, Kunnath SK, Valles R, Madan A, *et al.* IDARC2D Version 7.0: A Program for the Inelastic Damage Analysis of Structues. *Technical Report MCEER-09-0006* 2009(May 2016): 410.

9. Annexes - Fundamentals of nonlinear analysis using distributed plasticity elements

The damping models proposed in this thesis were implemented in a program made by the author during his doctoral studies. This program was written in Python with a singleton programming structure and comprises tens of thousands of lines of code, hundreds of classes and methods. This finite element program took approximately two years to be developed and can perform nonlinear static and dynamic analysis of frame structures in 2D and 3D. The program features different types of elements with distributed plasticity, sections, materials, numerical methods and others.

The development of this programme required the understanding and implementation of many concepts, models and mathematical methods necessary to predict the physical response of a building to extreme loads. This section presents them briefly.

9.1 Geometric nonlinearity

For robust structures and small loads, the formulation of the equilibrium equations is commonly performed in the undeformed configuration since the displacements will be small and do not have a major effect on the structure's response. However, for extreme loads or slender structures, the displacements can be large enough to magnify the effect of the load and cause second order effects, which will considerably influence the structure's response.

Nonlinear geometric effects are considered by formulating the equilibrium equations in the deformed configuration. The approach is not unique, but there are different options: the total Lagrangian, updated Lagrangian and corotational formulation. The total lagrangian formulation uses the reference system of the initial deformed configuration to formulate the FE equations. The updated Lagrangian takes the reference configuration of the previous converged step, and it is fixed for a certain period Δt[15], whereas in the corotational formulation, the reference configuration is continuously updated following the displacements and rotation of the element. Even if it is recognized that the corotational formulation is more accurate[18], each formulation has advantages that are not described in this document, but can be found elsewhere[18,19].

For extreme loads and systems susceptible to large deformations, disregarding nonlinear geometric effects in the numerical response of the structure may lead to erroneous and unconservative analyses. In general, it is always advisable to take them into account, even for non-slender structures.

The formulation of geometric problems can be easily implemented in 2D structures since the system's rotations can be summed algebraically. The latter was detailed in the different chapters of this dissertation. However, the extension of this formulation to 3D problems is cumbersome and requires the use of complex mathematics and lengthy derivations. The reason is that in 3D, the rotations in all three senses cannot be treated vectorially.

9.2 Material nonlinearity

Material nonlinearity means that the relationship between the change in deformations and the change in stresses is not constant but depends on the history and current strain of the material. The nonlinearity of the material can be modelled at the section level using direct relationships between the section resisting forces (axial force and moment) and the deformations (axial strain and curvature). This approach is known as concentrated plasticity because the non-linear relationship occurs only at specific points in the element. Another approach known as distributed plasticity defines the non-linearity of the material at the level of the fibres that make up the sections of the element. This methodology defines different observation points along the element where forces or displacements are interpolated to find each section's state at these points. Finally, the responses of the sections are integrated using

Gaussian quadrature's to find the deformations and forces of the element.

The first method corresponds to the simplest formulation for representing material nonlinearity because inelasticity is represented by springs or zero-length elements where inelastic deformation is expected to occur, typically at the ends of the element. The first approach has the disadvantage that specific curves must be defined for each element. This is not a major problem in steel structures because the cross-sections are standardised, and these curves can easily be determined. However, sections of concrete structures may present a more significant variability in terms of section shapes and distribution of reinforcing bars. This makes this procedure more difficult and implies that moment-curvature diagrams must be made for all sections before launching the analyses. It is common for this approach to consider that the moment and axial load are uncoupled, i.e., the moment will not be affected by the axial load present in the structure. This leads to inaccuracies because axial loading in concrete elements can significantly change the capacity of the elements. A solution to this problem has been the definition of specialised curves known as yield-surface, where axial loads and moments are coupled. These are known in commercial programs as P-M2-M3 hinges.

The second method has important advantages because the fibres that make up the section implicitly describe the interaction between axial force and moments. However, this method requires a discretisation of the cross-sections and storing the history of deformations and internal forces for each fibre, cross-section, and element. Additionally, it requires integrating the fibre response to find the response of the sections, then of the element and finally of the structure. This implies a much higher computational cost than the first method. Among the distributed plasticity methods, there is a simplified method that defines the plasticity in a finite element length.

Additionally, there are more complex methods using continuous elements where relationships between the different materials that make up the structure are defined, and the interaction between moment, axial load, and even shear stress is modelled. The latter is more computationally intensive. Further information about distributed plasticity elements is presented in the next section.

For the implementation of the damping models presented in this work, the second approach was used, using elements with distributed plasticity, specifically those known as force-based[83,84] and displacement-based elements[95], which are described in the following section. As mentioned above, this type of model requires the definition of cross-sections and constitutive rules. Table 9.1 and Table 9.2 present the cross-sections defined for the 2D and 3D elements, respectively.

Table 9.1 2D Cross-sections implemented in the software.

Shape	Formulation	Developed for	Additional comments
Rectangular	Euler-Bernoulli	Homogeneous material	
Rectangular	Euler-Bernoulli	Non-homogeneous material	Developed for reinforced concrete sections
Rectangular	Euler-Bernoulli	Non-homogeneous material	Developed for reinforced concrete walls
Rectangular	Timoshenko	Homogeneous material	
Rectangular	Timoshenko	Non-homogeneous material	Developed for reinforced concrete sections
Circular	Euler-Bernoulli	Homogeneous material	Rectangular fibres
Circular	Euler-Bernoulli	Homogeneous material	Radial fibres
Circular	Euler-Bernoulli	Non-homogeneous material	Developed for reinforced concrete sections
I-H shape	Euler-Bernoulli	Homogeneous material	Developed for steel structures

Table 9.2 3D cross-sections implemented in the program.

Shape	Formulation	Developed for	Additional comments
Rectangular	Euler-Bernoulli	Homogeneous material	
Rectangular	Euler-Bernoulli	Non-homogeneous material	Developed for reinforced concrete sections
I-H shape	Euler-Bernoulli	Homogeneous material	Developed for steel structures

The author implemented different material constitutive rules to provide multiple options for modelling typical concrete and steel structures. The constitutive material rules were mainly translated from the OpenSees platform; Dr. Danilo Tarquini shared some he elaborated on previous research, and others were implemented directly by the author. However, the author made different modifications to integrate them into his programme. Table 9.3 lists all of them.

Table 9.3 Material constitutive relations integrated and developed in this research

Name	Material	Original code source
BilinearUM		By the author
BilinearUM2		By the author
MenegottoPintoUM	Steel	SAGRES[96]
MenegottoPintoUM2	Steel	OpenSees[49]
ManderUM	Concrete	SAGRES[96]
KentScottParkConcrete	Concrete	OpenSees[49]
SelfCenteringMaterial	SMA	OpenSees[49]
Mander02	Concrete	OpenSees[49]
Mander03	Concrete	OpenSees[49]
Mander04	Concrete	OpenSees[49]
Kent03Shear02	Concrete	By the author
Mander03Shear02	Concrete	By the author

9.3 Distributed plasticity elements

Distributed plasticity models are more complex than concentrated plasticity models since they generally require a consistent and computationally more expensive formulation. During the last decades, different models of inelastic beams with distributed plasticity have been developed that vary in complexity.

Among the different formulations, the simplest is the one that defines a plastic hinge with a finite length where the plasticity is modelled through a section with fibres or specific moment-curvature curves, the deformations and forces in the element are found by integrating the response along the plastic length.

The formulation used in this work models the plasticity along the element through fibre sections where the uniaxial constitutive rules representing the real behaviour of the material (concrete, steel, aluminium, etc.) are attributed to each fibre. The deformation in the fibres is described using a linear distribution considering the deformation at the geometrical centre of the section and the curvature. The section response is found by integrating fibres response through the Newton-Cotes method. Subsequently, the element response is found by integrating the response of the sections along the element using Gaussian quadratures. Two types of elements can be defined through this formulation: force-based and displacement-based elements.

Initially, the most common model of nonlinear beams was the so-called displacement-based element, whose formulation relied on displacement interpolation functions used to find the deformation along the element and sections at the integration points to find the section and nodal forces later. Commonly, this element uses Hermite polynomials and a Lagrange linear function to interpolate the transverse and axial displacement, respectively, supposing linear curvature and constant average strain along the element. The latter is only valid when a linear elastic material is used. The displacement-based element model was gradually replaced by another superior beam model commonly known as force-based elements, which interpolates the nodal forces to find the exact internal forces along the element, regardless if a nonlinear material is considered. When such a formulation is used, special state determination algorithms, described in Spacone et al.[83,84] and Neuenhofer and Filippou[84] must be implemented because the nodal forces are unknown at the beginning of each time step.

The most complex distributed plasticity models discretize the element lengthwise and crosswise using solid elements. These models are compelling because they allow the modelling of the interaction between concrete and steel through a constitutive model. However, this formulation requires large amounts of time for both model development and simulation. This formulation is expected in the field of research or the design and verification of very specific and vital structures. However, this formulation is rarely used for common structures due to time and budget constraints.

9.3.1 Displacement-based elements

Displacement-based elements use displacement interpolation functions to find the deformation in the sections. These interpolation functions use Hermite polynomials and a Lagrange linear function to interpolate the transverse and axial displacement along the element. This interpolation equation implies that the element will have a constant axial deformation, and the curvature of each specific point of the section will vary linearly. This is an approximation because this is only true for linear prismatic elements. To better predict the behaviour of structural elements, it is necessary to discretise the element into several parts to represent a correct distribution of its internal deformations.

The compatibility equation governing these elements is expressed as follows

$$\mathbf{e}(x) = \begin{bmatrix} \varepsilon(x) \\ \chi(x) \end{bmatrix} = \begin{bmatrix} \frac{\partial}{\partial x} & \\ & \frac{\partial^2}{\partial x^2} \end{bmatrix} \begin{bmatrix} u_x(x) \\ u_y(x) \end{bmatrix} \tag{9.1}$$

The axial and transverse displacement is expressed in eq. (9.2) using a linear Lagrangian interpolation function and cubic Hermitian polynomials, respectively, as a function of the basic system deformations.

$$\begin{bmatrix} u_x(x) \\ u_y(x) \end{bmatrix} = \begin{bmatrix} \frac{x}{L} & 0 & 0 \\ 0 & x\left(1-\frac{x}{L}\right)^2 & \frac{x^2}{L}\left(\frac{x}{L}-1\right) \end{bmatrix} \begin{bmatrix} u_1^{bsc} \\ u_2^{bsc} \\ u_3^{bsc} \end{bmatrix} \tag{9.2}$$

Replacing eq. (9.2) in eq. (9.1) and carrying out the derivatives gives the following expression.

$$\begin{bmatrix} \varepsilon(x) \\ \chi(x) \end{bmatrix} = \begin{bmatrix} \frac{1}{L} & 0 & 0 \\ 0 & \frac{2x}{L^2} + \frac{4\left(\frac{x}{L}-1\right)}{L} & \frac{4x}{L^2} + \frac{2\left(\frac{x}{L}-1\right)}{L} \end{bmatrix} \begin{bmatrix} u_1^{bsc} \\ u_2^{bsc} \\ u_3^{bsc} \end{bmatrix} \tag{9.3}$$

The strain in each of the fibres is found thought the following eq. (9.4)

$$\varepsilon(y) = [1 \quad -y] \begin{bmatrix} \varepsilon(x) \\ \chi(x) \end{bmatrix} = \mathbf{B}(y)\mathbf{e}(x) \tag{9.4}$$

The stress in the fibre is found using the predefined material constitutive rules.

$$\boldsymbol{\sigma}(\mathbf{y}) = \mathbf{f}(\boldsymbol{\varepsilon}(\mathbf{y})) \tag{9.5}$$

Subsequently, the cross-section forces are found

$$\mathbf{s}(x) = \int_{\Omega} B^T \sigma(y) d\Omega \tag{9.6}$$

This integral is performed using Newton-Cotes quadrature through the following equation.

$$\mathbf{s}(x) = \begin{bmatrix} N(x) \\ M(x) \end{bmatrix} = \sum_{i=0}^{n} B^T \sigma(y) A \tag{9.7}$$

Where A is the area of the fibre, the elemental forces in the basic reference frame are derived employing the following equation, which is based on the virtual work principle.

$$\mathbf{p}^{bsc} = \int_0^{l_0} \mathbf{H}_e^t(x)\mathbf{s}(x)dx \tag{9.8}$$

9.3.2 Force-based elements

Due to its numerical superiority and extensive use in this thesis, the force-based element beam is presented in this chapter. The state determination corresponds to the one Neuenhofer and Filippou[84] described since performing the extra cycle in the sections mentioned by Spacone et al.[83] is unnecessary.

The governing equation of a 2D force-based element is expressed by eq. (9.9), relating the nodal forces at the basic reference ($\mathbf{p}^{bsc}$) system with the section forces ($\mathbf{s}$): axial load (N) and moment (M_z), thought an interpolation function ($\mathbf{H}(\mathbf{x})$) considering constant axial force and linear bending moment at each position (x) along the element. The loads inside the elements can be directly considered, which is a clear advantage of this model compared to a displacement-based formulation.

$$\mathbf{s}(x) = \begin{bmatrix} N(x) \\ M_z(x) \end{bmatrix} = \mathbf{H}(\mathbf{x}) \cdot \mathbf{p}^{bsc} = \begin{bmatrix} 1 & 0 & 0 \\ 0 & \frac{x}{L} - 1 & \frac{x}{L} \end{bmatrix} \begin{bmatrix} p_1^{bsc} \\ p_2^{bsc} \\ p_3^{bsc} \end{bmatrix} + \begin{bmatrix} N(x) \\ M_z(x) \end{bmatrix}_0 \tag{9.9}$$

The state determination algorithm starts using a known delta of displacement at the basic reference system for the current iteration ($\Delta\mathbf{u}^{bsc\,k}$) and the relationship between the forces and displacements of the last iteration ($\mathbf{k}^{bsc\,k-1}$) to find the increment of the nodal forces of the current iteration ($\Delta\mathbf{p}^{bsc\,k}$) as expressed by:

$$\Delta\mathbf{p}^{bsc\,k} = \mathbf{k}^{bsc\,k-1} \cdot \Delta\mathbf{u}^{bsc\,k} \tag{9.10}$$

This nodal force increment is used to find an approximate increment of the internal section forces for the current iteration ($\Delta\mathbf{s}^k$) using the previously mentioned interpolation function and subtracting the unbalanced section forces of the previous iteration $\Delta\tilde{\mathbf{s}}^{\mathbf{k-1}}$, which are explained later. It should be noted that the section forces vary with respect to the position in the element. The number of sections considered depends on the problem, but the position of the integration points are defined using Gaussian quadrature, specifically for force-based element the Gauss-Lobato quadrature is usually preferred over the Gauss-Legendre quadrature since it allows considering a section at the beginning and the end of the element.

$$\Delta\mathbf{s}^{\mathrm{k}}(\mathrm{x}) = \mathbf{H}(\mathrm{x}) \cdot \Delta\mathbf{p}^{\mathrm{bsc\,k}} \;+\; \Delta\tilde{\mathbf{s}}^{\mathbf{k-1}}(\mathrm{x}) \tag{9.11}$$

Next, an approximative increase of the section deformations (strain at the centroid and curvature) for the current iteration ($\Delta\mathbf{e}^{\mathrm{k}}$) are found using the increment of the section forces and the section flexibility matrix of the previous iteration ($\mathbf{f}^{\mathrm{k-1}}$) relating the deformations and forces of the sections.

$$\Delta\mathbf{e}^{\mathrm{k}}(\mathrm{x}) = \;\mathbf{f}^{\mathrm{k-1}}(\mathrm{x})\Delta\mathbf{s}^{\mathrm{k}}(\mathrm{x}) \tag{9.12}$$

The current total deformation of the sections is found by summing the deformation of the previous iteration ($\mathbf{e}^{\mathrm{k-1}}$) with the increment previously found. Next, this deformation is input in section (C) constitutive relation, where the cross-section, fibres, and materials are defined. The real section forces corresponding to the input deformations are found integrating the stress at each fibre according to its strain. Additionally, in this step, the flexibility matrix of the section for the current iteration ($\mathbf{f}^{\mathrm{k}}$) is found

$$\mathbf{s}^{\mathrm{k}}(\mathrm{x}) = \;\mathtt{C}(\mathbf{e}^{\mathrm{k}}(\mathrm{x})) \;=\; \mathtt{C}(\mathbf{e}^{\mathrm{k-1}}(\mathrm{x}) + \Delta\mathbf{e}^{\mathrm{k}}(\mathrm{x})) \tag{9.13}$$

The residual section deformations are found comparing the effective forces of the section with respect to the section forces of the previous step and section force increment found in eq. (9.11)

$$\mathbf{e}^{\mathrm{res\,k}}(\mathrm{x}) = \mathbf{f}^{\mathrm{k}}(\mathrm{x}) \cdot (\mathbf{s}^{\mathrm{k-1}}(\mathrm{x}) + \Delta\mathbf{s}^{\mathrm{k}}(\mathrm{x}) - \mathbf{s}^{\mathrm{k}}(\mathrm{x})) \tag{9.14}$$

These sectional residual deformations can be integrated to find the residual displacements at the elemental level. Using Gaussian quadrature, the integral can be expressed as a weighted sum of the function values at the specific position of the integration points (IP) defined by the quadrature rule.

$$\mathbf{u}^{\mathrm{bsc\ res\ k}} = \int_0^L \mathbf{H}^{\mathrm{t}}(\mathrm{x})\, \mathbf{e}^{\mathrm{res\ k}}(\mathrm{x})\mathrm{dx} \approx \frac{L}{2}\sum_{j=1}^{IP} \mathrm{w_j}\mathbf{H}_j^{\mathrm{T}}\mathrm{e}_j^{\mathrm{res\ k}} \tag{9.15}$$

Additionally, the elemental stiffness is found inverting the flexibility matrix of the element at the basic reference system. The latter is found integrating the section flexibility matrices as shown in eq. (9.16)

$$(\mathbf{k}^{\mathrm{bsc\ k}})^{-1} = \int_0^L \mathbf{H}_s^{\mathrm{T}}(\mathrm{x})\mathbf{f}^{\mathrm{k}}\mathbf{H}_{\mathrm{s}}(\mathrm{x})\mathrm{dx} \approx \frac{L}{2}\sum_{j=1}^{IP} \mathrm{w_j}\mathbf{H}_j^{\mathrm{T}}\mathbf{f}_j^{\mathrm{k}}\mathbf{H}_j \tag{9.16}$$

The residual displacements and the current stiffness matrix at the basic level are used to finally define the basic forces considering the basic forces of the previous iteration and the increment found with eq. (9.10)

$$\mathbf{p}^{\mathrm{bsc\ k}} = \mathbf{p}^{\mathrm{bsc\ k-1}} + \Delta\mathbf{p}^{\mathrm{bsc\ k}} - \mathbf{k}^{\mathrm{bsc\ k}}\mathbf{u}^{\mathrm{bsc\ res\ k}} \tag{9.17}$$

Normally the internal section forces are not in equilibrium with the section forces found with the interpolation function; therefore, these unbalanced section forces must be found to be considered in the next iteration through eq. (9.18).

$$\Delta\tilde{\mathbf{s}}^{\mathbf{k-1}}(\mathrm{x}) = \mathbf{H}(\mathrm{x})\mathbf{p}^{\mathrm{bsc\ i}} - \mathbf{s}^{\mathrm{k}}(\mathrm{x}) \tag{9.18}$$

Finally, the $\mathbf{p}^{\mathrm{bsc\ k}}$ is expressed in the global reference system and assembled in a vector considering the other elements of the structures and compared to the external forces applied to the structure. If the difference between both vectors falls below a tolerance criterium, the algorithm converges; otherwise, the increment of displacements is found, and the previous mentioned steps are performed again. The unbalanced section forces reduce to tolerable values once the algorithm converges. Further information about force-based elements can be found elsewhere[80].

9.4 Numerical methods

9.4.1 Newton-Cotes

Newton-Cotes is a group of numerical integration methods used to approximate the integral of a function. These methods use a set of equidistant points to approximate it with a polynomial, which is then integrated throughout interval interest. The most popular options are: the trapezoidal rule and Simpson's rule. In general, Newton-Cotes methods can be applied to any function over a finite interval, but their accuracy and computational cost depending on the number of points used in the approximation. Despite their limitations, Newton-Cotes methods remain popular in numerical analyses given their simplicity and ease of application. They are especially useful for integrating functions that are difficult to integrate analytically.

Table 9.4 Some Newton-Cotes formulas

n	Step size	Common name	Formula
1	$b - a$	Trapezoidal rule	$\frac{1}{2} h(f_0 + f_1)$
2	$\frac{b - a}{2}$	Simpson's rule	$\frac{1}{3} h(f_0 + 4f_1 + f_2)$
4	$\frac{b - a}{2}$	Rectangular rule, or midpoint rule	$2hf_0$

9.4.2 Gaussian Quadratures

Gaussian quadrature is a numerical integration technique used to approximate the definite integral of a function over a given interval. In the Gaussian quadrature, the nodes and weights are chosen such that the integral of a polynomial of degree n or less is exact. Specifically, if we have n+1 nodes and weights, then the integral of a polynomial of degree n or less is given by:

$$\int_{-1}^{1} f(x)dx \approx \sum_{i=1}^{n} \omega_i f(x_i) \tag{9.19}$$

where x_i is the points, and w_i is the weights. The most common type of Gaussian quadrature is the Gaussian-Legendre quadrature, which uses Legendre polynomials as the orthogonal polynomials. This quadrature rule is used for displacement-based elements shown in section 9.3.1.

A very common Gaussian quadrature is the Gauss-Lobatto quadrature which includes the endpoints of the integration interval. This quadrature rule is useful for functions that have singularities at the endpoints. Therefore, force-based elements are defined using this quadrature since they are defined using force interpolation functions. One of the main advantages of Gaussian quadrature is its high accuracy, even for a small number of nodes and weights. Additionally, it can be used for any integrable function over a finite interval.

9.4.3 Newton-Raphson

The Newton-Raphson method is an iterative numerical method used to solve equations. The method approximates a function with its tangent line at a given point, and its slope is equal to the derivative of the function at that point. The Newton-Raphson method uses this tangent line to find the zero of the function.

To use the method, an initial guess (x_0) for the root of the function. Subsequently, the tangent line to the function at that point, which has an equation of $y = f(x_0) + f'(x_0)(x - x_0)$. We then find the x-intercept of this tangent line, which is given by $x_1 = x_0 - \frac{f(x_0)}{f'(x_0)}$. This x_1 becomes the new guess, and the process is repeated until it accomplishes a convergence test with a specific criterion. This procedure is presented in Figure 9.1.

The Newton-Raphson method has many advantages over other numerical methods for finding roots. It converges very quickly, typically requiring only a few iterations, and can be used to find real or complex roots of a function. However, the method does have some limitations. It may fail to converge if the initial guess is too far from the root or the function has multiple roots in the same vicinity.

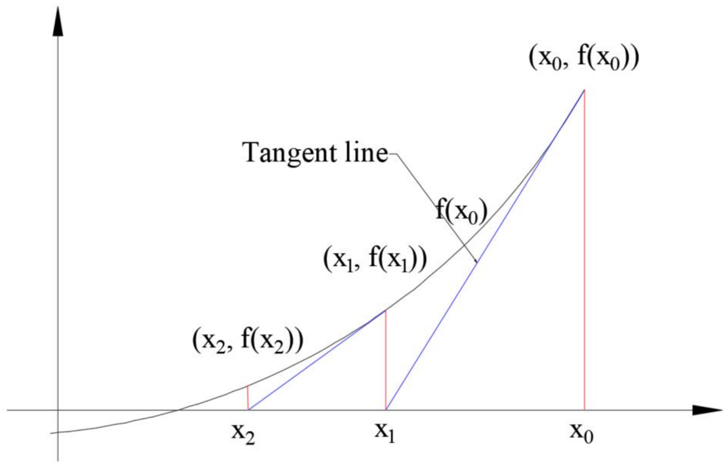

Figure 9.1 Newton Raphson method.

9.5 Viscoelasticity

Viscoelasticity is a mechanical model of materials which exhibit elastic and viscous behaviour simultaneously. The response of these materials is modelled using springs and dampers connected in series, parallel, or a combination of both.

The following equation formulates the constitutive rule of a Hooke's elastic spring.

$$\sigma = \varepsilon E \tag{9.20}$$

Where σ is the stress, ε is the strain, and E is Young's modulus. The inverse of Young's modulus is known as flexibility. A material governed by this constitutive rule will exhibit an instantaneous elastic deformation when an external load is applied. Additionally, this deformation will not vary with time, and when the external load is removed, the spring returns to its original position and shape.

The constitutive rule of a linear viscous damping element links stress and strain rates. The easiest way to assimilate this element type is to imagine a piston where deformation is achieved as the fluid inside the piston moves out. Equation (9.21) defines the behaviour of a dash-pot.

$$\sigma = \frac{d\varepsilon}{dt}\eta \tag{9.21}$$

Where η is known as the viscosity, this equation indicates that the stress in the dashpot is proportional to the strain rates. This type of behaviour governs numerous fluids, such as water, where the stress depends on how fast the change in deformations occurs. If the equation is integrated with respect to time, given eq. (9.22)

$$\sigma t = \varepsilon\eta + C \tag{9.22}$$

Assuming that the deformation is zero at the beginning and finding the strain, the eq. (9.23) is obtained

$$\varepsilon = \frac{\sigma}{\eta}t \tag{9.23}$$

The deformation will vary linearly when constant stress is applied to the damper. Immediately, the stress disappears after a certain period the deformation stops increasing. However, the deformation is permanent since no external load moves the piston back to its original position.

A material can simultaneously possess both elastic and viscous properties. Therefore, different models have been developed to predict this behaviour through systems of springs and dampers in series, parallel, or a combination of both. The model governing a material will be defined according to experimental tests.

9.5.1 Maxwell Model

The first model is a damping and a spring connected in series. The total deformation of the system can be divided into the spring deformation (ε_1) and the damper deformation (ε_2) described by eqs (9.20) and (9.23), respectively.

$$\varepsilon = \varepsilon_1 + \varepsilon_2 \tag{9.24}$$

Eq. (9.25) is obtained by deriving eq. (9.24) and replacing the terms that appear using eqs. (9.22) and (9.23).

$$\sigma + \frac{\eta}{E}\dot{\sigma} = \eta\dot{\varepsilon} \tag{9.25}$$

9.5.2 Kelvin-Voigt Model

The Kelvin-Voigt model consists of a spring and a damping unit placed in parallel. This model assumes that the spring and the damper have the same strains at each instant of time. Therefore, the total stress in the system is given by the following expression.

$$\sigma = \sigma_1 + \sigma_2 \tag{9.26}$$

Where σ_1 and σ_2 are the stress in the spring and the damper. Subsequently, the following equation, known as the standard form of the Kelvin-Voigt model, is obtained by replacing the stress definition in both components.

$$\sigma = E\varepsilon + \eta\dot{\varepsilon} \tag{9.27}$$

9.5.3 Kelvin chains and Maxwell models

The Kelvin-Voigt and Maxwell model corresponds to a damper and a spring in parallel and series, respectively. From these two formulations, it is possible to form chains of springs and dampers to create models that best fit experimental tests. The purpose of this section is not to describe this field in detail but to give the basic information the author used to understand and develop one of the damping models. Further details on viscoelasticity can be found in different books[97]

Table 9.5 Most common viscoelastic models

Model	Name	Differential equation / Inequalities
	Elastic solid	$\sigma = q_0\varepsilon$
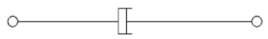	Viscous fluid	$\sigma = q_1\varepsilon$
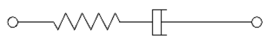	Maxwell fluid	$\sigma + p_1\dot{\sigma} = q_1\dot{\varepsilon}$
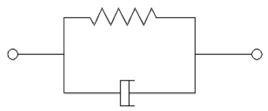	Kelvin solid	$\sigma = q_0\varepsilon + q_1\dot{\varepsilon}$
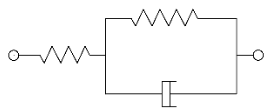	3-parameter solid	$\sigma + p_1\dot{\sigma} = q_0\varepsilon + q_1\dot{\varepsilon}$ $q_1 > p_1 q_0$
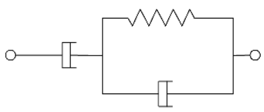	3-parameter fluid	$\sigma + p_1\dot{\sigma} = q_1\dot{\varepsilon} + q_2\ddot{\varepsilon}$ $p_1 q_1 > q_2$

9.6 Other topics

9.6.1 Energy dissipation in nonlinear time history analyses

Energy balances and the corresponding decomposition can be valuable tools to analyse the performance of damping models. The input energy (E_I) is transformed into (i) kinetic energy of the structural masses (E_K), (ii) potential energy stored elastically in the material (E_S), (iii) energy dissipated during hysteretic cycles in the inelastic excursions (E_M), and (iv) energy dissipated by the damping model (E_D). The energy balance equation for a nonlinear dynamic analysis of a MDoF [98–100] system is:

$$E_K(t) + E_D(t) + E_S(t) + E_M(t) = E_I(t) \tag{9.28}$$

The energy input by the earthquake for a system with N DoFs is:

$$E_I(t) = \int_0^t (\mathbf{P}_{Et}(t))\dot{\mathbf{U}}(t)dt = \sum_{i=1}^{N}\left(\int_0^t P_{Et,i}(t)\dot{U}_i(t)dt\right) \tag{9.29}$$

The kinetic energy of the system is given by:

$$E_K(t) = \int_0^t (\mathbf{M}\ddot{\mathbf{U}}(t))^{\mathbf{T}}\dot{\mathbf{U}}(t)dt = \sum_{i=1}^{N}\left(\int_0^t F_{M,i}(t)\dot{U}_i(t)dt\right) \tag{9.30}$$

Of particular interest to this work, the energy dissipated by the viscous damping model can be expressed by:

$$E_D(t) = \int_0^t (\mathbf{C}\dot{\mathbf{U}}(t))^{\mathbf{T}}\dot{\mathbf{U}}(t)dt = \sum_{i=1}^{N}\left(\int_0^t F_{D,i}(t)\dot{U}_i(t)dt\right) \tag{9.31}$$

Finally, the energy dissipated inelastically and stored elastically is represented by the force-displacement relation of the system, written as:

$$E_M(t) + E_s(t) = \int_0^t \mathbf{f}(\mathbf{U}(t))\dot{\mathbf{U}}(t)dt = \sum_{i=1}^{N}\left(\int_0^t f(U(t))_i\dot{U}_i(t)dt\right) \tag{9.32}$$

The above energy approach is used in this work to compare the performance of several damping models, which complements the analysis of other aspects of the structural response, such as displacements, velocities, accelerations, and internal forces.

9.6.2 Lumped and consistent mass formulation of beam and truss elements

Lumped and consistent mass formulation for a beam element

The lumped-mass matrix of a beam is expressed by (9.23). Where the total mass of the beam is lumped at each node, corresponding to the translational DOFs

$$\mathbf{m} = \frac{\rho AL}{2} \begin{array}{c} \begin{array}{cccc} \hat{d}_{1y} & \hat{\phi}_1 & \hat{d}_{2y} & \hat{\phi}_2 \end{array} \\ \begin{bmatrix} 1 & 0 & 0 & 0 \\ 0 & 0 & 0 & 0 \\ 0 & 0 & 1 & 0 \\ 0 & 0 & 0 & 0 \end{bmatrix} \end{array} \tag{9.33}$$

In this formulation, the inertia effect associated with rotational DOFs is not considered, but it is possible to calculate it for half of the beam segment about each end node employing the following expressions.

$$\mathrm{I} = \iiint_0^{L/2} \rho x^2 \, dV \tag{9.34}$$

$$\mathrm{I} = \int_0^{L/2} A\rho x^2 \, dx \tag{9.35}$$

$$\mathrm{I} = \frac{1}{3} A\rho \left(\frac{L}{2}\right)^3 \tag{9.36}$$

The lumped mass formulation has been preferred because the mass matrix is diagonal, making calculation more efficient and faster. Nevertheless, the consistent-mass formulation is preferred in some cases and can be obtained by solving the following equation.

$$\mathbf{m} = \iiint_0^{L} \rho \begin{Bmatrix} N_1 \\ N_2 \\ N_3 \\ N_4 \end{Bmatrix} \{N_1 \quad N_2 \quad N_3 \quad N_4\} dx \, dA \tag{9.37}$$

Where N_n are the shape functions[62]

$$N_1 = \frac{1}{L^3}(2x^3 - 3x^2L + L^3) \tag{9.38}$$

$$N_2 = \frac{1}{L^3}(x^3L - 2x^2L^2 + xL^3) \tag{9.39}$$

$$N_3 = \frac{1}{L^3}(-2x^3 + 3x^2L) \tag{9.40}$$

$$N_4 = \frac{1}{L^3}(x^3L - x^2L^2) \tag{9.41}$$

The consistent mass matrix is obtained by multiplying both vectors, performing the integration, and replacing limits.

$$\mathbf{m} = \frac{\rho AL}{420} \begin{bmatrix} 156 & 22L & 54 & -13L \\ 22L & 4L^2 & 13L & -3L^2 \\ 54 & 13L & 156 & -22L \\ -13L & -3L^2 & -22L & 4L^2 \end{bmatrix} \tag{9.42}$$

Consistent and lumped mass formulation for a truss element

The lumped mass formulation for a truss element is found lumping the mass of the element in both DOFs in each specific direction. As a consequence, the lumped mass matrix for a truss element is defined as:

$$\mathbf{m} = \frac{\rho AL}{2}\begin{bmatrix} 1 & 0 & 0 & 0 \\ 0 & 1 & 0 & 0 \\ 0 & 0 & 1 & 0 \\ 0 & 0 & 0 & 1 \end{bmatrix} \tag{9.43}$$

The consistent mass matrix of a truss requires the solution of Equation (9.37). The shape functions N are defined considering the axial and transversal displacement of the element in terms of the nodal displacement.

$$\mathbf{N} = \frac{1}{L}\begin{bmatrix} L - x & 0 & x & 0 \\ 0 & L - x & 0 & x \end{bmatrix} \tag{9.44}$$

Solving the system, consistent mass formulation is obtained.

$$\mathbf{m} = \frac{\rho AL}{6}\begin{bmatrix} 2 & 0 & 1 & 0 \\ 0 & 2 & 0 & 1 \\ 1 & 0 & 2 & 0 \\ 0 & 1 & 0 & 2 \end{bmatrix} \tag{9.45}$$

Consistent and lumped mass formulation of a plane frame.

To obtain the consistent and lumped mass formulation, it is necessary to combine the beam and truss mass matrix respecting each DOF—finally, eq. (9.46) is obtained.

$$\mathbf{m} = \frac{\rho AL}{2}\begin{bmatrix} 1 & 0 & 0 & 0 & 0 & 0 \\ 0 & 1 & 0 & 0 & 0 & 0 \\ 0 & 0 & 0 & 0 & 0 & 0 \\ 0 & 0 & 0 & 1 & 0 & 0 \\ 0 & 0 & 0 & 0 & 1 & 0 \\ 0 & 0 & 0 & 0 & 0 & 0 \end{bmatrix} \tag{9.46}$$

And the consistent mass is given by eq. (9.47)

$$\mathbf{m} = \frac{\rho AL}{420}\begin{bmatrix} 140 & 0 & 0 & 70 & 0 & 0 \\ 0 & 156 & 22L & 0 & 54 & -13L \\ 0 & 22L & 4L^2 & 0 & 13L & -3L^2 \\ 70 & 0 & 0 & 140 & 0 & 0 \\ 0 & 54 & -13L & 0 & 156 & -22L \\ 0 & 13L & -3L^2 & 0 & -22L & 4L^2 \end{bmatrix} \tag{9.47}$$

10. Annexes - Software developed

One of the main activities of this PhD was developing a finite element program where the analyses were performed, and damping models were implemented. Estimating how many lines of code the program has is complex since it depends on what is counted. However, it is estimated that the program has between 25000-50000 lines of code. All developments were not necessarily used in this research and were carried out to develop simulations that did not concern this dissertation.

10.1 Source code

Send an email to chepe852@hotmail.com, jfbaenau@eafit.edu.co or jose.baenaurrea@uclouvain.be

10.2 Comparison with existing programs

The software development took considerable time and tens of thousands of lines of code. Due to the program's size, it is not difficult to make mistakes. Hence, the program results were compared to ensure that the results obtained in this research are valid. However, all validations are not presented due to space constraints.

This section compares the results of the software developed in this research with OpenSees. Originally comparisons were also made with SeismoStruct, but these are not presented here since the distributed plasticity formulations were developed by researchers involved in OpenSees.

The results clearly show that the results between the two software are equivalent. This ensures that the results obtained in this dissertation are correct.

10.2.1 Static analysis - Steel structure using displacement-based elements.

The first comparison corresponds to a 7.5 m high 2D steel column composed of a rectangular cross-section of 40x40 cm with 50 fibres using the constitutive rule of Menegotto and Pinto. The column is modelled with a single element, and a displacement of 1.2 m is applied at the top. Figure 10.1 presents the force-displacement curve of the element where the results of the developed program and OpenSees are equivalent.

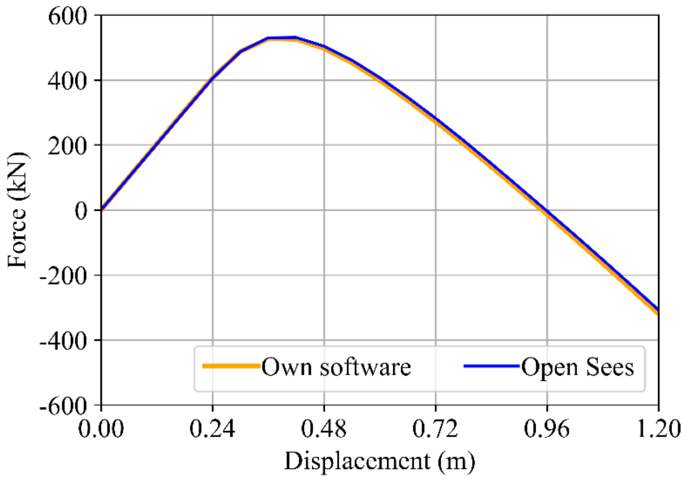

Figure 10.1 Force-Displacement curve of a steel structure using the program developed and OpenSees.

10.2.2 Static analysis - Steel structure using force-based elements.

The column presented in the previous section is also modelled with elements using force interpolation functions. The properties are the same as those presented in the last example. Figure 10.2 also shows that the results of the program and OpenSees are equivalent.

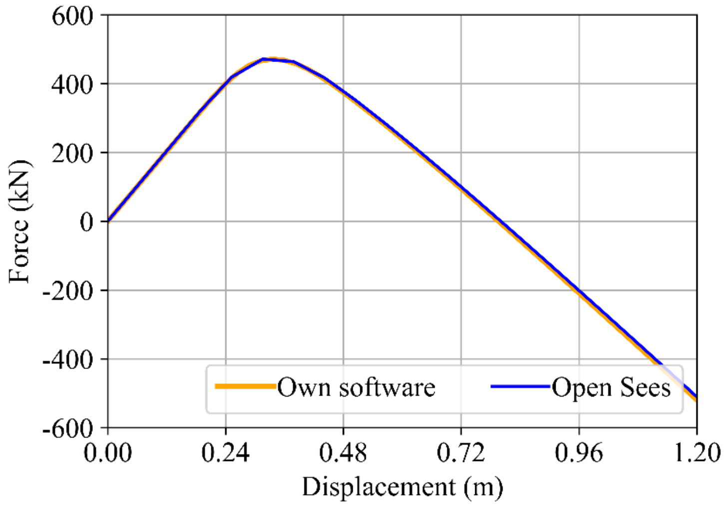

Figure 10.2 Force-Displacement curve of a steel structure using the program developed and OpenSees.

10.2.3 Static analysis - Reinforced concrete structure using displacement-based elements.

The software was evaluated by modelling concrete structures. The analysed system corresponds to a 2 m high concrete column composed of a rectangular cross-section of 30x30 cm with 50 concrete fibres and six steel fibres. The steel fibres are distributed evenly in pairs along the cross-section and correspond to 22 mm steel bars. An extreme displacement is applied to the column to see how the software behaves under high demands. The ultimate strains of the constitutive rules were removed in this particular case study. Figure 10.3 shows that the results are equivalent.

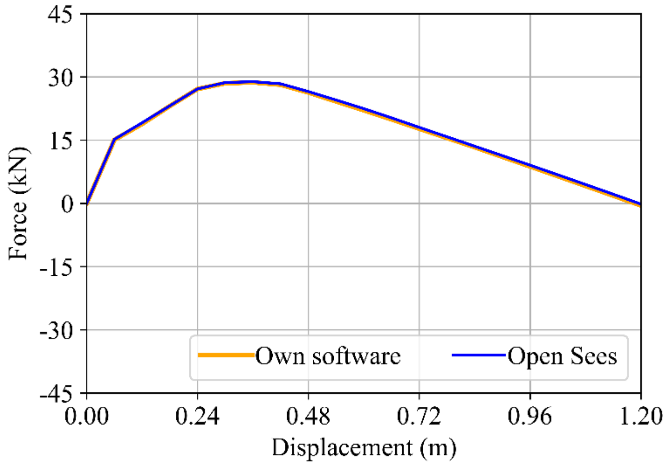

Figure 10.3 Force-Displacement curve of a RC structure using the program developed and OpenSees.

10.2.4 Static analysis – Reinforced concrete structure using force-based elements.

The above example was also employed to verify the response with elements using force interpolation functions, with a higher axial load. The results are shown in Figure 10.4. As in the previous cases, the results are equivalent.

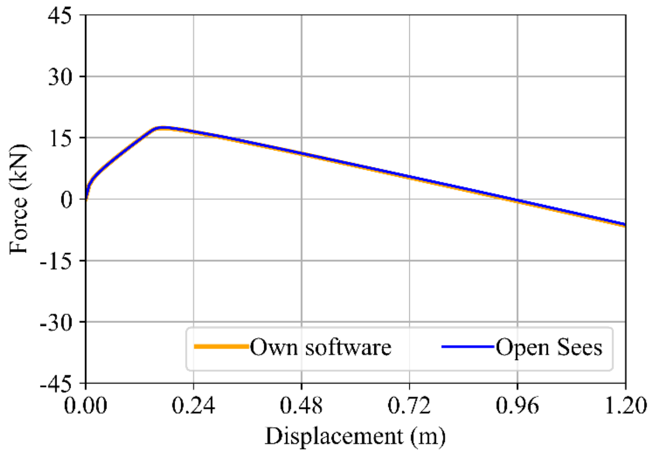

Figure 10.4 Force-Displacement curve of RC structure using the program developed and OpenSees.

10.2.5 Dynamic analysis of the steel frame presented by Bernal

The software was used to predict the response of the steel frame presented by Bernal[25] under the ground motion record of El Centro. However, the structure was simulated with distributed plasticity elements and not with concentrated plasticity, as indicated in the article. As in the previous cases, the results of both software are equivalent.

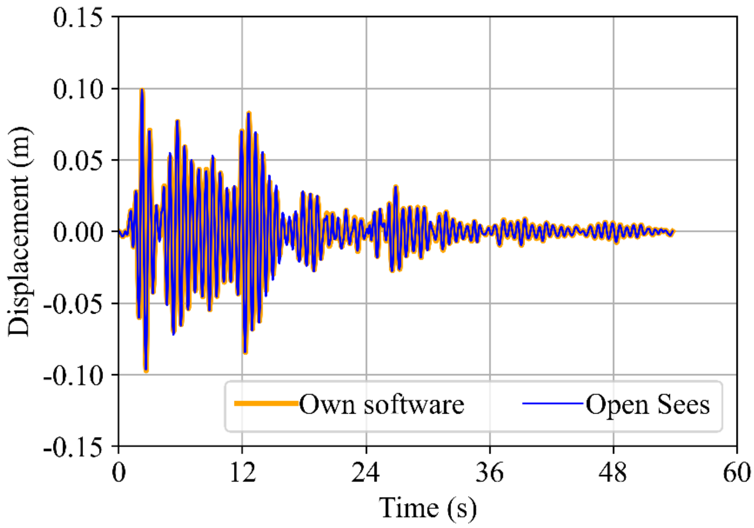

Figure 10.5 Time-history response of the frame presented in Bernal[25] using the program developed and OpenSees.